



HAL
open science

Integration of in situ stress measurements in a non-elastic rock mass

Bruno Gomes de Figueiredo

► **To cite this version:**

Bruno Gomes de Figueiredo. Integration of in situ stress measurements in a non-elastic rock mass. Earth Sciences. Université de Strasbourg, 2013. English. NNT : 2013STRAH022 . tel-01038115

HAL Id: tel-01038115

<https://theses.hal.science/tel-01038115>

Submitted on 23 Jul 2014

HAL is a multi-disciplinary open access archive for the deposit and dissemination of scientific research documents, whether they are published or not. The documents may come from teaching and research institutions in France or abroad, or from public or private research centers.

L'archive ouverte pluridisciplinaire **HAL**, est destinée au dépôt et à la diffusion de documents scientifiques de niveau recherche, publiés ou non, émanant des établissements d'enseignement et de recherche français ou étrangers, des laboratoires publics ou privés.

UNIVERSITÉ DE STRASBOURG
LABORATOIRE NATIONAL DE GÉNIE CIVIL

ÉCOLE DOCTORALE STUE
CNRS – UMR 7516

THÈSE soumise pour l'obtention du grade de Docteur de l'Université de Strasbourg
Spécialité : Géophysique

Bruno FIGUEIREDO

10 Septembre 2013

**Integration of *in situ* stress measurements
in a non-elastic rock mass**

**L'intégration des mesures de contraintes
in situ dans un massif rocheux non élastique**

Commission d'examen :

François Cornet	Université de Strasbourg/EOST	Directeur de thèse
Luís Lamas	Laboratoire National de Génie Civil (LNEC), Portugal	Co-Directeur de thèse
Frédéric Pellet	Université de Lyon/INSA	Rapporteur externe
José Lemos	Laboratoire National de Génie Civil (LNEC), Portugal	Rapporteur externe
Jean Schmittbuhl	Université de Strasbourg/EOST	Rapporteur interne

UNIVERSITÉ DE STRASBOURG
LABORATOIRE NATIONAL DE GÉNIE CIVIL

ÉCOLE DOCTORALE STUE
CNRS – UMR 7516

THÈSE soumise pour l'obtention du grade de Docteur de l'Université de Strasbourg
Spécialité : Géophysique

Bruno FIGUEIREDO

10 Septembre 2013

**Integration of *in situ* stress measurements
in a non-elastic rock mass**

**L'intégration des mesures de contraintes
in situ dans un massif rocheux non élastique**

Commission d'examen :

François Cornet	Université de Strasbourg/EOST	Directeur de thèse
Luís Lamas	Laboratoire National de Génie Civil (LNEC), Portugal	Co-Directeur de thèse
Frédéric Pellet	Université de Lyon/INSA	Rapporteur externe
José Lemos	Laboratoire National de Génie Civil (LNEC), Portugal	Rapporteur externe
Jean Schmittbuhl	Université de Strasbourg/EOST	Rapporteur interne

Abstract

In situ tests are essential for characterising the natural stresses that exist in a rock mass and such a characterisation is required for designing deep underground structures, such as caverns or tunnels. However, due to the various factors that influence rock stresses, such as rock heterogeneity or existing geological structures and the correlated spatial variability of rock mass properties, *in situ* tests provide information on the stresses only at the location where they have been performed. The results of these various types of measurements must be integrated later into a simple model to extrapolate them to the volume of interest for the design of the underground structures of concern.

When different types of measurement techniques are used at the same location, the results must be combined into a single inversion scheme to determine the stress field that best fits all the data. Numerical models are sometimes developed to integrate all the tests results within a single model that is used to determine the most probable stress state in the volume of interest for the design of the underground structures.

A case study is considered in which data produced by different techniques have been gathered in various locations within a rock mass in which topography effects are most likely significant. Measurements were performed for the design of a re-powering scheme that includes a new hydraulic conduit and an underground cavern that will primarily be excavated in granite.

The measurements included hydraulic tests, small flat jack tests and overcoring tests. Hydraulic testing provided the means to determine the complete stress profile in two 500 m deep vertical boreholes that reached the location of the future powerhouse cavern. Overcoring tests conducted in two 60 m deep vertical boreholes drilled from an existing adit some 160 m below ground surface provided information about a site located approximately 1.7 km away from the location of the hydraulic tests. Small flat jack tests performed near the location of overcoring tests provided further information on the stress state in the immediate vicinity of the adit.

The results of these various measurements revealed the existence of local stress heterogeneity, spatial variability in the rock mass properties, non-elastic behaviour of the rock mass for low stress levels and non-elastic stress variations close to the existing adit. A comparison between the results of the hydraulic and overcoring tests shows that the stresses estimated by both techniques are of similar magnitude. But a comparison between the results of the small flat jack tests and the overcoring tests conducted at

approximately the same location outline a significant discrepancy between the stress field close to the adit and that observed away from it.

An integrated approach for extrapolating the results from the various *in situ* tests to the rock mass volume of interest for the hydroelectric power scheme is presented. This approach includes the development of an equivalent continuum mechanics model, which is processed with the FLAC3D code from Itasca (2009). The model is used for identifying the parameters that minimise the misfit between the measured and calculated stresses. By performing a gravitational analysis and considering the elastic properties obtained from laboratory tests conducted on intact cores, a discrepancy is found between the sub-horizontal stresses measured *in situ* and the results obtained with the model. Then, the possible influence of tectonic stresses is investigated, and rejected, based on the data published in the World Stress Map database. In fact, the model shows that most of the hydraulic and overcoring data are consistent with a linearly elastic equivalent geomaterial, the properties of which correspond to a much softer material than suggested by laboratory tests on cores. This finding leads to conclude that the large-scale long-term stress field in this granitic massif is controlled by shear stress relaxation along the various fractures and faults that affect this massif. Hence the long-term behavior of this granite massif is found to differ markedly from the short-term one considered for interpreting overcoring tests (most likely because overcoring concerns only sane granit). Further, there is no need to introduce a tectonic stress component for fitting the data at this location, a fairly satisfactory feature given the altitude of the site.

However, the model cannot explain the flat jack data or two overcoring results obtained close to the adit from which the measurements were conducted. Hence, the equivalent geomaterial defined for this massif is not representative of the material close to the adit and cannot be used for evaluating the stress field in the vicinity of this adit.

This concludes that the rock mass rheology plays an important role on the *in situ* stresses. The characterisation of the rock mass rheology is difficult because it is out of reach of almost all laboratory and field testing methods due to the time scale involved. But, the knowledge of large-scale stress fields helps better constrain the long-term mechanical properties of the material under consideration.

Résumé

Les tests *In situ* sont essentiels pour caractériser les contraintes naturelles présentes au sein d'une masse rocheuse et une telle caractérisation est nécessaire pour concevoir des structures souterraines profondes, telles que des grottes ou des tunnels. Toutefois, en raison de divers facteurs influençant les contraintes de la roche, tels que son hétérogénéité ou des structures géologiques existantes, et la variabilité spatiale corrélée des propriétés de la masse rocheuse, les tests *in situ* ne fournissent des informations sur les contraintes que là où ils sont réalisés. Les résultats de ces divers types de mesures doivent être par la suite intégrés à un modèle simple afin de les extrapoler au volume désiré pour la conception des structures souterraines concernées.

Lorsque différents types de techniques de mesure sont utilisés au même endroit, les résultats doivent être combinés en un même plan d'inversion pour déterminer quel champ de contrainte s'applique le mieux aux données. Des modèles numériques sont parfois développés pour intégrer tous les résultats de tests en un seul modèle qui est utilisé pour déterminer l'état de contrainte le plus probable dans le volume concerné.

Considérons un cas d'étude dans lequel les données produites par différentes techniques ont été obtenues en divers points d'une masse rocheuse où les effets topographiques sont très probablement significatifs. Les mesures ont été effectuées pour la conception du réseau hydroélectrique. Le réseau comprend une conduite hydraulique ainsi qu'une nouvelle centrale souterraine placée à mi-parcours de la conduite et sera principalement creusé dans le granite.

Les mesures comprenaient des tests hydrauliques, des tests avec petits vérins plats et des tests par surcarottage. Les tests hydrauliques ont fourni le moyen de déterminer le profil de contrainte complet de deux puits de forage verticaux de 500 m de profondeur qui atteignaient l'emplacement de la future centrale souterraine. Les tests par surcarottage menés dans deux puits verticaux de 60 m de profondeur, percés depuis une galerie existante à quelques 160 m sous la surface du sol ont fourni des informations sur un site situé à environ 1,7 km du lieu des tests hydrauliques. Les tests avec les petits vérins plats réalisés près de l'emplacement des tests par surcarottage ont fourni de nouvelles informations sur l'état de contrainte dans le voisinage immédiat de la galerie.

Les résultats de ces différentes mesures révèlent l'existence de l'hétérogénéité locale des contraintes, la variabilité spatiale des propriétés de la masse rocheuse, le comportement non-élastique de la masse rocheuse pour un faible niveau de contraintes

et les variations non-élastiques des contraintes à proximité de la galerie d'accès existante. Si l'on compare les essais hydrauliques et les essais de surcarottage, leurs résultats sont concordent généralement. Mais la comparaison entre les résultats des essais de petits vérins plats et des essais de surcarottage effectués approximativement au même endroit montrent un écart important entre le champ de contraintes mesuré à proximité de la galerie d'accès et celui observé plus loin.

Les diverses données ont été intégrées à un modèle unique afin d'évaluer le champ de contrainte régional et ainsi d'extrapoler les résultats des divers tests au volume de masse rocheuse concerné par le plan hydroélectrique. Le modèle inverse proposé ici a pour but de déterminer le champ de contrainte régional naturel qui correspond le mieux aux données prélevées depuis la galerie existante. Ce modèle correspond à un géomatériau continu équivalent et les équations différentielles caractéristiques correspondantes sont résolues avec des différences finies explicites en utilisant le logiciel FLAC3D (Itasca, 2009).

Le modèle est utilisé pour identifier les paramètres qui minimisent le décalage entre les contraintes mesurées et calculées. En réalisant une analyse gravitationnelle et en tenant compte des propriétés élastiques obtenues grâce à des tests effectués en laboratoire sur des carottes intactes, une différence apparaît entre les contraintes subhorizontales mesurées *in situ* et les résultats obtenus avec le modèle.

Ainsi, la possible influence des contraintes tectoniques est étudiée, et rejetée, en se fondant sur les données publiées dans la base de données de la Carte du monde des contraintes. De fait, le modèle montre que la plupart des données hydrauliques et des tests par surcarottage sont cohérentes avec un géomatériau à élasticité linéaire équivalent, dont les propriétés correspondent à un matériau beaucoup plus souple que ce que suggèrent les tests en laboratoire sur les carottes.

Mais ce modèle simple n'explique pas la plupart des tests avec les petits vérins plats ni les deux tests par surcarottage proches de la galerie. Il peut être envisagé que le matériau équivalent à considérer près de la galerie doit prendre en compte les dommages causés par les explosions lors de la construction de celle-ci. De plus, pour un tel matériau, la déformation plastique pourrait être prise en compte lors de l'analyse des composantes de contrainte locale.

Cette étude conclut que la rhéologie de la masse rocheuse joue un rôle important sur les contraintes *in situ*. La caractérisation de la rhéologie de la masse rocheuse est difficile parce qu'elle dépasse toutes les méthodes de test en laboratoire et sur le terrain, en raison de l'échelle de temps concernée. Et les paramètres d'élasticité obtenus à partir des tests réalisés sur les carottes intactes pourraient être irréalistes dans la simulation du

comportement de la masse rocheuse avec des échelles spatiales et temporelles plus étendues, du fait qu'avec une grande échelle spatiale, la roche comprend un réseau de fractures naturelles important dont le comportement est dépendant du temps. Mais, la connaissance de champs de contrainte à grande échelle aide à mieux restreindre les propriétés mécaniques à long terme du matériau considéré.

Résumé étendu en français

Les tests *in situ* sont essentiels pour caractériser les contraintes naturelles présentes au sein d'une masse rocheuse et une telle caractérisation est nécessaire pour concevoir des structures souterraines profondes, telles que des grottes ou des tunnels. Toutefois, en raison de divers facteurs influençant les contraintes de la roche, tels que son hétérogénéité ou des structures géologiques existantes, et la variabilité spatiale corrélée des propriétés de la masse rocheuse, les tests *in situ* ne fournissent des informations sur les contraintes que là où ils sont réalisés. Les résultats de ces divers types de mesures doivent être par la suite intégrés à un modèle simple afin de les extrapoler au volume désiré pour la conception des structures souterraines concernées.

Lorsque différents types de techniques de mesure sont utilisés au même endroit, les résultats doivent être combinés en un même plan d'inversion pour déterminer quel champ de contrainte s'applique le mieux aux données. De tels plans d'intégration ont déjà été présentés par plusieurs auteurs, dont les suivants : tests de fracturation hydraulique (HF) et tests hydrauliques sur des fractures préexistantes (HTPF) (Cornet et Valette, 1984), tests hydrauliques (HF et HTPF) et vérins plats (Cornet, 1996), tests hydrauliques et mécanismes focaux de la sismicité induite (Cornet et Yin, 1995), tests hydrauliques et tests par surcarottage (Ask, 2004) et surcarottage et vérins plats (Lamas *et al.*, 2010).

Des modèles numériques sont parfois développés pour intégrer tous les résultats de tests en un seul modèle qui est utilisé pour déterminer l'état de contrainte le plus probable dans le volume concerné (Hart 2003, Lamas *et al.* 2010, Matsuki *et al.* 2009, Muralha *et al.* 2009, Sousa *et al.* 1986). Dans les régions montagneuses, ces modèles sont un outil essentiel pour évaluer l'influence de la topographie sur le champ de contrainte.

Les différences dues à la charge gravitaire trouvées entre les contraintes relevées par les tests *in situ* et les résultats du modèle numérique obtenus ont été justifiées par l'existence de contraintes tectoniques. En admettant cette hypothèse, une analyse élastique linéaire est habituellement effectuée pour déterminer la contrainte horizontale qui doit être appliquée aux limites du modèle afin d'obtenir une bonne concordance avec les données (Li *et al.*, 2009, McKinnon 2001, Tonon *et al.*, 2001).

Considérons un cas d'étude dans lequel les données produites par différentes techniques ont été obtenues en divers points d'une masse rocheuse où les effets topographiques sont très probablement significatifs. Les mesures ont été effectuées pour la conception du réseau hydroélectrique Paradela II, situé sur le fleuve Cávado, au nord

du Portugal. Le réseau comprend 10 kilomètres de conduite hydraulique ainsi qu'une centrale électrique placée à mi-parcours de la conduite (Figure 1) et sera principalement creusé dans le granite. Il comprend une nouvelle centrale souterraine, une chambre accueillant les vannes et une grande chambre d'équilibre avec plusieurs galeries situées à 500 m sous la surface du sol.

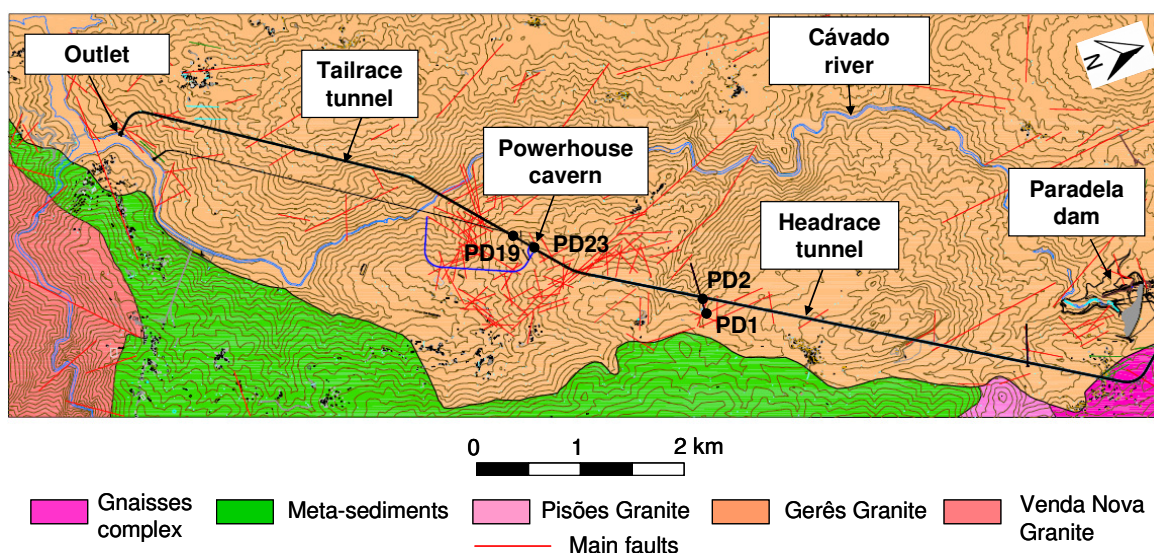


Figure 1 : Plan de réalimentation électrique Paradela II (avec l'aimable autorisation d'Énergie Du Portugal – EDP).

Les mesures comprenaient des tests hydrauliques, des tests avec petits vérins plats et des tests par surcarottage. Les tests hydrauliques ont fourni le moyen de déterminer le profil de contrainte complet de deux puits de forage verticaux de 500 m de profondeur qui atteignaient l'emplacement de la future centrale souterraine. Les tests par surcarottage menés dans deux puits verticaux de 60 m de profondeur, percés depuis une galerie existante à quelques 160 m sous la surface du sol ont fourni des informations sur un site situé à environ 1,7 km du lieu des tests hydrauliques. Les tests avec les petits vérins plats réalisés près de l'emplacement des tests par surcarottage ont fourni de nouvelles informations sur l'état de contrainte dans le voisinage immédiat de la galerie.

Les tests hydrauliques ont fourni le moyen de déterminer le profil de contrainte de deux puits de forage verticaux d'une profondeur de 500 m (PD19 et PD23 ; Figure 2a). Ces deux puits sont distants de 100 m et atteignent le futur emplacement de la centrale souterraine. Les tests ont été effectués entre 200 et 500 m de profondeur, c.-à-d. au-dessus et en dessous de l'altitude du lit de la proche rivière.

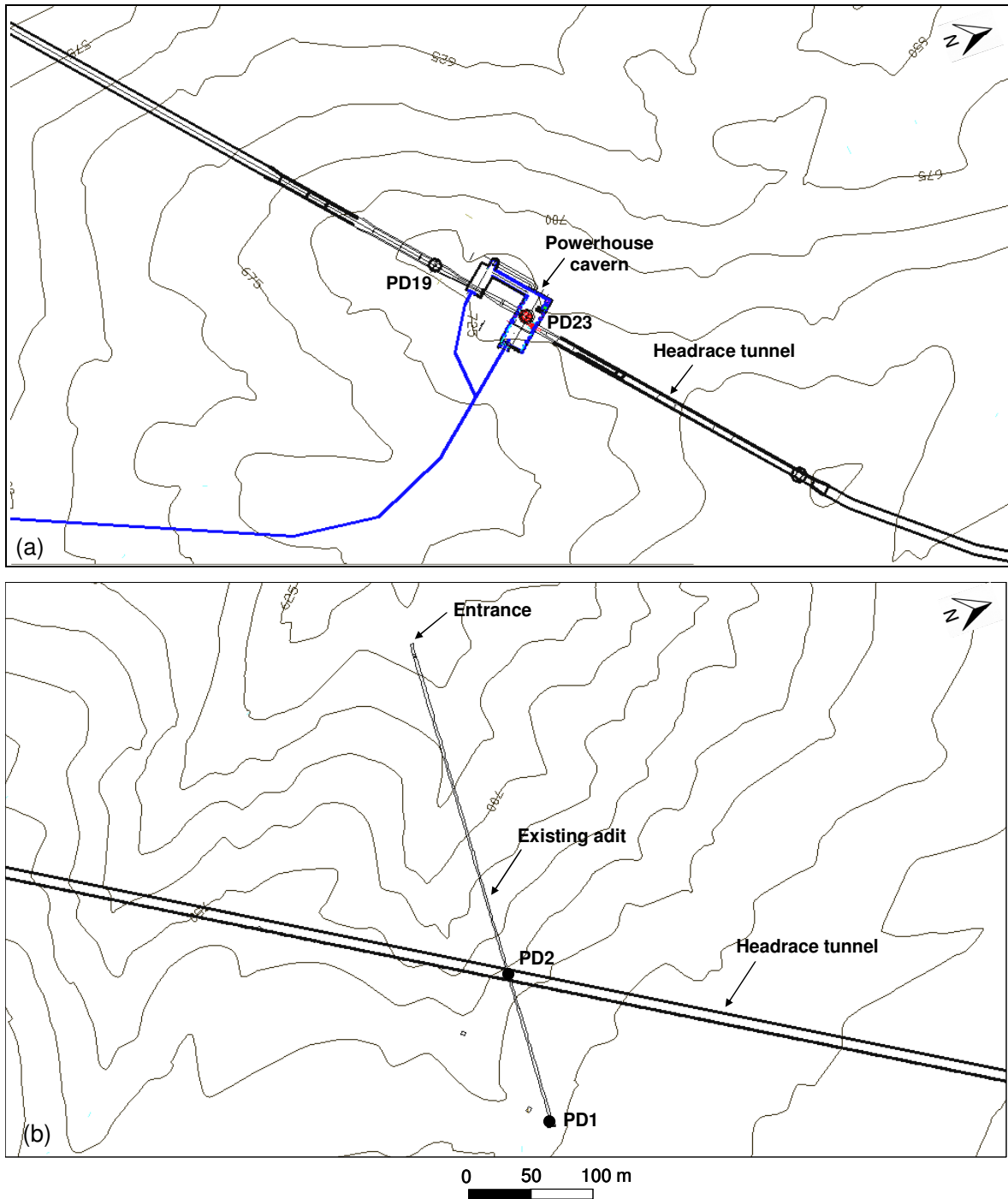


Figure 2 : Emplacement des tests hydrauliques (a) et des tests par surcarottage (b).

En un autre point, à environ 1,7 km du site des tests hydrauliques, des tests par surcarottage (OC) et avec petits vérins plats (SFJ) ont été effectués. Les tests par surcarottage ont été réalisés afin de déterminer le tenseur des contraintes complet à six profondeurs différentes dans deux puits de forages verticaux de 60 m (PD1 et PD2 ; Figure 2b), situés à environ 4550 m en aval de la prise d'eau. Ces puits sont séparés de 150 mètres et ont été percés depuis une galerie existante située à 160 mètres sous la

surface du sol. Dans le puits PD1, les tests ont été réalisés à des profondeurs comprises entre 205 et 251 m sous la surface du sol. Dans le puits PD2, les tests ont été effectués à des profondeurs situées entre 163 et 202 m sous la surface. Les deux tests ont été menés approximativement à la même profondeur dans les deux puits. Tous les tests ont été réalisés en dessous du lit de la rivière.

Les tests avec les petits vérins plats ont été effectués pour déterminer la contrainte normale sur divers plans perpendiculaires aux parois de la galerie située près des puits où les tests par surcarottage ont été menés. Quatre tests ont été réalisés dans un site (SFJ1) situé à moins de 3 m du puits de forage PD1, et huit tests dans des sites (SFJ2 et SFJ3) situés à moins de 50 m du puits PD2. La Figure 3 présente une coupe transversale verticale le long de l'axe de la galerie, ainsi que l'emplacement des tests par surcarottage et des tests avec les petits vérins plats.

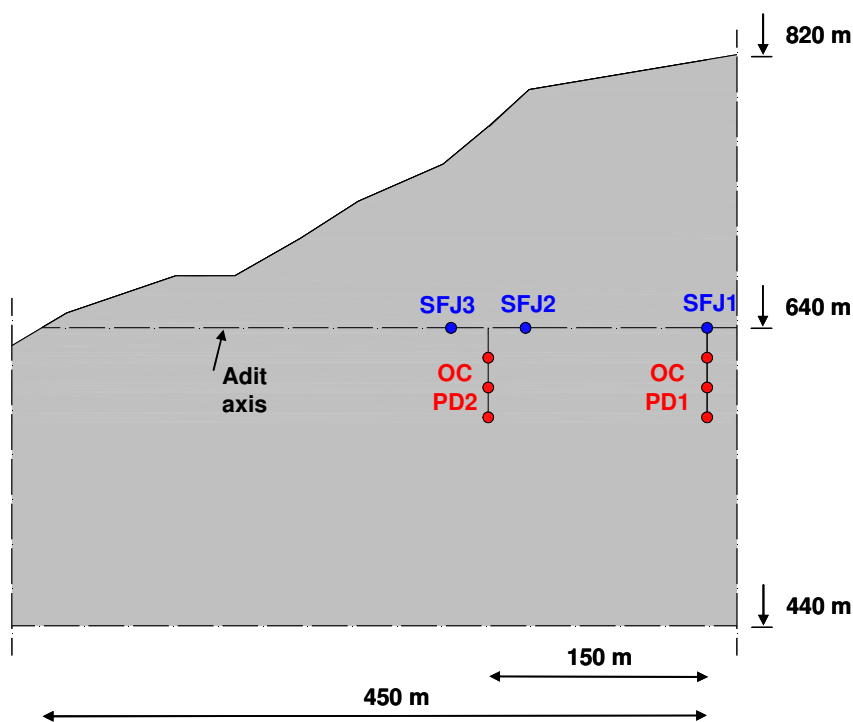


Figure 3 : Coupe transversale verticale le long de l'axe de la galerie montrant l'emplacement des tests par surcarottage et des tests avec les petits vérins plats.

Les tests hydrauliques ont nécessité deux techniques différentes, la fracturation hydraulique et le test hydraulique de fractures préexistantes, conformément aux procédures décrites par Haimson et Cornet (2009). Les tests de fracturation hydraulique impliquent la pressurisation d'une section de puits de forage intacte d'1 m de long, scellée à l'aide de deux packers jusqu'à ce que les parois du puits se fracturent. Au cours de ces mesures, le rapport pression intermédiaire *versus* temps est enregistré (Figure 4). La

pression nécessaire à la fracturation est appelée pression de rupture, P_b . La fracture se propage dans la direction qui offre le moins de résistance, qui est habituellement perpendiculaire à la contrainte principale minimum *in situ*. Lorsque l'injection s'arrête et que le système hydraulique reste scellé, la pression diminue immédiatement. Elle décroît d'abord très rapidement tandis que le liquide suit la pointe de la fracture qui s'étend toujours, puis nettement moins vite alors que la fracture se referme. La pression à laquelle la fracture se referme est appelée pression de fermeture P_s . Celle-ci représente le niveau transitoire entre la baisse rapide et la baisse lente de la pression et elle est considérée comme étant égale à la composante de contrainte agissant normalement sur le plan de la fracture (c.-à-d. la composante de contrainte principale minimum pour de vraies fractures hydrauliques). Ces cycles de pressurisation sont répétés plusieurs fois afin d'obtenir une redondance dans la détermination de la pression de fermeture.

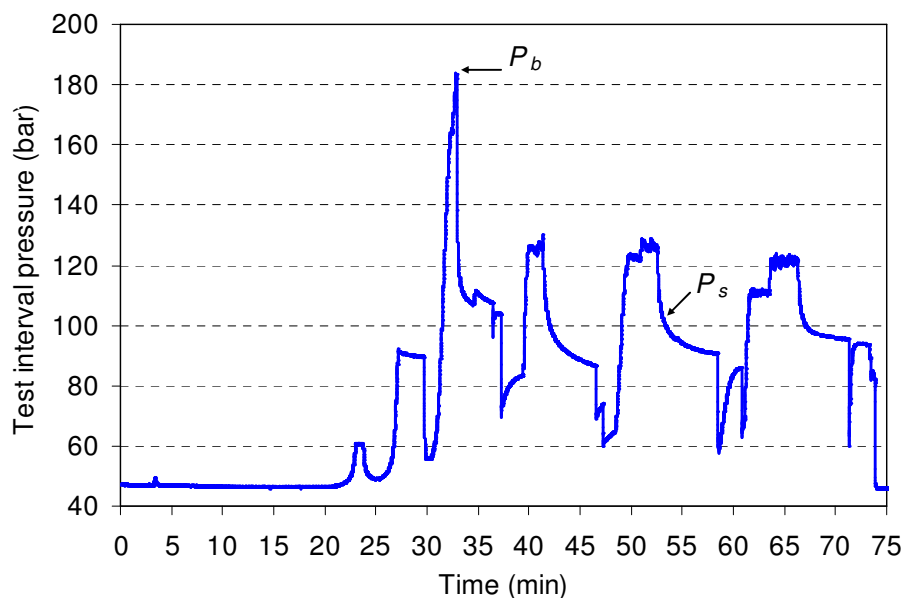


Figure 4 : Enregistrement réel du rapport pression intermédiaire *versus* temps dans un test de fracturation hydraulique.

Les tests hydrauliques de fractures préexistantes fournissent des mesures de la composante de contrainte normale exercée sur la fracture préexistante testée (Cornet 1993, Cornet et Valette 1984).

L'analyse des données hydrauliques revient à déterminer les contraintes normales exercées sur les plans de fracture testés, leur profondeur sous la surface et leur orientation par rapport au nord. L'inversion des données hydrauliques est réalisée pour déterminer le champ de contrainte complet le long des axes des puits, qui correspond aux

mesures de contrainte normale associées aux plans de fracture testés (Cornet et Valette 1984, Tarantola et Valette 1982).

La méthode de surcarottage se base sur la relaxation de contrainte autour d'un puits de forage et donne l'état de contrainte complet à l'endroit correspondant à travers une unique opération de surcarottage (Pinto et Cunha, 1986). Un test se présente comme suit : (1) forage d'un puits d'un diamètre de 140 mm jusqu'à la profondeur désirée ; (2) forage d'un puits concentrique d'un diamètre de 37 mm depuis le fond du large puits dans lequel l'instrument de mesure de la pression est inséré et collé aux parois à l'aide d'une résine époxy ; et (3) reprise du forage du large puits à une profondeur compatible avec la relaxation de contrainte complète autour de la cellule STT.

Après le surcarottage, la carotte avec l'instrument de mesure de la pression est récupérée, et le contenu de la mémoire (pressions, températures et durées) est transféré sur un ordinateur. La différence entre ces valeurs est calculée, ce qui correspond à la pression résultant du surcarottage. Afin de déterminer les constantes d'élasticité des carottes issues du surcarottage, elles sont placées à l'intérieur d'une chambre biaxiale dans laquelle une pression hydraulique radiale est appliquée, et la déformation en résultant à l'emplacement des dix jauges de déformation est mesurée.

Une fois que les pressions résultant du surcarottage sont mesurées et que les constantes élastiques sont déterminées, les six composantes de l'état de contrainte sont établies.

La méthode de test avec les petits vérins plats (Rocha *et al.* 1966) se fonde sur le principe de relaxation de contrainte partielle, suivi par une compensation de la contrainte (Habib et Marchand 1952). Avec cette technique, deux paires d'aiguilles sont placées à la surface de la masse rocheuse et la distance initiale qui les sépare est mesurée à l'aide de sondes numériques. Puis, entre les deux aiguilles, une fente de 10 mm d'épaisseur et d'une profondeur de 27 cm est creusée perpendiculairement à la surface de la masse rocheuse à l'aide d'un disque diamant de 60 cm de diamètre. En raison de la relaxation de contrainte partielle, des déformations apparaissent dans la direction normale de la fente et la distance entre les aiguilles diminue. Ensuite, un vérin plat circulaire constitué de deux minces plateaux de métal soudés ensemble est inséré dans la fente et mis sous pression jusqu'à ce que la distance entre les aiguilles soit restaurée. Pendant le test, la variation des déplacements relatifs des deux paires d'aiguilles dus à la contrainte appliquée est enregistrée. La contrainte nécessaire au retour des aiguilles à leur position initiale est appelée « contrainte d'annulation » et on estime qu'elle est égale à la composante de contrainte normale du plan de la fente.

Les données montrent une variabilité spatiale significative des propriétés de la masse rocheuse et une réaction non élastique aux faibles niveaux de contrainte.

L'analyse des données hydrauliques et du surcarottage démontre qu'une composante de contrainte principale est subverticale au sein de la majeure partie du volume testé. Les deux autres composantes sont subhorizontales et d'ampleur similaire. Certaines zones locales d'hétérogénéité ont été rencontrées, comme le prouve l'apparition de fractures obliques dans les enregistrements de l'imagerie électrique obtenus pour deux des tests de fracturation hydraulique. Des hétérogénéités locales expliquent la grande incertitude quant à l'orientation de la contrainte horizontale maximale.

Une comparaison entre les tests par surcarottage et les tests hydrauliques montre que, à l'exception des contraintes subverticales prélevées par surcarottage du puits de forage PD1 et des résultats des tests de surcarottage obtenus dans le puits PD2 proche de la galerie existante, les contraintes estimées par les deux techniques sont de magnitude similaire.

Une comparaison entre les tests avec les petits vérins plats et les tests par surcarottage effectués à peu près au même endroit révèle des différences significatives dans les résultats. Il apparaît que, près de la galerie, les contraintes soient très probablement influencées par le comportement rhéologique de la zone endommagée associée à la construction de la galerie.

Les diverses données ont été intégrées à un modèle unique afin d'évaluer le champ de contrainte régional et ainsi d'extrapoler les résultats des divers tests au volume de masse rocheuse concerné par le plan hydroélectrique. L'intégration des données pose plusieurs difficultés. Premièrement, les données sont collectées dans des endroits différents à l'aide de techniques de test différentes. Ensuite, les effets de topographie ont une influence significative sur la contrainte aux divers points de mesure. Qui plus est, les hétérogénéités locales (par ex. les zones fracturées et les failles), la variabilité spatiale des propriétés de la masse rocheuse et, potentiellement, la plasticité des zones proches de la galerie depuis laquelle les mesures du surcarottage et des tests avec les vérins plats ont été prélevées pourraient entrer en considération.

L'objectif est de développer un modèle suffisamment simple pour que les données restrictives soient plus nombreuses que les degrés de liberté du modèle. En effet, alors que le modèle devient plus complexe, la solution devient moins délimitée, l'apparente efficacité de la concordance entre les données et le modèle plus illusoire, et la conclusion moins utile.

Le modèle inverse proposé ici a pour but de déterminer le champ de contrainte régional naturel qui correspond le mieux aux données prélevées depuis la galerie

existante. Ce modèle correspond à un géomatériau continu équivalent et les équations différentielles caractéristiques correspondantes sont résolues avec des différences finies explicites en utilisant le logiciel FLAC3D (Itasca, 2009).

En raison de l'influence des effets topographiques, des modèles simulant les volumes de masse rocheuse de différentes dimensions ont été pris en considération lors de la réalisation de l'analyse gravitationnelle ($g = 9,81 \text{ m.s}^{-2}$), afin de faire correspondre les contraintes aux emplacements des divers tests. Les résultats de cette analyse ont indiqué que la région de 5 km de long et de 3 de large présentée en Figure 5 est suffisamment vaste pour obtenir des estimations fiables, car dans le cas de régions plus étendues, les variations maximales de magnitude de la contrainte principale aux emplacements des divers tests sont inférieures à 0,5 MPa. Dans cette région, l'altitude varie de 315 à 1030 m au-dessus du niveau de la mer (Figure 5). Une dimension de 2,5 km a été attribuée à l'axe vertical de sorte que les effets topographiques n'influencent pas les contraintes proches des limites basales du modèle.

La trame du modèle FLAC3D (Figure 6) est composée de 600 000 éléments. Cette trame est plus fine au-dessus du niveau de la mer, avec des éléments cubiques de 25 m de côté. En dessous du niveau de la mer, les éléments sont de 50 x 50 x 100 m. Du fait que les limites sont conditionnées par la charge gravitaire, les déplacements normaux aux limites latérales et basales sont restreints.

Le modèle est utilisé pour identifier les paramètres qui minimisent le décalage entre les contraintes mesurées et calculées. En réalisant une analyse gravitationnelle et en tenant compte des propriétés élastiques obtenues grâce à des tests effectués en laboratoire sur des carottes intactes, une différence apparaît entre les contraintes subhorizontales mesurées *in situ* et les résultats obtenus avec le modèle.

Plusieurs points ont été abordés, tels que l'existence de fractures et de failles, de contraintes tectoniques et de perturbations associées à la galerie existante utilisée pour les mesures avec les petits vérins plats. Il a été établi qu'aucun de ces effets n'avait un impact significatif sur la contrainte déterminée aux divers points de mesure.

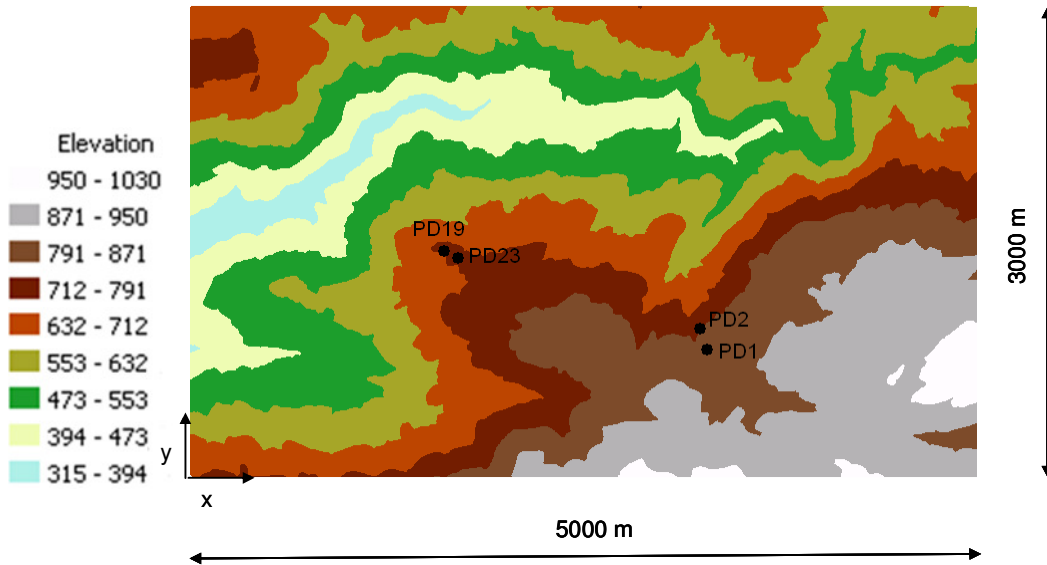
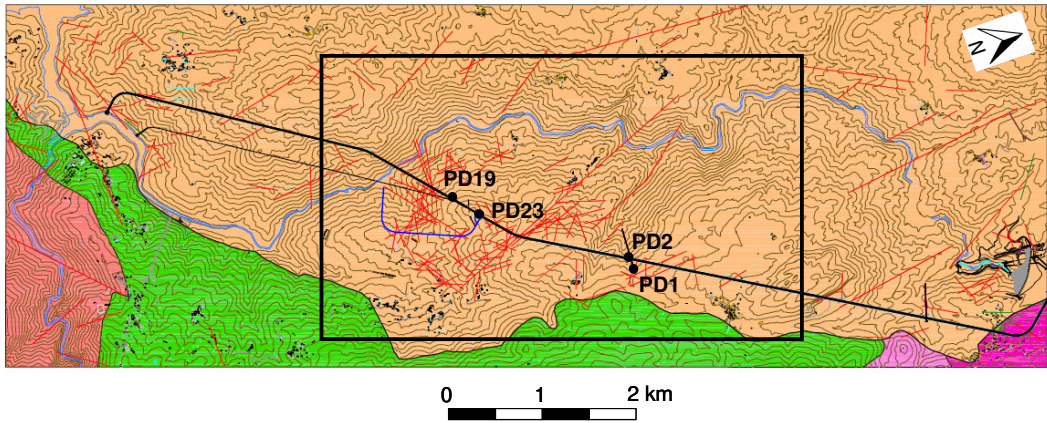


Figure 5 : Limites et relief détaillé de la région considérée dans le modèle FLAC3D.

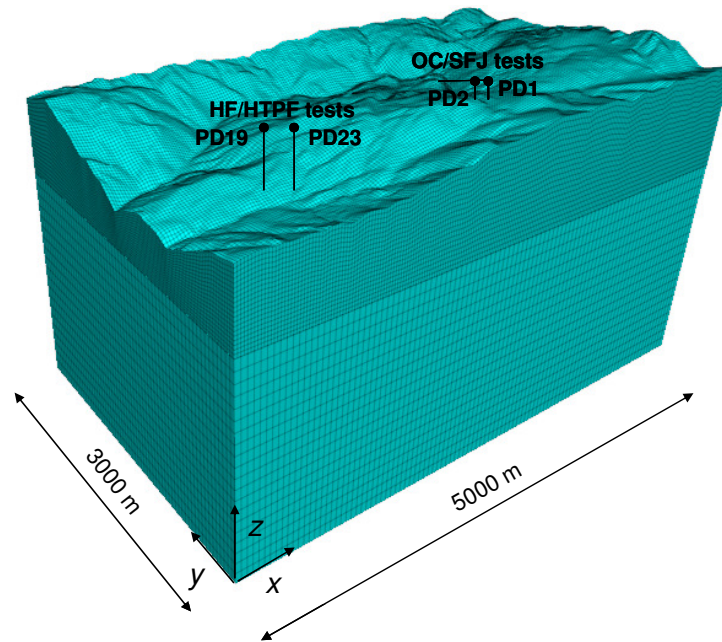


Figure 6 : Trame du modèle FLAC3D.

Parce que simuler le champ de contrainte transitoire n'est pas important pour interpréter les pressions mesurées *in situ*, un matériau à élasticité linéaire équivalent, avec des propriétés élastiques plus souples que celles obtenues par les tests réalisés en laboratoire sur des carottes intactes, est proposé afin d'étudier les effets rhéologiques.

Parce que changer le module élastique n'entraîne pas de modification du champ de contrainte dans une masse rocheuse homogène, les effets rhéologiques ont été modélisés en augmentant la valeur du coefficient de Poisson. Le modèle FLAC3D a été utilisé dans l'inversion de la valeur du coefficient de Poisson afin de minimiser les décalages obtenus entre les valeurs de contrainte mesurées et calculées. Les résultats montrent qu'un coefficient de Poisson de 0,47 permet une concordance satisfaisante entre les résultats obtenus à partir des données des tests hydrauliques et des tests par surcarottage, et celles générées par le modèle.

Le profil des contraintes mesurées et calculées (σ_n) dues à la charge gravitaire avec un coefficient de Poisson de 0,47 sont présentées en Figure 7. L'intervalle de confiance de 99 %, qui correspond à six écarts type de la loi de Gauss, apparaît dans les diverses mesures de contrainte normale. La différence entre la magnitude des contraintes normales mesurées et calculées est inférieure à trois écarts type dans environ 75 % des tests. Dans les tests restants, la différence varie entre 1,2 MPa et 1,3 MPa et est considérée acceptable, compte tenu des nombreuses hypothèses de simplification qu'implique ce modèle.

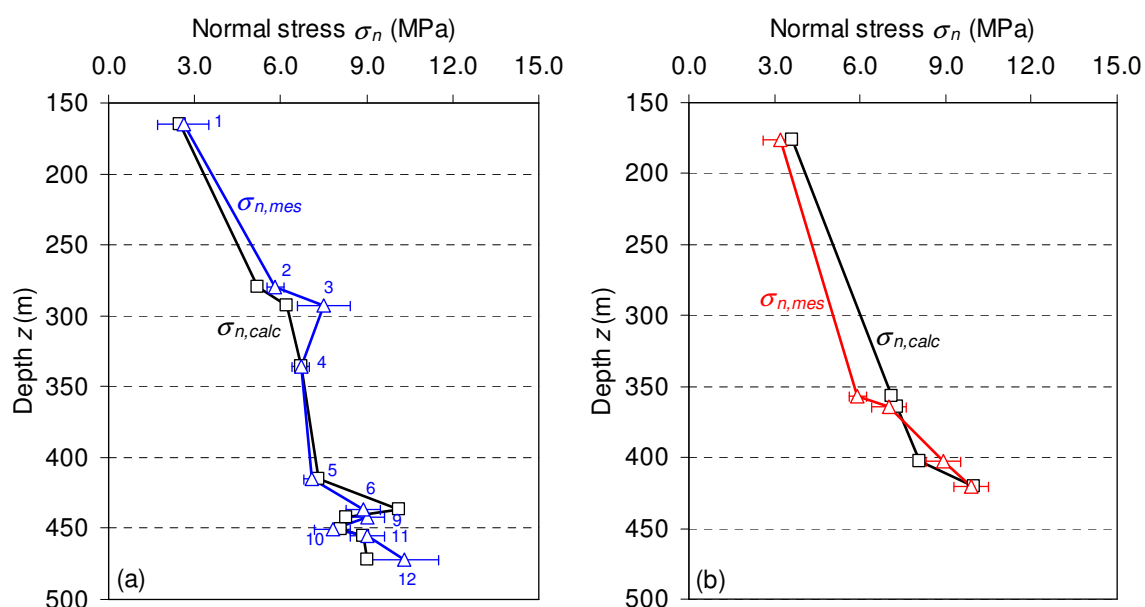


Figure 7 : Variation en fonction de la profondeur de la magnitude de la contrainte normale telle que mesurée par les tests hydrauliques ($\sigma_{n,mes}$) et générée par le modèle FLAC3D avec $\nu = 0,47$, en ne tenant compte que de la gravité, dans les puits de forage (a) PD19 et (b) PD23.

Comparons maintenant les contraintes mesurées et calculées aux emplacements des tests avec les petits vérins plats et des tests de surcarottage en considérant un coefficient de Poisson de 0,47 dans le modèle FLAC3D. Cette comparaison est présentée en figures 8 et 9 en termes de magnitude de contrainte normale pour les tests avec les vérins plats, et de magnitude de contrainte principale pour le surcarottage, respectivement.

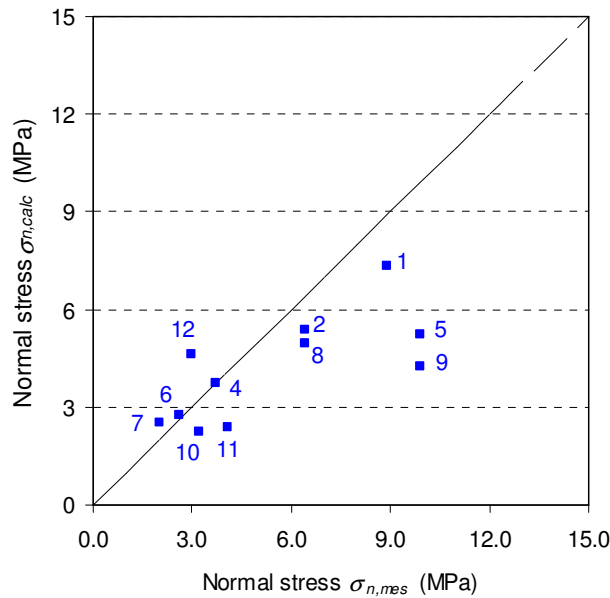


Figure 8 : Comparaison des magnitudes des contraintes normales obtenues par la technique utilisant les petits vérins plats ($\sigma_{n,mes}$) et avec le modèle FLAC3D ($\sigma_{n,calc}$), avec $\nu = 0,47$, en considérant uniquement les effets gravitaires.

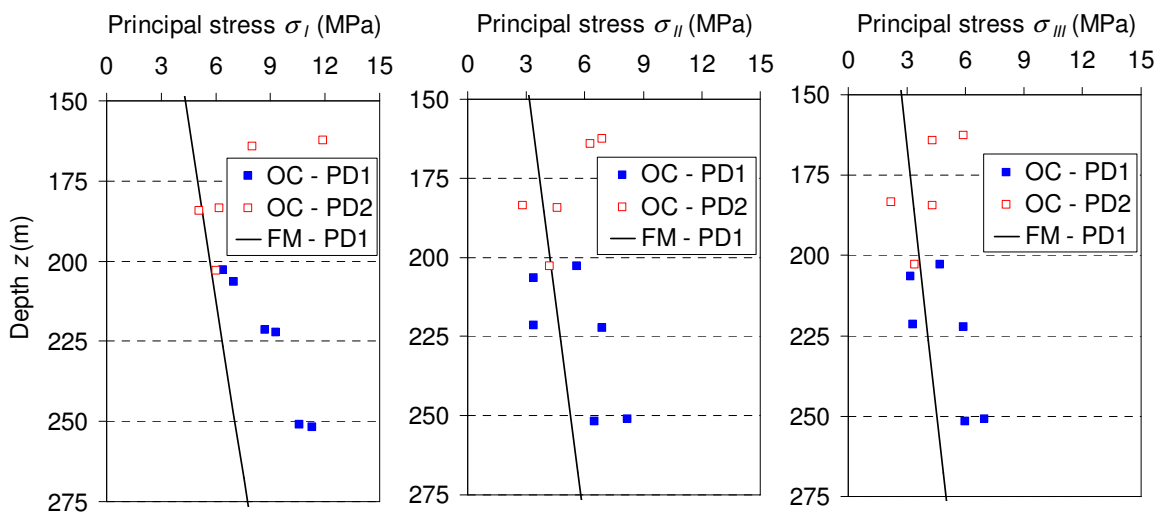


Figure 9 : Variation, en fonction de la profondeur, de la magnitude des contraintes principales (σ_I , σ_{II} , σ_{III}) obtenues par les tests de surcarottage (OC) et avec le modèle FLAC3D (FM), avec $\nu = 0,47$, en considérant uniquement les effets gravitaires.

La figure 8 montre que pour environ 55 % des tests avec les petits vérins plats, la différence entre les contraintes normales mesurées et calculées est supérieure à 1,0 MPa. Cependant, la figure 9 indique que, à l'exception des contraintes subverticales principales (σ) dans le puits de forage PD1 entre 225 et 250 m de profondeur, des deux tests de surcarottage réalisés près de la galerie et des tests avec les petits vérins, environ 80 % des contraintes principales mesurées et générées informatiquement concordent de manière satisfaisante (la différence entre les deux valeurs est inférieure à 1,5 MPa).

Ces résultats montrent qu'environ 80 % des mesures effectuées à distance de la galerie existante sont cohérentes avec un géomatériau à élasticité linéaire équivalent, dont les propriétés correspondent à un matériau beaucoup plus souple que ce que suggèrent les tests en laboratoire sur les carottes. Ces découvertes amènent à la conclusion que le champ de contrainte à grande échelle et à long terme dans ce massif granitique est contrôlé par la seule relaxation de contrainte le long des diverses fractures et failles de la roche. Ainsi, le comportement à long terme du massif granitique s'avère différer nettement de celui à court terme pris en compte pour interpréter les tests par surcarottage (très probablement parce que le surcarottage ne concerne que le granite sain). De plus, il n'est pas nécessaire d'introduire de composante de contrainte pour adapter les données à ce lieu, une caractéristique assez satisfaisante étant donnée l'altitude du site.

Mais ce modèle simple n'explique pas la plupart des tests avec les petits vérins plats ni les deux tests par surcarottage proches de la galerie. Il peut être envisagé que le matériau équivalent à considérer près de la galerie doit prendre en compte les dommages causés par les explosions lors de la construction de celle-ci. De plus, pour un tel matériau, la déformation plastique pourrait être prise en compte lors de l'analyse des composantes de contrainte locale.

Cette étude conclut que la rhéologie de la masse rocheuse qui est habituellement négligée joue un rôle important sur les contraintes *in situ*. La caractérisation de la rhéologie de la masse rocheuse est difficile parce qu'elle dépasse toutes les méthodes de test en laboratoire et sur le terrain, en raison de l'échelle de temps concernée. Et les paramètres d'élasticité obtenus à partir des tests réalisés sur les carottes intactes pourraient être irréalistes dans la simulation du comportement de la masse rocheuse avec des échelles spatiales et temporelles plus étendues, du fait qu'avec une grande échelle spatiale, la roche comprend un réseau de fractures naturelles important dont le comportement est dépendant du temps. Mais, la connaissance de champs de contrainte à grande échelle aide à mieux restreindre les propriétés mécaniques à long terme du matériau considéré.

Contents

CHAPTER 1. INTRODUCTION	1
1.1. General.....	1
1.2. Determination of the stress field in rock masses	2
1.2.1. Methods for measuring <i>in situ</i> stresses	2
1.2.2. Integration of <i>in situ</i> tests results using numerical modelling	3
1.3. Objectives.....	4
1.4. Thesis outline.....	5
CHAPTER 2. <i>IN SITU</i> STRESS MEASUREMENTS.....	7
2.1. Introduction.....	7
2.2. <i>In situ</i> tests.....	12
2.2.1. Hydraulic tests.....	12
2.2.2. Overcoring tests.....	24
2.2.3. Small flat jack tests.....	28
2.3. Laboratory test results.....	30
2.4. Stress measurement results	31
2.4.1. Hydraulic test results	31
2.4.1.1. Calibrations	31
2.4.1.2. Description of the pressure and fracture orientations data.....	37
2.4.1.3. Normal stress component determination	41
2.4.1.4. Fracture orientations determination	45
2.4.1.5. Summary of the pressure and fracture orientations data	46
2.4.1.6. Determination of the stress field	49
2.4.2. Overcoring test results	56
2.4.3. Small flat jack test results	61
2.5. Conclusion	65
CHAPTER 3. DETERMINATION OF THE REGIONAL STRESS FIELD	67
3.1. Introduction.....	67
3.2. Inverse model	68
3.3. The role of the topography on the <i>in situ</i> stresses distribution.....	72
3.3.1. Gravity loading	72
3.3.2. Tectonic loading.....	75

3.3.3. Gravity and tectonic loadings	78
3.4. Comparison between <i>in situ</i> tests and results from the FLAC3D model when considering gravity loading alone	83
3.5. Influence of faults and fractured zones.....	87
3.6. Testing the existence of tectonic stresses.....	90
3.7. Examining rheological effects.....	92
3.8. Design of the hydraulic pressure tunnel	98
3.9. Conclusion	98
CHAPTER 4. CONCLUSIONS	101
4.1. Summary and conclusions	101
4.2. New contributions	104
4.3. Recommendations	104
LIST OF REFERENCES.....	107
APPENDIX A:HYDRAULIC TEST RESULTS.....	111
APPENDIX B:OVERCORING TEST RESULTS.....	165
APPENDIX C:SMALL FLAT JACK TEST RESULTS	195

List of papers:

Papers in international conferences:

Figueiredo, B., Cornet, F.H., Lamas, L., Muralha, J., 2012. Effect of topography on distribution of *in situ* stresses due to gravity and tectonic loadings at Paradela site. Proceedings of the EUROCK 2012 – Rock Engineering and Technology for Sustainable Underground Construction, Stockholm.

Papers in international scientific journals:

Figueiredo, B., Cornet F.H., Lamas, L., Muralha, J., 2013a. Determination of the stress field in a granite rock mass – Part I: *in situ* measurements. International Journal of Rock Mechanics and Mining Sciences (submitted to publication in June 2013).

Figueiredo, B., Cornet F.H., Lamas, L., Muralha, J., 2013b. Determination of the stress field in a granite rock mass – Part II: an integrated solution. International Journal of Rock Mechanics and Mining Sciences (submitted to publication in June 2013).

List of figures

Figure 2.1: Satellite image of Portugal with the location of the Paradela II site (adapted from http://www.earth.google.com)	7
Figure 2.2: View of the Paradela II site.	8
Figure 2.3: Layout of the Paradela II hydroelectric repowering scheme (courtesy of Energy of Portugal-EDP).....	8
Figure 2.4: View of the Paradela dam.	9
Figure 2.5: Location of the (a) hydraulic tests and (b) overcoring tests.	10
Figure 2.6: Existing adit and vertical cutting plane along the adit axis showing the location of the overcoring and small flat jack tests.	11
Figure 2.7: Schematic diagram of the equipment used in hydraulic tests.	12
Figure 2.8: Packers and HTPF tool.	13
Figure 2.9: Hydraulic tests performed at the Paradela II site: (a) general view of the testing scheme, (b) downward movement of the upper packer, (c) downward movement of the system with the coiled tubing and (d) hydraulic pump.	14
Figure 2.10: Record of test interval pressure and flow rate as a function of time through a hydraulic fracturing test.....	16
Figure 2.11: (a) Calliper tool (Zemanek <i>et al.</i> , 1969), (b) HRAT tool, and (c) introduction of the HRAT tool into borehole PD23.....	18
Figure 2.12: STT cell and data acquisition unit.....	24
Figure 2.13: Orientation of the strain gauges in the STT cell.....	24
Figure 2.14: Sequence of execution of an STT stress measurement test.....	25
Figure 2.15: Record of strains and temperature as a function of time through an overcoring test.	26
Figure 2.16: Biaxial test chamber with the core.....	26
Figure 2.17: Steps of the small flat jack tests: (a) marking the tests location, (b) cutting the slot, (c) slot, anchor bolts and measurements pins, and (d) measuring the distance between the pins using digital transducers.....	28
Figure 2.18: Typical record of pressure as a function of displacement through a small flat jack test.	29
Figure 2.19: Comparison between the cores and the electrical images of the sets of fractures identified in borehole PD19.	32

Figure 2.20: Comparison between the cores and the electrical images of the sets of fractures identified in borehole PD23.	32
Figure 2.21: Plots of the magnetometers m_1 versus m_2 obtained: (a) before and (b) after the calibration.	34
Figure 2.22: Calibration curves for the test interval pressure obtained in boreholes (a) PD19 and (b) PD23.	35
Figure 2.23: Determination of the shut-in pressure using the (a) Aamodt and Kuriyagawa's method and (b) Hayashi and Haimson's method.....	42
Figure 2.24: (a) Comparison between electrical imaging (EI) logs obtained before (Pre Frac) and after (Post Frac) a hydraulic fracturing test, (b) adjustment of the fracture plane with a sinusoidal curve and (c) identification of the main fracture planes in the electrical imaging (EI) and HRAT logs.	46
Figure 2.25: Variation of the normal stress σ_n magnitudes as a function of depth.	50
Figure 2.26: Variation of the azimuth ϕ of the normal to the fracture planes obtained in hydraulic fracturing tests as a function of depth.	50
Figure 2.27: Inclined fractures shown in electrical images obtained before (Pre Frac) and after (Post Frac) a hydraulic fracturing test.	52
Figure 2.28: Pressure versus displacement curves obtained in biaxial tests performed in overcored cores. (a) linear and elastic behaviour; (b) non-linear and non-elastic behaviour.....	56
Figure 2.29: Comparison of the magnitudes of the principal stresses (σ_I , σ_{II} , σ_{III}) obtained by overcoring and hydraulic testing.	60
Figure 2.30: Three-dimensional model used for interpretation of the small flat jack tests.	63
Figure 2.31: Comparison between small flat jack and overcoring normal stress considering the far-field stress tensor resulting from the (a) inversion of overcoring data and (b) shallow overcoring tests results.	64
Figure 3.1: Limits and detailed elevation of the region considered in the FLAC3D model.....	69
Figure 3.2: Mesh of the FLAC model.	70
Figure 3.3: Contours of the principal stresses due to gravity loading: (a) maximum principal stress (σ_I), (b) intermediate principal stress (σ_{II}), and (c) minimum principal stress (σ_{III}).	73
Figure 3.4: Variation with depth below the surface of the principal stresses (σ_I , σ_{II} , σ_{III}) and the inclination of the maximum principal stress (σ_I) with respect to the vertical direction.....	74

Figure 3.5: (a) Unbalanced stress state due to the effect of topography when a uniform stress S_{xx} distribution is applied at the boundaries of a numerical model (b) Uniform normal displacement Δ_x applied at the boundaries to induce a horizontal unit stress σ_{xx} at the basal boundary of the model.....76

Figure 3.6: Orientation of the regional tectonic maximum horizontal compressive stress from the World Stress Map (Heidbach *et al.*, 2008).....77

Figure 3.7: Variation with depth of the stress tensor components for a constant unit tectonic stress S_{yy}78

Figure 3.8: Variation with depth of the magnitude of the principal stresses (σ , σ_I , σ_{III}) obtained at the location of borehole PD1 for the combined effect of gravity G and tectonic S_{yy} loadings.80

Figure 3.9: Variation with depth of the magnitude of the principal stresses (σ , σ_I , σ_{III}) obtained at the location of borehole PD19 for the combined effect of gravity G and tectonic S_{yy} loadings.81

Figure 3.10: Orientation of the principal stresses obtained for the tectonic S_{yy} loading at the locations of boreholes PD1 (left) and PD19 (right).82

Figure 3.11: Variation of the magnitudes of the normal stresses obtained by hydraulic testing ($\sigma_{n,mes}$) and with the FLAC3D model ($\sigma_{n,calc}$) run with gravity loading only in boreholes (a) PD19 and (b) PD23 as a function of depth.83

Figure 3.12: Variation of the magnitude of the principal stresses (σ , σ_I , σ_{III}) obtained from the inversion of the hydraulic data (HF/HTPF) and with the FLAC3D model (FM) run with gravity loading only as functions of depth85

Figure 3.13: Variation of the principal stress magnitude (σ , σ_I , σ_{III}) as obtained by overcoring (OC) and as computed with the FLAC3D model (FM) run with gravity loading only as functions of depth.....86

Figure 3.14: Location of the fractured zones in the FLAC3D model.87

Figure 3.15: Variation with depth of the maximum (σ_I) and minimum (σ_{III}) sub-horizontal principal stresses obtained from the inversion of the hydraulic data (HF/HTPF) and with the FLAC3D model (FM) by considering the existing fractured zones.....89

Figure 3.16: Variation with depth of the normal stress magnitudes as measured by hydraulic testing ($\sigma_{n,mes}$) and computed with the FLAC3D model ($\sigma_{n,calc}$) for the combined effect of gravity and tectonics in boreholes (a) PD19 and (b) PD23.....91

Figure 3.17: Soft linearly elastic material used for considering rheological effects.93

Figure 3.18: Variation with depth of the normal stress magnitudes as measured by hydraulic testing ($\sigma_{n,mes}$) and computed with the FLAC3D model with $\nu=0.47$, considering gravity effects only, in boreholes (a) PD19 and (b) PD23.....94

Figure 3.19: Variation with depth of the magnitude of the principal stresses ($\sigma_1, \sigma_{II}, \sigma_{III}$) obtained from the inversion of the hydraulic data (HF/HTPF) and with the FLAC3D model with $\nu=0.47$ considering gravity effects only.95

Figure 3.20: Comparison of the magnitudes of the normal stresses obtained by small flat jack technique ($\sigma_{n,mes}$) and with the FLAC3D model ($\sigma_{n,calc}$) with $\nu=0.47$ considering gravity effects only.96

Figure 3.21: Variation with depth of the magnitude of the principal stresses ($\sigma_1, \sigma_{II}, \sigma_{III}$) obtained by overcoring testing (OC) and with the FLAC3D model (FM) with $\nu=0.47$ considering gravity effects only.97

List of tables

Table 2.1: Comparison between the depths of the sets of fractures identified in the electrical imaging data (reading R_2) and in the cores extracted from boreholes PD19 and PD23.....	33
Table 2.2: Azimuth and inclination of the axis of borehole PD19.....	36
Table 2.3: Azimuth and inclination of the axis of borehole PD23.....	36
Table 2.4: Description of the pressure and fracture orientation data in borehole PD19. ...	38
Table 2.5: Description of the hydraulic tests conducted in borehole PD23.	40
Table 2.6: Normal stress results obtained from borehole PD19.	43
Table 2.7: Normal stress results obtained from borehole PD23.	44
Table 2.8: Summary of the hydraulic test results obtained from borehole PD19.....	47
Table 2.9: Summary of the hydraulic test results obtained from borehole PD23.....	48
Table 2.10: <i>A priori</i> values (p_0) and <i>a posteriori</i> values (p) for the far-field stress parameters.	53
Table 2.11: Results of the stress field at 475 m below the surface.....	54
Table 2.12: Comparison between <i>a priori</i> and <i>a posteriori</i> values for the nine tests solution.	55
Table 2.13: Comparison between <i>a priori</i> and <i>a posteriori</i> values for the fifteen tests solution.	55
Table 2.14: Biaxial tests results.	57
Table 2.15: Principal stress (σ , σ_{II} , σ_{III}) magnitudes and orientations obtained from interpreting the overcoring tests.....	58
Table 2.16: Results from the small flat jack tests.	61
Table 3.1: Cases considered in the study of the influence of the elastic modulus E_3 on <i>in situ</i> stresses.....	88
Table 3.2: Variation of the misfit value with the Poisson's ratio.	93

Acknowledgments

The author wishes to thank the institutions who contributed to this work: the Portuguese National Laboratory for Civil Engineering (LNEC), the University of Strasbourg and the company Energies of Portugal (EDP). Authorisation by Energies of Portugal (EDP) to publish the stress measurement results is acknowledged.

The financial support of the Foundation for Science and Technology who funded this research through PhD grant SFRH/BD/68322/2010 was also fundamental, having allowed several stays in Strasbourg throughout the thesis.

To my supervisor at University of Strasbourg, Professor François Cornet, and at LNEC, Principal Researchers Luís Nolasco Lamas and José Delgado Muralha, the author thanks their valuable advice and guidance.

To the technicians José Augusto Caneco and Luís Dias from the Portuguese National Laboratory for Civil Engineering and Alain Steyer and Miloud Talib from the University of Strasbourg, the author thanks their help in the data acquisition.

To my research colleagues and technicians at the Modelling and Rock Mechanics division (NMMR), the author thanks for their everyday support and for welcoming this young engineer at NMMR some years ago.

To my colleagues at LNEC, some already with their PhDs behind, others now are pursuing it, Luísa Braga Farinha, Juan Mata, Nuno Azevedo, Ricardo Santos, Carlos Serra and others.

Finally, I wish to thank my family, who defies me to always be better and with whom I am truly at home. My parents Adelaide and Aníbal and my sister Mafalda.

Symbols

E	Elastic modulus
δE	Standard deviation associated with the elastic modulus
ν	Poisson's ratio
$\delta \nu$	Standard deviation associated with the Poisson's ratio
E'	Equivalent elastic modulus of an equivalent geomaterial
ν'	Equivalent Poisson's ratio of an equivalent geomaterial
E_0	Shot term elastic modulus
ν_0	Shot term Poisson's ratio
$E(t)$	Variation of the elastic modulus with time
$\nu(t)$	Variation of the Poisson's ratio with time
ξ	Relaxation time
E_1	Elastic modulus in the plane of isotropy
E_3	Elastic modulus normal to the plane of isotropy
ν_{12}	Poisson's ratio characterizing lateral contraction in the plane of isotropy when compression is applied in this plane
ν_{13}	Poisson's ratio characterizing lateral contraction in the plane of isotropy when compression is applied perpendicular to plane of isotropy
G_{13}	Shear modulus in the plane perpendicular to plane of isotropy
σ_c	Compression strength of the rock mass
$\delta \sigma_c$	Standard deviation associated with the elastic modulus
F_t	Rupture force
σ_t	Tensile strength
$\delta \sigma_t$	Standard deviation associated with the tensile strength
D	Diameter
e	Thickness
ρ	Density
g	Gravitational acceleration
a, b	Empirical constants
P_a	Fluid pore pressure
P_b	Breakdown pressure
P_s	Shut-in pressure

P_h	Hydraulic pressure
z	Depth below the surface
z_0	Depth below the surface of the water level in the boreholes
P_m	Pressure measured in the test interval
P_m^A	Minimum value for the shut-in pressure in Aamodt and Kuriyahawa's method
P_M^A	Maximum value for the shut-in pressure in Aamodt and Kuriyahawa's method
P_m^H	Minimum value for the shut-in pressure in Hayashi and Haimson's method
P_M^H	Maximum value for the shut-in pressure in Hayashi and Haimson's method
φ	Azimuth of the borehole axis with respect to the North
β	Deviation of the borehole axis
x, y, z	Coordinates in the three dimensional space
X^m	Point with coordinates x, y, z
z_m	z -coordinate of the m^{th} fracture plane
ϕ_m	Direction of the normal to the m^{th} fracture plane with respect to the North
θ_m	Inclination of the normal to the m^{th} fracture with respect to the vertical direction
σ_n^m	Normal stress on the m^{th} fracture plane with normal n^m
δz	Uncertainty on depth determination
$\delta\phi$	Uncertainty on azimuth determination
$\delta\theta$	Uncertainty on inclination determination
$\delta\sigma_n$	Uncertainty on normal stress determination
$\sigma(z_m)$	Stress tensor at z -coordinate of the m^{th} fracture plane
α	Stress tensor with the gradients of the stress tensor components along the vertical direction
S_1	Maximum horizontal principal stress of the stress tensor $\sigma(z)$
S_2	Minimum horizontal principal stress of the stress tensor $\sigma(z)$
S_3	Vertical stress of the stress tensor $\sigma(z)$
λ	Orientation of the S_1 eigenvector
α_1	Vertical gradient of the maximum principal stress S_1
α_2	Vertical gradient of the intermediate principal stress S_2
α_3	Vertical gradient of the minimum principal stress S_3
η	Orientation of the α_1 eigenvector with respect to the S_1 eigenvector
σ_I	Maximum principal stress
σ_{II}	Intermediate principal stress
σ_{III}	Minimum principal stress

x_0	Column vector with all the expected <i>a priori</i> values for both the measurements d_0 and the unknowns p_0
d_0	Column vector with all the <i>a priori</i> values for the measurements
p_0	Column vector with all the <i>a priori</i> values for the unknowns
x^s	Column vector with all the <i>a posteriori</i> values for both the measurements and the unknowns
$f(x)$	Vectorial function of x defined by the error between the measured and calculated normal stresses
$f(x_k)$	Function $f(x)$ evaluated at the point x_k
f^m	m^{th} component of the function $f(x)$
x_j	j^{th} component of x
F_x	Matrix of the partial derivatives of the function $f(x)$ evaluated at the point x
F_k	Matrix of the partial derivatives of the function $f(x)$ evaluated at the point x_k
C_0	<i>A priori</i> covariance matrix
C	<i>A posteriori</i> covariance matrix
δ_n^m	Uncertainty on the normal stress determination on the m^{th} fracture plane
δ_l^m	Uncertainty on the orientation of the m^{th} fracture plane
$\sigma_{n,mes}$	Measured normal stress
$\sigma_{n,mes}^m$	Measured normal stress on the m^{th} fracture plane
$\sigma_{n,calc}$	Calculated normal stress
$\sigma_{n,calc}^m$	Calculated normal stress in the m^{th} fracture plane
σ_{mes}^n	Measured stress component in the n^{th} overcoring test
σ_{calc}^n	Calculated stress component in the n^{th} overcoring test
δ_σ^n	Uncertainty on the measured stress in the n^{th} overcoring test
δ_{bh}	Uncertainty on the deviation of the borehole axis
$L_x(V)$	Operator evaluated at the point x for any vector V
Q_x	Linear projector evaluated at the point x
$K_x(V)$	Second order partial derivative operator of the function $f(x)$ evaluated at the point x , for any vector V
σ_H	Maximum horizontal stress
σ_h	Minimum horizontal stress
σ_v	Vertical stress
ω_H	Orientation of the maximum horizontal stress

$\delta\sigma_H$	Uncertainty on the maximum horizontal stress
$\delta\sigma_h$	Uncertainty on the minimum horizontal stress
$\delta\sigma_v$	Uncertainty on the vertical stress
$\delta\omega_H$	Uncertainty on the direction of the maximum horizontal stress with respect to the North
σ_n	<i>A priori</i> value for the normal stress
σ_{nc}	<i>A posteriori</i> value for the normal stress
ϕ	<i>A priori</i> value for the azimuth of the normal to the fracture plane
ϕ_c	<i>A posteriori</i> value for the azimuth of the normal to the fracture plane
θ	<i>A priori</i> value for the inclination of the normal to the fracture plane with respect to the vertical axis
θ_c	<i>A posteriori</i> value for the azimuth of the normal to the fracture plane with respect to the vertical axis
p	Pressure applied during the biaxial or small flat jack tests
k	Constant that relates the pressure applied into the jacks with the displacement that is measured during the small flat jack tests
δ	Displacement between the pins measured during the small flat jack test
ε_i	Strain at the i^{th} strain gauge
σ_j	Column vector with the j ($j=1, \dots, 6$) components of the stress tensor
S_i^k	Six components of the stress tensor at the location of a given small flat jack
N_i^k	Generalized components of the normal to the k^{th} small flat jack plane
A_{ij}^k	Matrix of 36 coefficients that relates the stress normal to the k^{th} flat jack plane with the components of the far-field stress tensor
ψ^{FH}	Misfit function for hydraulic data
ψ^{OC}	Misfit function for overcoring data
ψ^{FHOC}	Misfit function for hydraulic and overcoring data
ω^{FH}	Weight factor for hydraulic data
ω^{OC}	Weight factor for overcoring data
S_{xx}, S_{yy}	Normal tectonic stress components applied in the x and y axis of a numerical model, respectively
S_{xy}	Shear tectonic stress component
Δ_x	Displacement applied in the x axis of a numerical model
d	Distance between the entrance of the exiting adit and the location of the small flat jack tests

G	Gravity loading
$\sigma_{n,calc}^k$	Calculated normal stress in the k^{th} small flat jack test
$\sigma_{n,grav}$	Normal stresses obtained due to gravity loading
$\sigma_{n,tect}$	Normal stresses obtained due to tectonic loading
A, B, C	Constants
$\sigma_{n,Sxx}$	Normal stresses calculated at location of the hydraulic tests due to a unit tectonic loading component S_{xx}
$\sigma_{n,Syy}$	Normal stresses calculated at location of the hydraulic tests due to a unit tectonic loading component S_{yy}
$\sigma_{n,Sxy}$	Normal stresses calculated at location of the hydraulic tests due to a unit tectonic loading component S_{xy}

Chapter 1.

Introduction

1.1. General

Stress field determinations are fundamental in civil, mining, petroleum, earthquake engineering, as well as in geophysics and geology. Stresses in rock masses are commonly divided into primary and secondary stresses. Secondary rock stresses are man-made, such as through excavations, whereas the primary, which are also known as *in situ* stresses, are the cumulative product of events in the geological history, e.g., gravitational, tectonic, residual, and terrestrial stresses (Amadei and Stephansson, 1997).

Recently, with the development of large underground constructions, such as underground power plants, underground waste repositories and underground petroleum storages, the knowledge of the *in situ* stresses is essential for their optimum design and construction. Compared with the surface works, the underground works have the advantage of causing less environmental impact, which helps understand their recent significant increase. Underground works enable the exploration of the good quality of rock masses in depth and, in the case of hydraulic tunnels and underground storage, enable the assurance of a good confinement due to the high stresses to which they are subjected.

An exact prediction of the stress spatial distribution is very difficult, since the current stress state is the end product of a series of past geological events, and influenced by the stiffness of the rock masses and the loads due to the gravity and tectonic movements. Furthermore, rock masses are rarely homogeneous and continuous, and stresses vary from place to place. Thus, methodologies that provide an adequate characterisation of the *in situ* stresses in rock masses are essential. These methodologies generally include a set of *in situ* tests and adequate models for the interpretation of the results.

1.2. Determination of the stress field in rock masses

1.2.1. Methods for measuring *in situ* stresses

Depending on the domain of application, the most commonly used stress determination techniques include hydraulic methods, relief methods and jacking methods. More techniques exist, and comprehensive reviews of stress determination methods may be found for example in Amadei and Stephansson (1997) and Ljunggreen *et al.* (2003).

The main objective of hydraulic methods (Cornet and Valette, 1984) is to measure *in situ* stresses by isolating a section of a borehole and applying a hydraulic pressure on its wall. The applied pressure is increased until existing fractures open or new fractures are created. The fluid pressure required to open, generate, propagate, sustain, and reopen fractures in rock at a given depth is measured and is related to the existing stress field. The directions of the measured stresses are inferred from the measurement of the orientation of the fractures. Explicit uncertainties associated with stress determination through hydraulic tests depend on the accuracy on the test location and on uncertainties on both normal stress measurements and fracture orientations. However, no hypothesis is formulated with respect to the stress-strain relationship for the rock mass and the only implicit uncertainties to be considered concern the *a priori* assumption proposed for describing spatial stress variation when large volumes of rock are considered.

Relief methods (Sjoberg *et al.* 2003) consist of the isolation of a rock sample from the stress field in the surrounding rock mass and the monitoring of its response. This can be achieved by different methods, such as overcoring or undercoring holes and cutting slots. However, the stresses are not related to applied pressures as in hydraulic methods. Instead, the stresses are inferred from strains or displacements created by the relief process and measured on the isolated rock samples, in boreholes, or on the surrounding rock associated with the relief process. The interpretation of the stress relief tests depends on a stress-strain (displacement) relationship for the rock. Uncertainties associated with such stress determination depend explicitly on the precision on measurements of both the stress relief induced strains or displacements and the rock elastic parameters. But they depend also implicitly on the validity of the hypotheses implied by the corresponding technique (e.g., homogeneity, linear elasticity, uniformity of the stress components within the volume where the data have been gathered).

In jacking methods (Habib and Marchand, 1951), the equilibrium of a rock mass is disturbed by cutting slots on the surfaces of rock excavations. This creates deformations that are measured by means of reference pins or strain gauges that are placed on either

side of the slots. Then, a jack is inserted into the slots and pressurised until the equilibrium is restored. The stresses normal to the slots are directly related to the pressure necessary to restore the equilibrium. Explicit uncertainties associated with stress determination through jacking methods depend on the uncertainties on both normal stress measurements and slot plane orientations. Implicit uncertainties depend on the knowledge of the rock's constitutive behaviour, the concentration factors along the tested rock mass surface required to relate the measured normal stresses to the stresses at the far-field, the geometry of the excavation and the uniformity of the stress component perpendicular to the jacks.

1.2.2. Integration of *in situ* tests results using numerical modelling

In situ tests only enable the characterisation of the rock stresses at the location where the tests are performed due to the various factors that influence rock stresses, such as the heterogeneities, the existing geological structures and the correlated spatial variability of rock mass properties. Thus, it is essential to consider a model that integrates the results of the various *in situ* measurements to extrapolate the results to a rock mass volume of interest for the design of the underground structures of concern.

When different types of measurement techniques are used at the same location, the results must be combined into a single inversion scheme to determine the stress field that best fits all the data. Such integration schemes have already been presented by several researchers: hydraulic fracturing (HF) tests and hydraulic tests on pre-existing fractures (HTPF) (Cornet and Valette, 1984), hydraulic tests (HF and HTPF) and flat jacks (Cornet, 1996), hydraulic tests and focal mechanisms of induced seismicity (Cornet and Yin, 1995), hydraulic tests and overcoring tests (Ask, 2004) and overcoring tests and flat jacks (Lamas *et al.*, 2010).

Numerical models are then sometimes developed to integrate all the tests results within a single model that is used to determine the most probable stress state in the volume of interest (Sousa *et al.* 1986, Hart 2003, Lamas *et al.* 2010, Matsuki *et al.* 2009, Muralha *et al.* 2009). In mountainous regions, with irregular terrain surfaces, these models are an essential tool to evaluate the influence of topography on the stress field, because analytical solutions, such as those provided by Savage *et al.* (1985) are not applicable.

The discrepancy found between the stresses provided by *in situ* tests and the results of the numerical models obtained due to gravity loading has been justified with the existence of tectonic stresses. By assuming this hypothesis, a linear elastic analysis is usually conducted to determine the horizontal stresses that must be applied to the model

boundaries to achieve a good fit with the data (Li *et al.* 2009, McKinnon 2001, Tonon *et al.* 2001). In this analysis, rheological effects are commonly neglected.

1.3. Objectives

At present, Portugal faces an important movement regarding underground construction in rock masses that is the return to the construction of new large hydroelectric power schemes, which had been stopped for many years mainly due to environmental constraints. Not only several large dams but also powerhouse reinforcements of existing schemes are in the design phase or already under construction. The powerhouse reinforcements have two main purposes: in some cases, they simply increase the production of electrical power through the installation of new turbines in new powerhouses, and in other cases, turbine-pump systems are installed to store energy during periods in which the production of electricity due to other sources (especially wind farms) exceeds the demand. Most of these schemes include large underground caverns and long hydraulic pressure tunnels with significant cross sections. The National Programme for Dams with High Hydroelectric Energy Potential includes the construction of several new dams that will involve the excavation of new shafts, powerhouses and long hydraulic circuits.

This thesis analysed a case study that included data that were obtained through different techniques (hydraulic, overcoring and flat jack testing) in various locations within a rock mass, in a mountainous region. The measurements were conducted for the design of a re-powering scheme of an existing hydroelectric system that includes a large underground cavern and a long hydraulic pressure tunnel. The aim of the present study is to develop a data integration approach to extrapolate the results of the various *in situ* tests to the rock mass volume of interest for the design of the underground hydroelectric power scheme. The specific objectives of the study are the following:

- to complement an existing *in situ* testing program, by performing additional *in situ* tests exclusively for this thesis;
- to develop an inverse model for the determination of the regional stress field that best fits the data provided by the various testing techniques;
- to evaluate the influence of the topography effects on the stress field obtained due to gravity and tectonic loadings;
- to estimate the role of tectonic and gravitational stresses in the global stress field;

- to compare *in situ* measurements obtained by overcoring and flat jack techniques in the vicinity of an existing adit;
- to study the influence of the compliance of existing large-scale fractured zones on the stress field;
- to investigate the influence of the rheological properties of the rock mass on the interpretation of the stress measurement results; and
- to use stress field information to ascertain the long-term mechanical properties of an equivalent geomaterial.

1.4. Thesis outline

In face of the objectives presented in the previous section, the thesis is structured in four chapters, of which this introduction is the first one.

Chapter 2, *In situ* stress measurements, discusses the collection and preliminary interpretation of the data obtained for this thesis. First, is described how hydraulic tests help determine the vertical stress profile. The overcoring tests are then described, and the results are combined in an inversion scheme to constrain the stress tensor at their location. Finally, the small flat jack tests are discussed, and their results are compared to those of the overcoring tests that were conducted at almost the same location.

Chapter 3, Determination of the regional stress field, presents an equivalent and continuum mechanics model to integrate the various data to assess the regional stress field. The model is used to analyse the role of topography on *in situ* stresses distribution due to gravity and tectonic loadings, to investigate the influence of the compliance of existing large-scale fractured zones and potential tectonic stresses on the stress field and to ascertain the long-term rheological characteristics of the equivalent geomaterial.

In the last chapter the more relevant and innovative conclusions are summarized and suggestions for future developments of the work are suggested.

Chapter 2.

In situ stress measurements

2.1. Introduction

The case study considered in this thesis refers to the re-powering scheme of the Paradela hydroelectric scheme located on the Cávado River in the North of Portugal (Figures 2.1 and 2.2). The Paradela II scheme includes a new 10 km hydraulic conduit and a powerhouse complex placed about halfway in the conduit (Figure 2.3) and will primarily be excavated in granite. It includes a new powerhouse cavern, a valves chamber and a large surge chamber with several adits located 500 m below ground level.



Figure 2.1: Satellite image of Portugal with the location of the Paradela II site (adapted from <http://www.earth.google.com>)



Figure 2.2: View of the Paradela II site.

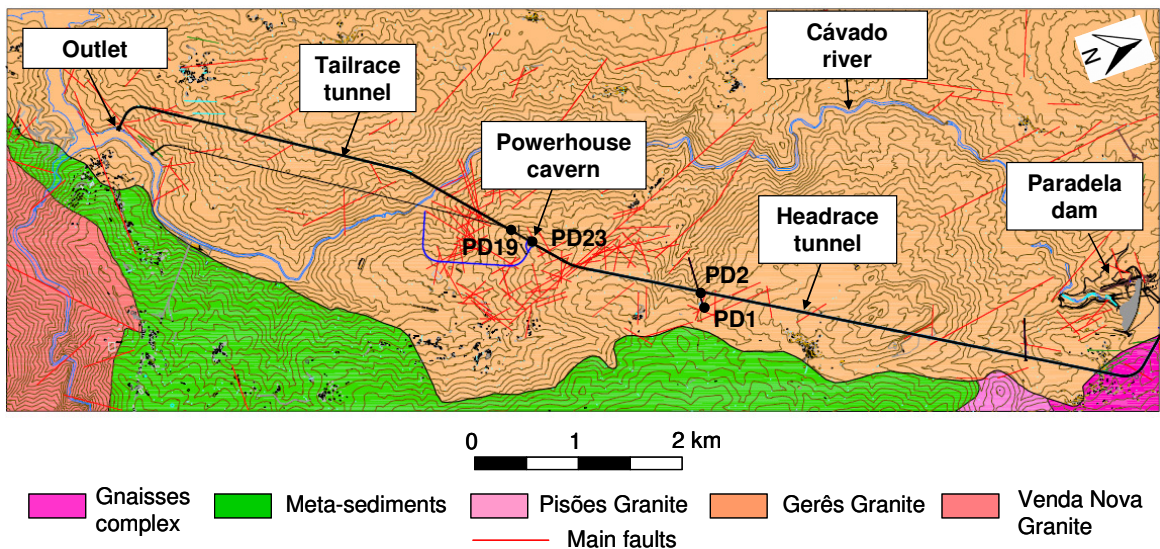


Figure 2.3: Layout of the Paradela II hydroelectric repowering scheme (courtesy of Energy of Portugal-EDP).

The water intake is placed at Paradela dam (Figure 2.4), which is a concrete face rockfill dam built in the 50's. The circuit will run approximately along the Cávado River exiting near the confluence of the Rabagão River (a left bank tributary). It will cross the flank of Serra do Gerês that corresponds essentially to an outcrop of the Gerês granite, which is a post-tectonic biotite granite with calcite plagioclase of medium size with porphyritic trends.



Figure 2.4: View of the Paradela dam.

In situ stress measurements were performed for the design of the re-powering scheme. Hydraulic tests provided the means to determine the natural stress profiles in two vertical 500 m deep boreholes (PD19 and PD23; Figure 2.5a). These two boreholes are separated by 100 m and reach the location of the future powerhouse cavern. The tests were conducted between 200 m and 500 m below the surface, i.e., above and below the ground surface, i.e., above and below the altitude of the nearby river bed.

In another location, approximately 1.7 km away from the hydraulic test site, OverCoring (OC) and Small Flat Jack (SFJ) tests were performed. Overcoring tests were conducted to determine the complete stress tensor at six different depths in two 60 m deep vertical boreholes (PD1 and PD2; Figure 2.5b), located approximately 4550 m downstream from the water intake. These boreholes are separated by 150 m and were drilled from an existing adit located 160 m below ground level and 170 m above the future hydraulic circuit. In borehole PD1, tests were conducted at depths between 205 m and 251 m below ground level. In borehole PD2, tests were conducted at depths between 163 m and 202 m below ground surface. Two tests were performed at approximately the same depth in each borehole. All of the tests were conducted above the river bed.

Small flat jack tests were performed to determine the stresses normal to various planes perpendicular to the walls of the existing adit near the boreholes where the overcoring

tests were performed. Four tests were performed at a site (SFJ1) located within 3 m of borehole PD1, and eight tests were performed at sites (SFJ2 and SFJ3) located within 50 m of borehole PD2. Figure 2.6 presents a vertical cross section along the axis of the adit, along with the location of the overcoring and small flat jack tests.

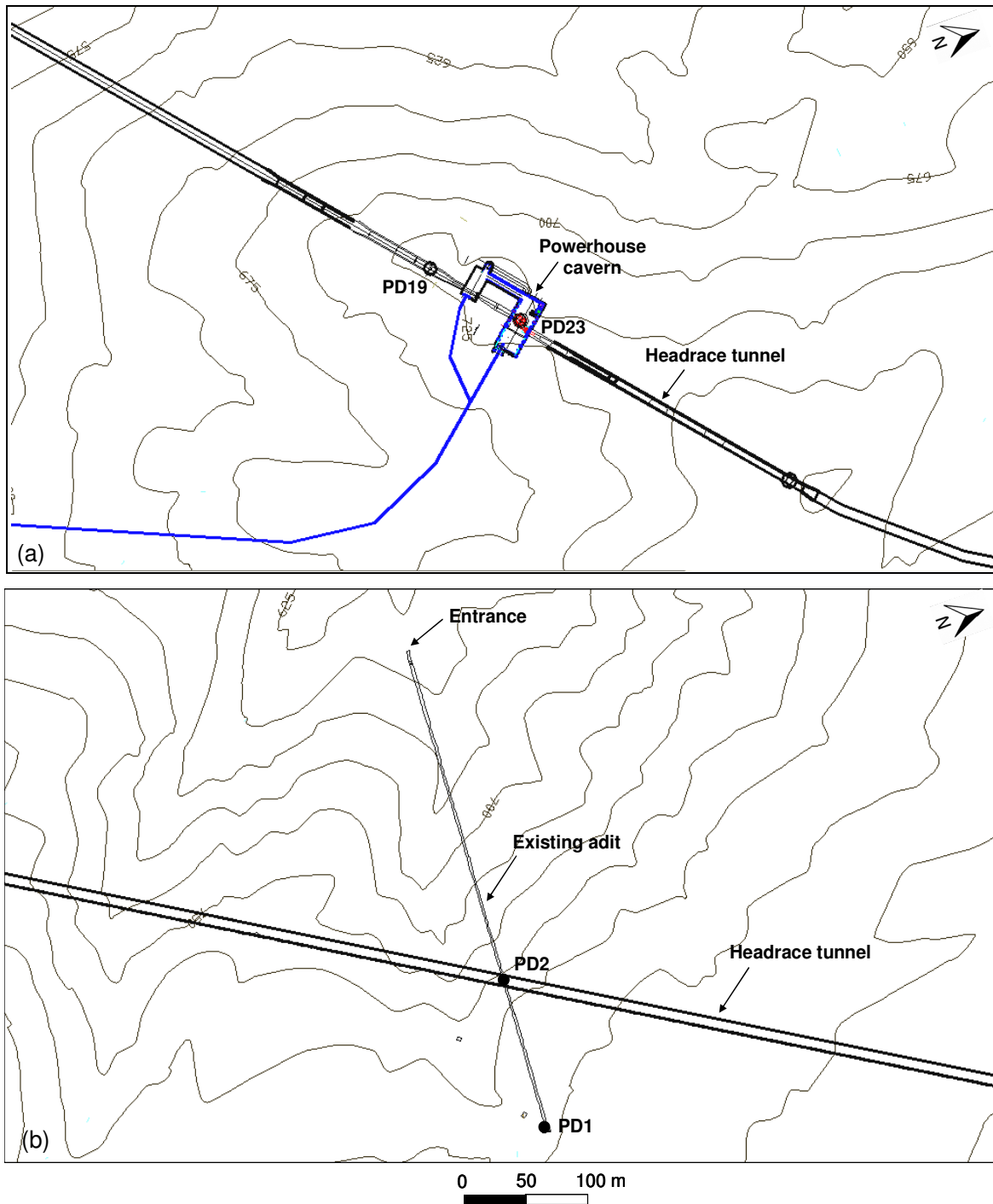


Figure 2.5: Location of the (a) hydraulic tests and (b) overcoring tests.

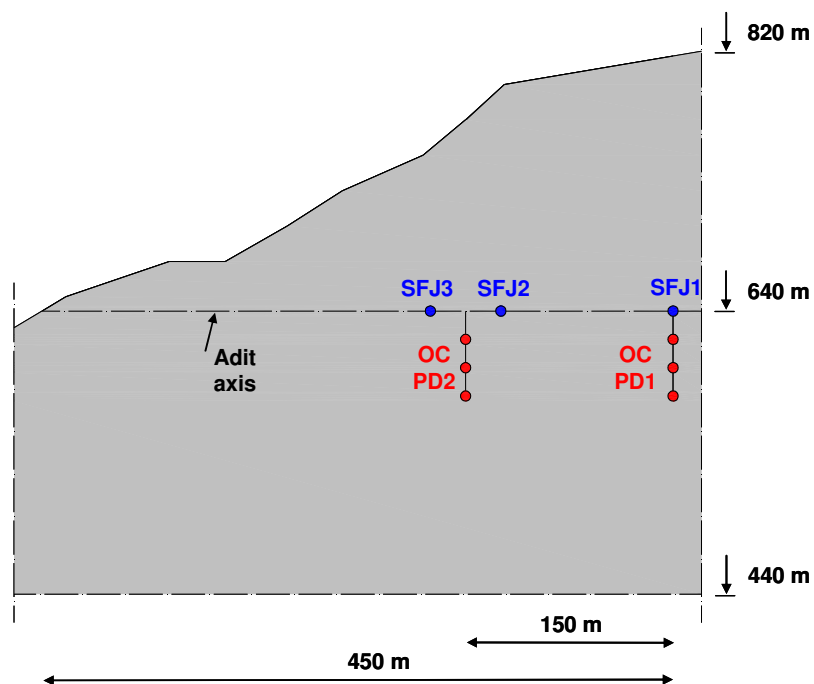


Figure 2.6: Existing adit and vertical cutting plane along the adit axis showing the location of the overcoring and small flat jack tests.

In this chapter, is discussed the collection and preliminary interpretation of the data. First, is described how hydraulic tests help determine the vertical stress profile. The overcoring tests are then described, and the results are combined in an inversion scheme to constrain the stress tensor at their location. Finally, the small flat jack tests are discussed, and their results are compared to those of the overcoring tests that were conducted at almost the same location.

2.2. In situ tests

2.2.1. Hydraulic tests

Testing technique

Hydraulic testing has involved two different techniques: Hydraulic Fracturing (HF) and Hydraulic Testing of Pre-existing fractures (HTPF), according to the procedures described by Haimson and Cornet (2003).

The hydraulic testing equipment that was used in these measurements includes a geophysical logging cable, an HTPF testing system, and all of the necessary recording equipment. The cable is moved within the borehole using a winch system that is driven by an electrical motor. A schematic view of the system is presented in Figure 2.7.

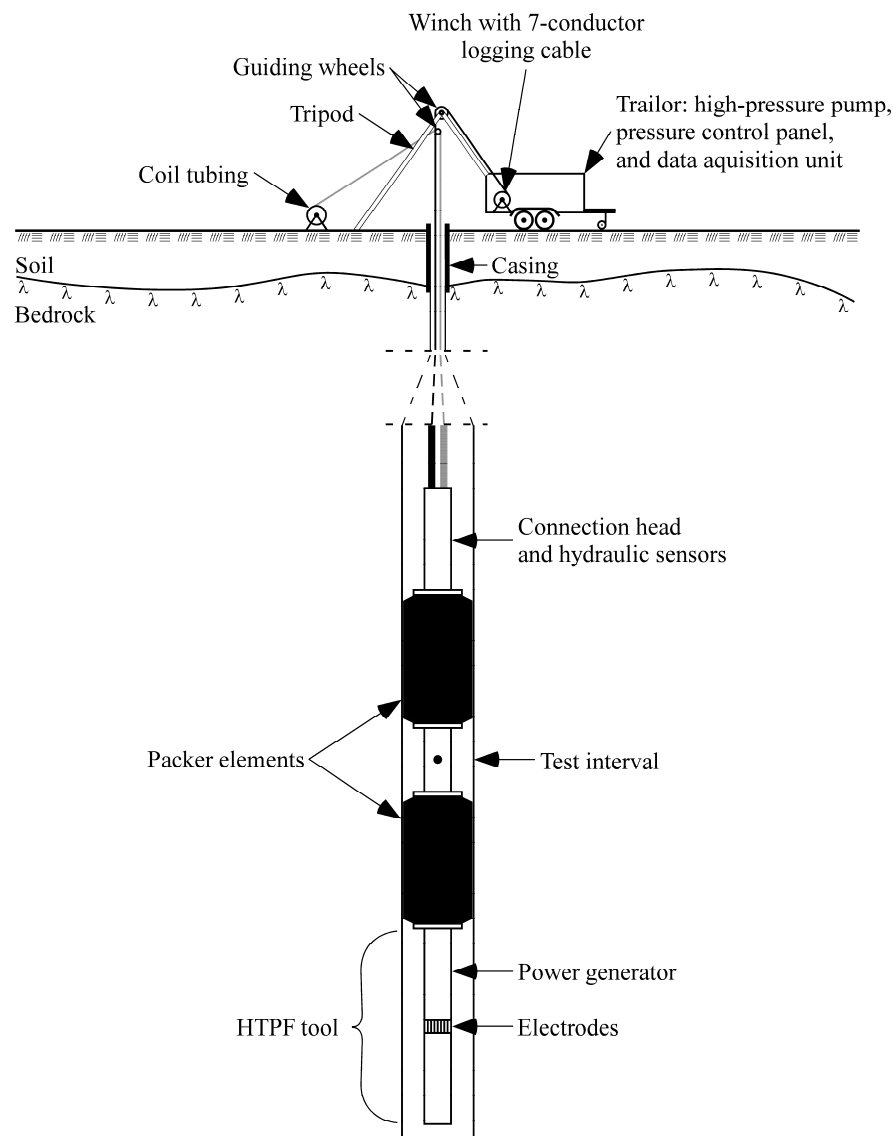


Figure 2.7: Schematic diagram of the equipment used in hydraulic tests.

The HTPF testing system includes two steel-reinforced packer elements, which are used to create or to reopen pre-existing fractures, and an electrical imaging device (HTPF tool), which provides a characterisation of the orientations of the fractures. The packers and the HTPF tool are shown in Figure 2.8.



Figure 2.8: Packers and HTPF tool.

In Figure 2.8, the top of the downhole assembly is shown in the lower-left corner and terminates with the upper packer element. The second and third parts on the figure include the lower packer element and a weight that is used to limit the associated friction problems (mounted below the HTPF tool). The lower-right corner on this figure shows the HTPF tool. The system is hydraulically connected to the surface by two coiled tubings that are attached to the logging cable with clamps that are sets at regular intervals. The coiled tubings (one is used for the packers, and the other is used for the test interval) are composed of stainless steel.

The HTPF tool (Mosnier and Cornet, 1989) is composed of a ring with 24 electrodes, which are set at various azimuths on a ring that is placed at the centre of the tool, 3 magnetometers and 2 inclinometers for measuring the position of the tool in three-dimensional space, and the electronic components required to transmit the signal to the surface. The electrical imaging technique has been adapted from the azimuthal laterolog described by Mosnier (Mosnier, 1982). During the measurement, an alternating electric voltage is applied between a distant electrode (the armour of the logging cable) and the 24 electrodes. The electric current emitted (or received) by each of the electrodes on the

central ring is proportional to the conductance of that part of the borehole wall facing the electrode. The focusing electrodes located on both sides of the electrode ring ensure that the electric current lines are normal to the borehole wall. The results can be displayed either as polar diagrams or graphically as horizontal bands composed of juxtaposed squares (one square per electrode). Because the intersection of a plane with a cylinder is an ellipse, planar fractures are easily detected in the horizontal bands diagrams by their characteristic sinusoidal shape.

Before the tests are conducted, the tripod and all of the equipment need to have been placed at the location of the boreholes (Figure 2.9a). The system, which includes the two packers and the HTPF tool, is then descended (Figure 2.9b), and the first reading (reading R_1) for the fracture depths and orientations is obtained through the HTPF tool.



Figure 2.9: Hydraulic tests performed at the Paradela II site: (a) general view of the testing scheme, (b) downward movement of the upper packer, (c) downward movement of the system with the coiled tubing and (d) hydraulic pump.

After the system reached 500 m below the surface, the system is ascended at a velocity of 2 m per minute, and the second reading (reading R_2) of the fracture depths and orientations is obtained. The images obtained in this log are essential for the selection of the location of the test intervals (homogeneous rock formation for hydraulic fracturing tests, single isolated fractures for hydraulic tests on pre-existing fractures).

In the next stage, the system is re-descended with the coiled tubing (Figure 2.9c) until it reaches the depth at which the tests will be conducted. During this movement, the third reading (reading R_3) of the fracture depths and orientations is obtained.

HF consists of the sealing of a 1-m-long intact borehole section with two inflatable packers. The sealed-off section is slowly pressurised using a hydraulic pump (Figure 2.9d) until the borehole wall fractures. During these measurements, the interval pressure and the flow rate as a function of time are recorded (Figure 2.10).

The pressure required to induce fractures is called the breakdown pressure P_b . The fracture propagates in the direction that offers the least resistance, which is usually the direction perpendicular to the minimum *in situ* principal stress. After the injection stops, the hydraulic system remains sealed, and the pressure immediately decreases: first very quickly as the fluid chases the still-extending fracture tip and then much slower as the fracture closes. The pressure at which the fracture closes is called the shut-in pressure P_s . The shut-in pressure is the transition between the fast and the slow pressure decays and is considered equal to the normal stress component acting on the fracture plane (i.e., the minimum principal stress component for true hydraulic fractures). These pressurisation cycles are repeated several times to obtain some redundancy in the reading of the shut-in pressure.

The peak pressures are discernibly lower compared with the first pressure cycle because the reopening of the fracture does not require overcoming the tensile strength of the rock, which yields the so-called fracture reopening pressure (P_r).

During the hydraulic testing of pre-existing fractures, instead of inducing new fractures in intact rock, the existing fractures in the borehole are identified and isolated between the two packers. This technique enables the measurement of the normal stress component supported by the pre-existing fractures (Cornet 1993, Cornet and Valette 1984). Using a low injection flow rate, the fluid pressure that exactly balances the normal stress across the fracture is measured. The method is repeated for other non-parallel fractures with known orientation.

After the hydraulic tests, the packers and the HTPF tool are progressively ascended, and the clamps are removed. During this movement, the fourth reading (R_4) of the fracture depths and orientations are obtained.

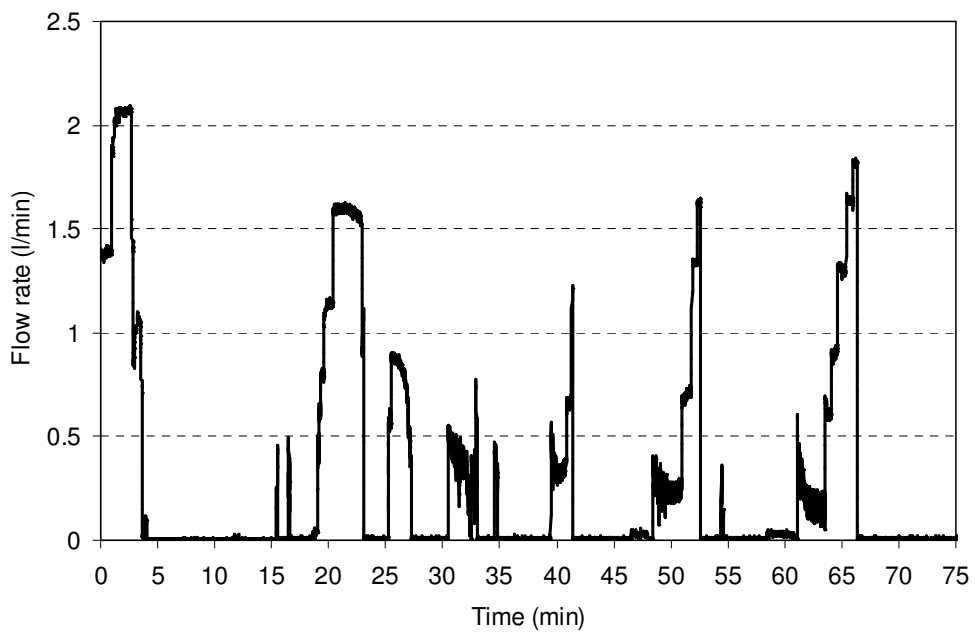
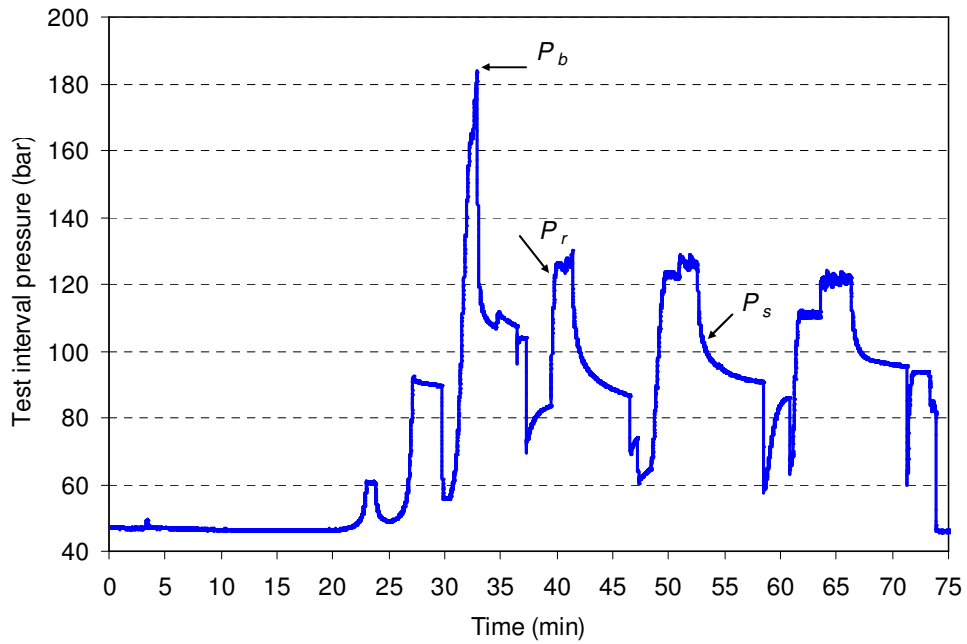


Figure 2.10: Record of test interval pressure and flow rate as a function of time through a hydraulic fracturing test.

The data were collected using a data acquisition system (PC with the LabVIEW system) that simultaneously integrates the surface data (injection flow rate, injection pressure, and depth of test, which is provided by the depth meter of the logging cable) and the downhole data (24 electrodes, downhole pressure for both the interval and the packers, and the tool orientation). A tension meter is also used to monitor the tension in the cable. In addition, the packer and interval pressures are monitored at the ground surface with high-precision electric pressure transducers. The flow rate is measured with a high-precision turbine type flow meter. As a safety procedure, a line printer was used during the testing to record the packer and interval pressures and the injected flow rate as a function of time.

The raw data corresponding to the pressure as a function of time and flow rate as a function of time curves are presented in Appendix A. The flow rate as a function of time curves are only presented for the tests done in borehole PD19, because due to a technical problem occurred with the flow meter, it was not possible to measure the flow rate during the tests done in borehole PD23. This appendix also shows the electrical images obtained before (Pre Frac) and after (Post Frac) the hydraulic tests, that were obtained from readings R_2 and R_4 , respectively.

In borehole PD23, a technical difficulty prevented from obtaining the tool orientation during logging. This difficulty was overcome by running a properly oriented high-resolution acoustic televiewer (HRAT) log. The equipment used in this log includes a calliper and a High-Resolution Acoustic Televiewer tool. All the field measurements were carried out using a surface unit constituted by a USB interface for a laptop computer that enables the automatic storage of all of the data in digital files.

The HRAT log was performed in two steps. First, a calliper log was performed to assess the state of the borehole walls before the HRAT tool was introduced. Three mechanically coupled arms (Figure 2.11a) provide a single continuous log of the borehole diameter, which is determined through contact with the borehole walls. The probe is descended with the arms retracted. Once the probe reaches the bottom of the borehole, the arms are opened and maintained open through the use of springs during the probe's ascent. Variations in the diameter with depth make the tool's arms open or close. This movement is recorded by the surface unit. Second, the high-resolution acoustic televiewer (HRAT) log is obtained with a probe (Figures 2.11b and 2.11c) that uses a fixed acoustic transducer and a rotating acoustic mirror to scan the borehole walls with a focussed ultrasound beam. The amplitude and travel time of the reflected acoustic signal are recorded simultaneously as separate image logs. The obtained log is an unwrapped high-resolution image of the borehole walls, in which all significant fractures are visible. The

directional information is also recorded in real time (azimuth and deviation in the borehole axis). The calliper and HRAT logs were performed as the instruments were moved upward at a constant speed equal to 2 m per minute.

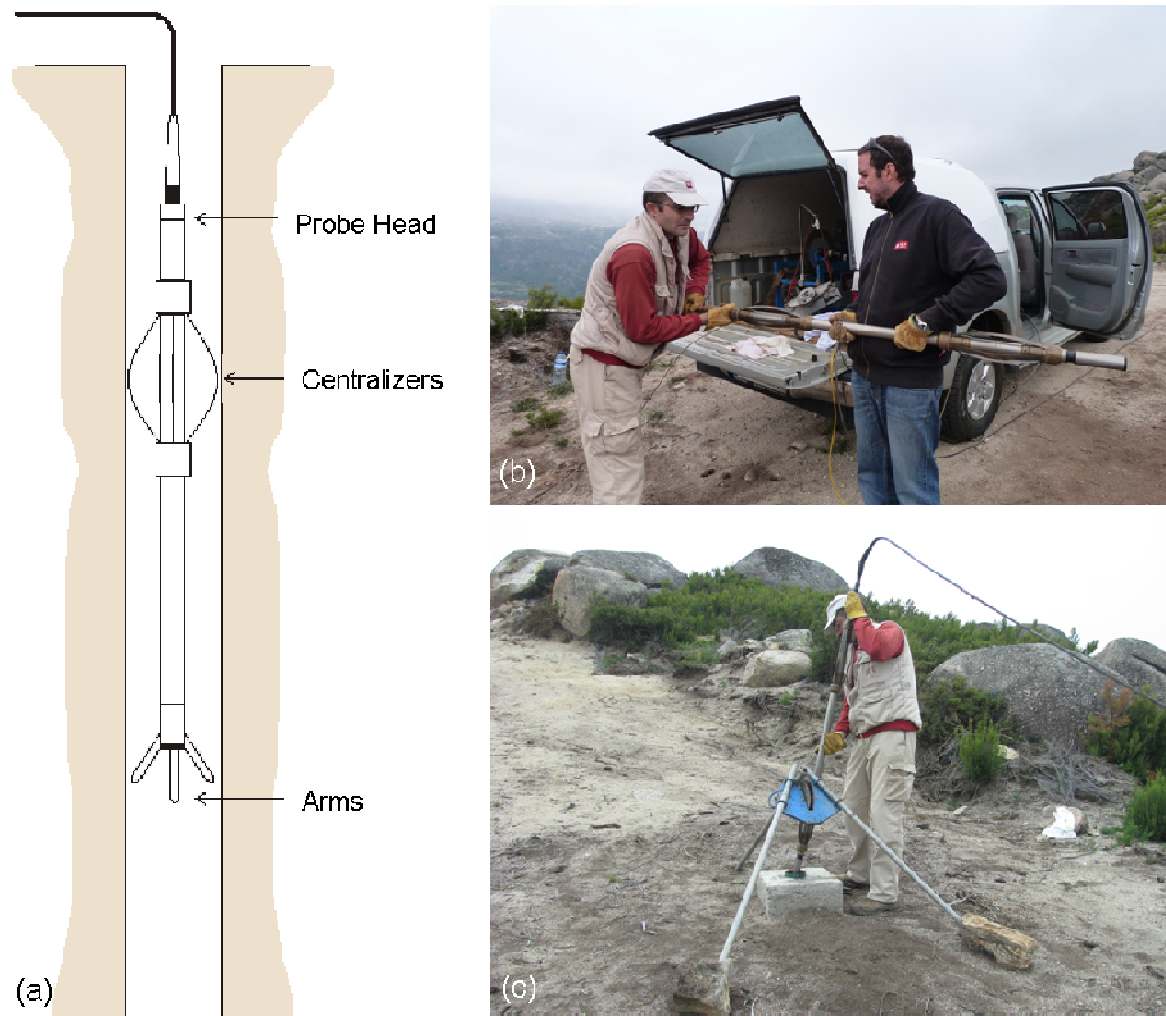


Figure 2.11: (a) Calliper tool (Zemanek *et al.*, 1969), (b) HRAT tool, and (c) introduction of the HRAT tool into borehole PD23.

Testing interpretation

The purpose of the stress field determination is to determine the stress tensor at each point where tests have been conducted so as to fit better the normal stress measurements obtained for all the tested fractures. The flow rate does not come explicitly into the determination of the stress field.

In the classical hydraulic fracturing technique, the borehole is assumed to be parallel to one of the principal stress directions. In addition, only four components of the stress tensor are determined with some reliability: the three Euler angles that define the orientations of the principal stresses and the minimum principal stress magnitude.

The hydraulic testing technique of pre-existing fractures does not require any *a priori* hypothesis of the relative orientation of the borehole axis. However, it requires testing at least eight or nine fractures with six different orientations to achieve a complete stress tensor determination because of the need to compensate uncertainties.

The combination of hydraulic fracturing and hydraulic tests of pre-existing fractures maintains the amount of tests required at a minimum and provides a complete determination of the stress tensor.

The measured normal stress σ_n^m on the m^{th} fracture plane with normal n^m , which is located at a point X^m with x , y , and z coordinates, can be written as follows:

$$\sigma_n^m = \sigma(X^m)n^m n^m, \quad (2.1)$$

where $\sigma(X^m)$ is the complete stress tensor at point X^m .

When a minimum of six different tests on fractures with different values of dip and azimuth are conducted within a rock mass volume that is sufficiently small that the gradient of the stress tensor components along the x , y , and z directions can be neglected, the set of equations (2.1) obtained for the total number M of hydraulic tests can be solved using a standard least squares method.

However, the stress gradient within the rock mass volume in which the data are collected is generally too large to be neglected. Thus, the measured rock mass volume is usually discretised into sub-volumes in which the stress field is approximated by a linear variation with x , y , and z coordinates. When the stress measurements are conducted in a vertical borehole and hence the horizontal gradients of the stresses are null, the stress tensor $\sigma(X^m)$ at point X^m can be calculated to be a linear function only of the vertical coordinate z , according to the following equation:

$$\sigma(X^m) = \sigma(z) + (z_m - z)\alpha, \quad (2.2)$$

where $\sigma(z)$ is the stress tensor along coordinate z , z_m is the coordinate of the m^{th} test, and α is the stress gradient tensor along the borehole axis. If the reference origin is coincident with the ground level, z and z_m are depths below the surface.

Accordingly, this approximation of the stress field requires the determination of twelve parameters: six of these parameters are associated with $\sigma(z)$, and the other six parameters are associated with α . The number of unknowns may be reduced depending on additional simplifying assumptions. By assuming that the vertical direction is a principal stress direction, a total of eight parameters are needed to describe the stress field: four of these are associated with $\sigma(z)$, and the other four are associated with α .

In this model, S_1 , S_2 and S_3 are the maximum and minimum horizontal stresses and the vertical stress at coordinate z , respectively, λ is the direction of the maximum horizontal principal stress with respect to the North, α_1 , α_2 , and α_3 are the nonzero eigenvalues of the vertical gradient of the stress tensor α , and η is the orientation of eigenvector α_1 with respect to the S_1 eigenvector. Then, for the m^{th} test, equations (2.1) and (2.2) yield the following error function (Cornet, 1993):

$$\sigma_n^m - (S_3 + \alpha_3(z_m - z))\cos^2 \theta_m - \frac{1}{2}\sin^2 \theta_m \left\{ \begin{array}{l} S_1 + S_2 + (\alpha_1 + \alpha_2)(z_m - z) + \\ + (S_1 - S_2)\cos 2(\phi_m - \lambda) + \\ + (\alpha_1 - \alpha_2)(z_m - z)\cos 2[\phi_m - (\lambda + \eta)] \end{array} \right\} = 0, \quad (2.3)$$

where σ_n^m is the normal stress on the m^{th} fracture plane, ϕ_m is the azimuth of the normal to the m^{th} fracture plane with respect to the north direction, and θ_m is the inclination of the normal to the m^{th} fracture plane with respect to the vertical direction.

To solve the inverse problem presented in equation (2.3), the method developed by Cornet and Vallette (1984), which is based on the least squares criterion (Tarantola and Valette, 1982), was applied. In this method, all of the measurements are assumed to obey a Gaussian law and are thus described by their expected value, their variance, and their covariances with other measurements. It is assumed that some *a priori* knowledge of the unknown parameters exists and can be formulated in terms of the expected value, the variance, and the covariances. In practice, large error bars are placed on the assumed central values of the unknowns.

Let x_0 be the point with all of the expected values for both the measurements and the parameters ($z_m, \theta_m, \phi_m, \sigma_n^m, \dots, S_1, S_2, S_3, \lambda, \alpha_1, \alpha_2, \alpha_3, \eta$). This variable then contains $4M+8=L$ components for M tested intervals. Let C_0 be the corresponding *a priori* covariance matrix, which is diagonal because the *a priori* values for the measurements d_0 and the parameters p_0 are supposed to be independent:

$$x_0 = \begin{bmatrix} d_0 \\ p_0 \end{bmatrix} \quad C_0 = \begin{bmatrix} C_{d_0 d_0} & C_{d_0 p_0} \\ C_{p_0 d_0} & C_{p_0 p_0} \end{bmatrix}. \quad (2.4)$$

Of all points x that belong to the l -dimensional space under consideration, there exists a set S of points x that exactly satisfies the condition

$$f(x) = 0, \quad (2.5)$$

where $f(x)$ is a vectorial function (with M components) of x that is defined by the error between the measured and the calculated normal stresses, as defined by equation (2.3).

The problem is then to find the x^s of S that is closest to x_0 according to the least squares criterion, i.e., the point x that satisfies

$$(x^s - x_0)^T C_0^{-1} (x^s - x_0) \quad \text{minimum over } S. \quad (2.6)$$

The components of x^s are referred to as the *a posteriori* values. If a point x^s satisfies the set of equations (2.5) and (2.6), it also satisfies equation (2.5) and the following equation:

$$(x^s - x_0)^T C_0^{-1} (x^s - x_0) \quad \text{stationary over } S. \quad (2.7)$$

The set of equations (2.5) and (2.7) contains, in addition to the solution to equations (2.5) and (2.6), local minima, saddle points, and local maxima. The solution of the system constituted by equations (2.5) and (2.7) is equivalent to the solution of the following equation (Tarantola and Valette, 1982):

$$x^s = x_0 + C_0 F^T (F C_0 F^T)^{-1} [F(x^s - x_0) - f(x^s)], \quad (2.8)$$

where F is the matrix of the partial derivatives of $f(x)$ valued at point x^s . Accordingly, the components F_{mj} of F are

$$F_{mj} = \frac{\partial f_m}{\partial x_j}, \quad (2.9)$$

where f_m is the m^{th} component of $f(x)$ and x_j is the j^{th} component of x . Thus, from equation (2.5), equation (2.8) may be solved with an iterative algorithm using the fixed point method (Tarantola and Valette, 1982):

$$x_{k+1} = x_0 + C_0 F_k^T (F_k C_0 F_k^T)^{-1} [F_k (x_k - x_0) - f(x_k)], \quad (2.10)$$

where F_k is evaluated at x_k . This iterative process is started at an arbitrary x , which is chosen to be x_0 . The iterative procedure is stopped when $f(x_k)$ is sufficiently close to zero.

The stationary point x obtained using the iterative process (2.10) corresponds to a strict local minimum of f if and only if $C_0^{-1} L_x Q_x$ is non-negative. In this term, Q_x is the linear projector defined by

$$Q_x = 1 - C_0 F_x (F_x C_0 F_x^T)^{-1} F_x, \quad (2.11)$$

and L_x is the operator defined by

$$L_x(V) = V - Q_x C_0 [K_x(V)]^T (F_x C_0 F_x^T)^{-1} F_x (x^s - x_0), \quad (2.12)$$

where V is any vector, F_x is the matrix of partial derivatives of $f(x)$ evaluated at point x , and K_x is the second-order partial derivative operator of $f(x)$ at point x .

The *a posteriori* variance and covariances associated with the unknowns provide a measure of the quality with which the unknowns have been resolved. If the *a posteriori* variance of the unknowns is small, the value has been well resolved; if it is nearly equal to the *a priori* variance, the corresponding unknown has not been well resolved.

If the problem is linear ($\eta \neq 0$), it can be shown that the *a posteriori* covariance matrix is given by the following equation:

$$C = Q_x C_0. \quad (2.13)$$

If the problem is non-linear, the expression (2.13) can still be used, but the value obtained depends on the final *value* x_{k+1} . However, when both $(x^s - x_0)^T C_0^{-1} (x^s - x_0)$ and $\|K_x\|$ are small, the linear approximation yields a satisfactory result.

Based on the obtained solution, the stress field components and their respective *a posteriori* variances are calculated along the boreholes axis, in the depth range of the measurements.

Interpretation of breakdown pressure and of reopening pressure for true hydraulic fracturing tests

In the classical theory of hydraulic fracturing, the breakdown pressure is taken advantage for determining the maximum horizontal principal stress magnitude σ_H according to the following equation:

$$-\sigma_H + 3\sigma_h + \sigma_t - aP_a - P_b = 0, \quad (2.14)$$

where σ_t is the so called tensile strength of the rock, P_b is the breakdown pressure, P_a is the far field pore pressure and a is a parameter that varies between 0 and 1 depending on the testing conditions (Schmitt and Zoback, 1989). It has also been proposed to consider equation (2.14) for interpretation of the reopening pressure, with the hypothesis that the corresponding tensile strength is zero. But many results have shown that this last proposition is not valid because of fluid penetration into the fracture before its actual opening, so that in most cases, the reopening pressure is in fact very close to the shut-in pressure (Cornet and Valette, 1984).

The large uncertainty that concerns the exact role of pore pressure influences strongly that associated with the determination of the maximum horizontal stress in equation (2.14). In fact this uncertainty is of the same order of magnitude as the pore pressure value itself. Further, experience has shown that in most cases, hydraulic fractures extend below the packer so that the real breakdown pressure is not the peak value reached in the interval but an undetermined packer pressure value. Hence, the breakdown pressure is not considered as a reliable stress estimate.

2.2.2. Overcoring tests

Testing technique

The Stress Tensor Tube (STT) test initially developed by Rocha and Silverio (1969) basically corresponds to an overcoring test. The overcoring method is based on the stress relief around a borehole and yields the complete stress state at the corresponding location through a single overcoring operation.

The STT strain measurement device (Figure 2.12) is a hollow epoxy resin cylinder with an outer diameter of 35 mm, an approximate length of 20 cm, and a thickness of 2 mm. The cell has 10 electrical resistance strain gauges embedded in positions normal to the faces of a regular icosahedron, which enables an equal sampling of the stress states in all directions (Pinto and Cunha, 1986).

Figure 2.13 shows, besides those angles, a sketch of the orientation of all 10 strain gauges in relation to the $Oxyz$ co-ordinate system associated to the STT cell, in which the Oz axis has the direction of the borehole, and the Ox axis is normal to the direction of the strain gauge 1.



Figure 2.12: STT cell and data acquisition unit.

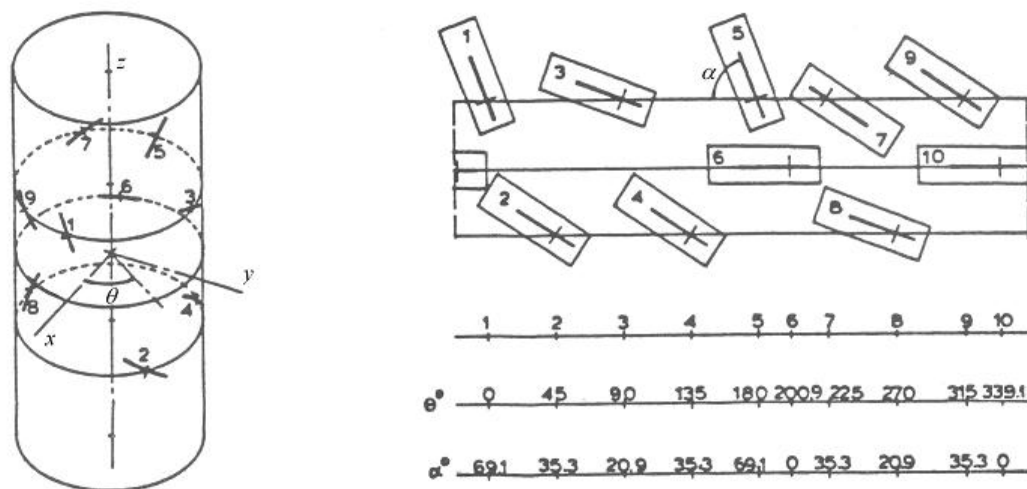


Figure 2.13: Orientation of the strain gauges in the STT cell.

The cell includes a metal capsule in which a small data acquisition unit is located. The cell also includes a thermocouple such that readings of all strain gauges and the temperature are conducted at fixed time intervals, and these readings are stored in local memory.

A test consists of the following (Figure 2.14): (1) drilling a borehole with a diameter of 140 mm to the depth of interest; (2) installing a borehole casing, with an inner diameter around 48 mm, with exterior centring devices; (3) drilling a concentric 37 mm diameter borehole from the bottom of the large diameter borehole using the casing as a guide; (4) inserting the STT cell into the 37 mm diameter borehole with the help of positioning rods and gluing to the rock by means of an epoxy resin, which is placed inside the cell just before its positioning; (5) removing the positioning rods and the borehole casing and lowering the large diameter core barrel; (6) resuming the drilling of the large diameter borehole to a depth compatible with a complete stress release around the STT cell.

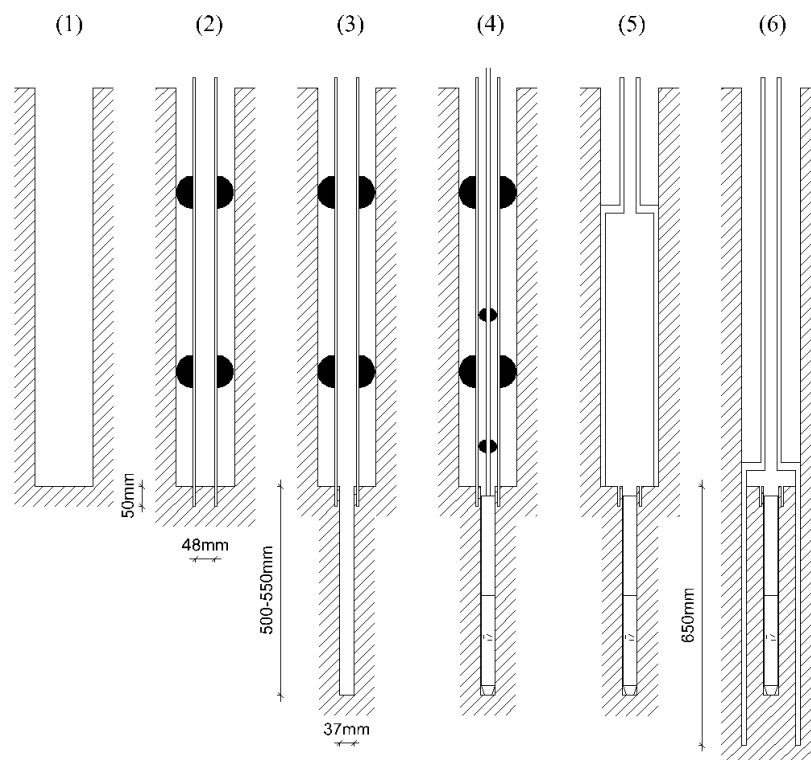


Figure 2.14: Sequence of execution of an STT stress measurement test.

After the overcoring, the core with the strain measurement device is recovered, and the content of the memory (strains, temperatures and times) is transferred to a computer. Appendix B shows the curves that were obtained in all overcoring tests. In Figure 2.15, the variation of the strains with time at the location of the ten strain gauges obtained during an overcoring test is shown. The dashed line represents the variation of the

temperature with time. Strain readings are taken before and after overcoring when the temperature is stabilised. The difference between these values is calculated, which corresponds to the strains that result from the overcoring.

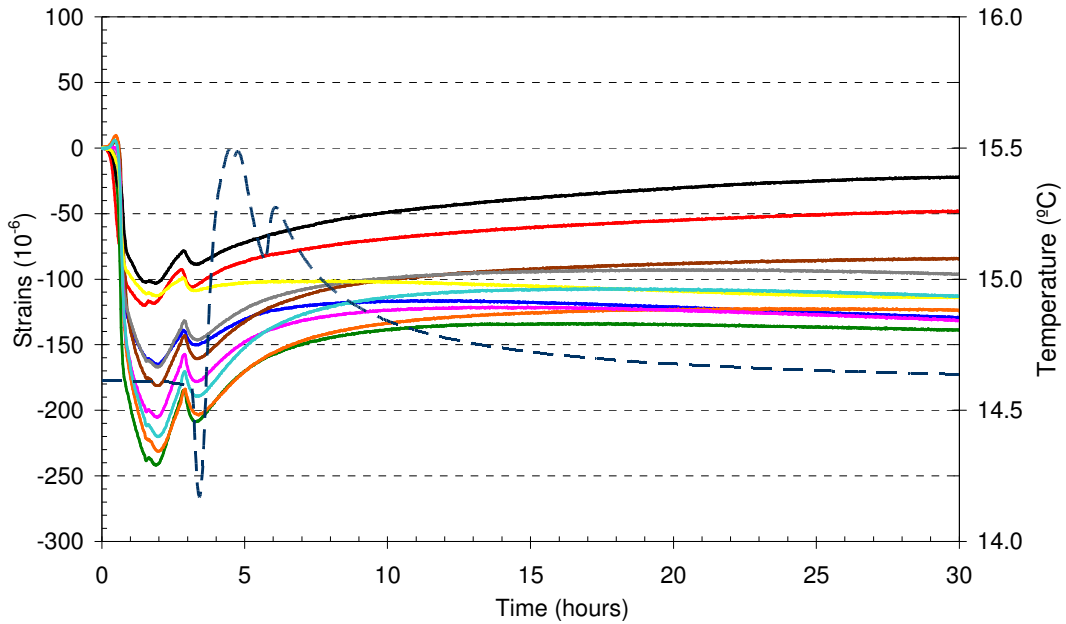


Figure 2.15: Record of strains and temperature as a function of time through an overcoring test.

To determine the elastic constants of the overcored cores, they are placed inside a biaxial chamber (Figure 2.16) in which a radial hydraulic pressure p is applied. Three loading and unloading cycles were performed. The first cycle achieves a maximum pressure of 2 MPa. In the other two cycles, a maximum pressure of 6 MPa is applied. The deformation at the location of the ten strain gauges that results from the applied pressure is measured. Appendix B shows the strains as a function of pressure through the biaxial tests.



Figure 2.16: Biaxial test chamber with the core.

Testing interpretation

The model used for interpreting the STT tests results assumes that the rock is homogeneous, linear, elastic and isotropic; that the relationship between the length and diameter of the cell is high; and that the stiffness of the hollow cylinder is significantly less than the stiffness of the rock. In this model, given the arrangement of the strain gauges, the strain ε_i measured by the strain gauge i ($i = 1, \dots, 10$) is expressed in cylindrical coordinates, through the following equation (Pinto and Cunha, 1986):

$$\varepsilon_i = \varepsilon_{zi} \sin^2 \alpha_i + \varepsilon_{\theta i} \cos^2 \alpha_i + \gamma_{\theta zi} \sin \alpha_i \cos \alpha_i, \quad (2.15)$$

where α_i is the angle between the direction of the strain gauge i and the xy plane, θ is the angle between the normal to the strain gauge i and the x axis.

Given these geometrical definitions, the strains $\varepsilon_{\theta i}$, ε_{zi} e $\gamma_{\theta zi}$ are expressed by:

$$\varepsilon_{\theta i} = \frac{1}{E} [M_1(\sigma_{xx} + \sigma_{yy}) + N(\sigma_{xx} - \sigma_{yy}) \cos(2\theta_i) - M_2\sigma_{zz} + 2N\sigma_{xy} \sin(2\theta_i)], \quad (2.16)$$

$$\varepsilon_{zi} = \frac{1}{E} [\sigma_{zz} - \nu(\sigma_{xx} + \sigma_{yy})], \quad (2.17)$$

$$\gamma_{\theta zi} = \frac{1}{E} [M_3(\sigma_{yz} \cos \theta_i - \sigma_{xz} \sin \theta_i)], \quad (2.18)$$

where E is the elastic modulus of the overcored core, σ_{xx} , σ_{yy} , σ_{zz} , σ_{xy} , σ_{yz} , σ_{xz} are the six components of the stress tensor and the parameters M_1 , M_2 , M_3 and N are functions of the geometrical and mechanical characteristics of the STT cell, and of the Poisson's ratio ν :

$$M_1 = 1.204165 - 0.083507\nu, \quad (2.19)$$

$$M_2 = 1.204165\nu - 0.083507, \quad (2.20)$$

$$M_3 = 4.424179(1 + \nu), \quad (2.21)$$

$$N = -2.444020(1 - \nu^2). \quad (2.22)$$

From these expressions, the strains ε_i at the location of the strain gauge i are related to the components of the *in situ* stresses σ_j ($j = 1, \dots, 6$) through the following matrix equation:

$$\varepsilon_i = a_{ij}\sigma_j, \quad (2.23)$$

where a_{ij} is a matrix with ten rows and six columns that depends on the elastic parameters (elastic modulus and Poisson's ratio) of the overcored core.

With the measured ten strains that result from a biaxial loading ($\sigma_{xx} = \sigma_{yy} = p$ and $\sigma_{zz} = \sigma_{xy} = \sigma_{yz} = \sigma_{xz} = 0$), the least squares method is applied to solve the matrix equation (2.23) and consequently determine the elastic constants. Once the strains resulting from the overcoring are measured and the elastic constants are determined, the least squares method is applied to determine the six components of the stress state in the co-ordinate system associated with the STT cell.

2.2.3. Small flat jack tests

The small flat jack testing method (Rocha *et al.*, 1966) is based on the principle of partial stress release followed by stress compensation (Habib and Marchand, 1952). In this technique, a single stress component is determined. Before the tests, the location of the tests is marked on the rock mass surface. In Figure 2.17a, the angles are between the horizontal and the slots plane.

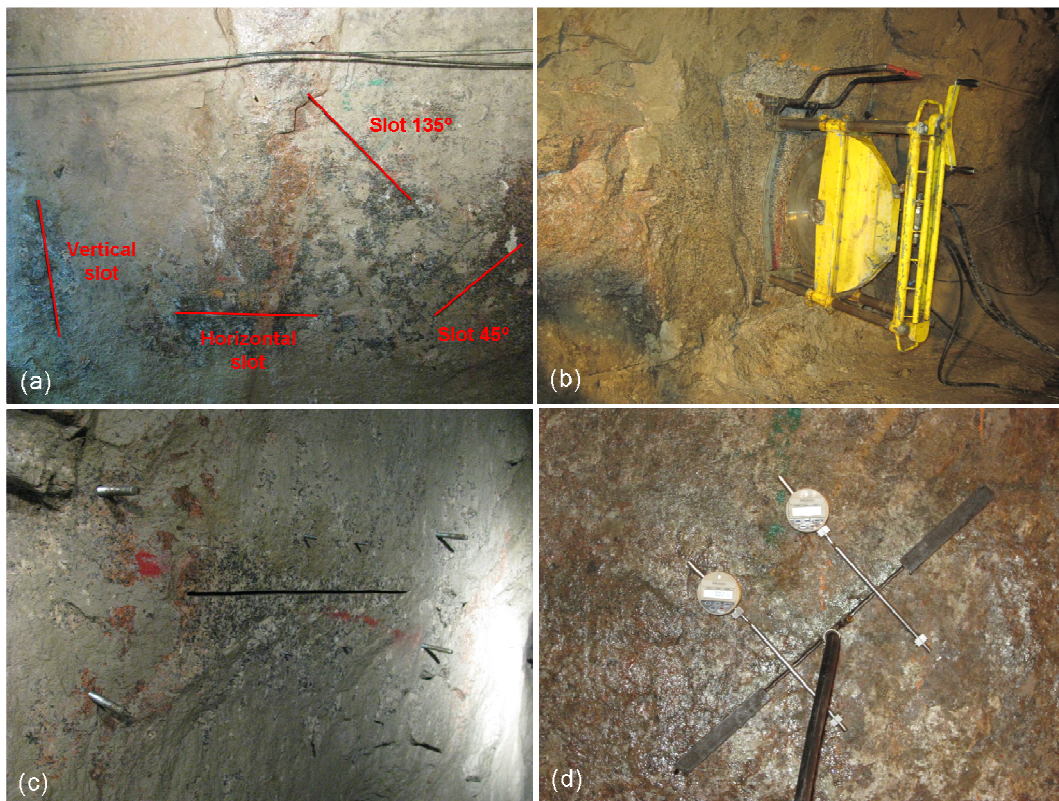


Figure 2.17: Steps of the small flat jack tests: (a) marking the tests location, (b) cutting the slot, (c) slot, anchor bolts and measurements pins, and (d) measuring the distance between the pins using digital transducers.

In this technique, two pairs of pins are placed on the rock mass surface, and the initial distance between them is measured. Then, between the two pairs of pins, a 10 mm-thick slot with a depth of 27 cm is cut perpendicular to the rock mass surface using a diamond disk with a 60 cm diameter (Figure 2.17b and 2.17c). Due to the partial stress relief, deformations in the direction normal to the slot occur and the distance between the pins decreases. Subsequently, a circular flat jack consisting of two thin metal plates welded together is inserted into the slot and pressurised until the distance between the pins is restored. The distance between the pins is measured using digital transducers (Figure 2.17d). During the test, the variation of the relative displacements in the two pairs of pins because of the applied pressure is recorded (Appendix C).

Figure 2.18 shows the average relative displacements as a function of pressure through a typical test. Generally, a non-elastic behaviour is observed because non-recoverable displacements are detected after unloading.

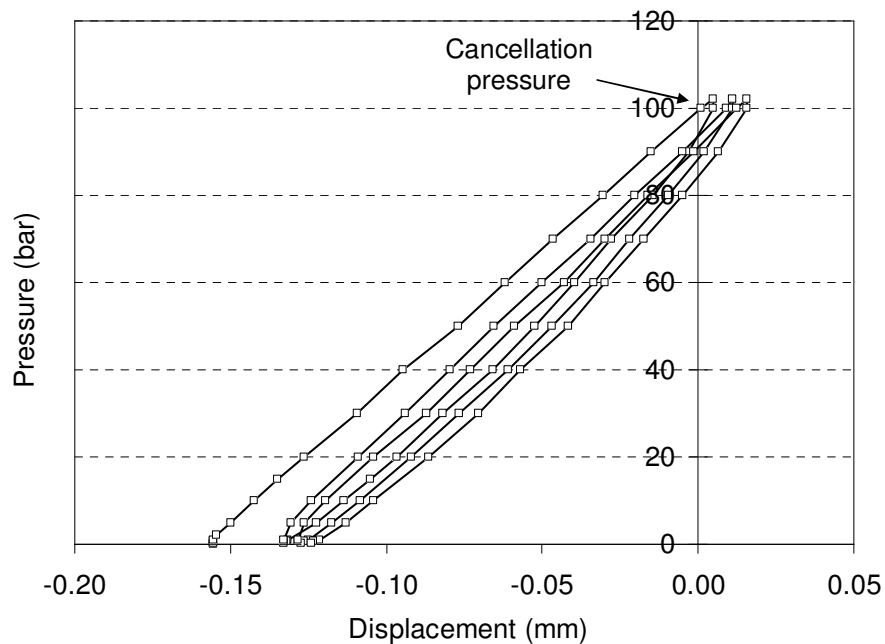


Figure 2.18: Typical record of pressure as a function of displacement through a small flat jack test.

The pressure required to restore the initial position of the pins is called the “cancellation pressure”, and it is assumed to be equal to the stress component normal to the slot plane. In each test, the cancellation pressure is obtained from the intersection of the average displacement curve with the vertical axis. In this determination, only the loading phase in first cycle was considered.

In addition to measuring *in situ* stresses, small flat jack tests are used to determine the elastic modulus E normal to the slots from the pressure p that is applied normal to the slots, the displacement δ that is measured at the location of the pins, and a constant k that depends on the geometric characteristics of the small flat jack using the following equation (Souza Martins, 1986):

$$\delta = \frac{k}{E} p \quad (2.24)$$

2.3. Laboratory test results

Several laboratory tests were conducted on sample cores extracted from various locations at the Paradela II site to determine the rock mass properties.

Uniaxial compression tests were performed on 25 sample cores to determine the elastic constants (elastic modulus and Poisson's ratio) and the uniaxial compression strength σ_c . Several loading and unloading cycles were used until a maximum uniaxial stress of 25 MPa was reached. The uniaxial stress as a function of the strains curves obtained revealed that the rock mass exhibits a linear and non-elastic behaviour at the time scale of the measurements, with a decrease in the permanent strains after the first cycle. The elastic parameters were determined assuming an elastic and linear behaviour of the rock mass during the second and third cycles. The uniaxial compression strength was calculated from the maximum stress applied in the last cycle until the rupture of the rock sample was achieved.

Diametral compression tests were also conducted to characterise the tensile strength σ_t of the rock mass. The tests consisted of the application of an increasing force at regular intervals along two geriatrics of a cylindrical sample, with a thickness approximately equal to their radius, until a tensile rupture in a direction perpendicular to the plane of the stress application is achieved. The tensile strength was determined by the following expression:

$$\sigma_t = \frac{2}{\pi} \frac{F_t}{De}, \quad (2.25)$$

where F_t is the rupture force, D is the diameter, and e is the thickness of the sample.

The following average and standard deviation (δE , $\delta \nu$, $\delta \sigma_c$, $\delta \sigma_t$) values were obtained for the elastic parameters, the uniaxial compression strength, and the tensile strength:

$$E = 44.6 \text{ GPa}, \delta E = 9.0 \text{ GPa}, \nu = 0.25, \delta \nu = 0.06$$
$$\sigma_c = 100.7 \text{ MPa}, \delta \sigma_c = 35.0 \text{ MPa}, \sigma_t = 8.3 \text{ MPa}, \delta \sigma_t = 3.0 \text{ MPa}$$

The standard deviations of the elastic modulus, Poisson's ratio, the uniaxial compression strength, and the tensile strength were approximately 25%, 28%, 35%, and 36% of the average values, respectively. This variation around the average values indicated a significant spatial variability in the rock mass properties.

Density measurements were conducted in nine samples to obtain a value of 2650 kg/m³.

2.4. Stress measurement results

2.4.1. Hydraulic test results

2.4.1.1. Calibrations

The analysis of the hydraulic tests was started through the calibrations of the pressures on the tested fracture planes and their depths and orientations.

Calibration of the depths data

The depths of the fracture planes given by the HTPF tool are subject to an error that is comparable to the values obtained by the core analysis. Thus, the calibration of the electrical imaging data (reading R_2) was conducted by taking the cores as a reference. A few characteristic, unambiguous, fracture sets on both logs were identified, and a rule for the depth correspondence was defined. Figures 2.19 and 2.20 show a comparison between the cores and the electrical imaging data for sets of fractures identified in boreholes PD19 and PD23, respectively. Table 2.1 presents a summary of the results. The depths presented in the table are in reference to the top of the fractures.

The table shows an average discrepancy of 0.5 m and 1 m between the electrical imaging data and the cores extracted from boreholes PD19 and PD23, respectively. A detailed comparison between other sets of fractures identified in cores and electrical imaging data showed that these discrepancies are repeated along the boreholes axis. Additionally, the comparison between the depth data provided by the HRAT and the electrical imaging logs enables to conclude that there is a discrepancy between those readings of approximately 1 m, which is repeated along the borehole PD23 axis.

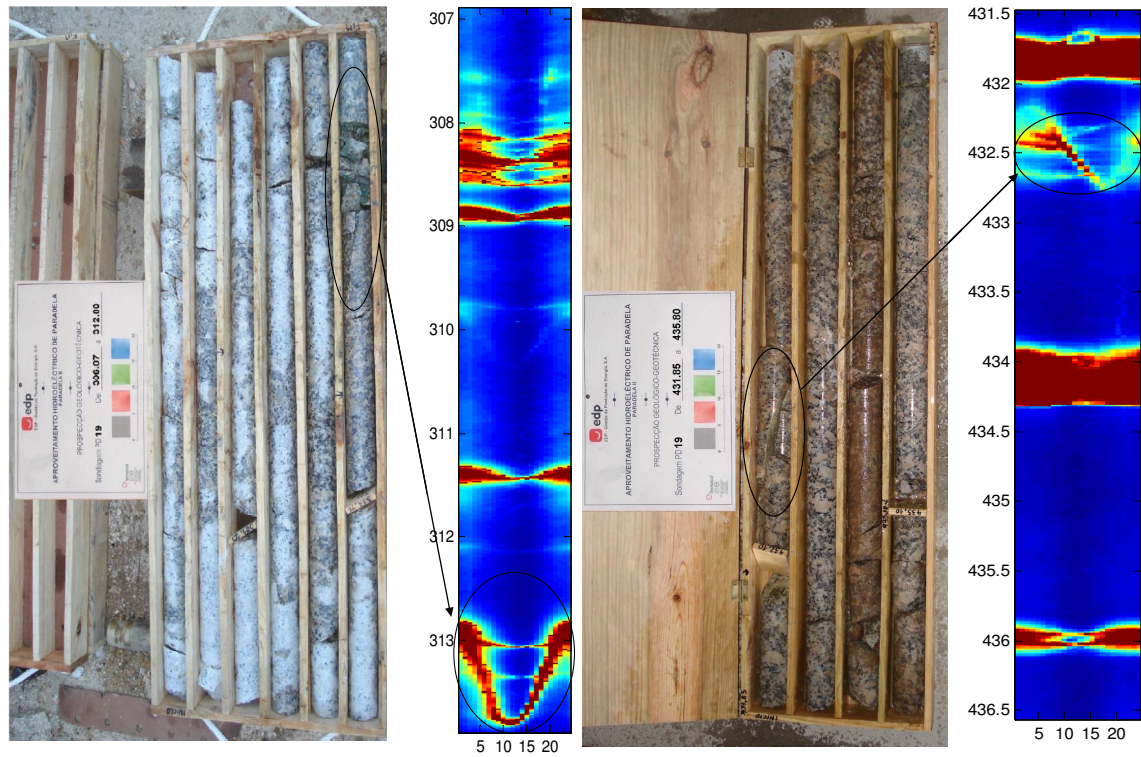


Figure 2.19: Comparison between the cores and the electrical images of the sets of fractures identified in borehole PD19.

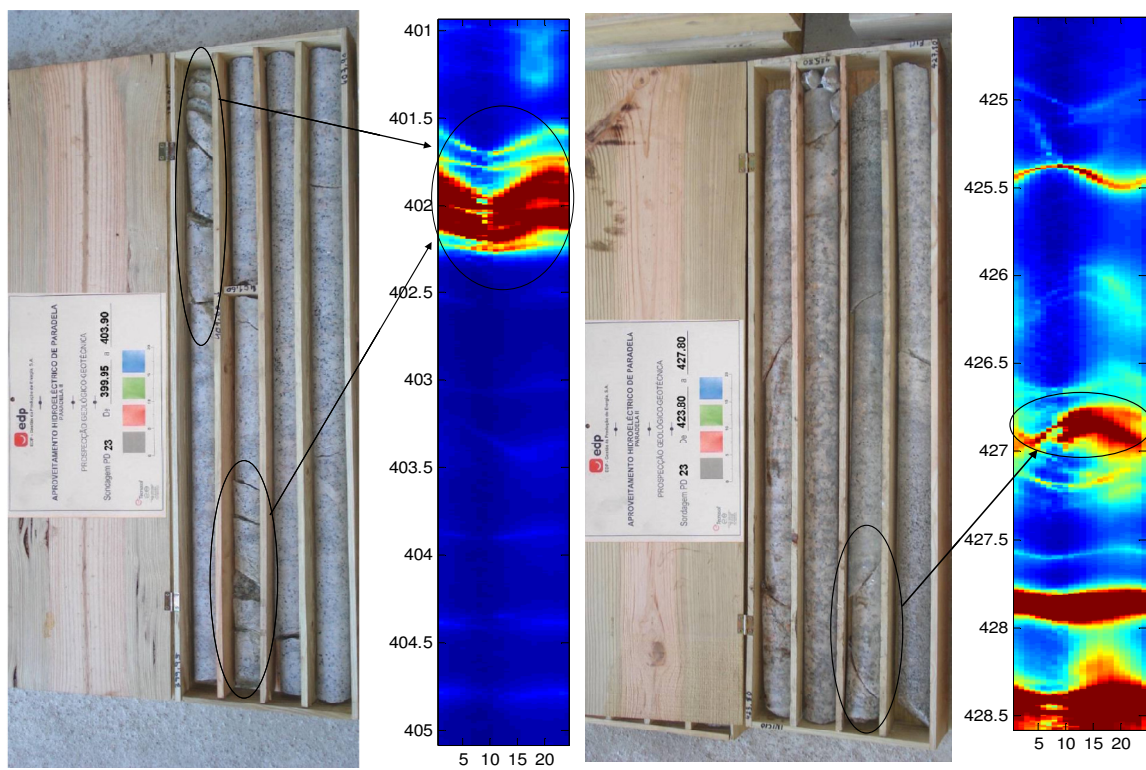


Figure 2.20: Comparison between the cores and the electrical images of the sets of fractures identified in borehole PD23.

Table 2.1: Comparison between the depths of the sets of fractures identified in the electrical imaging data (reading R_2) and in the cores extracted from boreholes PD19 and PD23.

Borehole	Depth z (m)		Discrepancy (m)	Average discrepancy (m)
	Cores	Reading R_2		
PD19	156.7	157.2	0.5	0.5
	312.4	313.0	0.6	
	432.3	432.7	0.4	
PD23	215.5	216.6	1.1	1.0
	400.6	401.6	1.0	
	425.9	426.8	0.9	

Thus, the values presented in Table 2.1 are considered offset values for correcting the depths obtained through the electrical imaging data (reading R_2) for both boreholes. To determine the correct depths obtained from readings R_1 , R_3 , and R_4 , the rule for depth discrepancy between these readings and reading R_2 was found. The depth values obtained through this method are then corrected with respect to the cores. A maximum uncertainty for the absolute depth determinations is set to 0.5 m.

Calibration of the fractures orientation data

The fracture orientation data include the direction of the normal to the tested fracture planes with respect to the north direction and its inclination with respect to the vertical direction. Obtaining these values properly requires a calibration of the magnetometers. This calibration was performed by adjusting the components of the magnetic field measured by the magnetometers with the components of the actual magnetic field at the location of the boreholes. Due to the technical problem that occurred with the magnetometers in borehole PD23, this calibration was only performed for the electrical logs obtained in borehole PD19.

Figure 2.21 presents the plots of the two magnetometers (m_1 and m_2) that measure the components of the magnetic field on the plane perpendicular to the borehole axis. The plots were obtained before (a) and after (b) the calibration for the reading R_2 obtained in borehole PD19. The plot obtained after the calibration constitutes a circle with radius equal to the norm of the vector that results from the projection of the actual magnetic field vector on the plane perpendicular to the borehole axis.

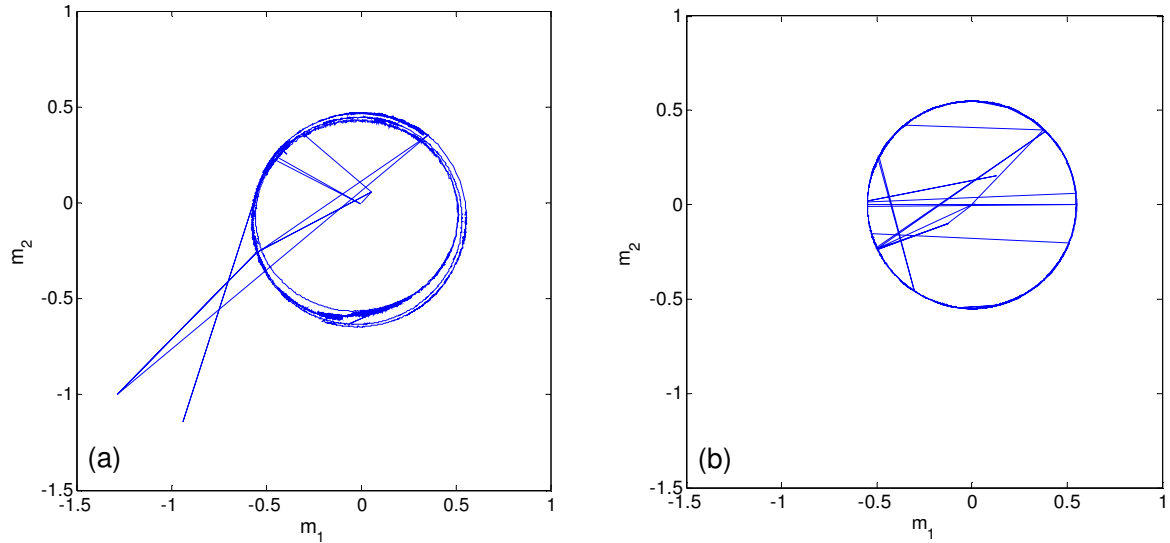


Figure 2.21: Plots of the magnetometers m_1 versus m_2 obtained: (a) before and (b) after the calibration.

Calibration of the pressures data

The calibration of the pressure in the test interval was achieved by comparing the pressures P_m measured in the interval during the electrical logs with the hydraulic pressures P_h obtained due to the weight of the water filling up both boreholes. The exact depth of the water level in the boreholes was measured because the imaging process stops when the cable head leaves the water. The hydraulic pressure P_h was calculated according to the following expression:

$$P_h = \rho g(z - z_0), \quad (2.26)$$

where ρ is the water density, g is the gravitational acceleration, z is the depth below the surface and z_0 is the depth of the water level in the boreholes.

Because the variation with depth of the pressure in the test interval depends on the logging velocity due to the water flow effect and because three different velocities were used during the logging operation, it has been found that it is more accurate to take the values of the depth when the packers and the tool are static compared with taking values as the system moves, even if it moves slowly. Hence, the depths at which clamps have been placed on the cable (for tying the coiled tubings) were used for the calibration of the pressure in the test interval. These depths were obtained by considering the reading R_3 and corrected according to the depth correspondence rule between this reading and the cores.

Figure 2.22 shows the calibration curves for the interval pressure obtained in boreholes PD19 and PD23. Within the depth range of the hydraulic tests, the maximum discrepancy between the pressures that were measured in boreholes PD19 and PD23 and the corresponding values calculated with the calibrations curves are 3 bar and 1 bar, respectively.

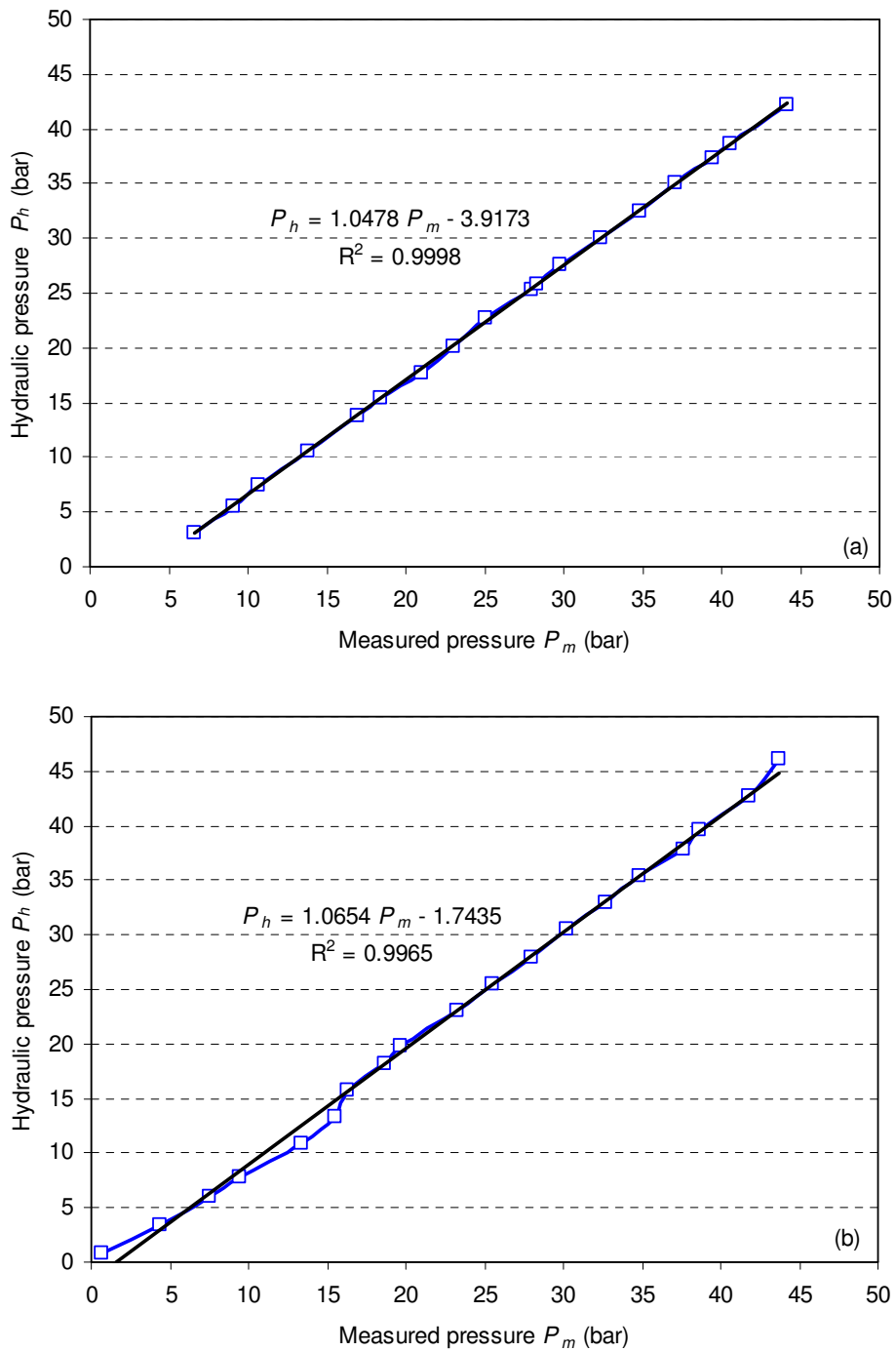


Figure 2.22: Calibration curves for the test interval pressure obtained in boreholes (a) PD19 and (b) PD23.

The calibration of the packer pressure is more difficult because there is air in the line at the beginning of the logging and it is not clear where the air is found. However, this calibration was not performed because the packer pressure values were not used in the determination of the *in situ* stresses.

Quality control for fracture orientation determinations

To evaluate the accuracy of the orientations provided by the tool, the azimuth φ and the deviation β of the borehole axis given by the tool were compared with those provided by the drilling company, which were treated as reference values.

In borehole PD19, the values of the azimuth and the deviation in the borehole axis were calculated by considering the readings R_1 , R_2 , and R_3 . The comparison with the reference values was made within the depth range of 375 m to 475 m because the deviation in the borehole axis is too small in the range of 0 m (the ground surface) to 375 m. For the borehole PD23 axis, the comparison was made by considering the azimuth and the deviation values obtained with the HRAT log as the tool ascends.

Tables 2.2 and 2.3 show the results for boreholes PD19 and PD23, respectively. For a given depth, the azimuth and deviation values that are shown are an average of the values obtained within a depth range of 1 m.

Table 2.2: Azimuth and inclination of the axis of borehole PD19.

Depth z (m)	Azimuth φ ($^\circ$)				Deviation β ($^\circ$)			
	Reference	Reading			Reference	Reading		
		R_1	R_2	R_3		R_1	R_2	R_3
375	26.1	-0.5	29.7	15.6	2.3	2.5	3.5	2.0
400	24.7	23.2	26.6	17.0	2.7	2.9	3.8	2.1
425	23.5	6.4	25.4	13.1	2.6	2.3	3.9	2.3
450	19.5	23.7	20.8	17.6	3.0	3.7	4.3	2.5
475	20.1	9.3	24.2	24.4	3.1	2.8	3.6	3.6

Table 2.3: Azimuth and inclination of the axis of borehole PD23.

Depth z (m)	Azimuth φ ($^\circ$)		Deviation β ($^\circ$)	
	Reference	HRAT log	Reference	HRAT log
375	5.8	8.0	2.7	3.0
400	7.2	9.0	3.0	3.4
425	7.4	9.0	1.4	3.0
450	7.0	6.0	3.7	3.6
475	4.8	12.0	3.6	4.0

The analysis of the results showed that the mean absolute differences between the azimuth of borehole PD19 given by the HTPF tool during readings R_2 and R_3 and those obtained by the drilling company are 2.6° and 6.9° , respectively. For reading R_1 , this discrepancy is higher (12.0°).

This analysis concludes that the fracture orientations obtained during the first upward movement at a constant velocity (reading R_2) are more reliable; hence, these orientations were treated as pre-fracture readings. As the tool descends for the first time (reading R_1), the tip of the tool may hit some asperities of the borehole walls. This might cause the tool axis to not be parallel to the borehole axis, which is a prerequisite for the reliable determination of the fracture orientations. During the second downward movement (reading R_3), the presence of the coiled tubing restricts the movement of the tool in the borehole, which influences the determination of the fracture orientations. Relative to the deviation in the borehole PD19 axis, the average absolute differences obtained during readings R_1 , R_2 , and R_3 are 0.3° , 1.0° , and 0.4° , respectively, which are acceptable.

For the borehole PD23 axis, the comparison between the values obtained by the drilling company and those obtained with the HRAT log showed that the average discrepancies are 2.8° and 0.6° for the azimuth and the deviation in the borehole axis, respectively, which are acceptable.

2.4.1.2. Description of the pressure and fracture orientations data

A description of the pressure and fracture orientations data obtained in boreholes PD19 and PD23 is presented in Tables 2.4 and 2.5, respectively.

Table 2.4: Description of the pressure and fracture orientation data in borehole PD19.

Test	Type	Description
1	HF	The breakdown pressure was clearly reached. Three cycles that gave reproducible values for the shut-in pressure were performed. The electrical images showed that a new sub-vertical fracture, which extends beyond the upper and lower limits of the test interval, was created.
2	HF	The breakdown pressure was clearly reached. Four cycles were conducted, but only the last three cycles gave reproducible values for the shut-in pressure. The electrical images showed that a new vertical fracture, which extends beyond the lower limit of the test interval, was created. An ambiguous structure was identified in the electrical images obtained before and after the test.
3	HF HTPF	The breakdown pressure was clearly reached. Three cycles that gave reproducible values for the shut-in pressure were performed. An existing fracture was identified in the electrical images obtained before and after the test, but a new fracture, which extends beyond the upper limit of the test interval, was created. The comparison between the electrical images obtained before and after the test does not enable to conclude whether the pre-existing fracture was actually activated.
4	HF HTPF	A slight breakdown pressure was reached. Three cycles were performed, and these gave reproducible values for the shut-in pressure. Several parallel fractures were identified in the test interval, and a new vertical fracture, which extended beyond the upper and lower limits of the test interval, was created. The comparison between the electrical images obtained before and after the test does not enable to conclude whether the pre-existing fracture was actually activated.
5	HTPF	The breakdown pressure was not reached. Four cycles were performed, but only the last three gave reproducible values for the shut-in pressure. The electrical images obtained before and after the test identified one inclined fracture in the test interval.
6	HF	The breakdown pressure was clearly reached. Three cycles that gave reproducible values for the shut-in pressure were conducted. The electrical images showed that a new vertical fracture, which extends beyond the upper and lower limits of the test interval, was created.
7	HTPF	The breakdown pressure was not reached. Three cycles that gave reproducible values for the shut-in pressure were performed. The electrical images obtained in the test interval before and after the test identified four fractures.

Table 2.4: Description of the pressure and fracture orientation data in borehole PD19 (continuation).

Test	Type	Description
8	HTPF	The breakdown pressure was not reached. Three cycles that gave reproducible values for the shut-in pressure were performed. The electrical images obtained before the test identified one pre-existing fracture in the test interval. However, the electrical images obtained after the test showed two practically parallel fractures. The mean value for their orientation was considered.
9	HF	The breakdown pressure was clearly reached. Three cycles were performed, and these gave reproducible values for the shut-in pressure. The electrical images obtained after the test showed that inclined fractures with respect to the borehole axis were created and extend beyond the lower limit of the test interval. The mean value for their orientation was considered.
10	HTPF	The breakdown pressure was not reached. Three cycles, which gave reproducible values for the shut-in pressure, were performed. The electrical images obtained before and after the test revealed one inclined fracture.
11	HF	The breakdown pressure was clearly reached. Three cycles were performed, and these gave reproducible values for the shut-in pressure. The electrical images obtained after the test show that a new vertical fracture, which extends beyond the upper and lower limits of the test interval, was created.
12	HF	The breakdown pressure was clearly reached. Several cycles were performed, but only the last three cycles gave reproducible values for the shut-in pressure. The electrical images obtained after the test showed that a new vertical fracture that extends beyond the lower limit of the test interval was created.

Table 2.5: Description of the hydraulic tests conducted in borehole PD23.

Test	Type	Description
1	HF	The breakdown pressure was clearly reached. Five cycles were performed, and these gave reproducible values for the shut-in pressure. A new vertical fracture that is not visible in the HRAT log was created. The electrical images obtained before and after the test do not clearly show whether the structures below the test interval are activated by the lower packer. A very high normal stress was measured, most likely due to the activation of these structures by the lower packer.
2	HF HTPF	The breakdown pressure was not reached. Of the three cycles that were performed, only the last two cycles gave reproducible values for the shut-in pressure. The electrical images obtained before and after the test revealed one inclined fracture in the test interval. The electrical images obtained after the test show that a new vertical fracture that extends beyond the lower limit of the test interval was created. These two fractures were also identified in the HRAT log.
3	HTPF	The breakdown pressure was reached. Three cycles were performed, and these gave reproducible values for the shut-in pressure. The electrical images obtained before and after the test enabled the identification of three pre-existing fractures in the test interval, two of which are parallel. The comparison between the electrical images obtained before and after the test does not enable to conclude which pre-existing fractures(s) is (are) activated. These fractures were also identified in the HRAT log.
4	HTPF	The breakdown pressure was not reached. Three cycles were performed, and these gave reproducible values for the shut-in pressure. The electrical images obtained before and after the test showed seven fractures in the test interval. The comparison between the electrical images obtained before and after the test does not enable to conclude which pre-existing fractures(s) is (are) activated. Three different sub-horizontal fractures were identified in the HRAT log. A sub-vertical fracture was found at the location of the upper packer only in the HRAT log. The mean value for the orientation of the parallel fractures was considered.
5	HTPF	The breakdown pressure was not reached. Three cycles were performed, and these gave reproducible values for the shut-in pressure. The electrical images obtained before and after the test revealed one inclined fracture in the test interval. This fracture was also identified in the HRAT log. A sub-vertical fracture was identified only in the HRAT log.

Table 2.5: Description of the hydraulic tests conducted in borehole PD23 (continuation).

Test	Type	Description
6	HF	The breakdown pressure was clearly reached. Three cycles, which gave reproducible values for the shut-in pressure, were performed. The electrical images obtained after the test show that a new vertical fracture, which extends beyond the upper and lower limits of the test interval, was created. This fracture was clearly visible in the HRAT log. A sub-horizontal fracture was identified only in the HRAT log.
7	HF	The breakdown pressure was clearly reached. Four cycles were performed, but only the last three cycles gave reproducible values for the shut-in pressure. The electrical images obtained after the test show that fractures inclined with respect to the borehole axis were created and that they extended beyond the upper limit of the test interval. The mean value for their orientation was considered. These fractures were clearly visible in the HRAT log.

2.4.1.3. Normal stress component determination

The stress normal to a tested fracture plane is directly related to the shut-in pressure that is measured during each test cycle. Using the curves of the interval pressure as a function of time, the methods developed by Aamodt and Kuriyagawa (Aamodt and Kuriyagawa, 1983) and Hayashi and Haimson (Hayashi and Haimson, 1991) were applied for each test cycle to determine the upper and lower bounds of the shut-in pressures. In this determination, only those cycles that gave reproducible values for the shut-in pressure were considered.

In Aamodt and Kuriyagawa's method, the final part of the pressure decay in the shut-in phase, fits a negative exponential equation:

$$P = e^{-at+b} + P_a, \quad (2.27)$$

where a and b are empirical constants, P is the pressure in the test interval, and P_a is designated the pore fluid pressure near the borehole. In practice, $f(t) = \ln(P - P_a)$ is plotted for various values of P_a . A Taylor expansion of equation (2.27) demonstrates that $P < P_a$ yields a graph similar to Figure 2.23a. This serves as a criterion for the determination of the reference pressure P_a . A linear regression is then computed from the final section of the hydraulic curve. Its departure from the experimental curve provides the smallest acceptable value for the shut-in pressure P_m^A . The maximum estimate of the shut-in pressure P_M^A is obtained through an extrapolation to the beginning of the shut-in process.

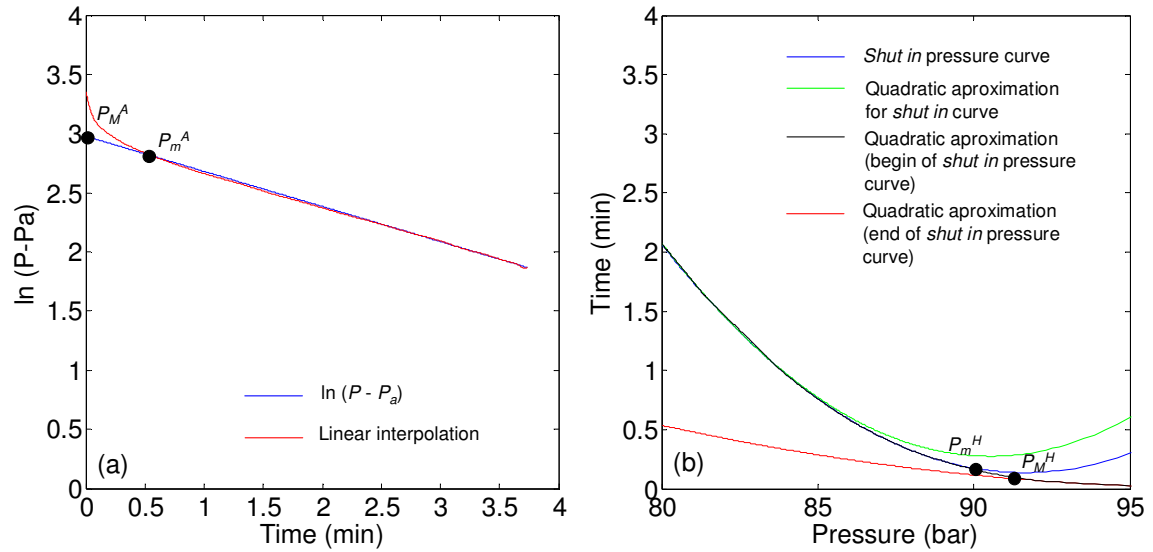


Figure 2.23: Determination of the shut-in pressure using the (a) Aamodt and Kuriyagawa's method and (b) Hayashi and Haimson's method.

In Hayashi and Haimson's method, the start and the end of the curves in the shut-in phase can be fitted with quadratic approximations (Figure 2.23b). The departures from these quadratic approximations yield the values of the borehole pressure P_M^H at the end of crack growth and P_m^H , which is the borehole pressure at the completion of crack closure. Thus, P_M^H and P_m^H are the upper and lower bounds for the shut-in pressure.

For each test sequence (at least three shut-in readings), the maximum and minimum values that result from the envelope of the intervals given by the Aamodt and Kuriyagawa's and the Hayashi and Haimson's methods were used to describe the 99% confidence limit interval for the normal stress, which is characterised by six standard deviations if one assumes that the errors obey a normal distribution.

The results are presented in Tables 2.6 and 2.7. In these tables, P_b is the breakdown pressure, P_m^A and P_M^A are the minimum and maximum values, respectively, for the shut-in pressure obtained with the Aamodt and Kuriyagawa's method, P_m^H and P_M^H are the minimum and maximum values, respectively, for the shut-in pressure obtained with the Hayashi and Haimson's method, and σ_n and $\delta\sigma_n$ are the normal stress measurement and its standard deviation, respectively, for the corresponding test depth.

Table 2.6: Normal stress results obtained from borehole PD19.

Test	Type	Cycle number	P_b (MPa)	Aamodt and Kuriyagawa's method		Hayashi and Haimson's method		σ_n (MPa)	$\delta\sigma_n$ (MPa)
				P_m^A (MPa)	P_M^A (MPa)	P_m^H (MPa)	P_M^H (MPa)		
1	HF	1	18.9	9.41	10.06	11.02	11.55	10.3	0.4
		2		9.26	9.47	10.76	11.18		
		3		9.77	9.87	11.41	11.59		
2	HF	1	13.7	8.74	8.99	9.05	9.46	9.0	0.2
		2		8.57	8.91	8.77	9.20		
		3		8.69	8.91	9.13	9.17		
3	HF	1	13.9	7.83	8.27	8.18	8.26	7.8	0.2
	HTPF	2		7.40	7.71	7.92	8.06		
		3		7.37	7.62	7.66	7.79		
4	HF	1	10.2	8.42	8.60	8.72	8.78	9.0	0.2
	HTPF	2		9.14	9.24	8.92	9.00		
		3		9.38	9.53	9.21	9.50		
5	HTPF	1	-	8.43	8.52	9.01	9.27	8.9	0.2
		2		8.97	9.11	9.14	9.14		
		3		8.97	9.14	9.17	9.37		
6	HF	1	13.0	6.83	6.86	7.09	7.47	7.1	0.1
		2		6.74	6.92	6.75	6.85		
		3		6.73	6.90	7.04	7.06		
7	HTPF	1	-	7.18	7.88	8.16	8.26	7.3	0.3
		2		6.39	7.20	7.58	8.20		
		3		6.41	7.14	7.66	7.86		
8	HTPF	1	-	5.10	5.68	5.83	6.06	5.6	0.2
		2		5.22	5.53	5.68	5.77		
		3		5.37	5.60	5.63	5.67		
9	HF	1	13.6	5.92	6.31	6.34	6.45	6.7	0.1
		2		5.99	6.21	6.35	6.46		
		3		6.07	6.20	6.26	6.28		
10	HTPF	1	-	7.34	8.09	7.81	8.18	7.5	0.3
		2		7.09	7.71	7.44	7.52		
		3		6.47	7.41	8.05	8.44		
11	HF	1	13.1	5.49	5.58	5.81	5.88	5.8	0.1
		2		5.66	5.74	5.85	5.88		
		3		5.79	5.87	5.86	6.00		
12	HF	1	7.2	1.59	1.61	2.41	3.16	2.6	0.3
		2		2.02	2.90	2.86	3.47		
		3		1.93	2.49	2.86	3.57		

Table 2.7: Normal stress results obtained from borehole PD23.

Test	Type	Cycle number	P_b (MPa)	Aamodt and Kuriyagawa's method		Hayashi and Haimson's method		σ_n (MPa)	$\delta\sigma_n$ (MPa)
				P_m^A (MPa)	P_M^A (MPa)	P_m^H (MPa)	P_M^H (MPa)		
1	HF	1	26.0	19.44	20.37	21.02	21.05	20.2	0.5
		2		19.16	20.08	20.89	21.23		
		3		20.57	21.69	20.55	20.62		
		4		20.39	21.41	20.03	20.30		
		5		18.64	19.98	20.21	21.00		
2	HF	1	-	9.33	9.57	10.09	10.38	9.9	0.2
	HTPF	2		9.75	9.94	10.25	10.47		
3	HTPF	1	12.4	8.21	8.99	9.07	9.39	8.9	0.2
		2		8.71	9.27	9.62	9.65		
		3		8.93	9.44	9.43	9.65		
4	HTPF	1	-	9.01	9.68	9.07	9.34	9.7	0.2
		2		9.61	10.03	9.93	10.06		
		3		9.71	10.10	10.17	10.36		
5	HTPF	1	-	6.81	7.35	7.29	7.71	7.0	0.2
		2		6.68	7.38	7.34	7.49		
		3		6.32	7.02	7.18	7.53		
6	HF	1	14.4	5.57	6.02	6.03	6.23	5.9	0.1
		2		5.57	5.84	5.75	5.84		
		3		5.46	5.75	5.71	5.84		
7	HF	1	10.4	2.63	3.01	3.44	3.67	3.2	0.2
		2		2.72	2.97	2.93	3.17		
		3		2.71	2.79	2.93	3.10		

2.4.1.4. Fracture orientations determination

The geometry and orientation of the tested fracture planes are determined through a comparison between the orientated electrical images obtained before and after the hydraulic tests. Two sinusoidal curves that completely cover the extent of the identified fracture plane in the electrical imaging logs were drawn to identify extreme values for the azimuth of the normal to the tested fracture planes and its inclination with respect to the vertical direction. From the scatter described by the two sinusoidal curves, a 99% confidence limit interval is defined for the two angles, which corresponds to six standard deviations, if one assumes that the errors obey a normal distribution.

In borehole PD23, a comparison between the electrical imaging and HRAT logs provided the proper orientation of all the hydraulically tested fractures for this borehole. In this way, the main fractures located as near as possible of the tested fracture planes were identified in both logs. By assuming the main fractures orientation given by the HRAT log as correct, a correspondence law was made for the discrepancy between the readings provided by the two logs. In some tests, the tested fracture planes were also visible in the HRAT log which enabled to estimate the orientations directly from this log. In these cases, the fractures plane orientations obtained in this way are practically equal with respect to those obtained from the re-orientation of the electrical imaging logs.

Figure 2.24 shows a comparison of electrical imaging logs along with the location of the test interval obtained before and after a hydraulic fracturing test (a) and the adjustment of the fracture plane located in the test interval with a sinusoidal curve (b). This figure also shows a comparison between the electrical imaging and HRAT logs (c), in which the main fractures located near the tested fractures are identified in both logs.

Appendix A presents the fracture orientations determination for each hydraulic test. For borehole PD19, the electrical images are orientated with respect to the magnetic North. For borehole PD23, the electrical images are orientated with respect to the electrode 1.

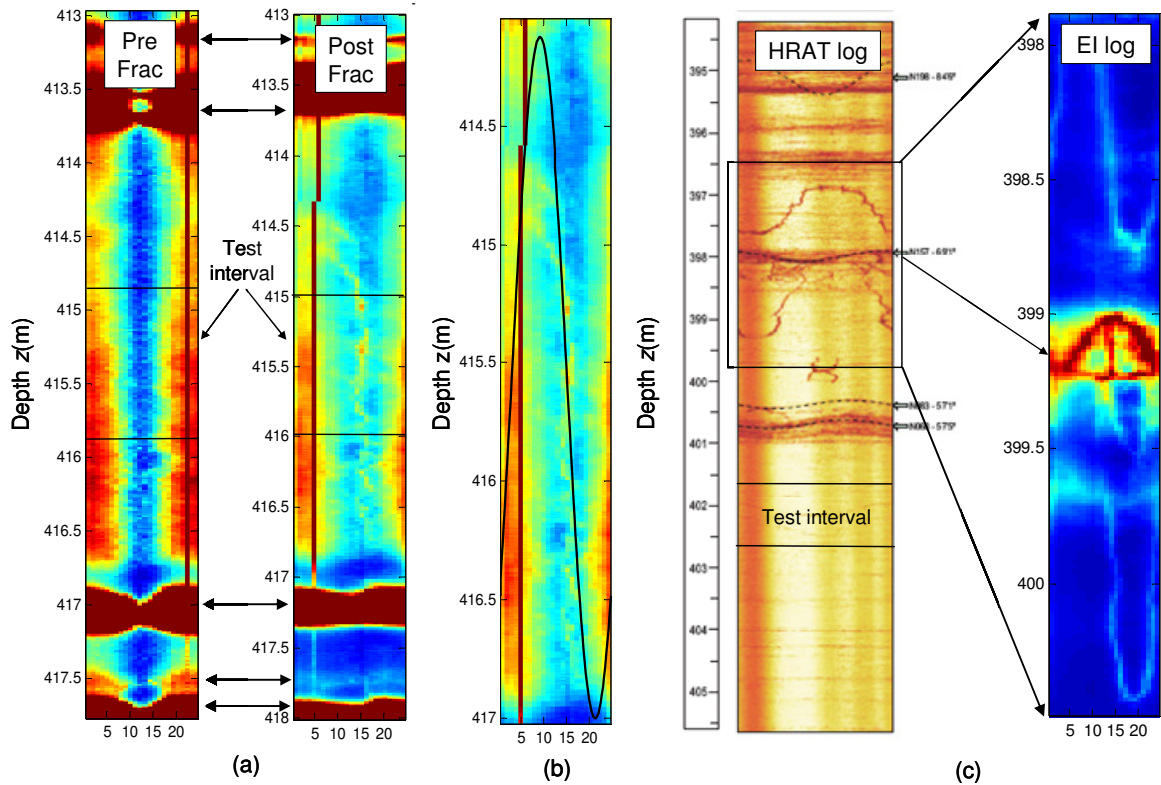


Figure 2.24: (a) Comparison between electrical imaging (EI) logs obtained before (Pre Frac) and after (Post Frac) a hydraulic fracturing test, (b) adjustment of the fracture plane with a sinusoidal curve and (c) identification of the main fracture planes in the electrical imaging (EI) and HRAT logs.

2.4.1.5. Summary of the pressure and fracture orientations data

Tables 2.8 and 2.9 present a summary of the hydraulic test results. In these tables, z is the depth of the tests, ϕ is the azimuth of the normal to the fracture plane with respect to the North (positive eastward), θ is the inclination angle of the normal to the fracture plane with respect to the vertical direction, and σ_n is the normal stress measurement for the corresponding depth interval. The standard deviations associated with z , ϕ , θ and σ_n are δz , $\delta\phi$, $\delta\theta$ and $\delta\sigma_n$, respectively. In Table 2.9, the orientations marked with * were only obtained with the HRAT log. The tables show that eight tests are ambiguous because two or more fracture planes were observed in the test interval.

Table 2.8: Summary of the hydraulic test results obtained from borehole PD19.

Test	Depth		Azimuth		Dip		Normal stress	
	z (m)	δz (m)	ϕ ($^{\circ}$)	$\delta\phi$ ($^{\circ}$)	θ ($^{\circ}$)	$\delta\theta$ ($^{\circ}$)	σ_n (MPa)	$\delta\sigma_n$ (MPa)
1	471.8	0.5	108	4	87	2	10.3	0.4
2	455.5	0.5	18	7	90	2	9.0	0.2
3	450.1	0.5	126	5	90	2	7.8	0.2
	450.4	0.5	281	6	60	1		
4	442.1	0.5	133	5	90	2	9.0	0.2
	442.2	0.5	303	5	42	2		
5	436.3	0.5	108	6	32	2	8.9	0.2
6	414.9	0.5	133	4	90	2	7.1	0.1
7	393.4	0.5	270	4	66	2	7.3	0.3
	393.9	0.5	284	3	79	2		
	394.1	0.5	277	5	52	2		
	394.3	0.5	50	5	38	2		
8	379.3	0.5	88	3	57	2	5.6	0.2
9	335.6	0.5	119	3	61	2	6.7	0.1
10	293.1	0.5	14	2	44	3	7.5	0.3
11	279.8	0.5	22	4	90	2	5.8	0.1
12	164.6	0.5	320	7	86	2	2.6	0.3

Table 2.9: Summary of the hydraulic test results obtained from borehole PD23.

Test	Depth		Azimuth		Dip		Normal stress	
	z (m)	δz (m)	ϕ ($^{\circ}$)	$\delta\phi$ ($^{\circ}$)	θ ($^{\circ}$)	$\delta\theta$ ($^{\circ}$)	σ_n (MPa)	$\delta\sigma_n$ (MPa)
1	490.7	0.5	199	5	90	2	20.2	0.5
2	421.8	0.5	19	5	90	2	9.9	0.2
	420.9		33	5	42	2		
3	402.4	0.5	348	5	68	2	8.9	0.2
	402.5		252	5	34	3		
4	377.4*	0.5	215*	5*	81*	3*	9.7	0.2
	377.8*		106*	5*	12*	3*		
	377.8*		46*	5*	20*	3*		
	378.4		2	5	35	2		
	377.9		137	5	22	2		
	377.9		59	5	24	2		
5	364.7*	0.5	325*	5*	81*	3*	7.0	0.2
	364.6		252	5	35	2		
6	356.8	0.5	269	4	90	2	5.9	0.1
	357.0*		33*	5*	6*	3*		
7	176.6	0.5	243	3	77	2	3.2	0.2

* orientation obtained from the re-orientation of the electrical logs by using the HRAT log

2.4.1.6. Determination of the stress field

The inversion of the hydraulic data was conducted to determine the complete stress field along the axes of the boreholes that fits with the normal stress measurements associated with the tested fracture planes. Before determining the stress field, a preliminary analysis of the results shown in Tables 2.8 and 2.9 is performed.

Figure 2.25 shows the variation of the normal stress magnitudes obtained from HF and HTPF as a function of depth. Figure 2.26 shows the variation of the azimuth of the normal to the fracture planes obtained from the HF tests only as a function of depth. In these tests, the fracture planes are parallel to the axes of the boreholes. Two different groups are noted. The black line represents the azimuth of the fractures observed when the measured normal stress is close to the expected minimum stress magnitude at the correlative depth. The green line represents a perpendicular set of azimuths.

The analysis shown in Figure 2.25 indicates that most of the values are included in a domain delimited by two straight lines the slope of which are respectively 0.0165 MPa/m and 0.0255 MPa/m, which are the gradients of the minimum and the maximum principal stress magnitudes, respectively.

Two tests yielded results that were different from the regional trend: test number 1 in borehole PD23 and test number 8 in borehole PD19. These results were not included in the stress inversion procedure.

For test number 1 in borehole PD23, the normal stress magnitude is significantly larger than all the other values by more than 10 MPa. However, the measurement is reproducible and satisfies all the prerequisite conditions of validity. It is important to determine whether the measurement is meaningful or whether it results from a specific local condition, in which case the test has no relevance to the stress determination. A detailed examination of both the electrical and the HRAT images shows a clear inclined fracture below the lower packer. In comparison to other post-fracture images, no other fracture is observed within the tested interval. This result strongly suggests that flow occurred within the inclined fracture below the packer. In such conditions, the pressure applied by the packer is also applied on some parts of the inclined fracture such that its opening remains very limited in azimuth. The stress analysis for such fractures has been discussed by Cornet *et al.* (2003), who showed that the shut-in pressures in such configurations do not yield the far-field normal stress value. Therefore, it is concluded that because of the specific geometric conditions, this test does not yield any information on the normal stress supported by the plane.

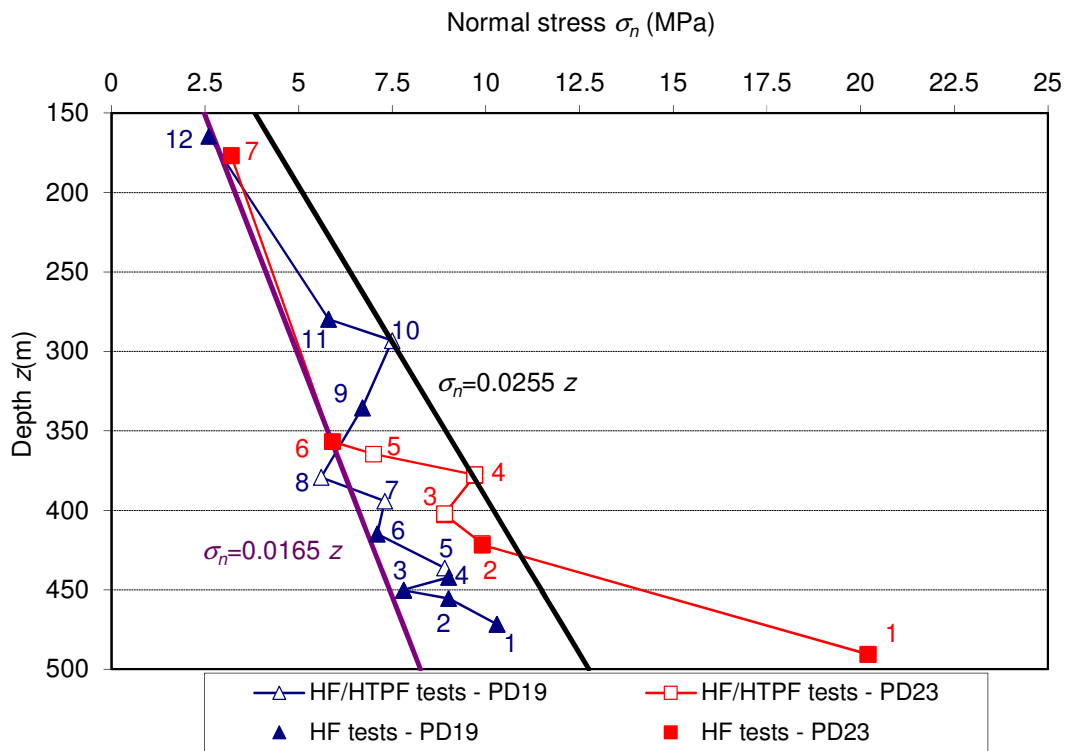


Figure 2.25: Variation of the normal stress σ_n magnitudes as a function of depth.

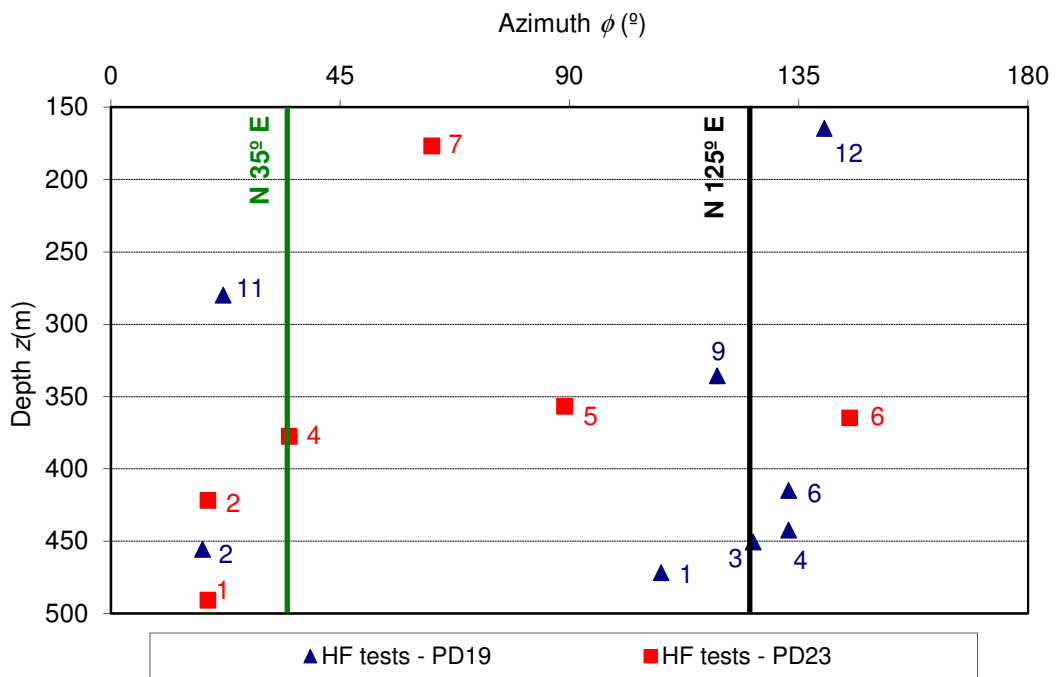


Figure 2.26: Variation of the azimuth ϕ of the normal to the fracture planes obtained in hydraulic fracturing tests as a function of depth.

For test number 8 conducted in borehole PD19, the measured normal stress is more than three standard deviations smaller than the expected trend. This test satisfies all prerequisite conditions. The pre-existing fracture is clearly identified. The pressure tests are fully satisfactory. It is considered a valid test for a stress evaluation. However, approximately 20 m above the test location, a strongly altered zone was observed in the electrical imaging log. This zone dips steeply and is therefore not very far from the tested fracture. It seems reasonable to assume that it is the cause for the local low stress value. This test result shows the limits of large scale stress evaluation campaigns. Rocks always exhibit some heterogeneity, and therefore, stress components may vary from those predicted by an ideal homogeneous model. This is further discussed in the next chapter.

Additionally, test number 7 in borehole PD19 and test number 4 in borehole PD23 resulted in four and seven different fractures observed within the tested interval, respectively. These results were not included in the database, and only a total of 15 tests were considered for the determination of the stress field.

The analysis shown in Figures 2.25 and 2.26 reveals that the normal stress magnitudes measured for sub-vertical fractures that are nearly perpendicular to each other are very similar. This result suggests that differences between the maximum and minimum principal horizontal stress magnitudes are likely to be fairly small. Another possibility is that some strong stress heterogeneity exists in the rock mass due to the effects of local faults and fractures. This local heterogeneity is suggested by the inclined fractures with respect to the borehole axis in the hydraulic fracturing tests (Figure 2.27). This type of fracture was observed in two of the tests: test number 9 in borehole PD19 and test number 7 in borehole PD23.

In the inversion of the hydraulic data, the following assumptions are considered: (i) the linear stress variation holds over the complete domain of investigation, as suggested by Figure 2.25; (ii) the vertical direction is a principal direction in most of the domain that was tested, which is justified because most fractures in hydraulic fracturing tests are sub-vertical; and (iii) the horizontal gradient of the stresses between the two boreholes (PD19 and PD23) is negligible, which is justified by their close proximity.

Based on these hypothesis, the 8-parameter model described before was applied. Due to the influence of topography effects on the *in situ* stress distribution, a linear stress variation with depth may not be reasonable in regions close to ground level. Because these effects are not as significant in the depth range between 280 m and 490 m below the surface, where the majority of measurements were performed, the hydraulic data was inverted by equation (2.3) and considering z equal to z_0 , which corresponds to the centre of the measurements, located 385 m below the surface.

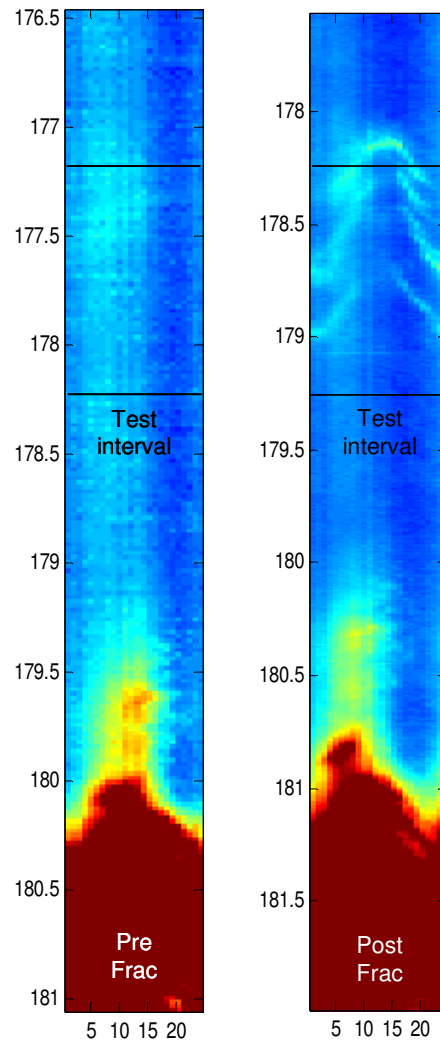


Figure 2.27: Inclined fractures shown in electrical images obtained before (Pre Frac) and after (Post Frac) a hydraulic fracturing test.

In the Tarantola and Valette's algorithm, the *a priori* values for the principal stresses S_1 , S_2 and S_3 were set to 10 MPa with associated large *a priori* standard deviations (10 MPa). The direction λ of the maximum horizontal principal stress was set to N43°E (the direction of the maximum horizontal principal stress at approximately 450 m) with no rotation η with depth. A small *a priori* standard deviation (5°) was set for these two angles.

The vertical gradient of the minimum horizontal principal stress (α_2) was chosen as 0.0165 MPa/m, as suggested by Figure 2.25. Based on this figure, the vertical gradients of the maximum horizontal principal stress (α_1) and vertical stress (α_3) were set to 0.0255 MPa. The *a priori* standard deviation values associated with the gradients of the principal stresses were set to 0.02 MPa/m.

In general, the modelling proceeds as follows. First, an inversion of the results from the nine tests for which only one fracture plane had been observed is run. Next, the inversion is undertaken by considering the complete set of fifteen tests, which includes the tests with two possible fracture planes. All 64 possible combinations of fracture planes are considered. For each fracture plane combination, the stress field solution is calculated according to the least squares procedure (Tarantola and Valette, 1982). The misfit for the i^{th} test ($i = 1, \dots, 15$) is defined as the absolute value of the difference between the measured normal stresses ($\sigma_{n,mes}$) and calculated normal stresses ($\sigma_{n,calc}$) associated with the stress field solution. The quality of the solution is characterised by the sum of the fifteen misfits. The set of fracture planes that yields the smallest value of the misfit is identified. The solution associated with it is defined as the solution of the inversion of the set of fifteen tests. Table 2.10 shows the *a priori* values (p_0) and the *a posteriori* values (p) of the far-field stress parameters that were obtained by applying this procedure to hydraulic data.

Table 2.10: *A priori* values (p_0) and *a posteriori* values (p) for the far-field stress parameters.

Parameter	<i>A priori</i> values p_0	<i>A posteriori</i> values p	
		9 tests	15 tests
S_1 (MPa)	10.0	9.9	8.8
S_2 (MPa)	10.0	6.3	6.2
S_3 (MPa)	10.0	8.7	9.4
λ ($^\circ$)	43	60	4
α_1 (MPa/m)	0.0255	0.0319	0.0276
α_2 (MPa/m)	0.0165	0.0156	0.0152
α_3 (MPa/m)	0.0255	0.0242	0.0244
η ($^\circ$)	0	3	-3

This model yields the stress field at 475 m below the surface, as shown in Table 2.11. In this table, $\delta\sigma_H$, $\delta\sigma_h$, $\delta\sigma_v$ and $\delta\omega_H$ are the *a posteriori* standard deviations on the maximum horizontal (σ_H), minimum horizontal (σ_h) and vertical (σ_v) stresses, and the orientation (ω_H) of the maximum horizontal stress, respectively.

Table 2.11 shows that the magnitudes of the vertical and horizontal stresses are well constrained. In fact, the *a posteriori* standard deviations associated with these stress components are less than 10% of the expected values.

Table 2.11: Results of the stress field at 475 m below the surface.

Number of tests	σ_H (MPa)	$\delta\sigma_H$ (MPa)	σ_h (MPa)	$\delta\sigma_h$ (MPa)	σ_v (MPa)	$\delta\sigma_v$ (MPa)	ω_H (°)	$\delta\omega_H$ (°)
9	12.8	1.0	7.7	0.3	10.9	0.4	62	4
15	11.3	0.3	7.6	0.2	11.6	0.3	2	2

The *a posteriori* value for the gradient of the vertical stress is less than the density of the rock mass (2650 kg/m³). This result is consistent with the fact that in mountainous areas, the principal stress directions are not vertical for locations close to the ground surface.

Using the stress field solutions shown in Table 2.10, the *a posteriori* values for normal stresses on the fracture planes were calculated. The comparison between the *a priori* and *a posteriori* values for the azimuths (ϕ and ϕ_c , respectively), inclinations (θ and θ_c , respectively) and normal stresses (σ_n and σ_{nc} , respectively) for the nine and fifteen tests stress field solution is shown in Tables 2.12 and 2.13, respectively. An average misfit of 0.3 MPa and a largest misfit of 1.3 MPa are observed for the solution identified with results from nine tests. These values are 0.3 MPa and 2.1 MPa for the set of fifteen tests. The sum of the misfits is 2.4 and 5.1 MPa for the sets of nine and fifteen tests, respectively. For both cases, only one test has *a posteriori* value for the normal stress that differs from the *a priori* value by more than 3 standard deviations of the measurements.

A search for other solutions was conducted by relaxing the *a priori* standard deviation on the direction of the maximum horizontal principal stress at the centre of the measurements and its rotation with depth. The model has been used to calculate the range of possible solutions at a depth of 475 m by considering the set of fifteen tests. From the range of possible solutions for the maximum and minimum horizontal stresses, vertical stress and orientation of the maximum horizontal stress, the following 99% confidence intervals were obtained:

$$9.9 \text{ MPa} \leq \sigma_H \leq 12.7 \text{ MPa}$$

$$7.1 \text{ MPa} \leq \sigma_h \leq 9.7 \text{ MPa}$$

$$10.2 \text{ MPa} \leq \sigma_v \leq 12.5 \text{ MPa}$$

$$N0^\circ\text{E} \leq \omega_H \leq N70^\circ\text{E}$$

The large uncertainty in the orientation of the maximum horizontal stress results from the fact that both horizontal principal stress magnitudes are not very different from each other; therefore, their orientation is strongly influenced by local heterogeneities.

Table 2.12: Comparison between *a priori* and *a posteriori* values for the nine tests solution.

Borehole	Test	z (m)	z_c (m)	ϕ ($^\circ$)	ϕ_c ($^\circ$)	θ ($^\circ$)	θ_c ($^\circ$)	σ_n (MPa)	σ_{nc} (MPa)
PD19	1	471.8	471.8	108	106	87	87	10.3	10.1
	2	455.5	455.5	18	8	90	90	9.0	9.1
	3	-	-	-	-	-	-	-	-
	4	-	-	-	-	-	-	-	-
	5	436.3	436.2	108	118	32	33	8.9	9.5
	6	414.9	414.9	133	133	90	90	7.1	7.1
	9	335.6	335.6	119	116	61	60	6.7	6.6
	10	293.1	293.2	14	15	44	43	7.5	6.2
	11	279.8	279.8	22	20	90	90	5.8	5.8
	12	164.6	164.6	320	319	86	86	2.6	2.8
PD23	2	-	-	-	-	-	-	-	-
	3	-	-	-	-	-	-	-	-
	5	-	-	-	-	-	-	-	-
	6	-	-	-	-	-	-	-	-
	7	176.6	176.6	243	243	77	77	3.2	3.2

Table 2.13: Comparison between *a priori* and *a posteriori* values for the fifteen tests solution.

Borehole	Test	z (m)	z_c (m)	ϕ ($^\circ$)	ϕ_c ($^\circ$)	θ ($^\circ$)	θ_c ($^\circ$)	σ_n (MPa)	σ_{nc} (MPa)
PD19	1	471.8	471.9	108	118	87	87	10.3	8.2
	2	455.5	455.5	18	43	90	90	9.0	9.3
	3	450.1	450.1	126	121	90	90	7.8	8.0
	4	442.1	442.1	133	140	90	90	9.0	8.8
	5	436.3	436.2	108	104	32	35	8.9	9.5
	6	414.9	414.8	133	121	90	90	7.1	7.3
	9	335.6	335.7	119	122	61	58	6.7	6.5
	10	293.1	293.2	14	14	44	43	7.5	6.7
	11	279.8	279.8	22	23	90	90	5.8	5.8
	12	164.6	164.6	320	320	86	86	2.6	2.7
PD23	2	421.8	421.8	19	16	90	90	9.9	9.7
	3	402.5	402.5	252	252	34	34	8.9	8.9
	5	364.7	364.7	325	321	81	81	7.0	7.2
	6	356.8	356.8	269	268	90	90	5.9	5.8
	7	176.6	176.6	243	243	77	77	3.2	3.3

2.4.2. Overcoring test results

The *in situ* stresses are determined from the strains measured during the overcoring operation and from the elastic constants determined from the biaxial tests done in the overcored cores.

In the majority of biaxial tests, the obtained pressure *versus* strains curves show a linear and elastic behaviour (Figure 2.28a). In these cases, the calculation of the elastic constants is performed by considering the strains measured by the ten strain gauges associated with the average of the first unloading cycle at 6.0 MPa and the second loading cycle at the same pressure. However, in some cases, the behaviour of the rock core is non-linear and non-elastic for small pressures (in the 0 MPa to 2 MPa range, Figure 2.28b. This may indicate the closure of existing microfissures when the biaxial loading is applied. In these cases, the calculation of the elastic constants is made by neglecting the pressure *versus* strain curves obtained between 0 MPa and 2 MPa.

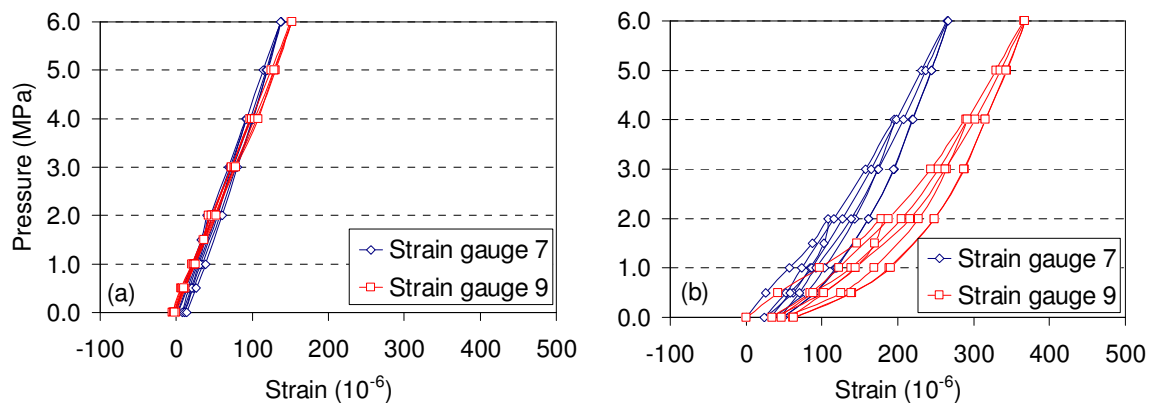


Figure 2.28: Pressure *versus* displacement curves obtained in biaxial tests performed in overcored cores. (a) linear and elastic behaviour; (b) non-linear and non-elastic behaviour.

Also, in some cases it was verified that the readings given by some strain gauges are incorrect, which may result of their malfunction or some inefficient contact between the glue and the borehole walls. For this reason, the readings provided by these strain gauges were not considered in the calculations. To determine the elastic constants of the overcored core extracted from borehole PD1 at 251.7 m depth below the ground surface, only the first loading cycle was considered. Due to the impossibility in determining the elastic constants of the overcored core extracted from borehole PD2 at 164.1 m depth below the ground surface, the elastic constants were obtained by considering the biaxial test results obtained in the core extracted at approximately the same depth, with the same

lithology, alteration and fracturing degree. The obtained elastic constants are shown in Table 2.14.

Table 2.14: Biaxial tests results.

Borehole	Test	Depth z (m)	E (GPa)	ν
PD1	1	202.8	74	0.39
	2	206.5	57	0.34
	3	221.5	73	0.26
	4	222.2	71	0.28
	5	250.9	50	0.26
	6	251.7	40	0.25
PD2	1	162.5	55	0.40
	2	164.1	55	0.40
	3	183.5	43	0.17
	4	184.1	57	0.42
	5	201.5	75	0.24
	6	202.9	61	0.46

By considering the set of six biaxial tests obtained in each borehole, the following average (E and ν) and standard deviation (δE and $\delta \nu$) values for the elastic constants were obtained:

Borehole PD1: $E = 60.8$ GPa, $\delta E = 12.9$ GPa, $\nu = 0.30$, $\delta \nu = 0.05$

Borehole PD2: $E = 57.7$ GPa, $\delta E = 9.5$ GPa, $\nu = 0.35$, $\delta \nu = 0.11$

The standard deviations of the elastic modulus are approximately 21% and 16% of the average values, whereas the standard deviations for Poisson's ratio are approximately 17% and 31% of the average values for boreholes PD1 and PD2, respectively. This analysis outlines a significant dispersion of the elastic parameters around their average values. The values of Poisson's ratio determined from biaxial testing are considerably greater than those obtained from uniaxial compression tests, which may be explained due to the development of microcracks normal to the axes of the cores and consequent tensile strains in this direction during biaxial testing.

The magnitude and orientation of the principal stresses (σ_I , σ_{II} , σ_{III}) obtained in each test are presented in Table 2.15. In this table, the orientations are described by two

angles; the first angle is the direction of the principal stress component with respect to the North, and the second angle is the inclination with respect to the horizontal plane.

Table 2.15: Principal stress (σ_I , σ_{II} , σ_{III}) magnitudes and orientations obtained from interpreting the overcoring tests.

Borehole	Test	Depth z (m)	Principal stress magnitudes (MPa)			Principal stress orientations ($^\circ$)		
			σ_I	σ_{II}	σ_{III}	σ_I	σ_{II}	σ_{III}
PD1	1	202.8	6.4	5.6	4.7	325/66	85/12	179/20
	2	206.5	7.0	3.4	3.2	249/86	147/1	56/4
	3	221.5	8.7	3.4	3.3	354/86	231/2	141/4
	4	222.2	9.3	6.9	5.9	36/64	188/23	283/11
	5	250.9	10.6	8.2	7.0	94/54	200/11	298/34
	6	251.7	11.3	6.5	6.0	26/73	150/10	242/14
	Inversion	225.9	9.7	6.0	5.9	48/78	184/8	275/8
PD2	1	162.5	11.9	6.9	5.9	94/79	260/11	350/3
	2	164.1	8.0	6.3	4.3	328/75	229/2	139/15
	3	183.5	6.2	2.8	2.0	324/79	177/10	86/6
	4	184.4	5.1	4.6	4.3	285/63	24/5	116/26
	5	201.5	-1.9	-3.6	-4.0	267/77	69/12	160/4
	6	202.9	6.0	4.2	3.4	289/39	147/45	36/20
	Inversion	190.3	4.4	3.4	3.1	301/62	193/13	94/25

All the overcoring data obtained in each borehole are considered in matrix equation 2.23 to calculate the stress tensor that fits best with all the overcoring stress measurements at the centre of each tested rock mass volume. In this global inversion of the overcoring data obtained in each borehole, the following assumptions are made: (i) the rock mass exhibits an isotropic, linear, elastic behaviour; (ii) the influence of topography on the overcoring tests results is negligible (which is reasonable given that at the depth of the tests, one of the principal stresses is practically sub-vertical); (iii) the vertical gradient of the stress tensor components is neglected (in both boreholes, measurements were conducted within a depth range smaller than 50 m); and (iv) the influence of the adit on the overcoring test results is negligible (tests considered for the inversion are located out of the range of the adit's perturbation zone).

Based on these hypotheses, a 6-parameter model is used in the inversion of the overcoring data. These parameters refer to the six components of the stress tensor at the centre of the tested rock mass volume. In borehole PD1, all the overcoring test results are

considered in the inversion. In borehole PD2, the stresses obtained at 201.5 m below the surface are questionable, considering the expected stresses at this depth due to gravity loading as well as the stress values obtained in the other tests. Furthermore, in this borehole, the stresses obtained in the two tests done close to the adit are significantly higher than the stresses obtained for other tests. These three tests results were not included in the inversion. The results of the inversion are presented in Table 2.15.

The table shows that the maximum principal stress (σ_I) is sub-vertical and that the other two principal components (σ_{II} and σ_{III}) are sub-horizontal and of similar magnitude. Due to this, the dispersion observed for the direction of sub-horizontal principal stresses is not significant. In borehole PD1, the stresses are significantly greater than in borehole PD2, which is not explained by only the discrepancy in the depth of the two tested rock mass volumes.

Although the overcoring and hydraulic tests were conducted at locations separated by approximately 1.7 km, results may be compared because no important faults are identified between these locations. Figure 2.29 shows the variation with depth of the principal stress magnitudes (σ_I , σ_{II} , σ_{III}) obtained by overcoring and hydraulic testing. In this figure, the lines represent the lower and upper bounds of a 99% confidence interval obtained from the inversion of the set of fifteen hydraulic tests, in which the far-field stress solution is presented in Table 2.10. The points represent the overcoring test results obtained in boreholes PD1 and PD2. The figure also shows the results of the inversion (INV) of the overcoring data at the centre of the rock mass volume tested in boreholes PD1 and PD2. In the hydraulic tests, the maximum principal stress (σ_I) is assumed to be vertical. In overcoring tests, this stress component is found to be sub-vertical.

The figure shows that the magnitudes of the sub-vertical stress components obtained using the overcoring method in borehole PD1 are significantly higher with respect to those obtained by hydraulic testing. In fact, the overcoring technique often leads to high stresses in the direction parallel to the borehole axis. This has been justified by large deformations that occurred in this direction as a result of the glue yield caused by the heat generated during the drilling operation (Ask, 2004). The magnitudes of the sub-horizontal stress components obtained by overcoring in borehole PD1 are slightly higher (about 1.5 MPa) than those obtained by hydraulic testing. This result may be attributed to the different role of topography on the distribution of *in situ* stresses at the location of hydraulic and overcoring tests.

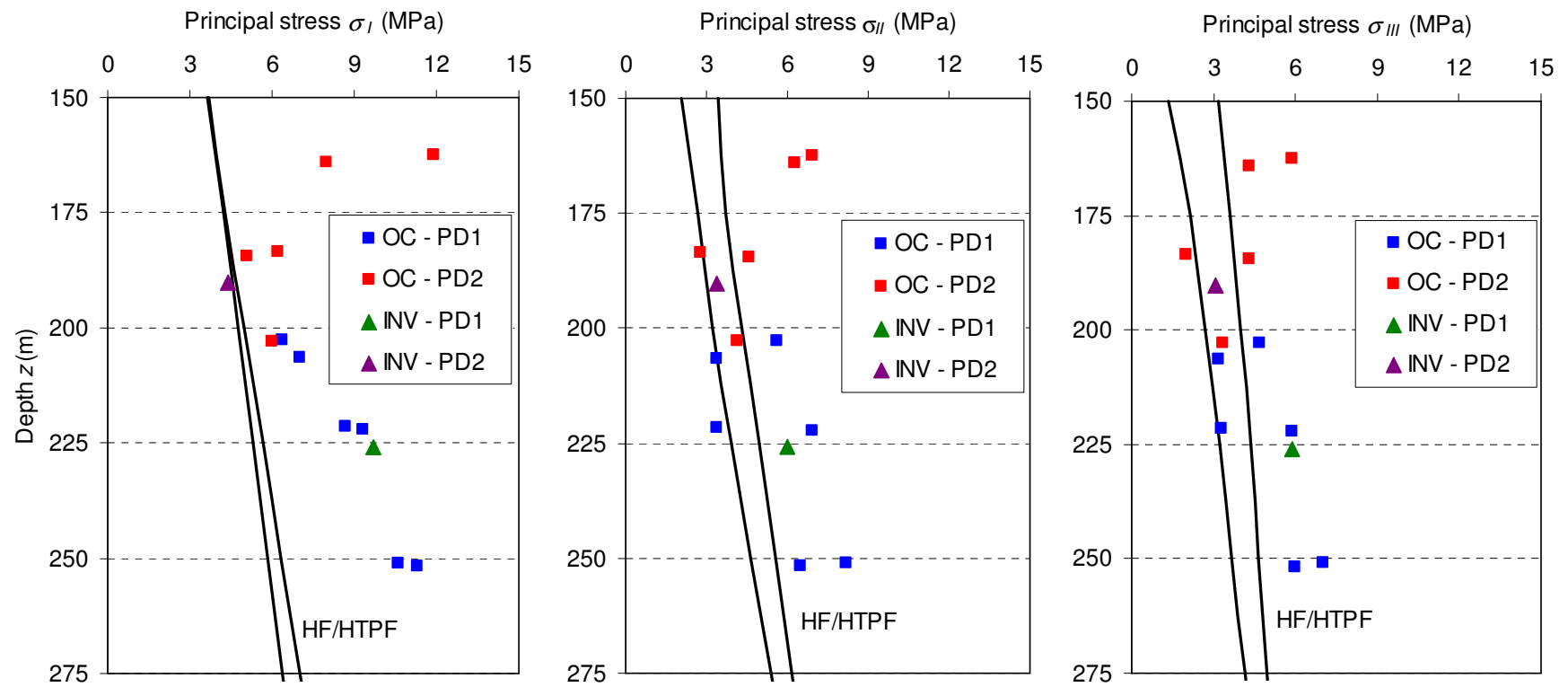


Figure 2.29: Comparison of the magnitudes of the principal stresses (σ_I , σ_{II} , σ_{III}) obtained by overcoring and hydraulic testing.

2.4.3. Small flat jack test results

The results of the small flat jack tests are presented in Table 2.16. In this table, d is the distance between the test location and the adit's entrance, ϕ is the azimuth of the normal to the slot with respect to the North, θ is the inclination of the azimuth with respect to the vertical direction, σ_n is the normal stress, and E is the elastic modulus normal to the plane of the slot.

Table 2.16: Results from the small flat jack tests.

Location	Test	d (m)	ϕ ($^{\circ}$)	θ ($^{\circ}$)	σ_n (MPa)	E (GPa)
SFJ1	1	447	0	0	8.9	30.9
	2	448	110	45	6.4	45.1
	3	437	110	90	9.4	35.9
	4	446	290	45	3.7	30.9
SFJ2	5	332	0	0	9.9	30.8
	6	333	290	45	2.6	37.9
	7	331	290	90	2.0	26.2
	8	332.5	110	45	6.4	23.6
SFJ3	9	278	0	0	9.9	32.5
	10	275	290	45	3.2	22.9
	11	279	290	90	4.1	36.8
	12	280	110	45	3.0	31.6

In tests numbers 1, 5 and 9, similar sub-vertical stress components were measured, with values of 8.9 MPa, 9.9 MPa and 9.9 MPa, respectively.

The comparison of the horizontal stress components with respect to the vertical direction, obtained at the three locations, enables to conclude that the component measured in test number 3 is significantly higher than in the other tests. The rock was observed to have viscoelastic behaviour because the slot was subjected to a significant closure due to the considerable time interval that occurred between the end of the cut by the diamond disk and the beginning of the test. This leads to a high cancellation pressure for restoring the initial position of the pins. This test result was discarded from further analyses.

By considering the set of elastic modulus values obtained in each test location, the following average and standard deviation values were obtained:

SFJ1: $E = 35.7$ GPa, $\delta E = 5.8$ GPa

SFJ2: $E = 29.6$ GPa, $\delta E = 5.4$ GPa

SFJ3: $E = 31.0$ GPa, $\delta E = 5.0$ GPa

The analysis of the results reveals a significant dispersion of the elastic modulus around their average values because the standard deviations are approximately 16%, 18% and 16% of the average values at locations SF1, SFJ2 and SFJ3, respectively. Comparing the elastic modulus values determined in small flat jacks with those that were obtained by the biaxial tests conducted in overcored rock cores (Table 2.14), it can be concluded that they are considerably smaller. This result may be explained in two ways. On the one hand, the rock mass volume tested with flat jacks is larger than that used in overcoring testing and hence includes a considerable number of existing microfissures. On the other hand, the flat jack tests were conducted on the walls of the adit, where blasting damage caused by the construction method may be significant, while overcoring tests were conducted on intact cores. This is further discussed in the next chapter where data are integrated in a single model.

The determination of the complete stress tensor at a given point from small flat jack tests requires a minimum of six tests conducted in six different directions. Because there are not enough small flat jack tests for such a determination, the results obtained using small flat jacks and using overcoring for tests conducted at locations close to each other are compared.

In this comparison, the following assumptions are made: (i) the rock has a linear, elastic and isotropic behaviour; (ii) the vertical gradient of the stress tensor components is negligible; and (iii) the lateral stress variation between the locations of the various tests is negligible.

The stresses provided by the small flat jack technique do not correspond to the far-field stress components because they are influenced by the existing adit. In this way, the six components of the stress tensor S_i^k ($i = 1, \dots, 6$) that are acting at the location of the k^{th} small flat jack test and the six components of the far-field stress tensor σ_j ($j = 1, \dots, 6$) at this location are related by the following equation:

$$S_i^k = A_{ij}^k \sigma_j, \quad (2.28)$$

where A_{ij}^k is a matrix of 36 influence coefficients that depends on the geometry of the adit at the location of the k^{th} small flat jack test.

A three-dimensional numerical model of finite differences was developed using the code FLAC3D (Itasca, 2009) (Figure 2.30). This model is a 30 m×30 m×5 m solid and includes the rectangular cross section of the adit with dimensions 2.4 m×2.0 m. Note that the elastic modulus has no effect on the solution. A Poisson's ratio value of 0.25 obtained from uniaxial compression tests conducted on intact cores was considered. However, variations of the Poisson's ratio between 0.25 and 0.35 do not result in changes larger than 5% for the stresses in the walls of the existing adit.

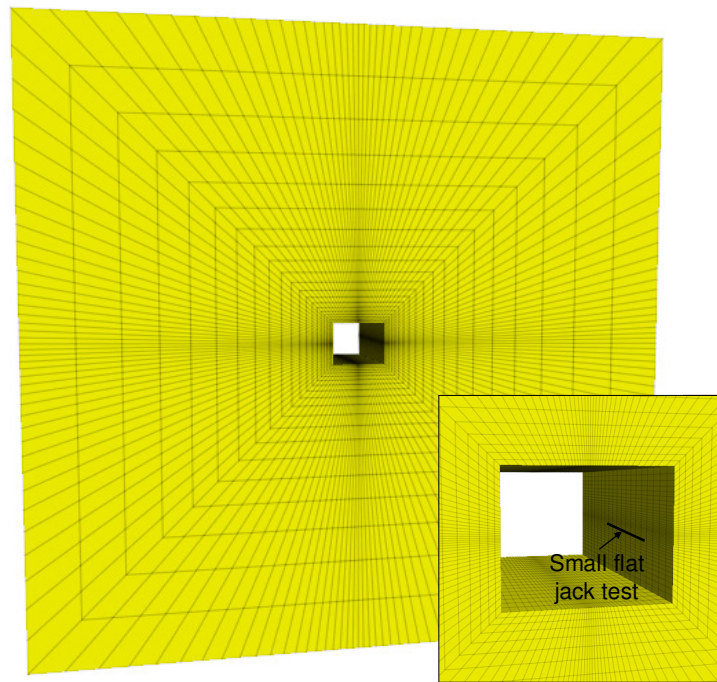


Figure 2.30: Three-dimensional model used for interpretation of the small flat jack tests.

The influence coefficients were determined from six calculations; in each calculation, a unit value of one of the stress tensor components σ_j ($j = 1, \dots, 6$) is used with null values for the other components. As a result of each calculation, the stress tensor components S_i^k ($i = 1, \dots, 6$) at the location of the k^{th} small flat jack tests are obtained. After the influence coefficients are determined, the normal stresses $\sigma_{n,calc}^k$ at the location of the k^{th} small flat jack test are calculated with the following equation:

$$\sigma_{n,calc}^k = S_i^k N_i^k, \quad (2.29)$$

where N_i^k ($i = 1, \dots, 6$) are the generalised components of the normal to the k^{th} small flat jack plane.

Equation (2.29) is used to calculate the normal stresses at the location of the small flat jack tests by considering the far-field stress tensor components obtained from the overcoring testing. Two different far-field stress conditions are considered. First, the stress tensor components that result from the inversion of overcoring data are considered. Second, the average stress tensor components of the overcoring tests results obtained close to the adit, in boreholes PD1 and PD2, are considered.

A comparison between the normal stresses obtained this way and the stresses actually measured with the small flat jacks is shown in Figure 2.31. Figure 2.31 shows that there is a significant discrepancy (greater than 1.0 MPa) between the stresses measured using the two testing methods in approximately 75% of the tests. It is concluded that the stresses measured in the adit walls using small flat jacks are not consistent with the stresses measured at a similar location by overcoring.

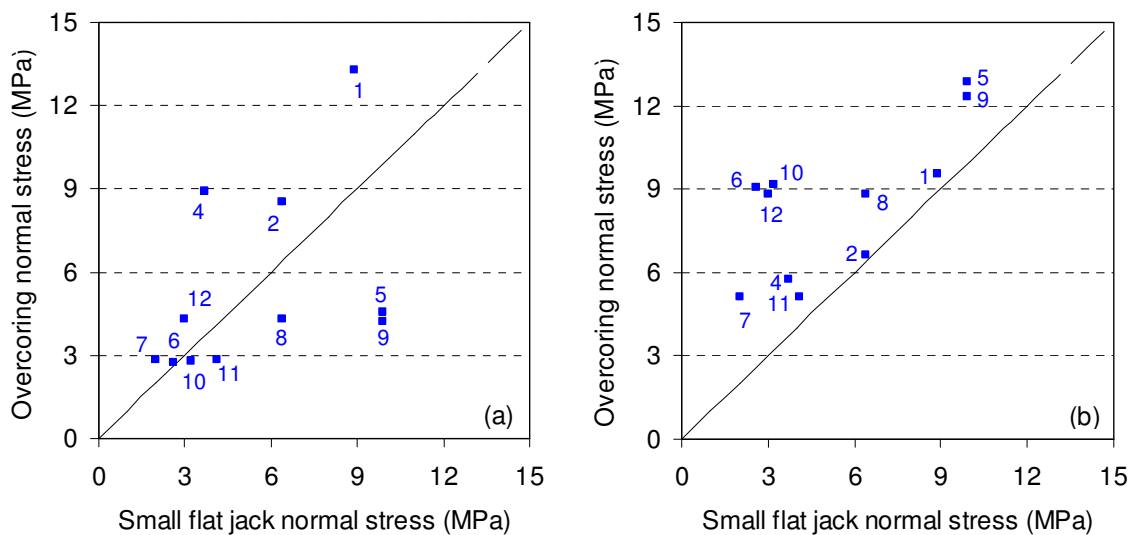


Figure 2.31: Comparison between small flat jack and overcoring normal stress considering the far-field stress tensor resulting from the (a) inversion of overcoring data and (b) shallow overcoring tests results.

Because no local heterogeneities were identified in the borehole logs that justify these stress variations, it is concluded that the small flat jack tests and shallow overcoring tests are influenced by the adit. Detailed analysis of the causes of this disagreement remains to be conducted. It seems likely that this disagreement is associated with the mechanical behaviour of the damaged zone that was caused by blasting when the adit was constructed.

2.5. Conclusion

Several *in situ* stress measurements were conducted for the design of an underground reinforcement power scheme that includes a large powerhouse cavern and a hydraulic pressure tunnel. The measurements include hydraulic tests in two 500 m deep vertical boreholes, overcoring tests in two 60 m deep vertical boreholes drilled from an existing adit and small flat jack tests in the walls of the adit.

The data shows a significantly spatial variability of the rock mass properties and a non-elastic behaviour for the low stress levels.

The analysis of the hydraulic and overcoring data demonstrates that one principal stress component is sub-vertical within most of the volume that was tested. The other two components are sub-horizontal and of similar magnitude. Some local zones of heterogeneity were encountered, as demonstrated by the appearance of inclined fractures in the electrical imaging logs obtained for two of the hydraulic fracturing tests. Local heterogeneities explain the large uncertainty in the orientation of the maximum horizontal principal stress direction.

A comparison between the overcoring and hydraulic tests shows that, with the exception of the sub-vertical stresses obtained by overcoring in borehole PD1 and the overcoring test results obtained in borehole PD2 close to the existing adit, the stresses estimated by both techniques are of similar magnitude.

A comparison between the small flat jack and overcoring tests conducted at approximately the same location reveals significant differences in the results. It appears that, close to the adit, the stresses are most likely influenced by the rheological behaviour of the damaged zone associated with the construction of the adit.

Chapter 3.

Determination of the regional stress field

3.1. Introduction

The previous chapter presented stress measurement data obtained at different locations in a mountainous region of northern Portugal. The objective was to characterise the regional stresses for the design of a re-powering scheme of an existing hydroelectric system that includes an underground large cavern and a hydraulic pressure tunnel. The *in situ* measurements include overcoring and hydraulic tests conducted in boreholes as well as flat jack tests performed in the walls of an existing adit.

The aim of this chapter is to integrate these various data to assess the regional stress field and consequently to extrapolate the results of the various tests to the rock mass volume of interest for this hydroelectric scheme. The integration of the data faces several difficulties. First, the data were collected at different locations using different testing techniques. Second, topography effects influence the stresses at the locations of the various measurements. Furthermore, local heterogeneities (e.g., fractured zones and faults), the spatial variability of the rock mass properties and, possibly, plasticity for zones close to the adit from which the overcoring measurements and the flat jack tests were conducted may have to be considered.

The objective is to develop a model that is simple enough such that the constraining data are more numerous than the number of degrees of freedom of the model. Indeed, as the model becomes more complicated, the solution becomes less constrained, the apparent efficiency of the fit between the data and model becomes more illusory, and the conclusion becomes less useful.

A linearly elastic model is used for integrating results gathered away from the adit (fifteen normal stress measurements obtained by hydraulic testing and the six components of nine stress tensors determined at the location of the overcoring tests). This model is used to analyse the influence of topography effects on *in situ* stress distributions

due to gravity and tectonic loadings. Furthermore, this model is used to investigate the influence of the compliance of existing large-scale fractured zones and potential tectonic stresses and to determine the proper elastic constants for the equivalent geomaterial. It has provided the means to identify a simple model that satisfactorily reproduces (in a least squares sense) the different measurements obtained away from the adit.

3.2. Inverse model

The aim of any inversion scheme is to determine the model parameters that minimise the differences between a number of observations and predictions from a model. This determination requires a model definition, a definition of the misfit for describing the discrepancy between observed and predicted values, and a normative measure of the misfit for quantifying the residuals for all observations (Gephart and Forsyth, 1984). Two types of normative methods are commonly used: the l_1 -norm considers the sum of the absolute values of the error between observations and predictions; the l_2 -norm considers the sum of the squares of the error between observations and predictions. The l_1 -norm is more robust than the l_2 -norm and yields smaller variances for the error. Furthermore, it is less influenced by atypical data (Parker and McNutt, 1980).

The inverse problem concept is more general than the back analysis concept (Giorda and Sakurai, 1987). With the back analysis, only one model is assumed for describing the observations, whereas for the inverse problem, several hypotheses for the model are tested.

The inverse model that is proposed here is meant to help determine the natural regional stress field that best fits the data gathered away from the existing adit. This model considers an equivalent continuous geomaterial, and the corresponding characteristic differential equations are solved with explicit finite differences using the software FLAC3D (Itasca, 2009).

Due to the influence of topography effects, models simulating rock mass volumes with different dimensions were considered when performing the gravitational analysis ($g=9.81 \text{ m.s}^{-2}$) for fitting stresses at the locations of the various tests. The results of this analysis indicated that the region 5 km long and 3 km wide shown in Figure 3.1 is sufficiently large for obtaining reliable estimates because for larger regions, the maximum variations in the principal stress magnitude at the locations of the various tests are less than 0.5 MPa. In this region, the elevation varies between 315 m and 1030 m above sea level (Figure 3.1). A 2.5 km dimension was assigned to the vertical direction so that topography effects do not influence the stresses close to the basal boundary of the model.

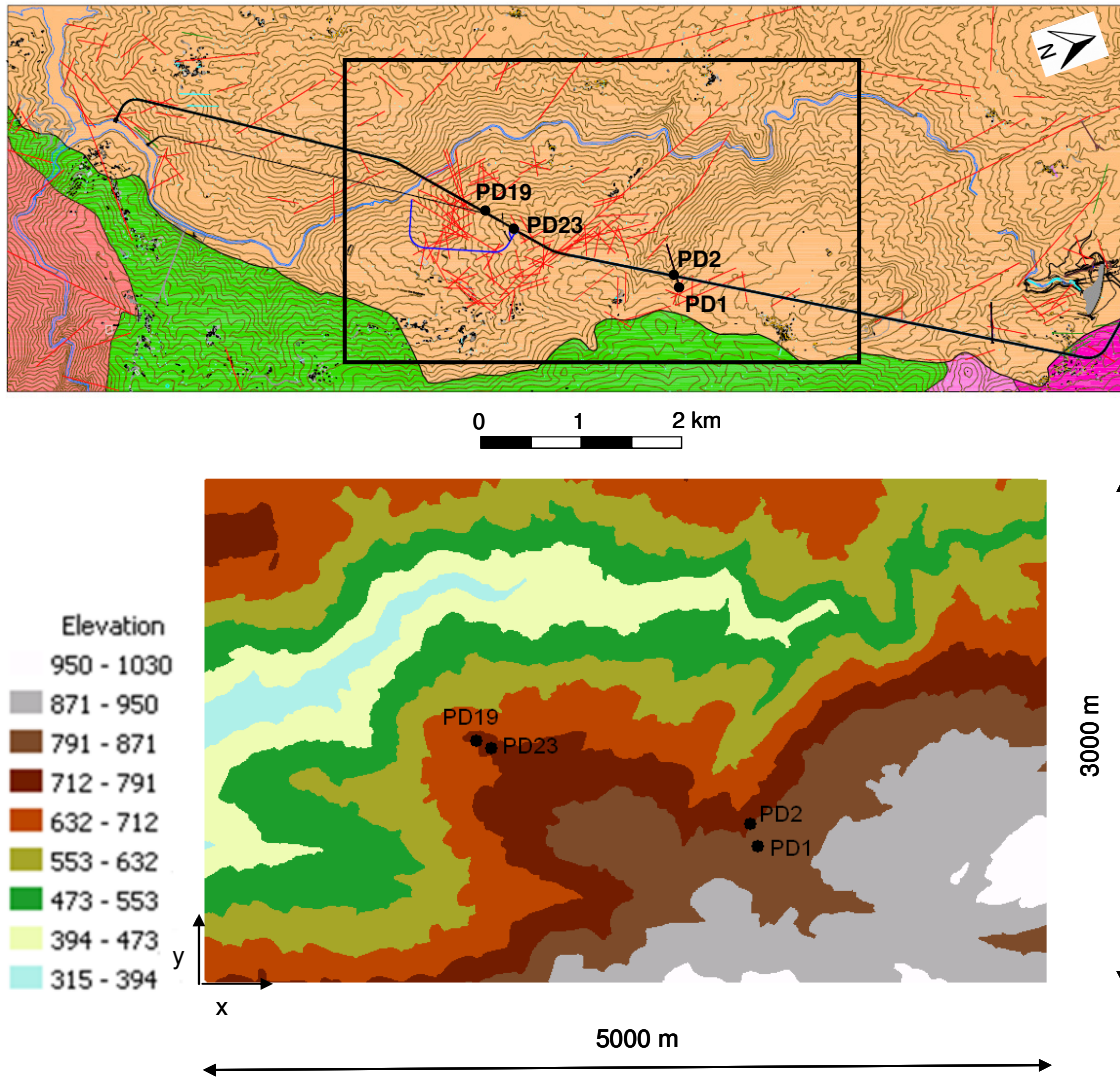


Figure 3.1: Limits and detailed elevation of the region considered in the FLAC3D model.

The mesh of the FLAC3D model (Figure 3.2) is composed of 600,000 elements. This mesh is finer above sea level, with cubic 25 m-sided elements. Below sea level, the elements are 50 m×50 m×100 m. As boundary conditions with gravity loading, displacements normal to the lateral and basal boundaries are restricted.

The l_1 -norm method was used to minimise the misfit between the measured and calculated stresses, normalised by the uncertainty on the data. Consequently, the misfits are adimensional.

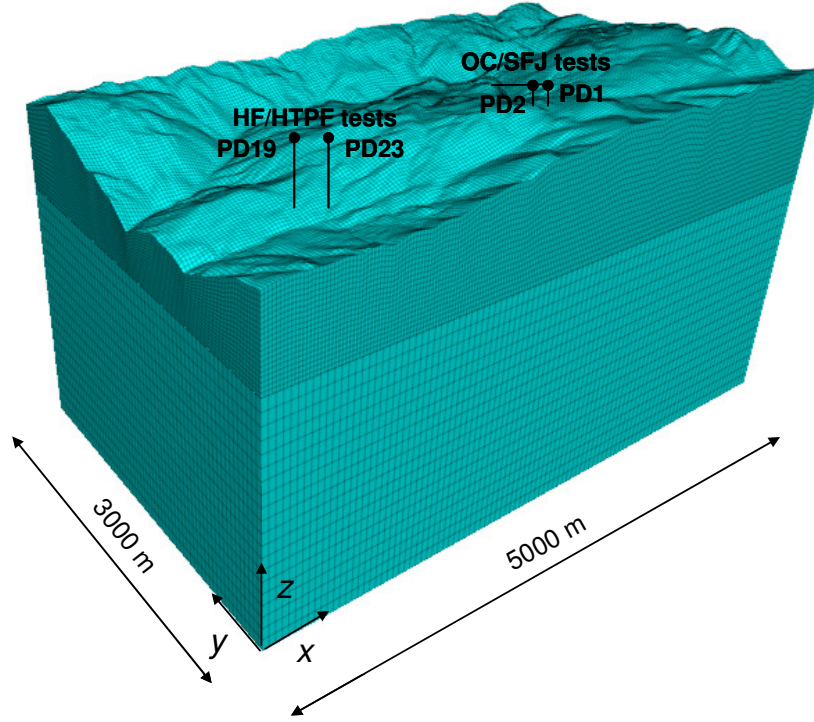


Figure 3.2: Mesh of the FLAC model.

For hydraulic data, the misfit ψ^{HF} is expressed as follows (Yin and Cornet, 1994):

$$\psi^{HF} = \sum_{m=1}^M \frac{|\sigma_{n,mes}^m - \sigma_{n,calc}^m|}{\delta_n^m + \delta_f^m}, \quad (3.1)$$

where M is the number of hydraulic tests; $\sigma_{n,mes}^m$ and $\sigma_{n,calc}^m$ are the measured and calculated normal stresses obtained at the location of the m^{th} hydraulic test, respectively; δ_n^m is the uncertainty on the normal stress determination for the m^{th} fracture plane; and δ_f^m is the uncertainty on the normal stress associated with uncertainties on the orientation of the m^{th} fracture plane.

The uncertainties on the normal stresses due to the uncertainty on the fracture plane orientation were estimated using the FLAC model. Uncertainties obtained in this way are of the same order of magnitude as the uncertainties associated with the shut-in pressure measurements.

For the overcoring data, the uncertainties are associated with the strain measurement technique, the orientation of the strain gauges in the three dimensional space and the determination of elastic properties of the overcored cores. The misfit ψ^{OC} that was used is simplified and is defined as follows:

$$\psi^{OC} = \sum_{n=1}^N \frac{|\sigma_{mes}^n - \sigma_{calc}^n|}{\delta_{\sigma}^n + \delta_{bh}}, \quad (3.2)$$

where N is the number of overcoring tests; σ_{mes}^n and σ_{calc}^n are the measured and calculated stresses obtained at the location of the n^{th} overcoring test, respectively; δ_{σ}^n is the uncertainty associated with the stress determination; and δ_{bh} is the uncertainty on the stress associated with uncertainties on the orientation of the borehole axis.

Because the overcoring tests were conducted within a small depth range (approximately 60 m) in vertical boreholes, the uncertainty associated with the orientations of these boreholes was neglected. By considering the several pairs of the overcoring test results obtained approximately at the same depth, a maximum uncertainty of 1.5 MPa was set for the corresponding stress magnitude determinations.

The hydraulic testing and overcoring methods are of different natures. Therefore, the global misfit when combining hydraulic and overcoring data should include weighting factors. A simplified global misfit was used that considers: (1) the volume, or area, involved in a given measurement for each of the methods; (2) the individual misfit related to the misfit obtained in the combined solution. The general global misfit ψ^{HFOC} can be expressed as follows (Yin and Cornet, 1994):

$$\psi^{HFOC} = \omega^{HF} \psi^{HF} + \omega^{OC} \psi^{OC}, \quad (3.3)$$

The weighting factors for the hydraulic and overcoring data, ω^{HF} and ω^{OC} , respectively, are given by the following expressions (Ask, 2004):

$$\omega^{HF} = \frac{A^{HF}}{A^{REV}} \cdot \frac{\psi^{HF}}{\psi_{min}^{HF}}, \quad (3.4)$$

$$\omega^{OC} = \frac{V^{OC}}{V^{REV}} \cdot \frac{\psi^{OC}}{\psi_{min}^{OC}}, \quad (3.5)$$

where A^{HF} and A^{REV} denote the measurement area and the area involved in the representative elementary volume (REV) in hydraulic testing, respectively; V^{OC} and V^{REV} are the corresponding notations associated with the overcoring technique (measurement volume and REV volume, respectively); and ψ_{min}^{HF} and ψ_{min}^{OC} are the minimums of equations (3.1) and (3.2), respectively.

The area involved during hydraulic testing depends on the injected volume, but it was set to 1 m², which corresponds to 1 litre of water injected into a fracture with a mean width of 1 m (assuming no loss of water due to rock mass permeability). The volume involved in overcoring measurements was set to the average volume of the resulting hollow rock cylinder. The scale of the stress measurements was not determined. As an approximation, the REV was set to 1 m³ (i.e., area 1 m²).

The suggested global misfit function gives more weight to the hydraulic data than to the overcoring data. Once the global minimum was found (minimum of ψ^{HFOC}), the 90% confidence interval could be estimated using the following expression (Parker and McNutt, 1980):

$$\psi_{90\%}^{HFOC} = \frac{1.645(\pi/2 - 1)^{1/2}(M+N)^{1/2} + M+N}{(M+N) - W} \cdot \psi_{\min}^{HFOC}, \quad (3.6)$$

where W is the number of unknown parameters of the model used to describe the regional stress field.

3.3. The role of the topography on the *in situ* stresses distribution

3.3.1. Gravity loading

The FLAC model has been used for the evaluation of the role of topography on the distribution of *in situ* stresses due to gravity loading G . A linear elastic and isotropic behaviour of the rock mass is assumed. The elastic properties are set according to the average values obtained from uniaxial compression tests conducted in intact cores. Thus, the elastic modulus, Poisson's ratio, and the density are set to 45 GPa, 0.25, and 2650 kg/m³, respectively. These values for the elastic modulus and Poisson's ratio were considered in a first approach, although these may be unrealistic in a simulation of the behaviour of the rock mass at a larger scale compared with the scale of the laboratory tests. Figure 3.3 shows the contours of the principal stresses (σ_I , σ_{II} , σ_{III}) obtained due to gravity loading. Figure 3.4 shows the variation with the depth below the surface of the principal stress (σ_I , σ_{II} , σ_{III}) magnitudes and the inclination of the maximum principal stress (σ_I) with respect to the vertical direction. These values were obtained at the locations of the overcoring tests (boreholes PD1 and PD2) and the hydraulic tests (boreholes PD19 and PD23). The dashed lines represent the stresses that would result from gravity loading assuming a horizontal ground surface ($\sigma_I = \rho g z$, $\sigma_{II} = \sigma_{III} = [\nu/(1-\nu)]\sigma_I$).

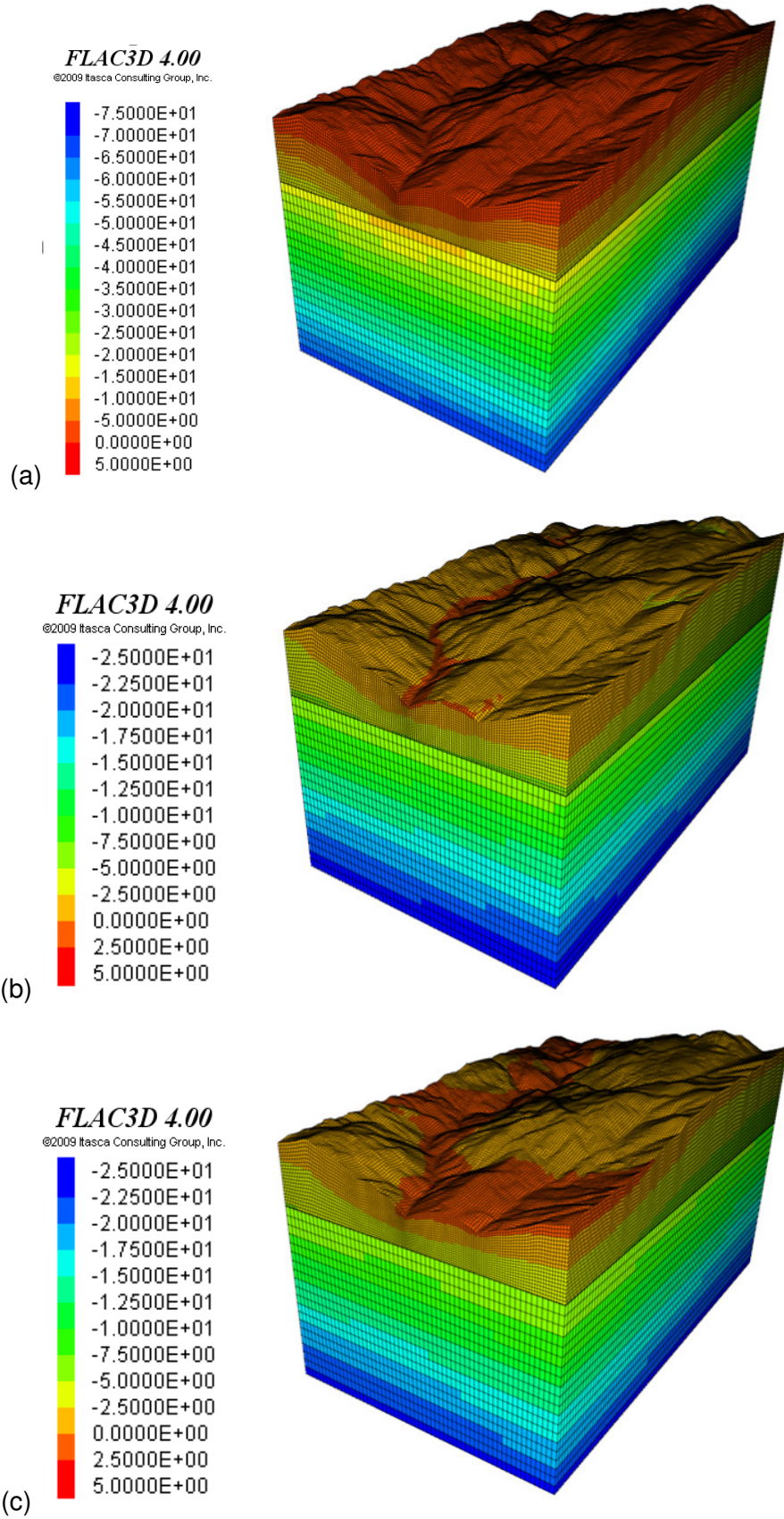


Figure 3.3: Contours of the principal stresses due to gravity loading: (a) maximum principal stress (σ_1), (b) intermediate principal stress (σ_{II}), and (c) minimum principal stress (σ_{III}).

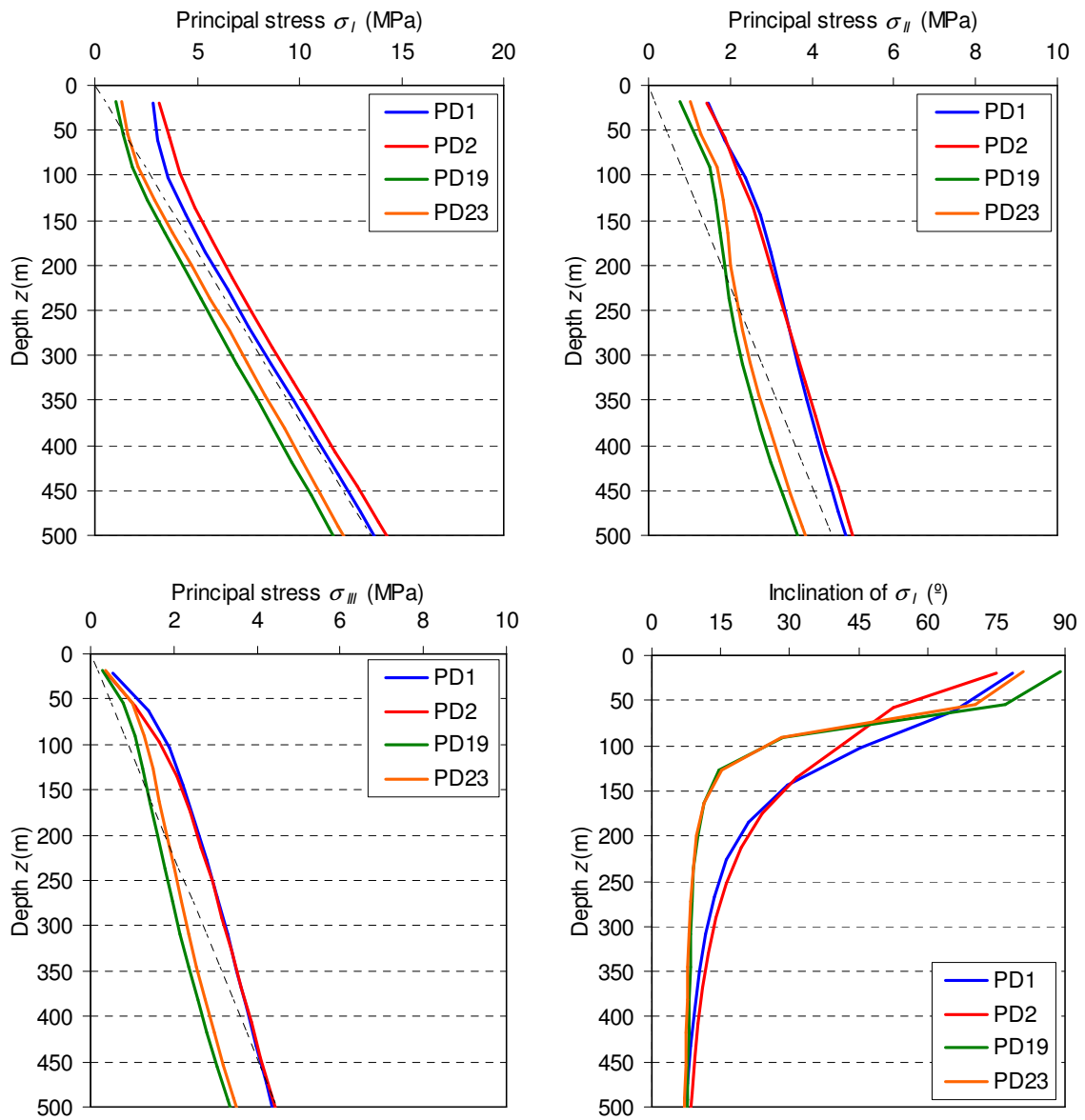


Figure 3.4: Variation with depth below the surface of the principal stresses (σ_I , σ_{II} , σ_{III}) and the inclination of the maximum principal stress (σ_I) with respect to the vertical direction.

The analysis of Figure 3.4 enables to conclude that the stress magnitudes at the locations of the overcoring and hydraulic tests are different due to the topography effects. At depths greater than 200 m below the surface, the horizontal stress magnitudes in boreholes PD1 and PD2 are about 1 MPa larger than in boreholes PD19 and PD23. For the vertical stress component, this difference is about 1.5 MPa.

However, the comparison of the stresses between boreholes PD1 and PD2 and between boreholes PD19 and PD23 showed that these are similar. In fact, the distance between each pair of boreholes is smaller than 150 m, which is fairly small, and leads to no significant horizontal stress gradients. In all boreholes, at the surface level, the maximum principal stress (σ_I) is sub-horizontal. As the depth below the surface increases, the influence of the topography on the inclination of the principal stresses with respect to the vertical direction vanishes. Consequently, the maximum principal stress (σ_I) becomes aligned with the borehole axis, and the intermediate (σ_{II}) and minimum (σ_{III}) principal stresses become aligned with the horizontal plane. This was verified at 250 m below the surface in boreholes PD1 and PD2 and at 150 m below the surface in boreholes PD19 and PD23. This shows that the topography effects are more significant at location of the overcoring data. At the both locations, the two sub-horizontal stress components are of similar magnitude, and, hence, the rotation of their directions with increasing depth is meaningless.

3.3.2. Tectonic loading

The role of the topography on the distribution of *in situ* stresses due to tectonic loading is analysed. Usually, tectonic stresses are considered in numerical models through the application of the horizontal stress components at their lateral boundaries. The main drawback of this technique is that stress components can be applied only at the boundaries of models that simulate rock masses at a scale that is sufficiently large that the topography effects are negligible compared with the length assigned to the vertical direction of the models. Otherwise, without assuming certain artificial boundary conditions, such as prescribed displacement boundary conditions and prescribed stress boundary conditions, unbalanced stresses occur due to topography effects. The problem consists in evaluating the potential influence of the boundary conditions on the calculated stresses with the model.

Figueiredo *et al.* (2012) presented a numerical technique for solving the unbalanced stress state problem to estimate the role of topography when both tectonic and gravity stresses are active. An example is considered of a unit and uniform compressive stress

component S_{xx} applied at the lateral boundaries of a model. Due to the topography effect, an unbalanced stress state occurs when this loading condition is applied (Figure 3.5a).

The proposed technique consists of the application of a uniform normal displacement Δ_x at the lateral boundaries of a model to yield a unit horizontal stress σ_{xx} at the elements of the basal boundary of the model (Figure 3.5b). For this method to be successful, the stresses at the basal boundary of the model must not be influenced by topography effects. This may be achieved by extending the model in the vertical direction. In this approach, non-uniform stress S_{xx} distributions are generated at the lateral boundaries of the model. These stress distributions are balanced and account for the effects of topography.

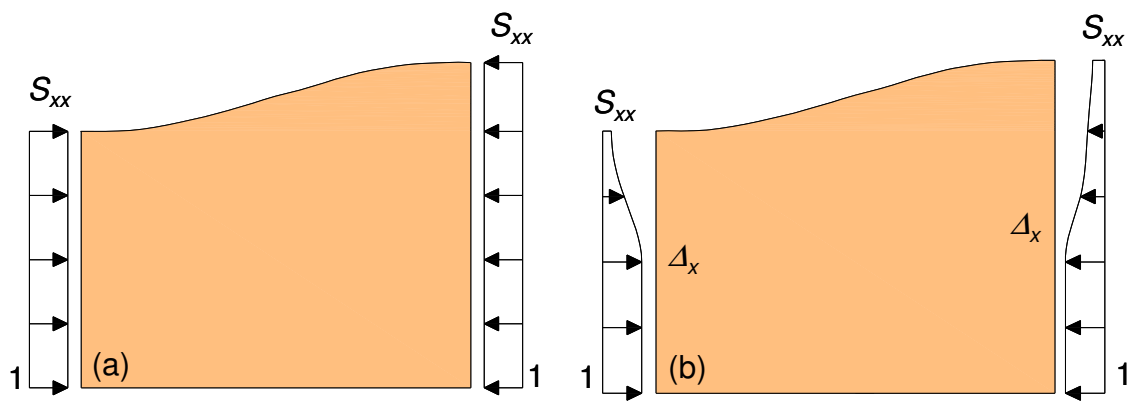


Figure 3.5: (a) Unbalanced stress state due to the effect of topography when a uniform stress S_{xx} distribution is applied at the boundaries of a numerical model (b) Uniform normal displacement Δ_x applied at the boundaries to induce a horizontal unit stress σ_{xx} at the basal boundary of the model.

An equivalent procedure is to apply unit stress components in all elements of the model and preventing the normal displacements at the lateral and basal boundaries. However, for those models that aim to simulate the poor quality of the rock mass near the surface by decreasing the local elastic modulus, this loading condition is not effective, since it leads to stress distributions that are unaffected by the variability of the elastic modulus.

This technique was applied to study the influence of topography on the distribution of the stress tensor components due to a unit tectonic S_{yy} component at the locations of the boreholes where the hydraulic and overcoring tests were conducted. This component is approximately parallel to the maximum horizontal compressive stress from the World Stress Map database (Figure 3.6).

Figure 3.7 shows the variation with depth of all stress tensor components at the locations of boreholes PD1 and PD2, where the overcoring tests were conducted, and at locations of boreholes PD19 and PD23, where the hydraulic tests were conducted, that

were obtained for the unit tectonic horizontal stress S_{yy} component introduced into the FLAC3D model.

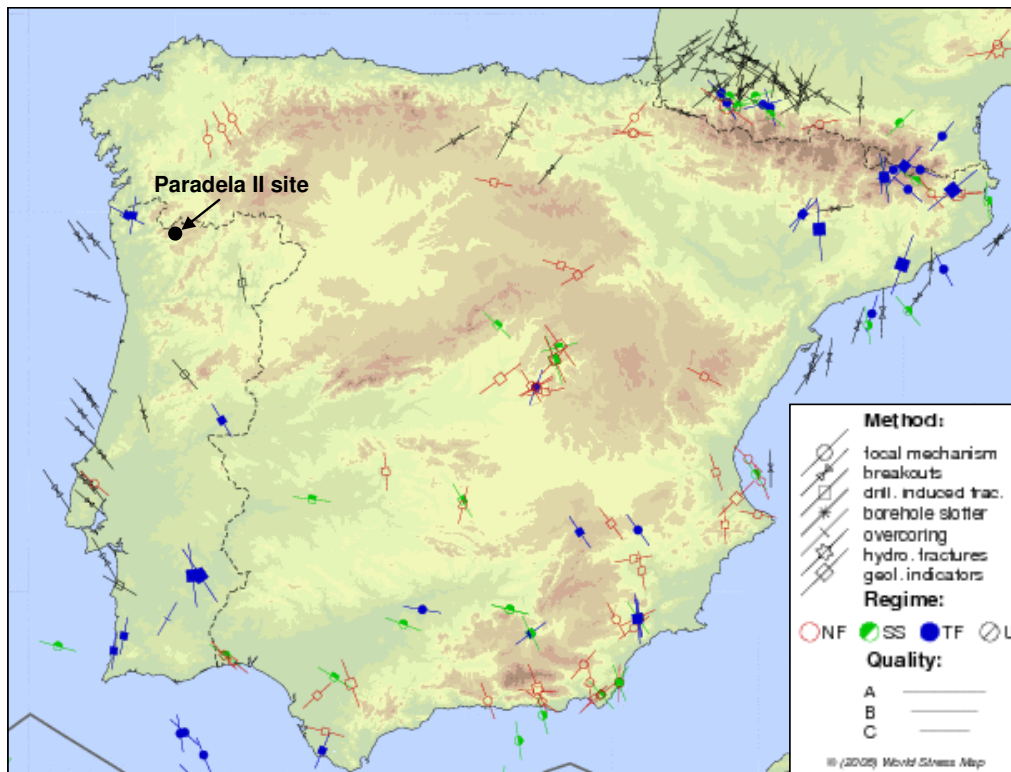


Figure 3.6: Orientation of the regional tectonic maximum horizontal compressive stress from the World Stress Map (Heidbach *et al.*, 2008).

The stresses displayed in this figures were compared with the stresses that would result from the same unit stress loading assuming a horizontal ground surface, which are represented in the figure by dashed lines. The figure shows that the stresses σ_{yy} vary 45% along a depth range of 1000 m at the location of the overcoring tests. At the location of boreholes PD19 and PD23, variations of 80% and 60%, respectively, were found along a depth range of 1000 m. At the both locations, variations in the horizontal stresses σ_{xx} and the vertical stresses σ_{zz} that reach maximums of 10% and 5%, respectively, were also observed. The shear stresses σ_{xy} , σ_{yz} , and σ_{xz} exhibit variations that reach maximums of 10%, 15%, and 5%, respectively.

This analysis concludes that the stress profiles are different at the locations of the overcoring and the hydraulic data: the effect of topography is higher at the locations where the overcoring tests were conducted.

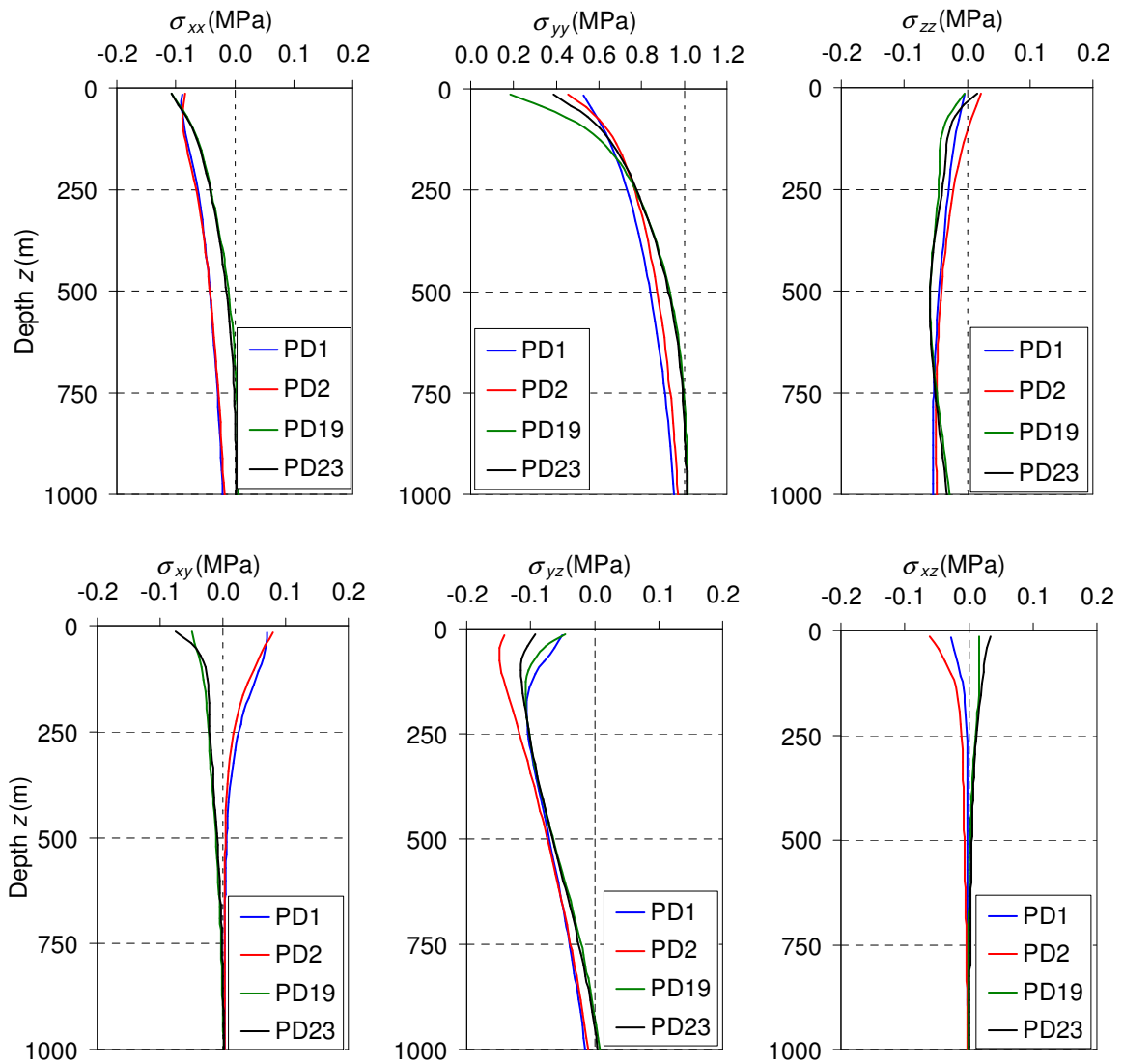


Figure 3.7: Variation with depth of the stress tensor components for a constant unit tectonic stress S_{yy} .

3.3.3. Gravity and tectonic loadings

The influence of the tectonic loading S_{yy} component on the results obtained for the gravity loading G is analysed. Three values have been considered: S_{yy1} , S_{yy2} and S_{yy3} equal to 1, 5 and 10 MPa, respectively. Figures 3.8 and 3.9 show the variation with depth of the principal stresses magnitudes at location of boreholes PD1 and PD19, respectively. Figure 3.10 shows the orientation of the principal stresses directions with depth at the locations of boreholes PD1 and PD19 for the combined effect of gravity G and tectonic S_{yy1} , S_{yy2} and S_{yy3} loadings. The orientations of the principal stresses are shown in a lower hemisphere stereographic projection in which the direction of the x axis of the FLAC

model is shown. The results obtained for the magnitudes and orientations of the principal stresses at the location of boreholes PD2 and PD23 are not presented because these are very similar to the results obtained at the locations of boreholes PD1 and PD19, respectively.

In borehole PD1, the combined effect of gravity G and unit tectonic S_{yy} loadings result in intermediate (σ_{II}) and minimum (σ_{III}) principal stresses that are sub-horizontal at depths greater than 250 m below the surface. When the tectonic loading S_{yy} increases to 5 MPa and 10 MPa, the minimum principal stress (σ_{III}) remains sub-horizontal at depths greater than 250 m below the surface; however, the intermediate principal stress (σ_{II}) is sub-horizontal at depths greater than 500 m and 750 m below the surface.

In borehole PD19, the minimum principal stress (σ_{III}) is sub-horizontal as the result of the combined effect of gravity and tectonic loadings. When the unit tectonic S_{yy} loading is applied, the intermediate principal stress (σ_{II}) is sub-horizontal at depths greater than 250 m below the surface. This stress component is sub-horizontal at depths greater than 750 m and 1000 m below the surface for a tectonic loading component S_{yy} equal to 5 MPa and 10 MPa, respectively.

At both locations, as the tectonic loading increases, the minimum (σ_{III}) and intermediate (σ_{II}) principal stresses become aligned with the x and y axes of the FLAC model, respectively. The direction of the maximum principal stress (σ_I) is practically constant with increasing depth for all loading conditions and is practically aligned with the y axis of the FLAC model. However, its inclination with respect to the vertical direction varies substantially with increasing depth when the tectonic loading increases. The magnitude of the minimum principal stress (σ_{III}) is practically unaffected by the tectonic loading because this loading is applied in the perpendicular direction. The magnitude of the maximum principal stress (σ_I) obtained due to gravity loading at the locations of boreholes PD1 and PD19 is not influenced at depths of 600 and 700 m, respectively, when a tectonic loading is applied. Thus, at greater depths, the magnitude of this stress component is controlled by gravity loading.

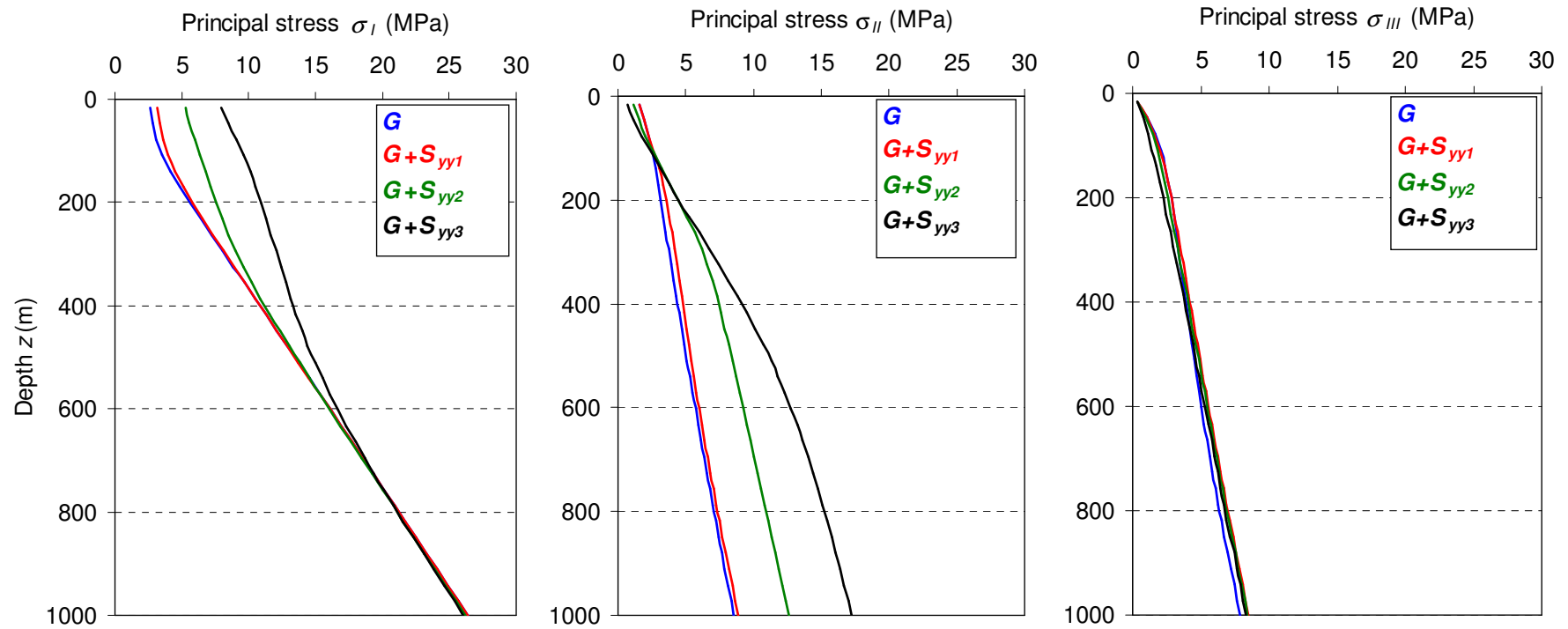


Figure 3.8: Variation with depth of the magnitude of the principal stresses (σ_I , σ_{II} , σ_{III}) obtained at the location of borehole PD1 for the combined effect of gravity G and tectonic S_{yy} loadings.

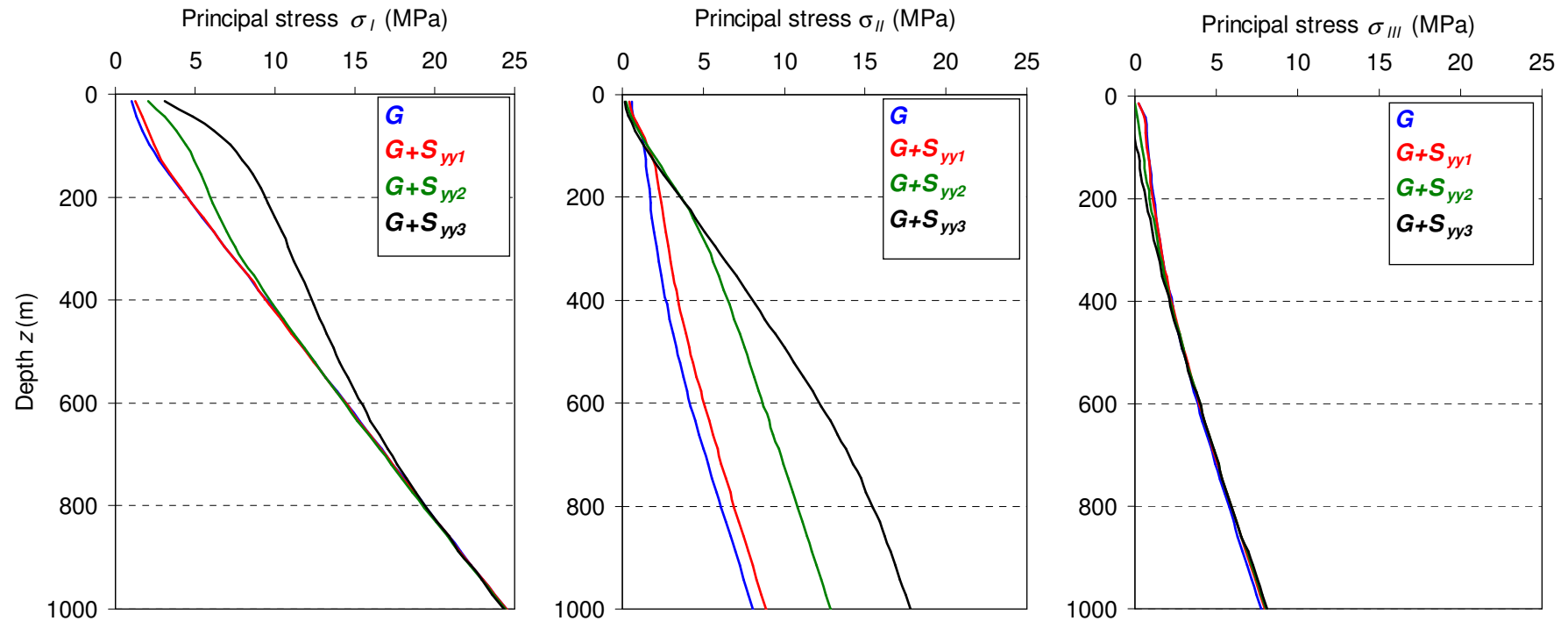


Figure 3.9: Variation with depth of the magnitude of the principal stresses (σ_I , σ_{II} , σ_{III}) obtained at the location of borehole PD19 for the combined effect of gravity G and tectonic S_{yy} loadings.

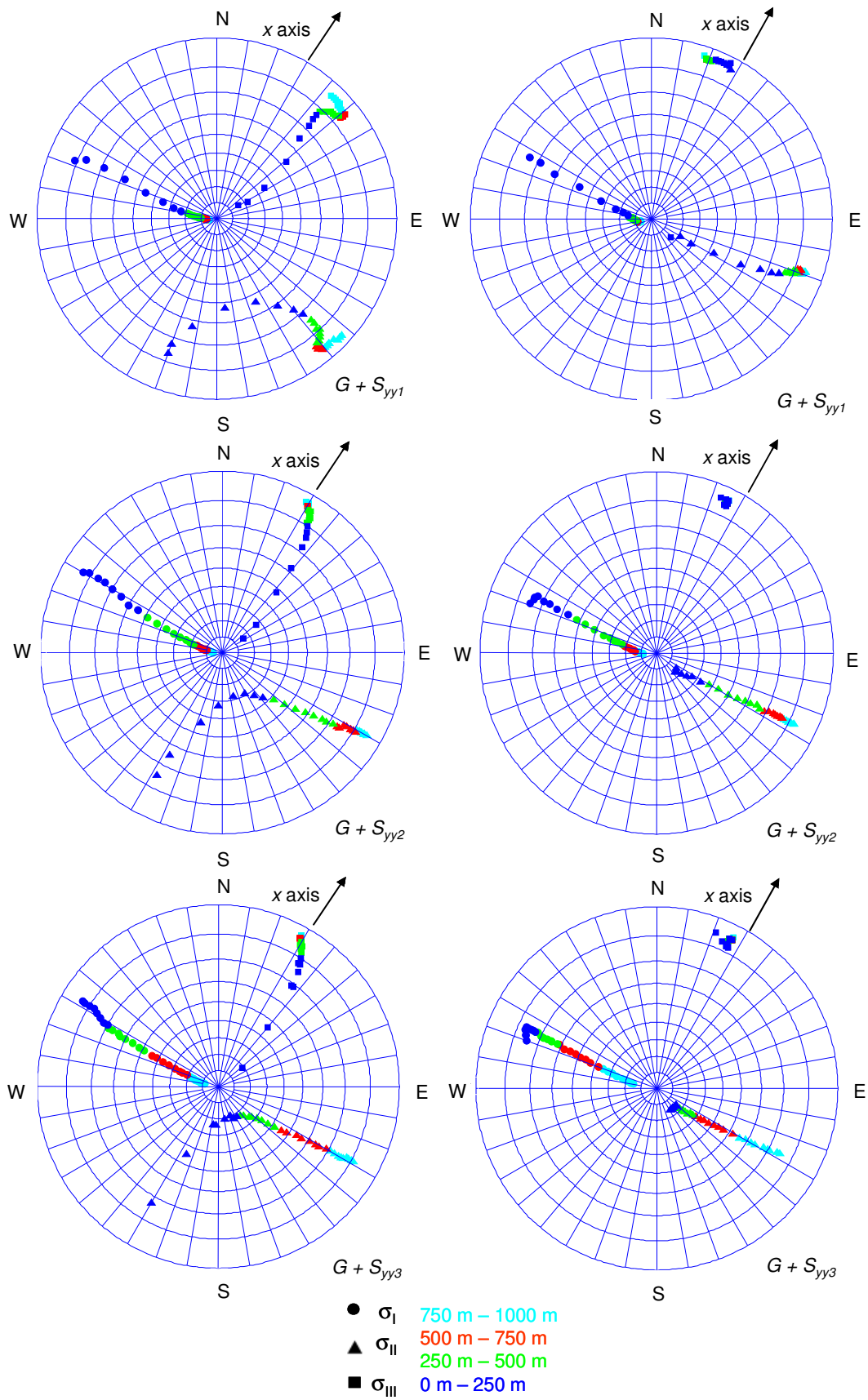


Figure 3.10: Orientation of the principal stresses obtained for the tectonic S_{yy} loading at the locations of boreholes PD1 (left) and PD19 (right).

3.4. Comparison between *in situ* tests and results from the FLAC3D model when considering gravity loading alone

A comparison between hydraulic and overcoring data, on the one hand, and the FLAC3D model results obtained by performing a gravitational analysis, on the other hand, was undertaken. The elastic properties used in the model were those measured during a set of uniaxial compression tests conducted on intact cores extracted from the rock mass at various locations. The average values for the elastic constants (elastic modulus E and Poisson's ratio ν) are 45 GPa and 0.25, respectively, and for the density is 2650 kg/m³.

In the hydraulic tests, the comparison was first made in terms of the normal stresses (σ_n) on the tested fracture planes in boreholes PD19 and PD23 (Figure 3.11). In the ambiguous tests with two observed fracture planes, the stresses were associated with the fracture plane for which the difference between the measured and calculated stress values was the smallest. A 99% confidence interval, which corresponds to six standard deviations for a Gaussian law, is shown for the various normal stress measurements. In boreholes PD19 and PD23, the sum of the absolute differences between the measured and calculated normal stresses is 33.4 MPa and 10.1 MPa, respectively. The highest differences are observed for the hydraulic fracturing tests, in which sub-horizontal stresses were measured.

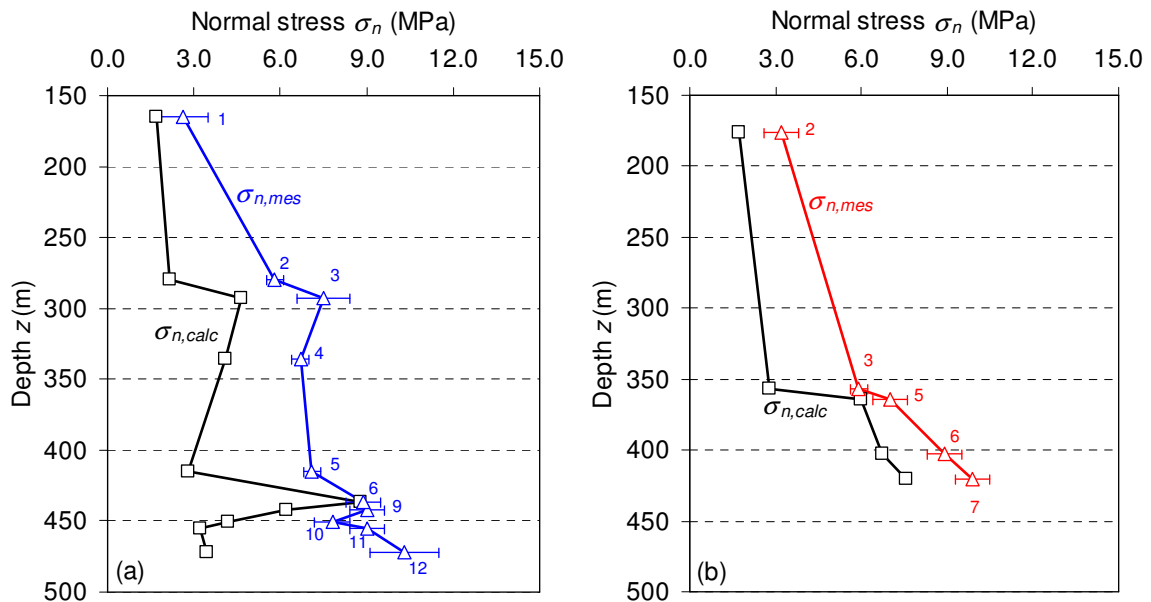


Figure 3.11: Variation of the magnitudes of the normal stresses obtained by hydraulic testing ($\sigma_{n,mes}$) and with the FLAC3D model ($\sigma_{n,calc}$) run with gravity loading only in boreholes (a) PD19 and (b) PD23 as a function of depth.

Secondly, a comparison was performed in terms of the principal stress (σ_I , σ_{II} , σ_{III}) magnitudes obtained with the FLAC3D model and from the inversion of the fifteen hydraulic tests set using an 8-parameter model. The results of this comparison are displayed in Figure 3.12. The FLAC3D model results obtained for borehole PD23 are not presented because they are comparatively similar to the results obtained for borehole PD19. The 99% confidence limit for the calculated stresses with an 8-parameter model is shown. In the presented depth range, the maximum principal stress (σ_I) provided by the FLAC3D model is sub-vertical and the other two components (σ_{II} and σ_{III}) are sub-horizontal.

As shown in Figure 3.12, the inversion of the hydraulic data provides values for the horizontal principal stress components that are considerably larger than the values computed using the FLAC3D model when considering only gravity loads.

In Figure 3.13, the results from the overcoring data only (as obtained in boreholes PD1 and PD2) are compared with the linearly elastic homogeneous model, as expressed in terms of the principal stress magnitudes. The lines represent the values computed with the FLAC3D, and the dots represent the results from overcoring. The FLAC3D model results obtained for borehole PD2 are not presented because they are comparatively similar to the results obtained for borehole PD1.

Within the corresponding depth range, the maximum principal stresses (σ_I) obtained by overcoring and with the FLAC3D model are sub-vertical. The principal stresses σ_{II} and σ_{III} are sub-horizontal and of similar magnitudes. The figure shows that the measured sub-horizontal stresses are considerably larger than the calculated stresses. For the sub-vertical stresses, the measured and calculated stresses are only consistent in five of the eleven overcoring tests. In these tests, the differences between the measured and calculated stress values are less than 1.5 MPa.

Hence, the differences between the measured stresses by hydraulic and overcoring testing and the respective calculated stresses are found to be larger than the uncertainties on the measurements, indicating that this model is not acceptable.

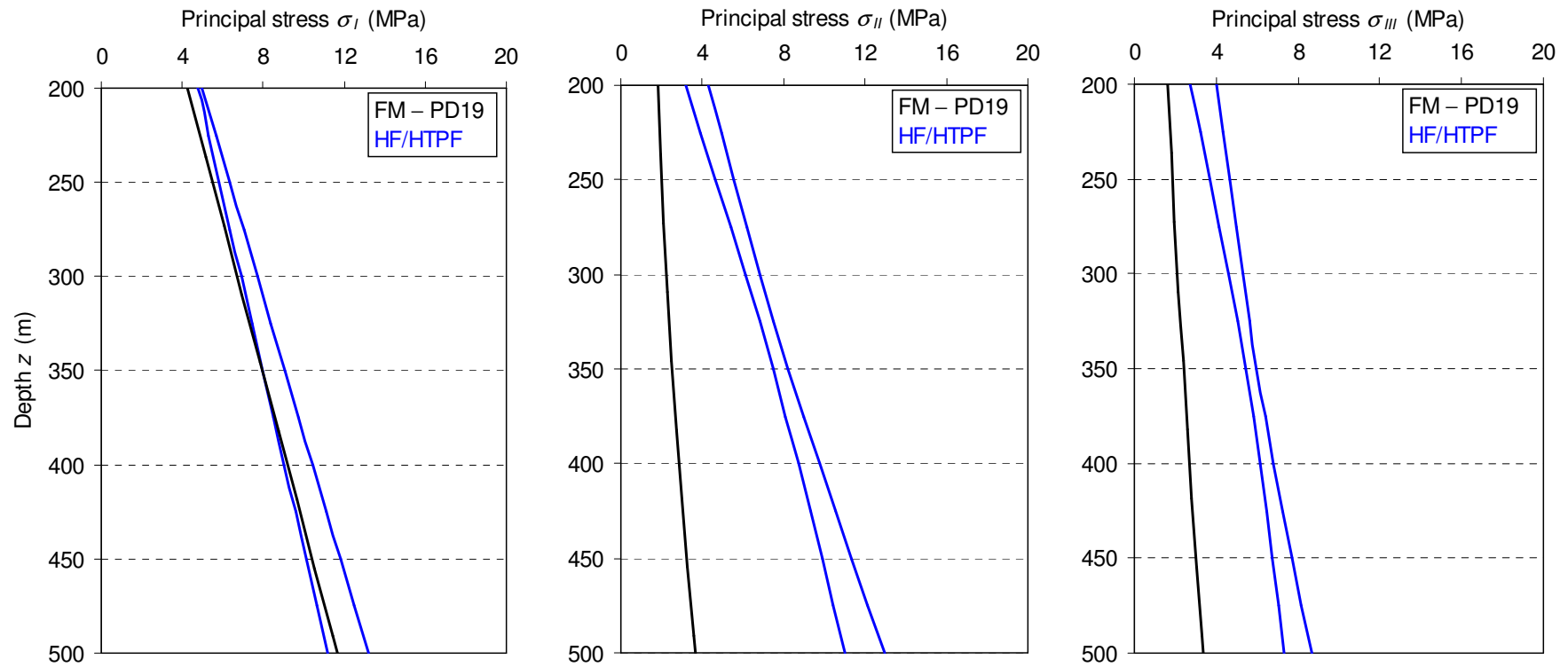


Figure 3.12: Variation of the magnitude of the principal stresses (σ_I , σ_{II} , σ_{III}) obtained from the inversion of the hydraulic data (HF/HTPF) and with the FLAC3D model (FM) run with gravity loading only as functions of depth

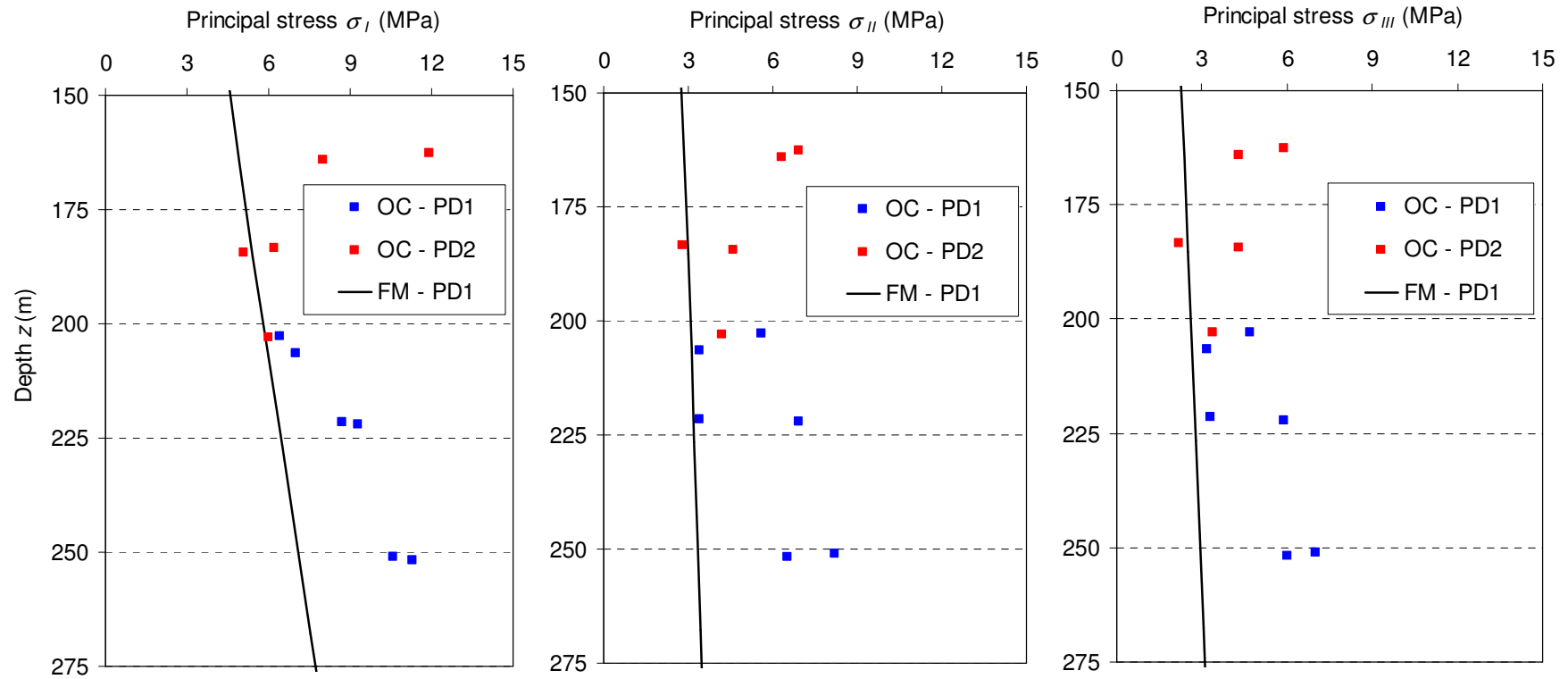


Figure 3.13: Variation of the principal stress magnitude (σ_I , σ_{II} , σ_{III}) as obtained by overcoring (OC) and as computed with the FLAC3D model (FM) run with gravity loading only as functions of depth.

3.5. Influence of faults and fractured zones

The geological survey of the region highlights the existence of two fractured zones that include several sub-vertical fractures with a significant dispersion on their azimuths (Figure 3.14). The possible influence on the magnitude and orientation of the sub-horizontal stresses at location of hydraulic tests was therefore investigated. The FLAC3D model was used for a numerical analysis of this influence at the location of hydraulic tests.

The fractures constitute weakness planes and hence represent a damage that can be simulated, in a very simple manner, by decreasing the elastic modulus values normal to them, thus resulting in a lower stiffness in the corresponding direction.

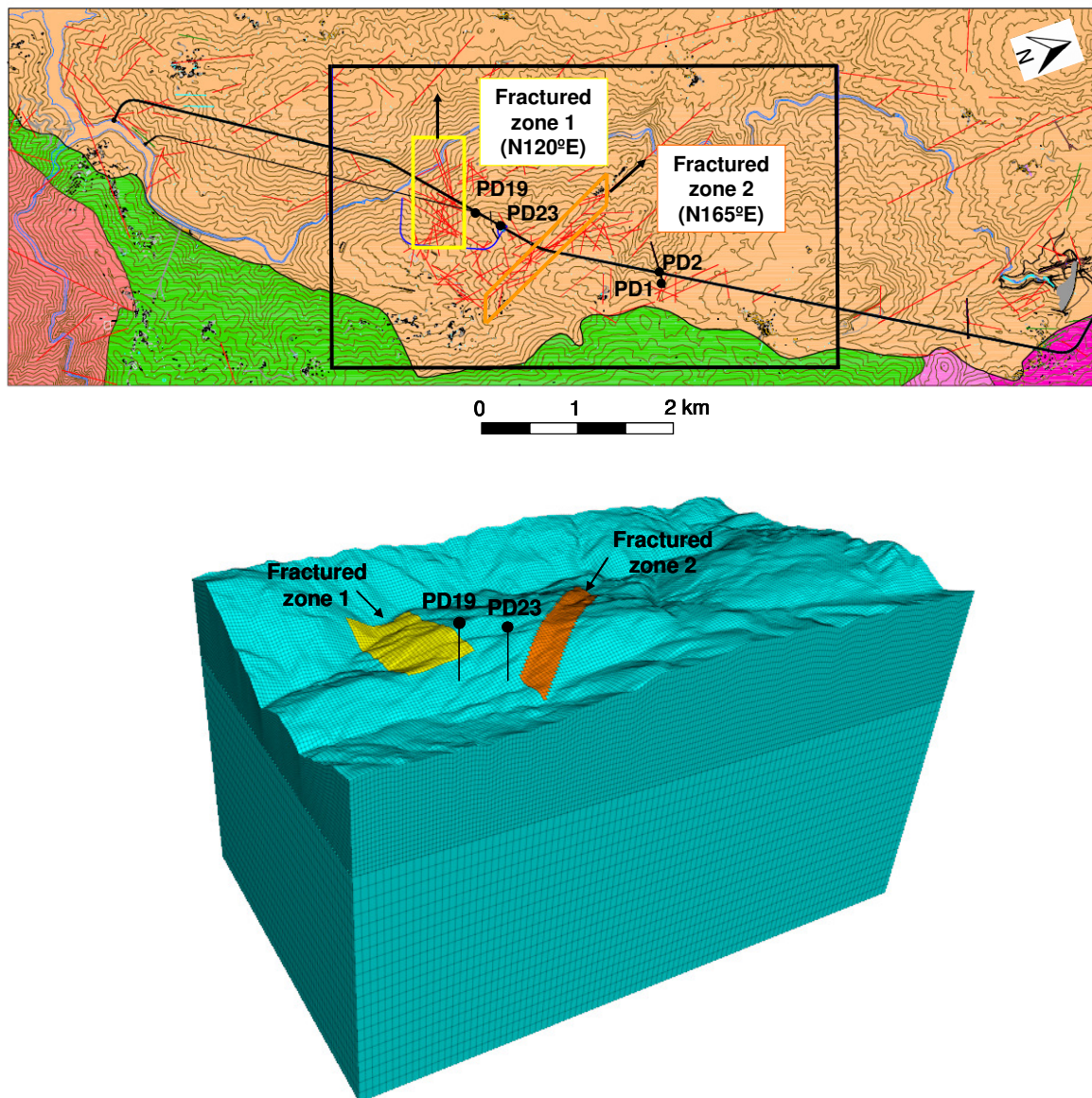


Figure 3.14: Location of the fractured zones in the FLAC3D model.

In this numerical simulation, four assumptions are made: (i) the preferential directions of the weakness planes in fractured zones 1 and 2 are N120°E and N165°E, respectively, as shown in Figure 3.14; (ii) the weakness planes are vertical; (iii) the behaviour of the non-fractured zones is isotropic with the elastic properties obtained from uniaxial compression tests results; and (iv) the rock mass behaviour in the fractured zones is described by a transversely isotropic model with the planes of symmetry coincident with the weakness planes.

The transversely isotropic model is described by two angles that define the orientation of the planes of symmetry with respect to the North and five elastic constants: E_1 and E_3 are the elastic moduli in the plane of symmetry and normal to it, respectively; ν_{12} and ν_{13} are the Poisson's ratios characterising lateral contraction in the plane of symmetry when compression is applied in the plane and normal to it, respectively; and G_{13} is the shear modulus in the plane perpendicular to the plane of symmetry.

By considering the gravity loading, a parametric analysis was performed regarding the influence of the modulus E_3 normal to the planes of symmetry on the principal stress magnitude at the location of the hydraulic tests. This elastic modulus value decreased, first separately in fractured zones 1 and 2 and then in both zones. The cases that were considered are listed in Table 3.1.

Table 3.1: Cases considered in the study of the influence of the elastic modulus E_3 on *in situ* stresses.

Case	Fractured zone	E_1 (GPa)	E_3 (GPa)	ν_{12}	ν_{13}	G_{13} (GPa)
R	1	45.0	45.0	0.25	0.25	18.0
	2	45.0	45.0	0.25	0.25	18.0
A	1	45.0	15.0	0.25	0.25	8.2
	2	45.0	45.0	0.25	0.25	18.0
B	1	45.0	45.0	0.25	0.25	18.0
	2	45.0	15.0	0.25	0.25	8.2
C	1	45.0	15.0	0.25	0.25	8.2
	2	45.0	15.0	0.25	0.25	8.2

As a simplification, the elastic constant G_{13} was calculated as a function of the other parameters using Saint Venant's principle, which is shown in the following equation:

$$G_{13} = \frac{E_1 E_3}{E_1 + E_3 + 2\nu_{13} E_1} \quad (3.7)$$

The results were compared with those obtained in the reference case (R), in which the overall rock mass has an isotropic and elastic behaviour. Figure 3.15 shows the variation with depth of the sub-horizontal principal stress magnitudes obtained for borehole PD19. The results obtained in borehole PD23 were similar and are thus not presented. A comparison was performed with the respective stress profiles obtained from the inversion of the set of fifteen hydraulic tests with an 8-parameter model.

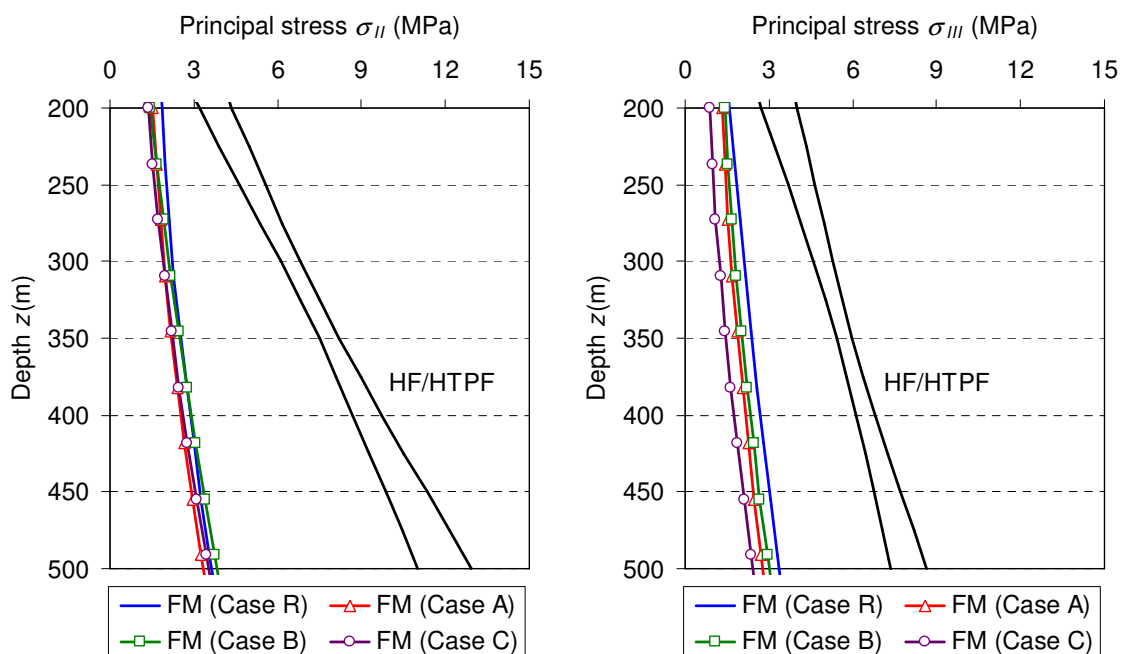


Figure 3.15: Variation with depth of the maximum (σ_{II}) and minimum (σ_{III}) sub-horizontal principal stresses obtained from the inversion of the hydraulic data (HF/HTPF) and with the FLAC3D model (FM) by considering the existing fractured zones.

Figure 3.15 shows that the inclusion of the fractured zones leads to maximum variations of 0.5 MPa and 1.0 MPa in the maximum and minimum sub-horizontal principal stresses, respectively, at a 500 m depth, and these variations are not significant. For all the cases, the discrepancies in the magnitudes of the two sub-horizontal principal stresses were less than 1.0 MPa. Because of this, the rotation of the maximum horizontal principal stress direction obtained with the FLAC3D model at a 500 m depth (between N50°E and N66°E) is not significant.

This finding shows that discrepancies between the FLAC3D model and the results from inversion cannot be explained by the presence of the fractured zones outlined by the geological survey.

3.6. Testing the existence of tectonic stresses

To improve the fit between the FLAC3D model and the data, the possibility of introducing a so-called tectonic component is considered, as proposed previously in the literature for different sites (Li *et al.* 2009, McKinnon 2001, Tonon *et al.* 2001). The horizontal stress components to be introduced in the FLAC model were calculated to reproduce the normal stress profiles obtained by hydraulic testing.

Several assumptions were made: (i) the rock mass exhibits a linear, isotropic and elastic behaviour; (ii) the total stress field may be decomposed into gravity and tectonic components; (iii) the vertical component is equal to the weight of the overlying material and is of gravitational origin; (iv) the vertical components of the far field tectonic stress tensor are zero; and (v) with exception of the zones close to the ground level, where the topography effects are important, the tectonic stresses were constant in depth.

Based on these assumptions, the normal stress ($\sigma_{n,mes}$) measured on each tested fracture plane can be decomposed into a normal component due to gravity ($\sigma_{n,grav}$) and a component associated with the tectonic ($\sigma_{n,tect}$) loading:

$$\sigma_{n,mes} = \sigma_{n,grav} + \sigma_{n,tect} \quad (3.8)$$

Unit normal (S_{xx} , S_{yy}) and shear stress (S_{xy}) components were introduced in the FLAC model, according to the technique described in section 3.3.2. As a result, non-uniform and balanced stress distributions were generated at the lateral boundaries that consider the influence of topography effects on the stress field.

The normal stress magnitudes $\sigma_{n,Sxx}$, $\sigma_{n,Syy}$ and $\sigma_{n,Sxy}$ at the location of each tested fracture plane due to unit tectonic stress components S_{xx} , S_{yy} and S_{xy} were computed. The normal stress magnitudes due to tectonic loading ($\sigma_{n,tect}$) can be estimated as a linear combination of the unit response normal stresses according to the following equation:

$$\sigma_{n,tect} = A\sigma_{n,Sxx} + B\sigma_{n,Syy} + C\sigma_{n,Sxy}, \quad (3.9)$$

where the coefficients A , B and C are unknowns.

Substitution equation (3.9) into equation (3.8) yields:

$$\sigma_{n,mes} = \sigma_{n,grav} + A\sigma_{n,Sxx} + B\sigma_{n,Syy} + C\sigma_{n,Sxy} \quad (3.10)$$

Denoting the right side of equation (3.9) $\sigma_{n,calc}$, the misfit in equation (3.1) is minimised to determine coefficients A , B and C . The following values are obtained:

$$A = 4.9, B = 5.1, C = 0.0$$

A comparison between the measured and computed normal stress (σ_n) magnitudes obtained when combining tectonic and gravity loadings is shown in Figure 3.16.

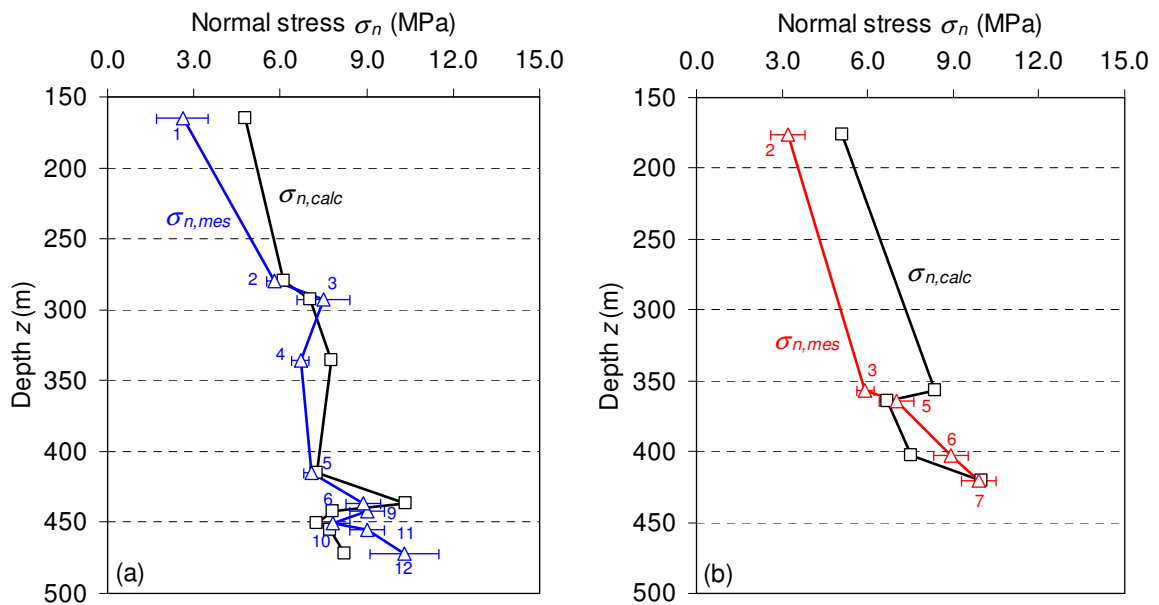


Figure 3.16: Variation with depth of the normal stress magnitudes as measured by hydraulic testing ($\sigma_{n,mes}$) and computed with the FLAC3D model ($\sigma_{n,calc}$) for the combined effect of gravity and tectonics in boreholes (a) PD19 and (b) PD23.

Figure 3.16 shows that the differences between the measured and calculated normal stress magnitudes are greater than the uncertainties on the measurements for approximately 60% of the tests. These differences may result from the various simplifying assumptions. However, note that the values for A , B and C that best fit the results are such that parameter C is null, whereas parameters A and B are similar, which means that to fit the FLAC3D model results with the data, compressive normal stresses of similar magnitudes and null shear stresses must to be introduced in the FLAC model.

Furthermore, the mean orientation (N35°E) for the orientation of the maximum horizontal principal stress measured at a 475 m depth is nearly perpendicular to the direction given by the World Stress Map database (Figure 3.6), which shows that the tectonic stress in this region is approximately orientated NO-SE. This analysis concludes that at depth of the various stress measurements, the existence of a tectonic stress component is not likely.

3.7. Examining rheological effects

The analysis conducted in this last section is based on the linearly elastic behaviour of the rock mass. In reality, the current stress state within a rock mass is the response of the material to a series of past geological events and depends on time. However, time effects are absent from an elastic analysis. In addition, the elastic parameters obtained from tests conducted on intact cores may be unrealistic in a simulation of rock mass behaviours at larger space and time scales because at a large space scale, the rock mass includes an important natural fracture network that may have a time-dependent behaviour. Creep, an important time-dependent effect in rock masses, is characterised by an increase in strain with time, and its influence on *in situ* stress distributions may be assessed by using a visco-elastic model (e.g., the Maxwell model). In this model, the time-dependent elastic modulus $E(t)$ and Poisson's ratio $\nu(t)$ are given by the following equations (Amadei and Stephanson, 1997):

$$E(t) = E_0 e^{-(t/\xi)}, \quad (3.11)$$

$$\nu(t) = 0.5(1 - e^{-(t/\xi)}) + \nu_0 e^{-(t/\xi)}. \quad (3.12)$$

where E_0 and ν_0 are the short-term elastic modulus and Poisson's ratio, respectively; t is the time; and ξ is the relaxation time (time required for an exponential variable to decrease to $1/e$ of its value).

For large amounts of time, the long-term elastic modulus and Poisson's ratio approach zero and 0.5, respectively. Because simulating the transient stress field is not important for interpreting the stresses measured *in situ*, an equivalent linearly elastic material with softer elastic properties (elastic modulus E' and Poisson's ratio ν') than the properties obtained from uniaxial compression tests performed in intact cores is proposed for considering rheological effects (Figure 3.17).

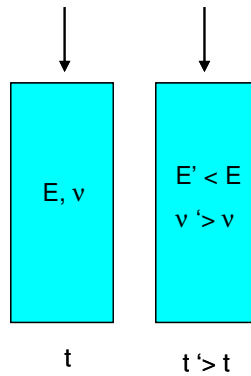


Figure 3.17: Soft linearly elastic material used for considering rheological effects.

Because changing the elastic modulus does not induce changes in the stress field for a homogeneous rock mass, the rheological effects were modelled by increasing the Poisson's ratio value. The FLAC3D model was used in the inversion of the Poisson's ratio value to minimise the misfits defined by equations (3.1) to (3.3). The results presented in Table 3.2 show that a Poisson's ratio value of 0.47 provides a satisfactory fit between the results obtained from both hydraulic and overcoring data and those computed with the model. By setting W to one, equation (3.6) was used to calculate a 90% confidence interval for the minimum of the global misfit. The interval obtained in this way corresponds to a Poisson's ratio value that ranges between 0.45 and 0.49.

Table 3.2: Variation of the misfit value with the Poisson's ratio.

ν	ψ^{HF}	ψ^{OC}	ψ^{HFOC}
0.25	56.7	43.9	295.0
0.35	37.1	38.5	126.3
0.45	13.2	35.3	16.4
0.46	11.8	35.1	13.2
0.47	10.9	34.9	11.5
0.48	12.2	34.3	14.2
0.49	12.6	34.6	14.9

The profiles of the measured and calculated normal stresses (σ_n) due to gravity loading with a 0.47 Poisson's ratio are shown in Figure 3.18.

The difference between the measured and calculated normal stress magnitudes is less than three standard deviations of the measurements in approximately 75% of the tests. In the remaining tests, this difference varies between 1.2 MPa and 1.3 MPa and is considered acceptable given the many simplifying assumptions implied by this model.

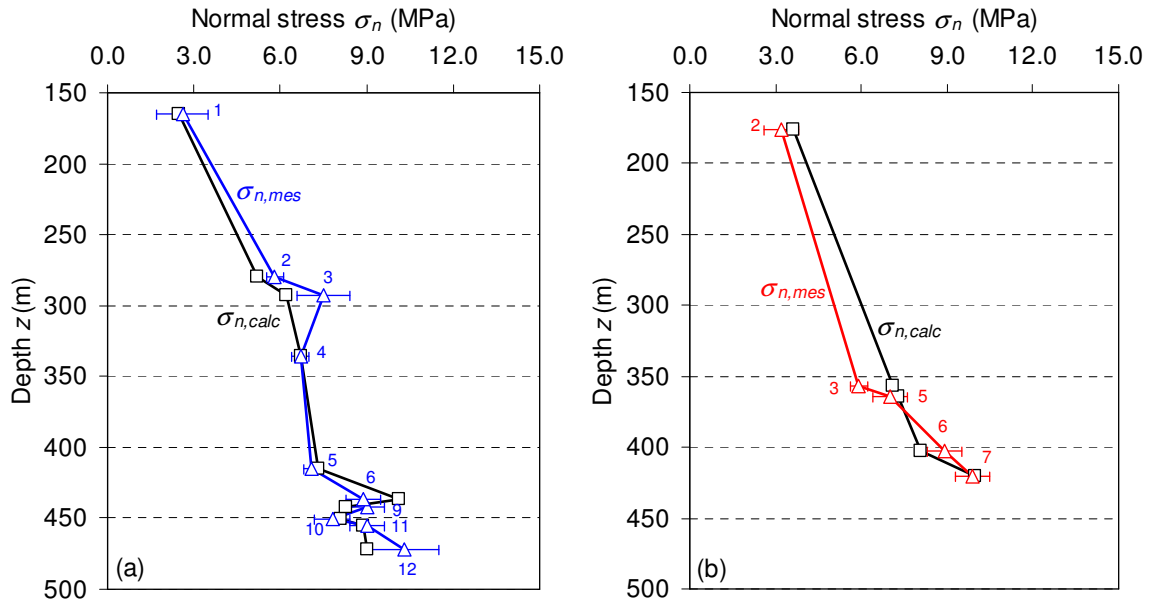


Figure 3.18: Variation with depth of the normal stress magnitudes as measured by hydraulic testing ($\sigma_{n,mes}$) and computed with the FLAC3D model with $\nu=0.47$, considering gravity effects only, in boreholes (a) PD19 and (b) PD23.

A comparison between the principal stress profiles obtained with the linearly elastic model with a Poisson's ratio of 0.47 and those obtained from the inversion of the hydraulic data with an 8-parameter model is shown in Figure 3.19. This comparison shows that at a depth of 500 m, the average differences are 0.3 MPa for the sub-vertical (σ) stress and 1.0 MPa for the minimum horizontal (σ_{II}) principal stress. However, this difference reaches 2.4 MPa for the maximum horizontal stress (σ_I) and is larger than expected. In fact, the 8-parameter model considered in the inversion leads to a wide range of possible stress field solutions that depend on the large implicit uncertainty associated with the hypothesis of uniformity of the stress field. In practice, various heterogeneous zones exist, as demonstrated by the inclined fractures observed for some of the tests.

The measured and calculated stresses at the location of the small flat jack and overcoring tests were compared considering a Poisson's ratio value of 0.47 in the FLAC3D model. This comparison is shown in Figures 3.20 and 3.21 in terms of the normal stress magnitudes for small flat jack tests and principal stress magnitudes for overcoring tests, respectively.

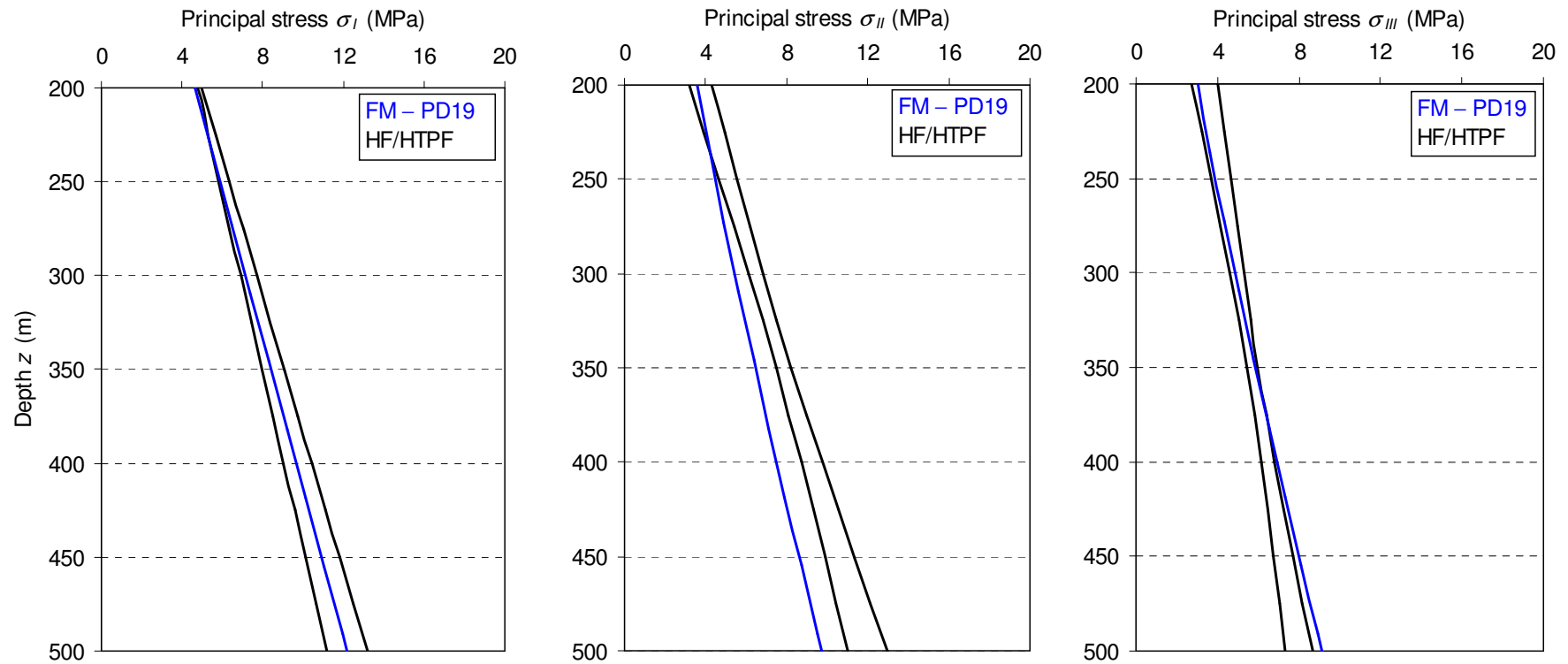


Figure 3.19: Variation with depth of the magnitude of the principal stresses (σ_I , σ_{II} , σ_{III}) obtained from the inversion of the hydraulic data (HF/HTPF) and with the FLAC3D model with $\nu=0.47$ considering gravity effects only.

Figure 3.20 shows that for approximately 55% of the small flat jack tests, the discrepancy between the measured and calculated normal stresses is greater than 1.0 MPa. Figure 3.21 shows that with the exception of the sub-vertical principal stresses (σ) in borehole PD1 between depths of 225 m and 250 m and the two overcoring tests conducted close to the adit and the flat jack tests, approximately 80% of the measured and computed principal stresses are in satisfactory agreement (the difference between both values is less than 1.5 MPa).

Hence, most of the hydraulic and overcoring data can be explained by a linearly elastic massif under a gravitational load provided that the Poisson's ratio for the equivalent material is considerably larger than that considered for the short-term response during uniaxial compression and overcoring tests, which enables to conclude that the large-scale long-term stress field in this granitic massif is controlled by shear stress relaxation along the various fractures and faults that affect this massif.

However, this simple model does not explain most of the small flat jack tests or the two overcoring tests close to the adit. It may be proposed that the equivalent material to be considered near the adit must take into account damages caused by blasting during the construction of the adit. Furthermore, for such a material, plasticity is likely to be considered when analysing the local stress components.

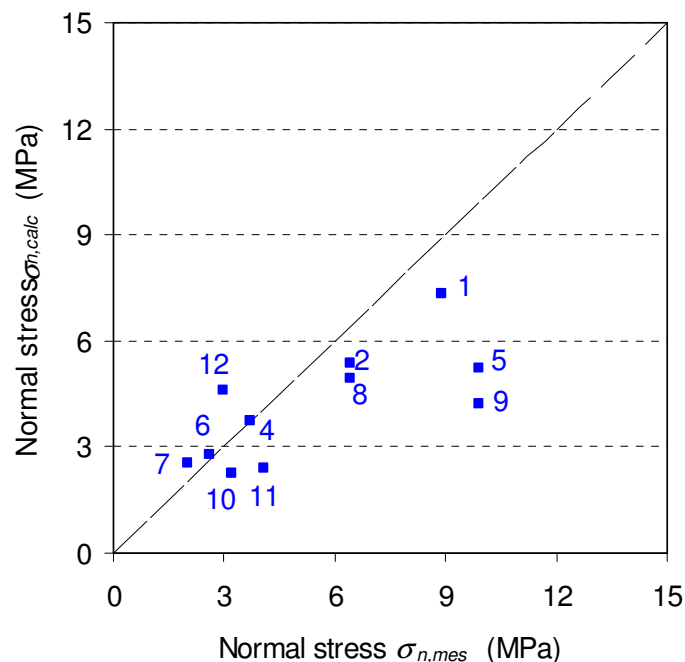


Figure 3.20: Comparison of the magnitudes of the normal stresses obtained by small flat jack technique ($\sigma_{n,mes}$) and with the FLAC3D model ($\sigma_{n,calc}$) with $\nu=0.47$ considering gravity effects only.

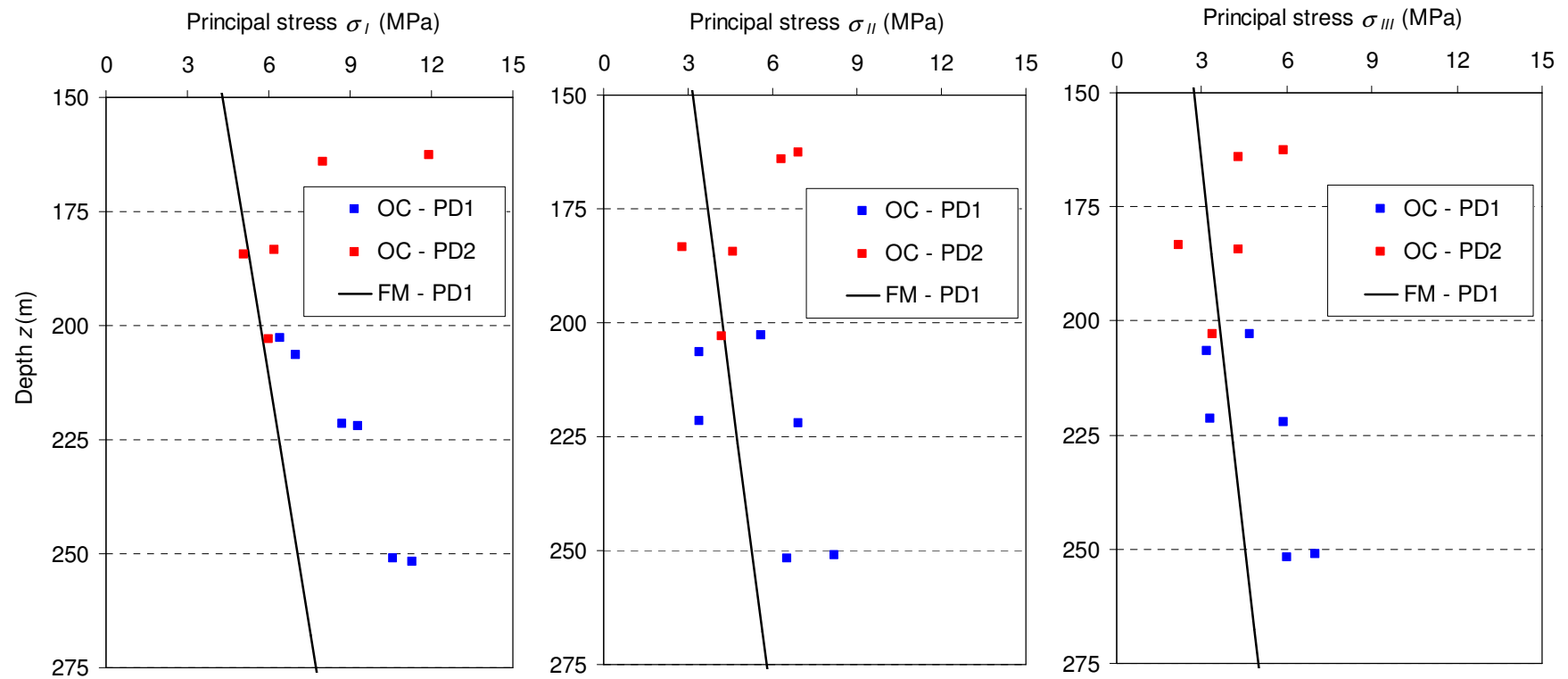


Figure 3.21: Variation with depth of the magnitude of the principal stresses (σ_I , σ_{II} , σ_{III}) obtained by overcoring testing (OC) and with the FLAC3D model (FM) with $\nu=0.47$ considering gravity effects only.

3.8. Design of the hydraulic pressure tunnel

The safe design of the unlined hydraulic pressure tunnel requires the prevention of water leakage by hydraulic opening (hydraulic jacking) in the surrounding rock. Hydraulic jacking can be prevented by positioning the unlined tunnel in competent rock and under enough rock to provide confinement and watertight conditions.

The most used criterion, proposed by Selmer-Olsen (1974) is based on the condition that along its alignment the internal water pressure is always less than the minimum *in situ* principal stress in the surrounding rock mass. Because the stress field is influenced by local heterogeneities (e.g, local fractures and faults), the design of the tunnel should be made in terms of the minimum value for the minimum principal stress magnitude instead of the average value.

In the presented case study, this minimum can be estimated by taking into account the shut-in pressure measured in hydraulic test number 8 conducted in borehole PD19, at 375 m depth below the surface. Indeed, this normal stress measurement is influenced by local heterogeneities (see section 2.4.1.6). The measured normal stress is smaller than the minimum principal stress obtained with the FLAC3D model ($\nu=0.47$) in 0.7 MPa. The trend for the minimum principal stress obtained by considering a null stress value at the ground level and the normal stress measured in this test leads to a 1.0 MPa decrease at 500 m depth below the surface (233 m above the sea level). Since the profile of the hydraulic pressure tunnel is located between 230 m and 672 m above the sea level, a 1 MPa maximum decrease in the minimum principal stress magnitude obtained with the FLAC3D model ($\nu=0.47$) should be considered for the design of the hydraulic pressure tunnel.

3.9. Conclusion

This chapter presented a single linearly elastic model that helps extrapolate the *in situ* results to any point of interest for the design of the hydroelectric scheme. The model considers an equivalent and continuum material, and involves a 15 km² area with a 2.5 km vertical extension, including the location of the *in situ* measurements.

The model was used to calculate the stresses at location of the hydraulic and overcoring data obtained due to gravity and tectonic loadings. The comparison of the stresses obtained in this way with the stresses that would result for a horizontal ground surface, showed how topography effects have a different impact on the stress field at the locations of the overcoring and hydraulic data. Due to gravity loading, at the depth of the

overcoring and hydraulic tests, one principal stress component is sub-vertical and the other two components are sub-horizontal and of similar magnitude. But, for a depth greater than 200 m depth below the surface, in boreholes PD1 and PD2, the magnitudes of the sub-vertical and sub-horizontal principal stresses are greater than the correspondent stress magnitudes in boreholes PD19 and PD23, in 1.5 MPa and 1.0 MPa, respectively.

Several issues have been discussed, such as the influence of the compliance of local fractures and faults, the existence of tectonic stresses and the perturbations associated with the existing adit used for the small flat jack measurements. None of these effects were found to have a significant impact on the stress determined at the locations of the various measurements.

However, the model was found to fit reasonably well approximately 80% of the measurements away from the adit provided that a very high Poisson's ratio (0.47) is considered. This Poisson's ratio value is considerably larger than that measured on the cores, a feature that is attributed to the creeping of the material filling the various fractures and faults that affect the massif.

However, this model does not fit the results from the flat jack and overcoring tests conducted in the immediate vicinity of the adit. For this domain, it seems likely that blasting damages associated with the construction of the adit altered the local material properties such that the simple linearly elastic model is not relevant.

Chapter 4.

Conclusions

4.1. Summary and conclusions

This thesis presented a methodology to integrate various *in situ* stress measurements results provided by different testing techniques at different locations in a mountainous region. The measurements were carried out for the design of an underground reinforcement power scheme that includes a large powerhouse cavern and a hydraulic pressure tunnel. The measurements included hydraulic tests in two 500 m deep vertical boreholes, overcoring tests in two 60 m deep vertical boreholes drilled from an existing adit and small flat jack tests in the walls of the adit.

Some local zones of heterogeneity were encountered, as demonstrated by the appearance of inclined fractures in the electrical imaging logs obtained for two of the hydraulic fracturing tests and by the shut-in pressure measured in one of the tests which was found to be smaller than the expected minimum principal stress in more than three standard deviations of the measurement. Laboratory tests conducted on intact cores showed a significant spatial variability of the rock mass properties and a non-elastic behaviour for low stress levels.

A comparison between the results of the hydraulic and overcoring tests showed that the stresses estimated by both techniques are of similar magnitude. However, the stresses measured in the adit walls using small flat jacks were not consistent with the stresses measured at a similar location by overcoring technique.

The data gathered away from the adit (fifteen normal stress measurements obtained by hydraulic testing and the six components of nine stress tensors determined at the location of the overcoring tests) were integrated in a single model to extrapolate the results of the measurements to a rock mass volume equal to, or larger than, the rock mass volume where the measurements have been conducted. To keep the model simple enough so that constraining data are more numerous than the number of degrees of freedom of the

model, an equivalent and continuum mechanics model was developed using the FLAC3D code that enabled to evaluate the stress field in a region of 15 km², including the location of the *in situ* measurements. This model was used in an inversion scheme to find the regional stress field that fits best the stresses at location of the overcoring and hydraulic data.

The comparison of the stresses obtained with the model with the stresses that would result for a horizontal ground surface, showed how topography effects have an impact on the stress field. The influence of topography effects on the stress field was found to be more significant at the location of the overcoring data. Due to gravity loading, at the location of the overcoring and hydraulic data, one principal stress component is sub-vertical and the other two components are sub-horizontal and of similar magnitude, which is consistent with the results of the *in situ* measurements provided by the two testing techniques. When considering the elastic properties measured on cores, the measured and calculated stresses with the FLAC3D model didn't fit. Actually, the difference between measured and calculated values was much larger than the uncertainties on the measurements, and hence the model was not acceptable.

Several assumptions were made to find the proper model to predict the stresses at the locations of the various *in situ* measurements. Firstly, the horizontal stress components to be introduced in the model to fit the normal stresses measured by hydraulic testing were calculated in order to investigate the possible influence of tectonic stresses. The results of this calculation showed that to fit the FLAC3D model results with the data, compressive normal stresses of similar magnitude and null shear stresses must be considered, which is not consistent with the orientation of the regional tectonic maximum horizontal compressive suggested by the World Stress Map database and with the range of possible solutions for this orientation at 475 m depth below surface that resulted from the inversion of the hydraulic data. Therefore, the existence of tectonic effects in the zone of interest was considered unlikely.

Then, the influence of the compliance of existing large-scale fractured zones on the stresses at location of the hydraulic data was analysed. This analysis was carried out through the consideration of a transversely isotropic model for the fractured zones and the decrease of the elastic modulus values normal to them, thus resulting in a lower stiffness in the corresponding direction. This resulted in a maximum decrease of 1.0 MPa in the magnitude of the sub-horizontal stresses at the location of the hydraulic tests. Thus, this model was found to be unacceptable to describe the regional stress field.

Finally, the rheological effects were examined through the consideration of an equivalent linearly elastic material with softer elastic properties than the properties

obtained from tests conducted on intact cores. This analysis concluded that this model is consistent with 80% of the data gathered away from the adit. This assumes that, in the long-term, shear stresses supported by the various fractures that affect this massif have been nearly completely relaxed. Hence the long-term behavior of this granite massif is found to differ markedly from the short-term behavior considered for interpreting overcoring tests. The rock mass cannot be considered elastic, because the rock mass doesn't resist shear stresses in a long-term perspective, and the magnitudes of the horizontal and vertical components are similar after some time, at a geological scale.

However, when an elastic solution is considered, this model doesn't explain the results of the small flat jack tests nor of the two overcoring tests close to the adit. Hence, the equivalent geomaterial defined for this massif is not representative of the material close to the adit and cannot be used for evaluating the stress field in its vicinity. To explain these data, an elasto-plastic model (e.g. Mohr Coulomb, Hoek Brown) should be considered. By considering a small shear strength associated with the pre-existing fractures close to the adit, a relaxation of the shear stresses occurs and hence the deformations increase.

The stress measurements techniques applied in the case study presented in this thesis have both positive and negative aspects. Indeed, the hydraulic testing technique provides reliable information on the magnitude of the minimum principal stress component, but is found less accurate for the determination of the magnitude and orientation of the maximum horizontal principal stress, which depends on the large implicit uncertainty associated with the hypothesis of uniformity of the stress field. The overcoring method provides a determination of the complete stress tensor at a given point but the stress magnitudes along the borehole axis are found to be larger than expected. The small flat jack technique provides reliable determination of the stress component normal to a given plane but the results are found to be mostly likely influenced by the disturbance caused by the excavation of the adit. However, the integration of *in situ* stress measurements using continuum mechanics modelling provided means to compensate the weak point of one technique by the strong point of the other technique and provided some understanding of the spatial variation of the regional stress field. This in turn was taken in advantage to provide some insight on the loading mechanism at the origin of the measured stresses and on the long-term rheological properties of an equivalent geomaterial, which are difficult to determine from the laboratory and field testing methods due to the time scale involved.

4.2. New contributions

The main original contributions of this thesis are the following:

- to propose an equivalent linearly elastic material with softer elastic properties than the properties obtained from tests performed in intact cores;
- to combine the hydraulic and overcoring data with the FLAC3D model in an inversion scheme to determine the regional stress field that fits best both data;
- to compare the *in situ* test results provided by overcoring and flat jack methods in the vicinity of an existing adit; and
- to use stress field information to ascertain the long-term rheological properties of an equivalent geomaterial that explain the obtained data.

4.3. Recommendations

The determination of the regional stress field in rock masses is an area still wide open to new work and innovation. The future developments of the work are grouped in two parts: uncertainty reduction in the *in situ* stress measurements and integration of data with numerical modelling.

Regarding the uncertainty reduction in the *in situ* stress measurements, it is proposed:

- to evaluate the explicit uncertainties of the overcoring technique by performing a large number of overcoring tests per borehole;
- to study the influence of the glue hardening process prior to overcoring through laboratory testing under known tri-axial stress states;
- to study the influence of temperature changes associated with the overcoring process in the test results, by laboratory tests and numerical modelling;
- to study properly the mechanism that sometimes leads to stresses higher than expected in the borehole axis direction in the overcoring method;
- to use complementary acoustic and electrical images obtained before and after the hydraulic tests to reduce the explicit uncertainty associated with the fracture orientations determination; and
- to compare the results of the overcoring and hydraulic tests done in the same location, in future *in situ* testing programmes.

Regarding the integration of data with numerical modelling, it is proposed:

- to combine elastic models used to explain the stress measurements data at the far-field with more complex rheological models to explain the data close to excavations;
- to develop numerical models that take into account the non-elastic behaviour of the rock mass;
- to consider the spatial variability of the rock mass properties from a statistical point of view, and its influence on the stress field;
- to evaluate the uncertainties on the stress field obtained with numerical models, by taking into account the uncertainties associated with the choice of the model, rock mass elastic properties and boundary conditions;
- to determine weights to integrate various *in situ* tests results provided by different testing techniques using numerical modelling, depending on the nature and number of tests performed by each testing technique, and the tested rock mass volume; and

List of references

- Aamodt, R.L. and Kuriyagawa, M., 1983. Measurement of instantaneous shut-in pressure in crystalline rock. In: Zoback, M.D., Haimson, B., editors. Hydraulic fracturing stress measurements. Washington, DC: National Academy Press: p. 139–42.
- Amadei, B. and Stephansson, O., 1997. Rock stress and its measurements, Chapman and Hall Publ., London.
- Ask, D., 2004. New Developments of the Integrated Stress Determination Method and Application to the Aspo Hard Rock Laboratory, Sweden. PhD Thesis, Royal Institute of Technology, Stockholm.
- Cornet, F.H., 1993. The HTPF and the Integrated Stress Determination Methods. *Comprehensive Rock Engineering*, 3, (J. Hudson, Ed.). Pergamon Press, Oxford: p. 413–32.
- Cornet, F.H., 1996. A complete 3D stress determination for the design of an underground power station. Proceedings of the 2nd North American Rock Mechanics Symposium, NARMS'96 (Eds. Aubertin, M., Hassani, F., Mitri, H.), Montréal, Canada, A.A. Balkema Publ., Rotterdam; p. 755–61.
- Cornet, F.H., Doan, M.L. and Fontbonne, F., 2003. Electrical imaging and hydraulic testing for a complete stress determination. *International Journal of Rock Mechanics and Mining Sciences*, 40: p. 1225–41.
- Cornet, F.H. and Valette, B., 1984. *In situ* stress determination from hydraulic injection test data. *Journal of Geophysical Research*, 89: p. 11527–37.
- Cornet F.H. and Yin J.M., 1995. Analysis of induced seismicity for stress determination and pore pressure mapping. *Pageoph*, 145, p. 677–700.
- Figueiredo, B., Cornet F.H., Lamas, L. and Muralha J., 2012. Effect of topography on distribution of *in situ* stresses due to gravity and tectonic loadings at Paradela site. Proceedings of the EUROCK 2012 – Rock Engineering and Technology for Sustainable Underground Construction, Stockholm.
- Gephart, W. and Forsyth, W., 1984. An improved method for determining the regional stress tensor using earthquake focal mechanism data: application to the San Fernando Earthquake Sequence. *Journal of Geophysical Research*, 89: p. 9305–20.

- Gioda, G. and Sakurai, S., 1987. Back analysis procedures for the interpretation of field measurements in geomechanics. *International Journal of Numerical and Analytical Methods in Geomechanics*, 16: p. 555–83.
- Habib, P. and Marchand, R., 1952. Mesures des pressions de terrains par l'essai de verin plat. *Annales de l'Institut Technique du Bâtiment et des Travaux Publics, Série Sols et Foundations*, 58: p. 966–71.
- Haimson, B.C. and Cornet, F.H., 2003. ISRM Suggested Methods for rock stress estimation – Part 3: Hydraulic fracturing (HF) and/or hydraulic testing of pre-existing fractures (HTPF). *International Journal of Rock Mechanics and Mining Sciences*, 40: p. 1011–20.
- Hart, R., 2003. Enhancing rock stress understanding through numerical analysis. *International Journal of Rock Mechanics and Mining Sciences*, 40: p. 1089–97.
- Hayashi, K. and Haimson, B.C., 1991. Characteristics of *shut in* curves in hydraulic fracturing stress measurements and the determination of the *in situ* minimum compressive stress. *Journal of Geophysical Research*, 96 (B11): p. 18311–21.
- Heidbach, O., Tingay, M., Barth, A., Reinecker, J., Kurfeß, D. and Müller, B., 2008. The release of the World Stress Map (available online at www.world-stress-map.org).
- Itasca, 2009. FLAC3D, Version 4.0, User's Manual. Itasca Consulting Group, Minneapolis, USA.
- Lamas, L., Muralha, J. and Figueiredo, B., 2010. Application of a global interpretation model for assessment of the stress field for engineering purposes. Proceedings of the 5th International Symposium on In-Situ Rock Stress, Beijing.
- Li, G., Mizuta, Y., Ishida, T., Li, H., Nakama, S. and Sato, T., 2009. Stress field determination from local stress measurements by numerical modelling. *International Journal of Rock Mechanics and Mining Sciences*, 46: p. 138–47.
- Ljunggren, C., Chang, Y., Janson, T. and Christiansson, R., 2003. An overview of rock stress measurement methods. *International Journal of Rock Mechanics and Mining Sciences*, 40: p. 975–989.
- Matsuki, K., Nakama, S. and Sato, T., 2009. Estimation of regional stress by FEM for a heterogeneous rock mass with a large fault. *International Journal of Rock Mechanics and Mining Sciences*, 46: p. 31–50.

- McKinnon, S.D. 2001. Analysis of stress measurements using a numerical model methodology. *International Journal of Rock Mechanics and Mining Sciences*, 38: p. 699–709.
- Mosnier, J., 1982. Detection électrique des fractures naturelles ou artificielles dans un forage. *Annals of Geophysics*, 38: p. 37–40.
- Mosnier, J. and Cornet, F.H., 1989. Apparatus to provide an image of the wall of a borehole during a hydraulic fracturing experiment. In: Louwrier K, Staroste E, Garnish JD, Karkoulias V, editors. Fourth International Seminar on the Results of EC Geothermal Energy Research and Demonstration, Proceedings, Dordrecht: Commission of the European Communities, Kluwer Academic Publishers: p. 205–12.
- Muralha, J., Lamas, L. and Esteves, C., 2009. State of stress assessment for the Picote II underground powerhouse design. Proceedings of the International Symposium on Rock Mechanics - SINOROCK2009, Hong Kong.
- Parker, R.L. and McNutt, M.K., 1980. Statistics for one-norm misfit measure. *Journal of Geophysical Research*, 85: p. 4429–30.
- Pinto J.L. and Cunha A.P., 1986. Rock stresses determinations with the STT and SFJ techniques. *In Rock Stress and Rock Stress Measurements*, Lulea.
- Rocha, M., Lopes, B. and Silva, N. 1966. A new technique for applying the method of flat jack in the determination of stresses inside rock masses. Proceedings of the 7th International Congress on Rock Mechanics, 2: p. 57–65.
- Rocha, M. and Silvério, A., 1969. A new method for the complete determination of the state of stress in rock masses. *Géotechnique*, 19 (1): p. 116–32.
- Savage, W.Z., Swolfs, H.S. and Powers, P.S., 1985. Gravitational stresses in long symmetric ridges and valleys. *International Journal of Rock Mechanics and Mining Sciences and Geomechanics Abstracts*, 22: p. 291–302.
- Schmitt, D.R. and Zoback, M.D., 1989. Poroelastic effects in the determination of the maximum horizontal principal stress in hydraulic fracturing tests—a proposed breakdown equation employing a modified effective stress relation for tensile failure. *International Journal of Rock Mechanics and Mining Sciences and Geomechanics Abstracts*, 26: p. 499–506.
- Selmer-Olsen, R., 1974. Underground openings filled with high pressure water or air. *Bulletin of the International Association of Engineering Geology*, 9: pp. 91–5.

- Sjoberg, J. and Klasson, H., 2003. Stress measurement in deep boreholes using the Borre (SSPB) probe. *International Journal of Rock Mechanics and Mining Sciences*, 40: pp 1205 – 1223.
- Sousa, L.R., Martins, C.S. and Lamas, L.N., 1986. Development of the techniques of measurement and the interpretation of the state of stress in rock masses. Application of the Castelo do Bode tunnel. Proceeding of the 5th International Congress on IAEG. Buenos Aires.
- Souza Martins, C., 1986. Contribution for the study of underground works associated with hydroelectric schemes (in Portuguese). LNEC's internal report 24/86.
- Tarantola, A. and Valette, B., 1982. Generalized non-linear inverse problem solved using the least square criterion. *Reviews of Geophysics and Space Physics*, 20: p. 219–32.
- Tonon, F., Amadei, B., Pan, E. and Frangopol, D.M., 2001. Bayesian estimation of rock mass boundary conditions with applications to the AECL underground research laboratory. *International Journal of Rock Mechanics and Mining Sciences*, 38: p. 995–1027.
- Yin, J.M. and Cornet, F.H., 1994. Integrated stress determination by joint inversion of hydraulic tests and focal mechanisms. *Geophysical Research Letters*, 21: p. 2645–48.
- Zemanek, J. 1969. The borehole televiewer – a new logging concept for fracture location and other types of borehole inspection. *Journal of Petroleum Technology*: p. 219–32.

APPENDIX A

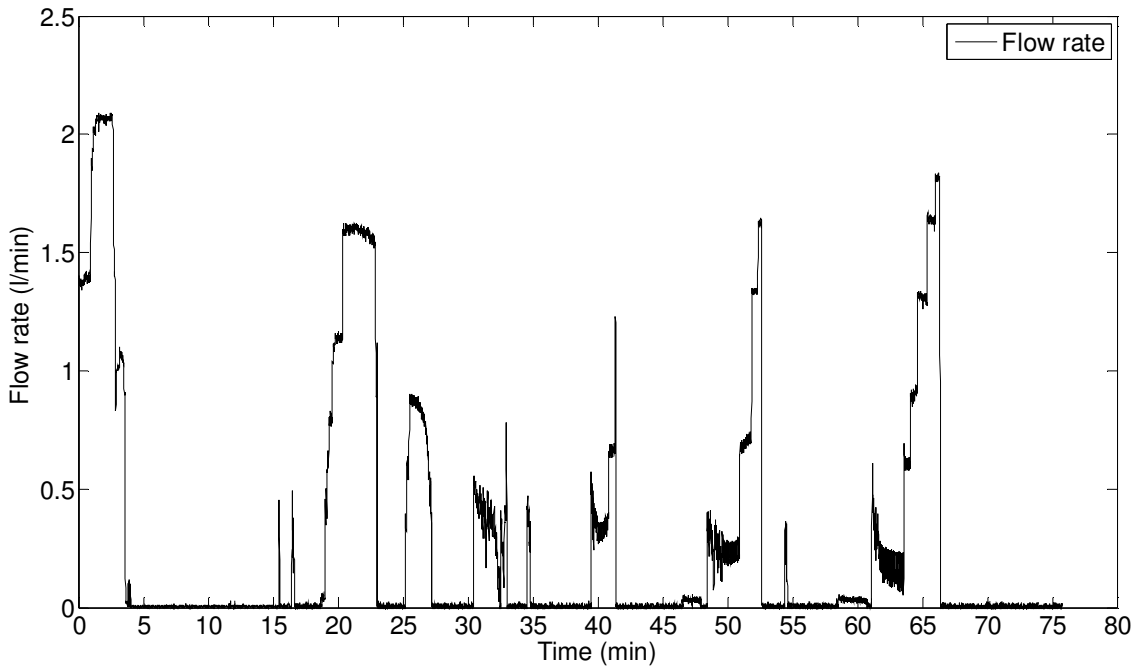
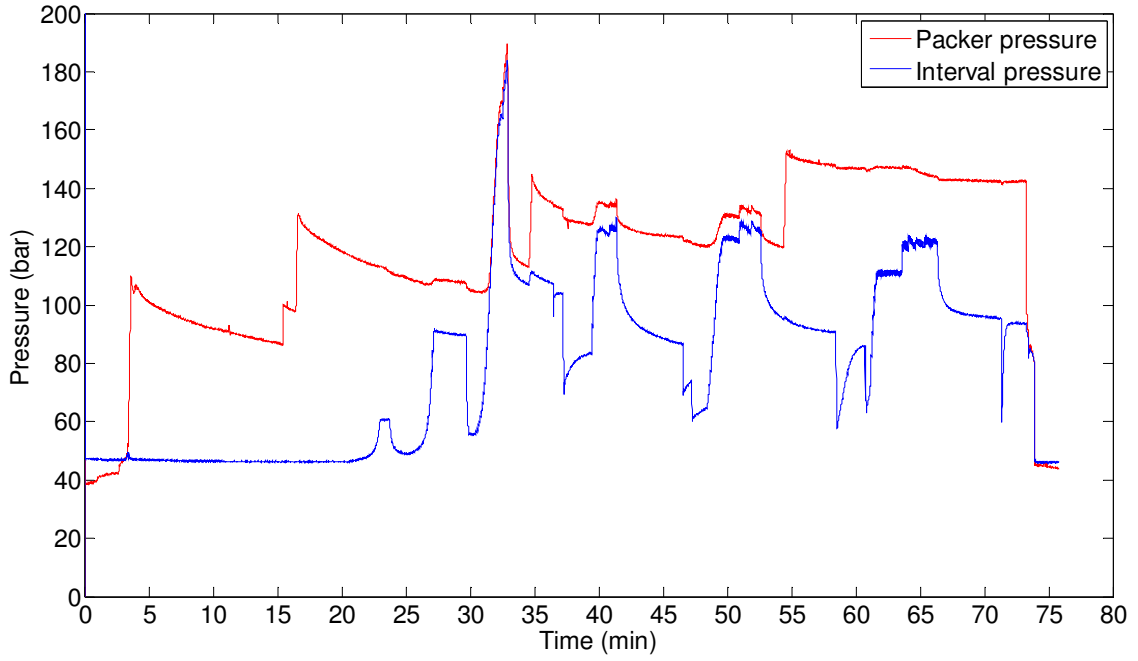
Hydraulic test results

APPENDIX A1

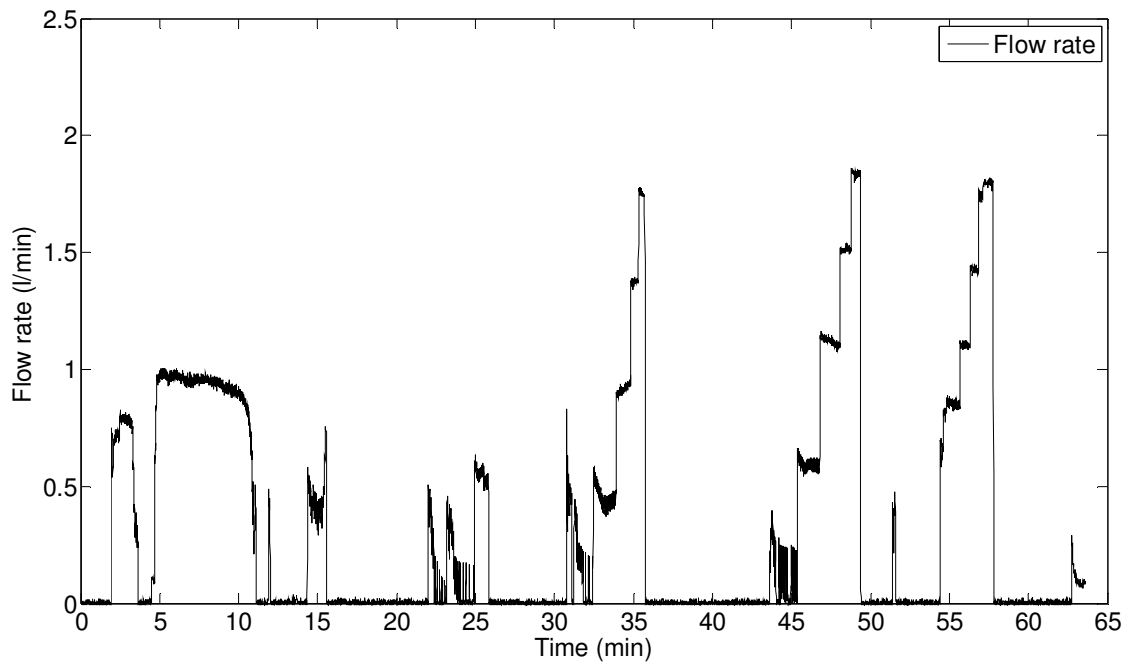
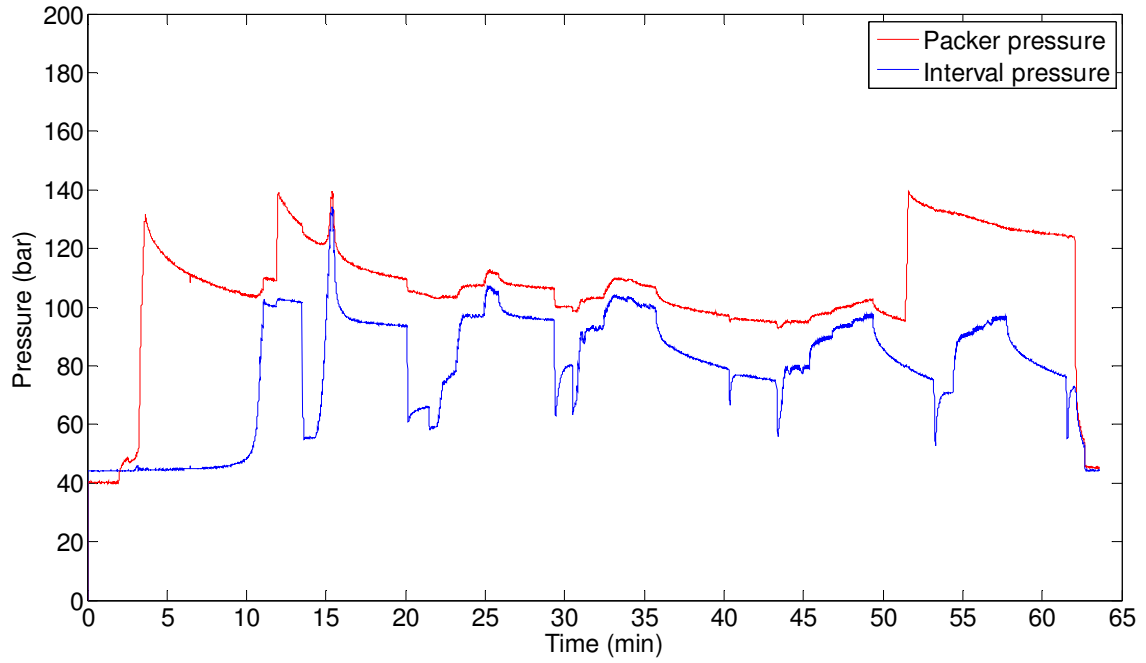
Raw pressure and flow rate data

Borehole PD19

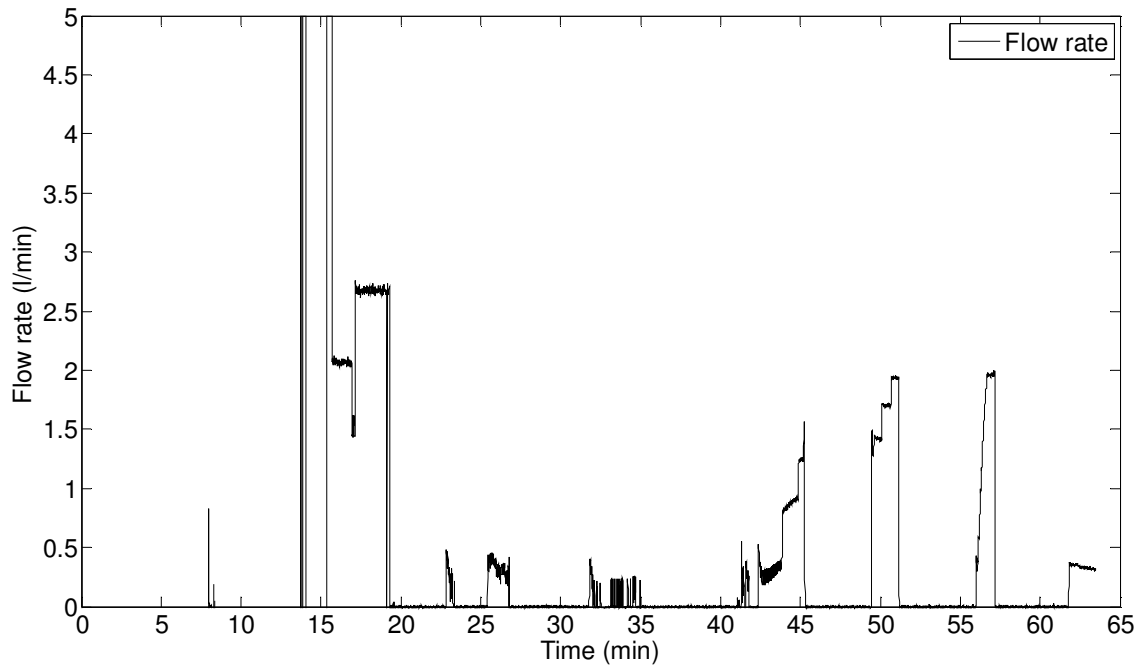
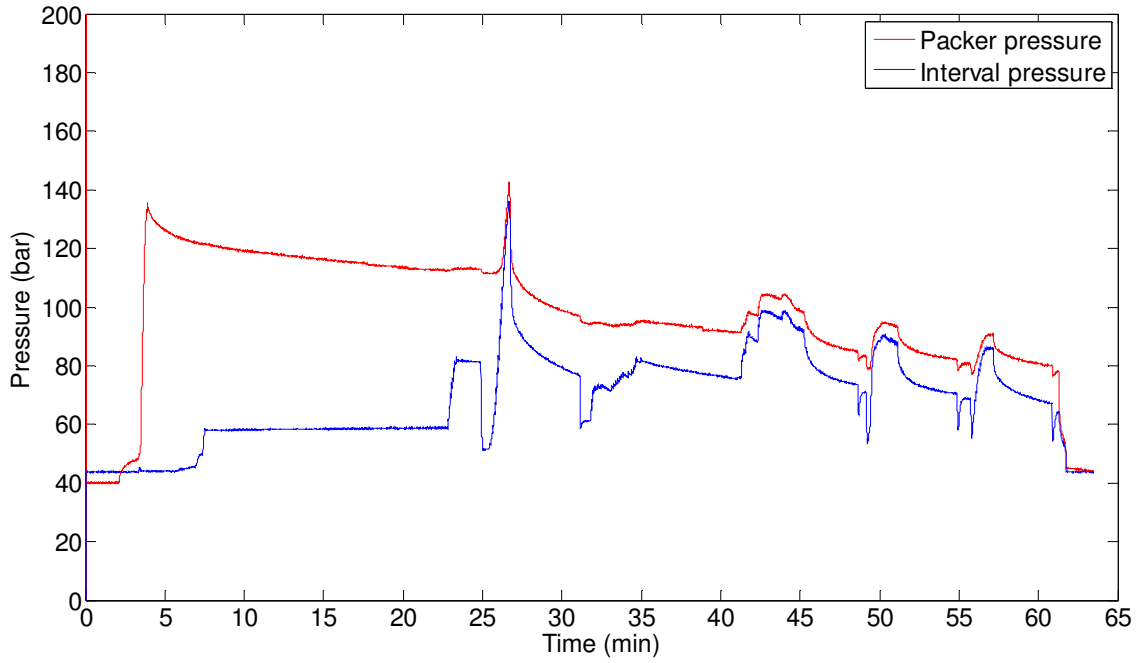
Test 1



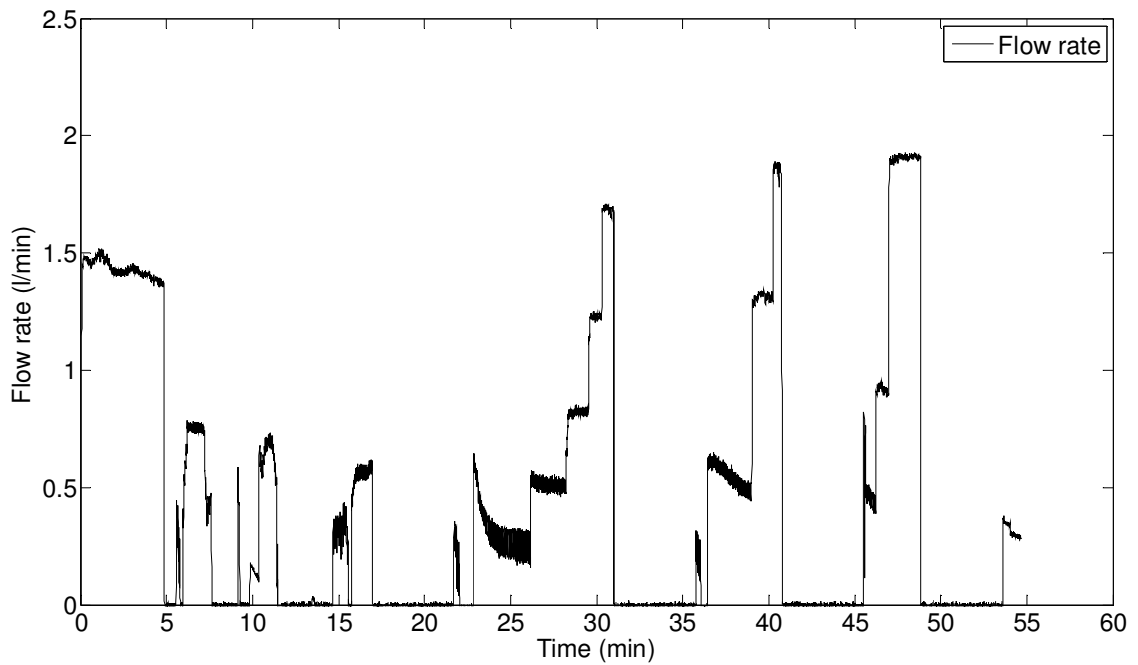
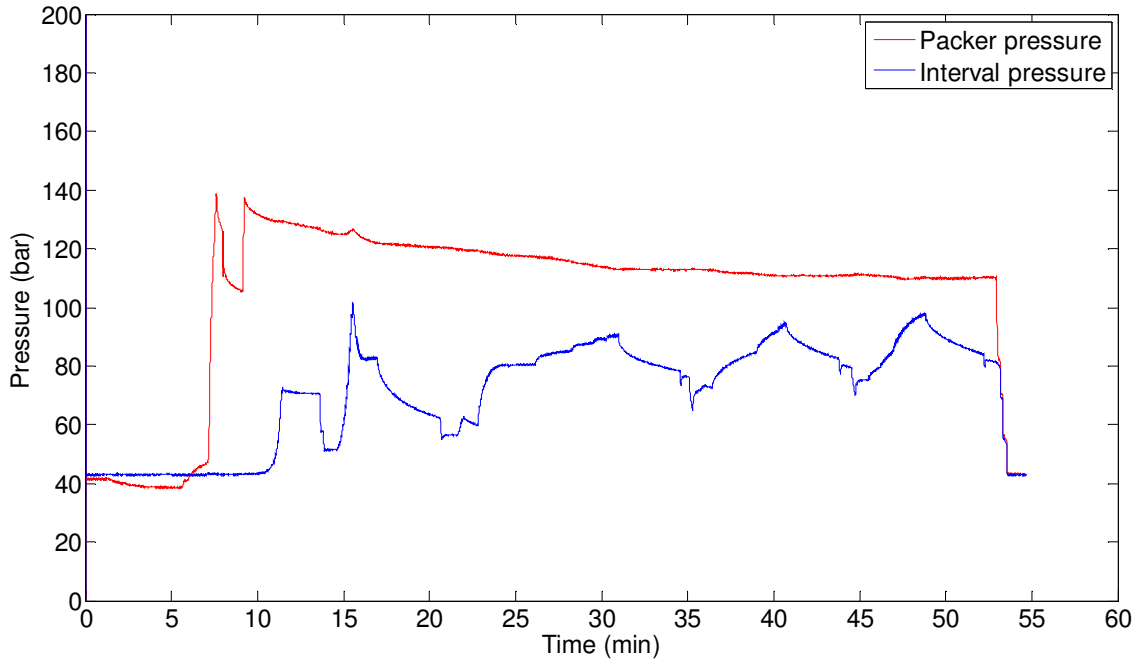
Test 2



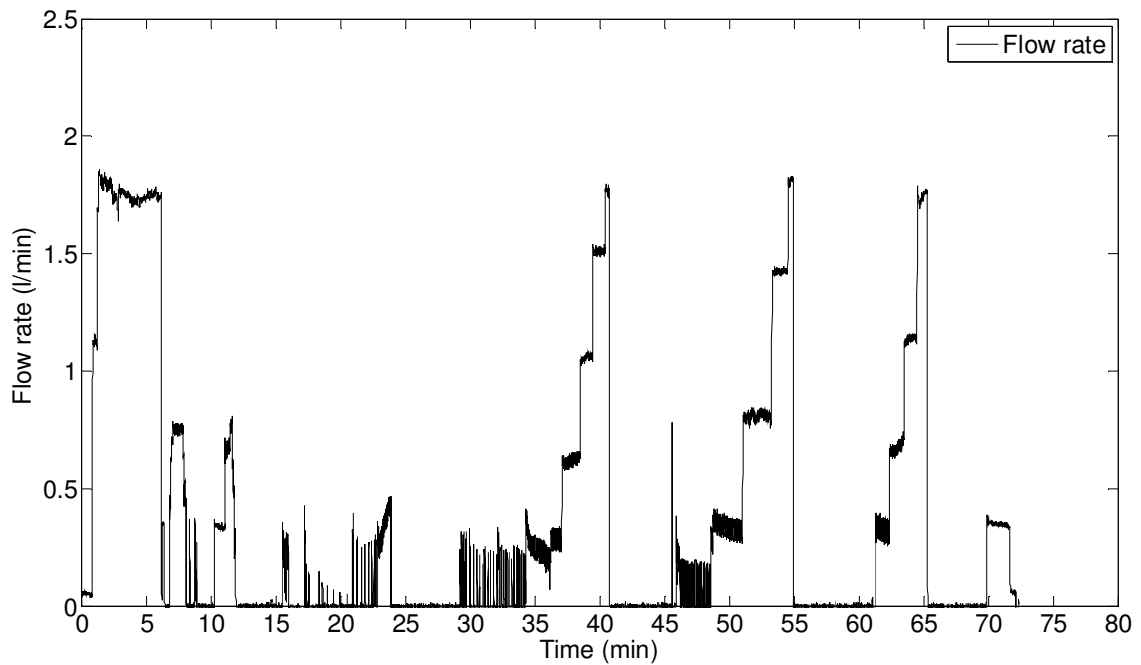
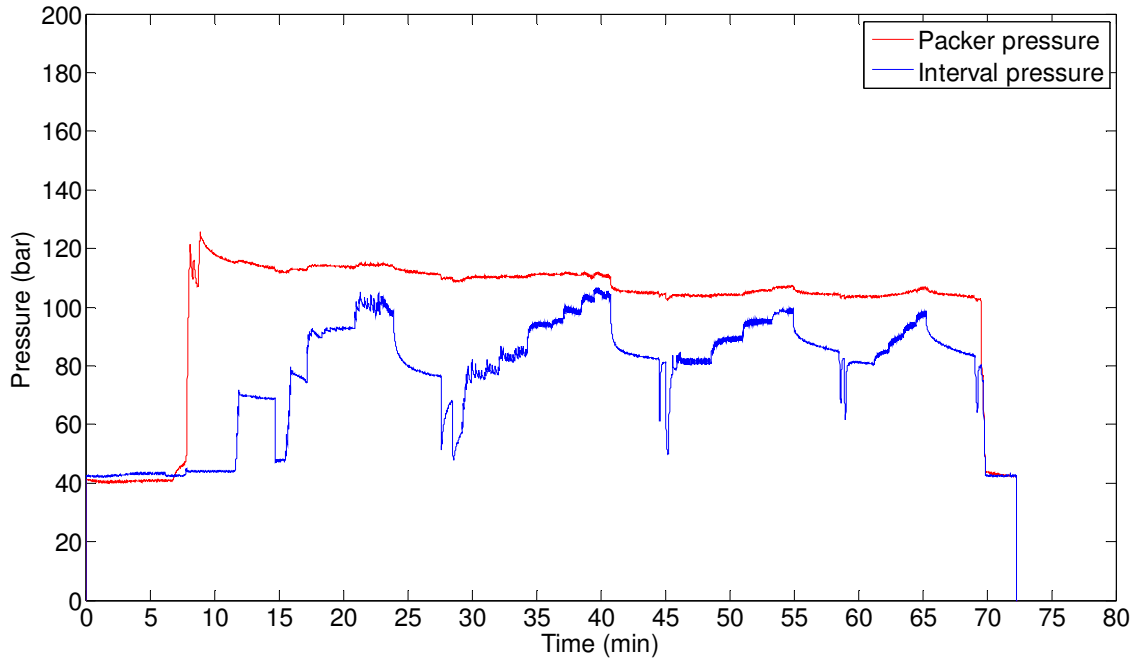
Test 3



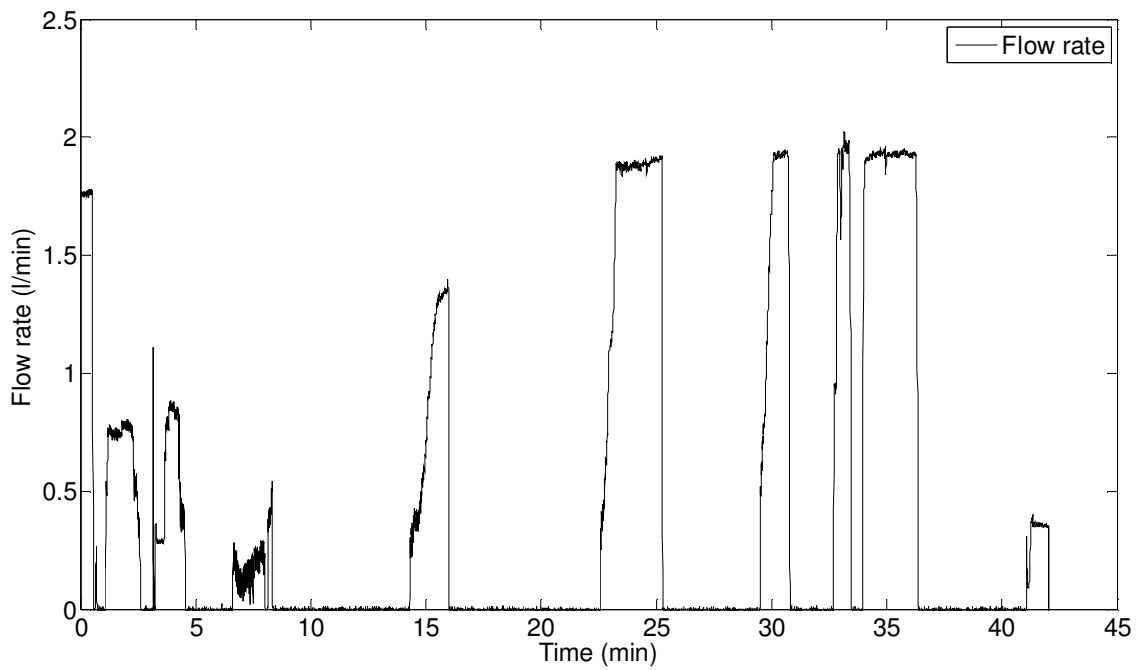
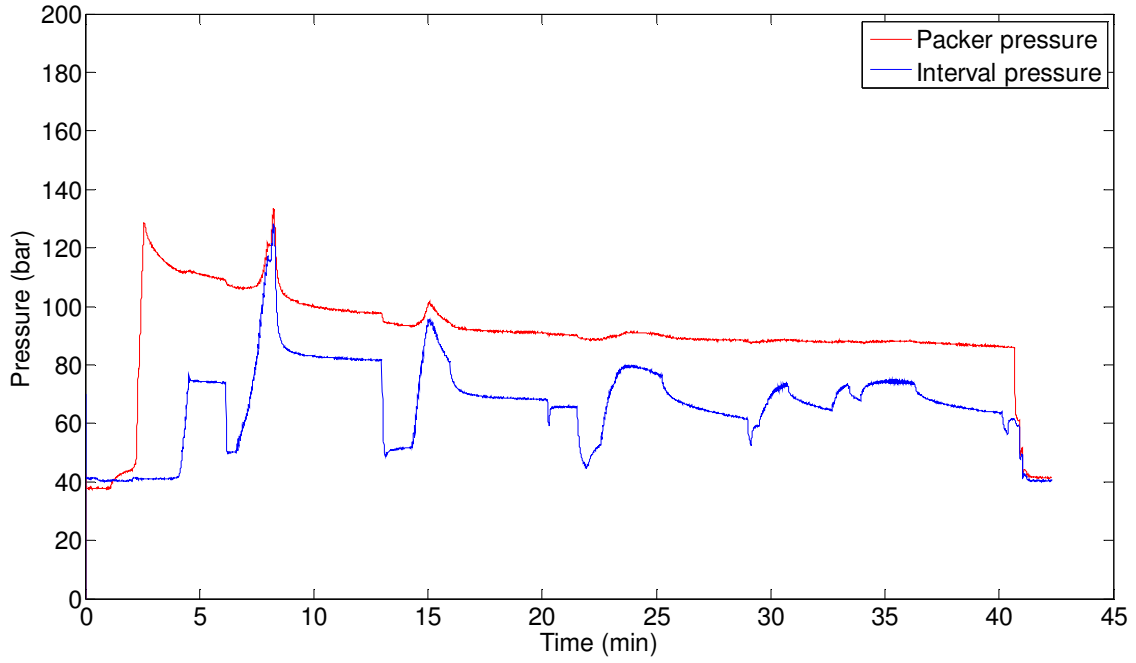
Test 4



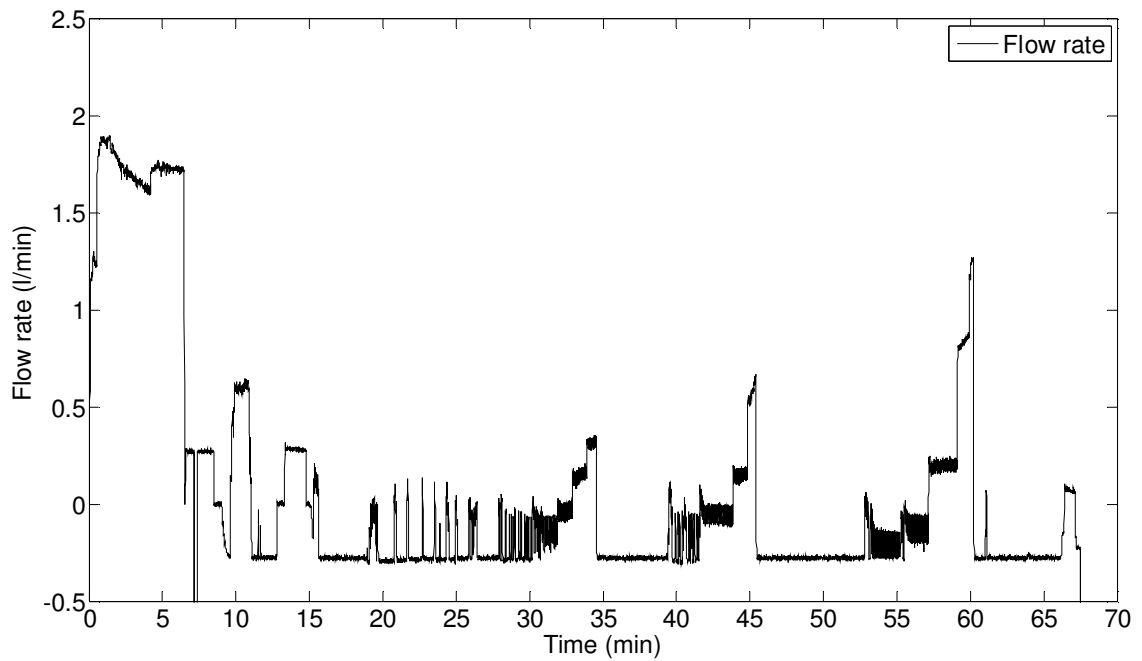
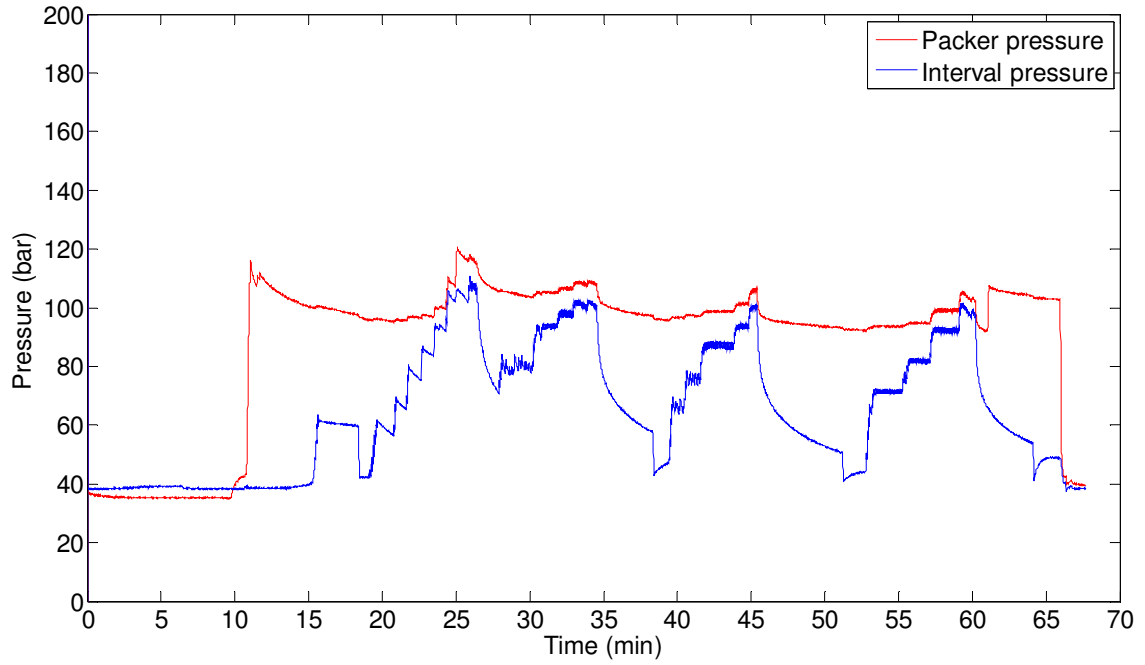
Test 5



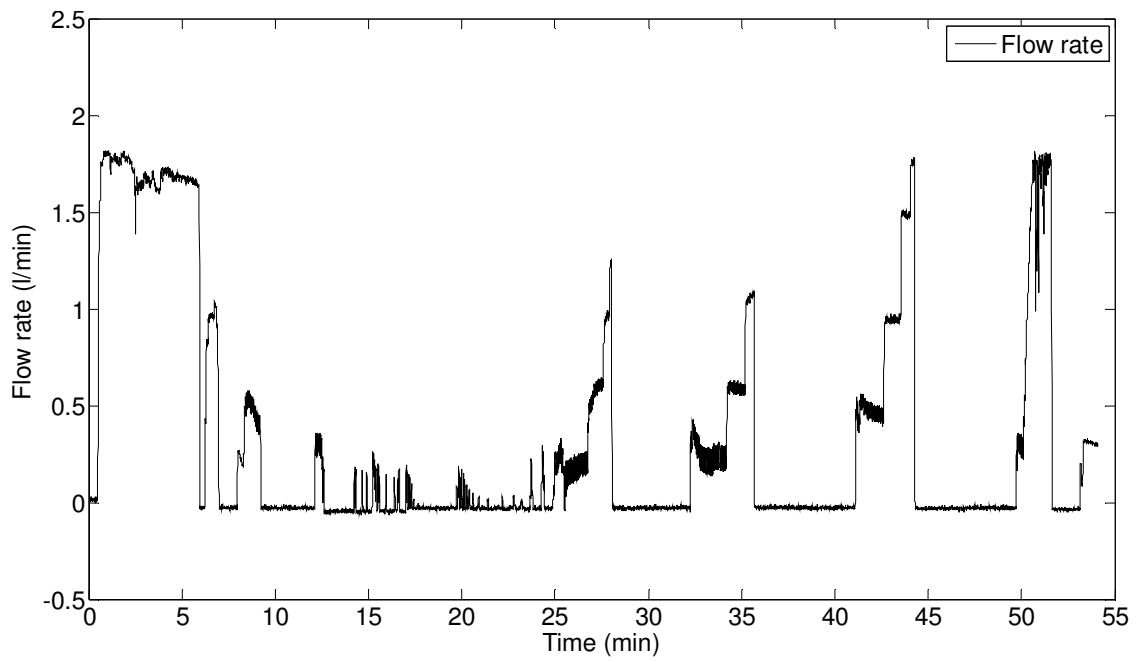
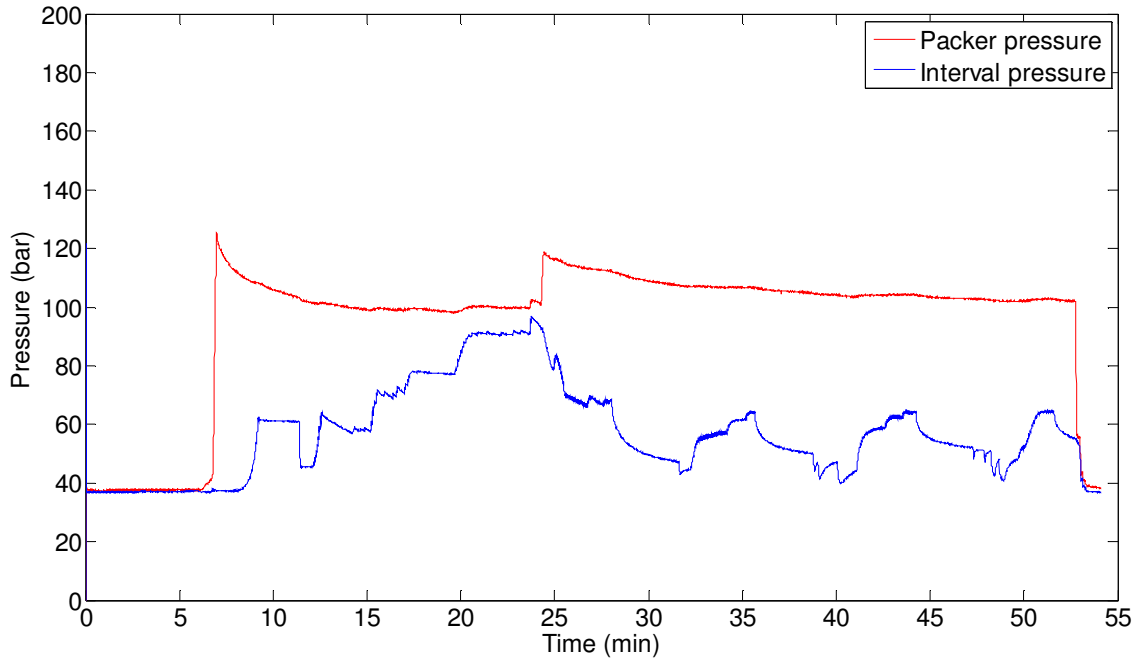
Test 6



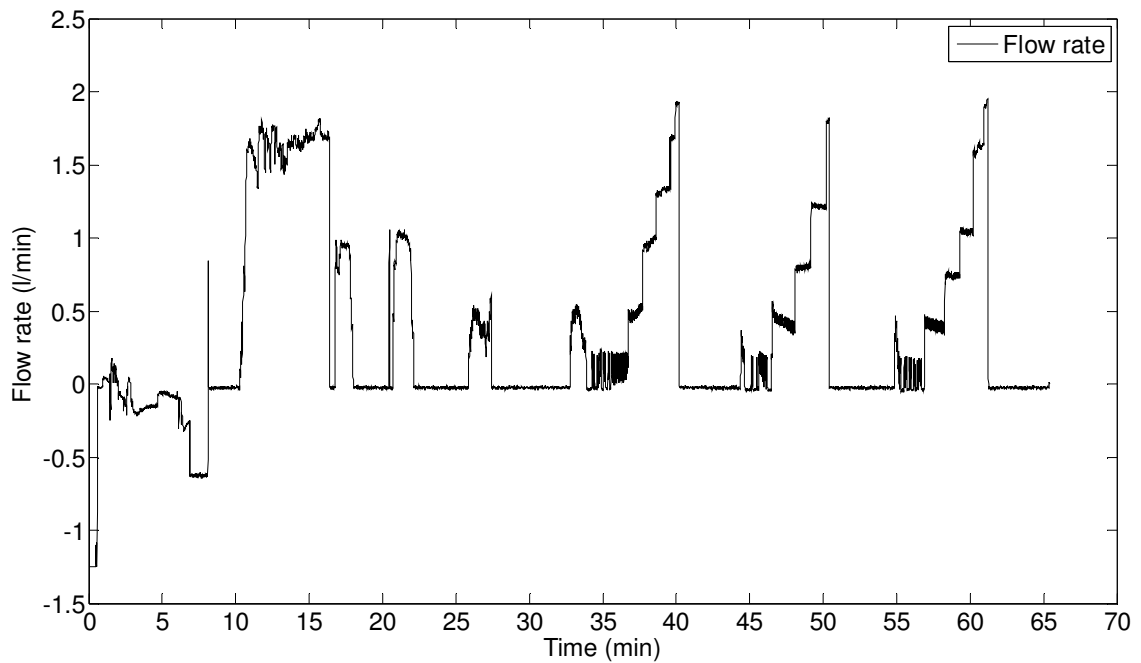
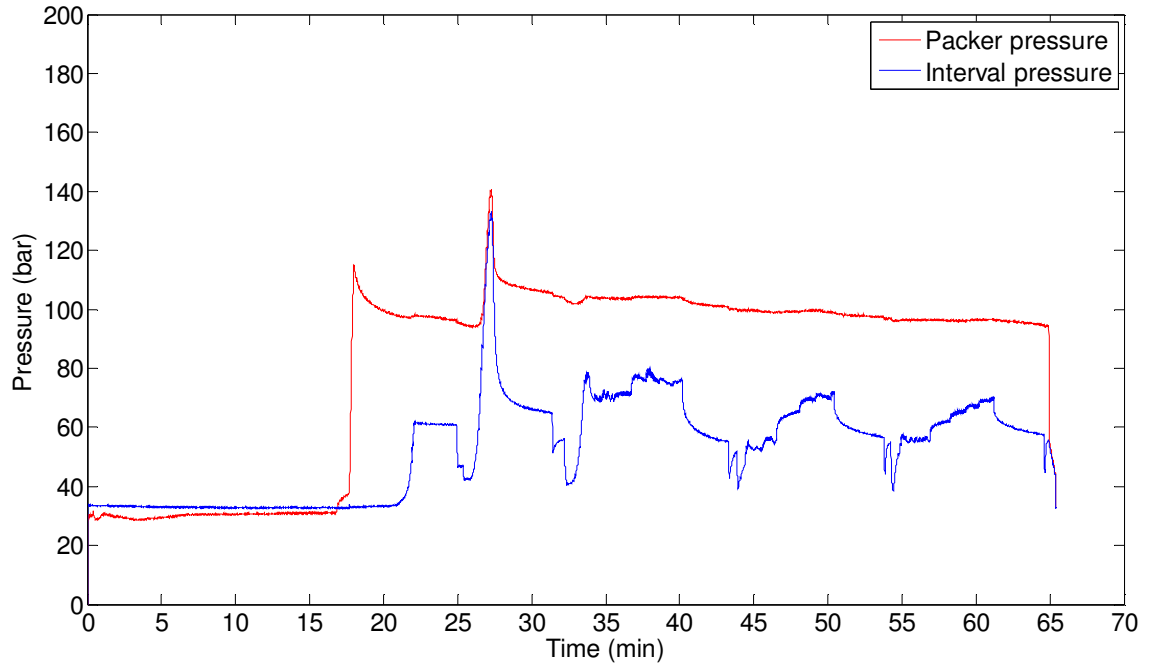
Test 7



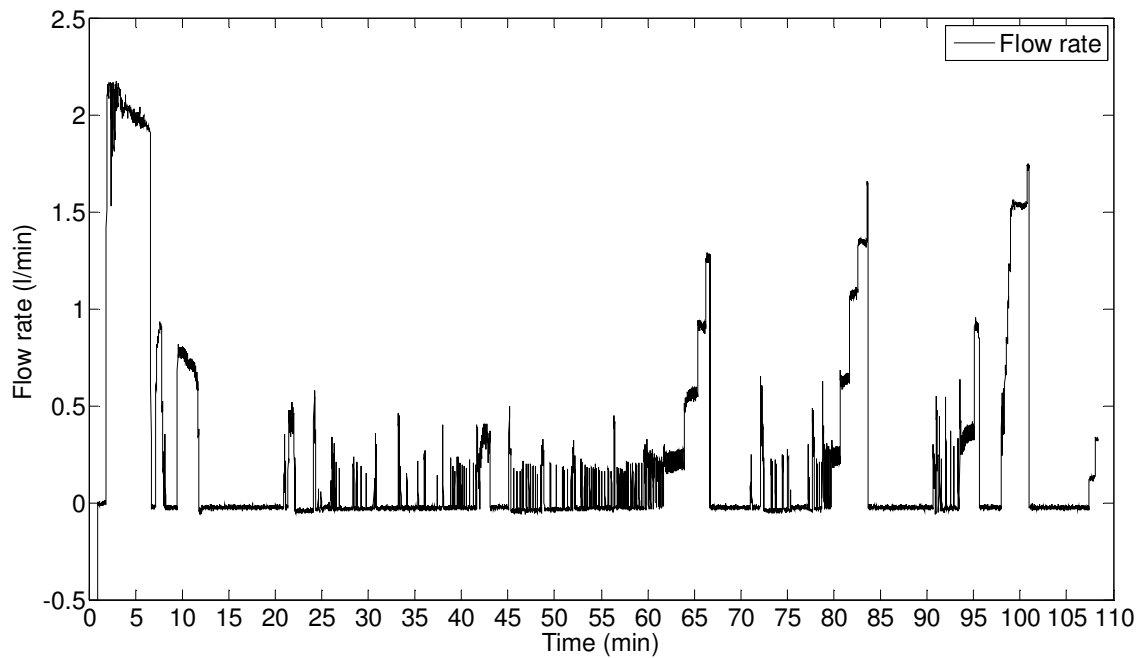
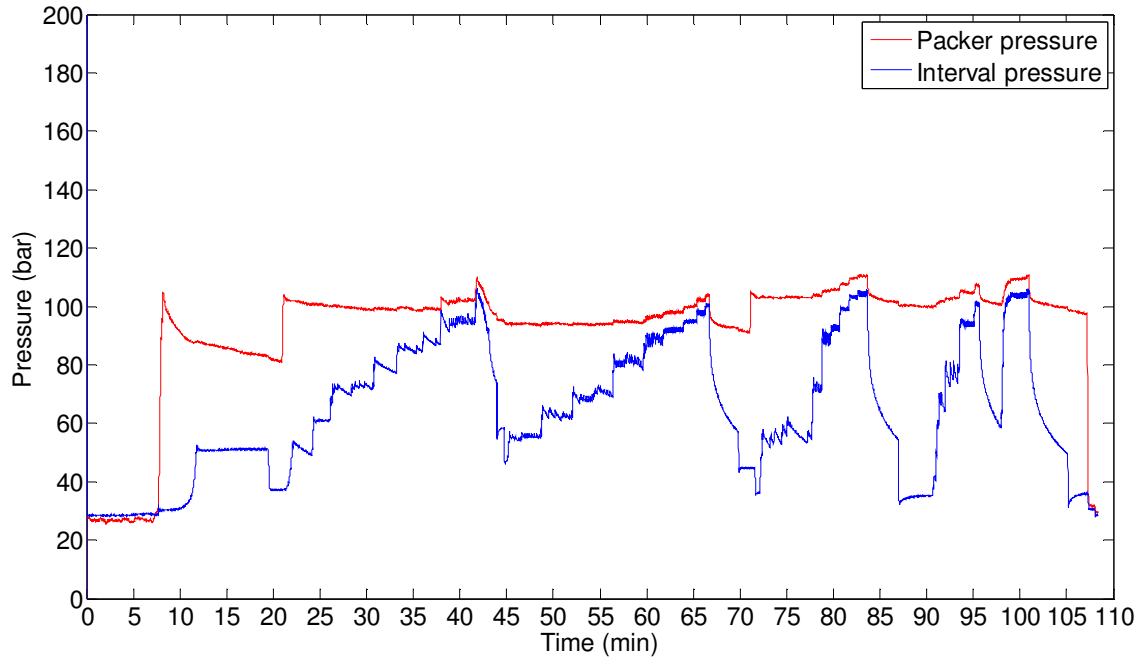
Test 8



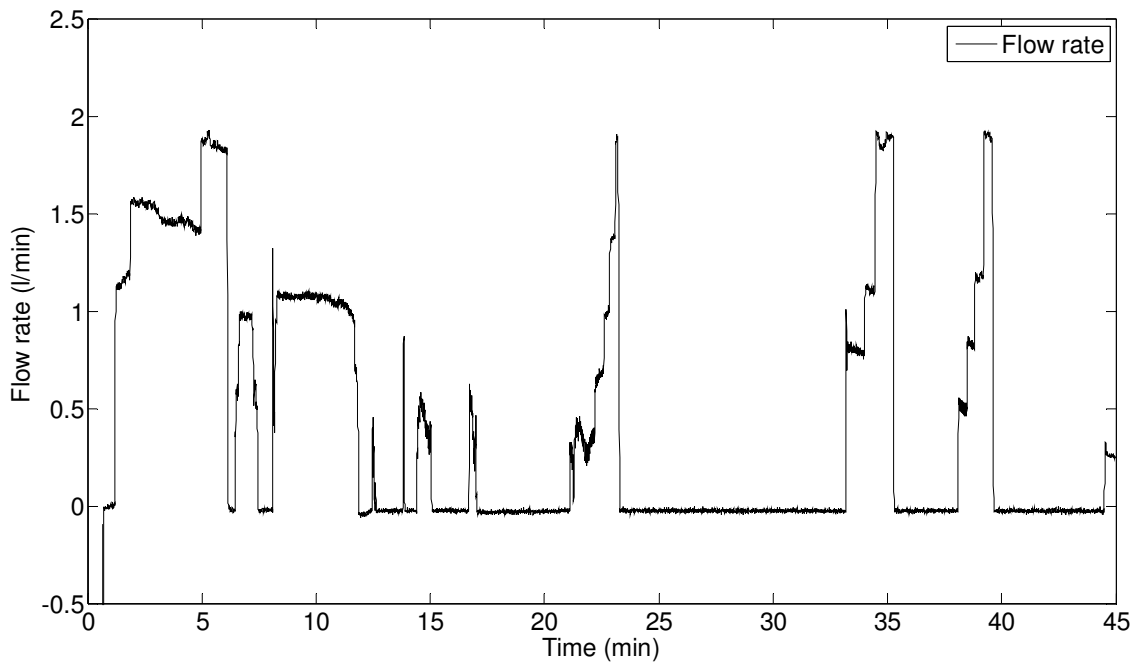
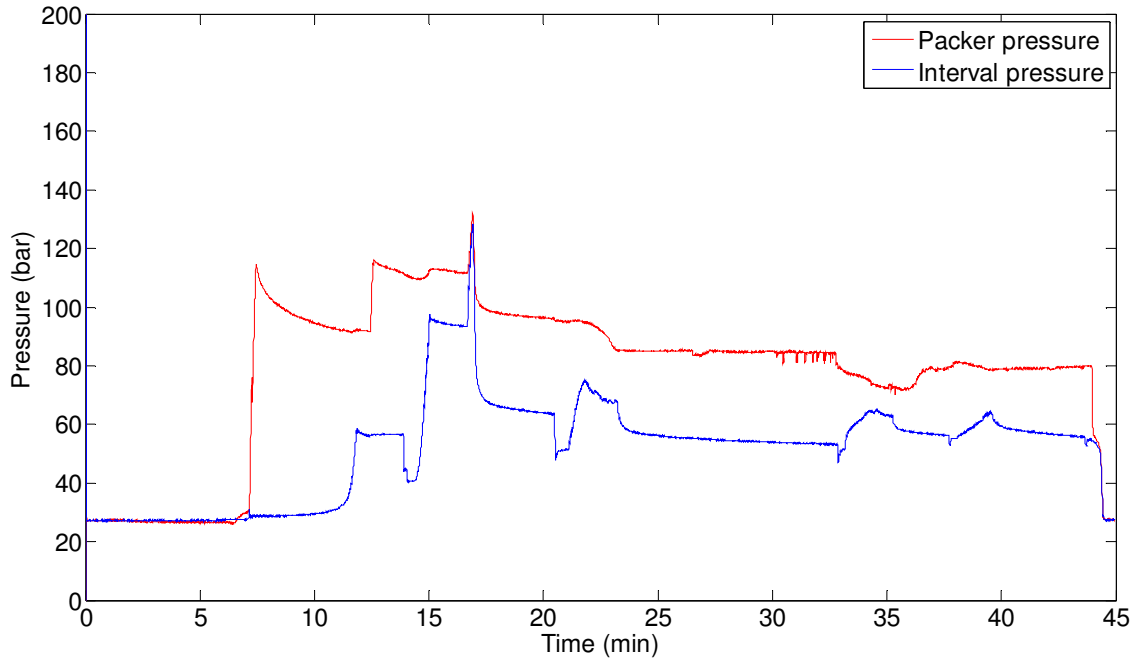
Test 9



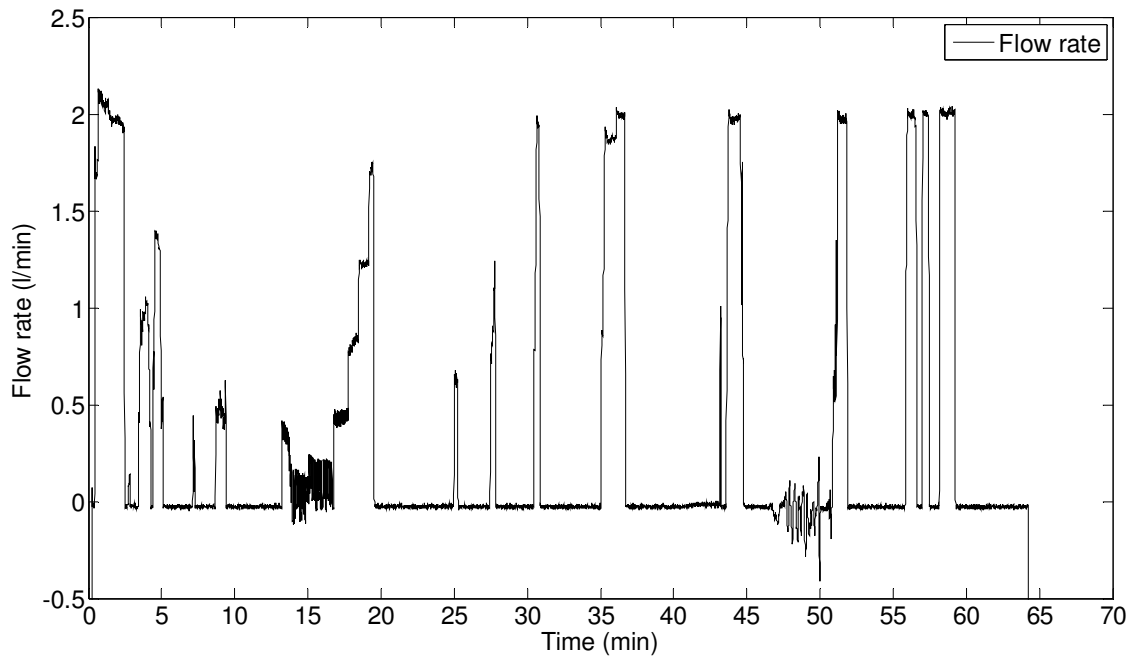
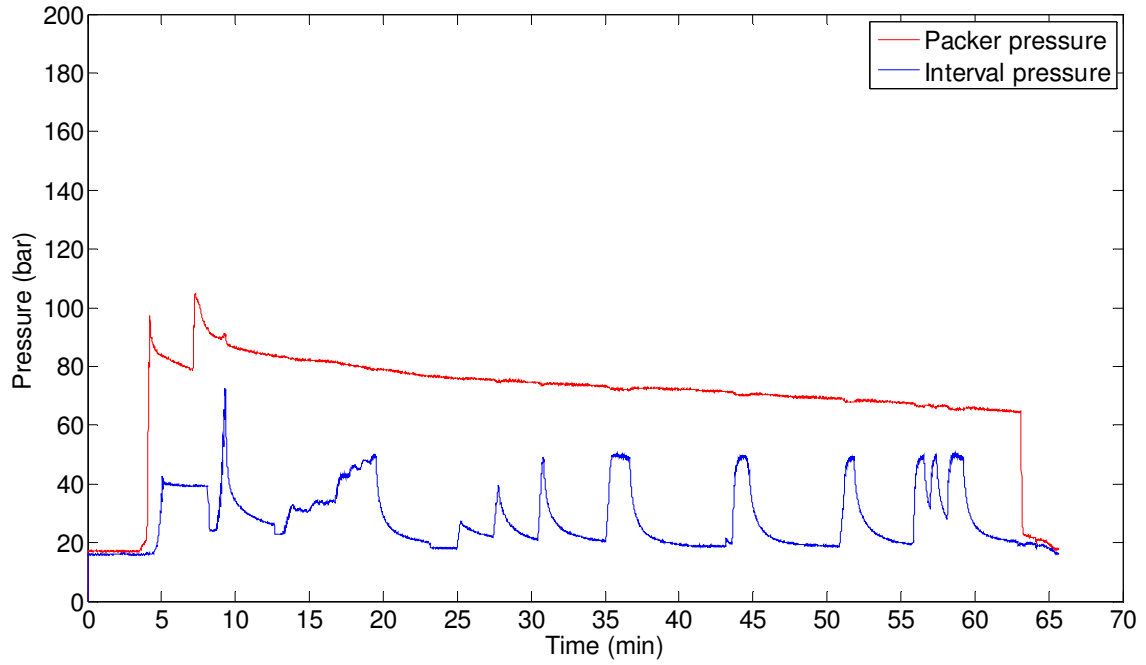
Test 10



Test 11

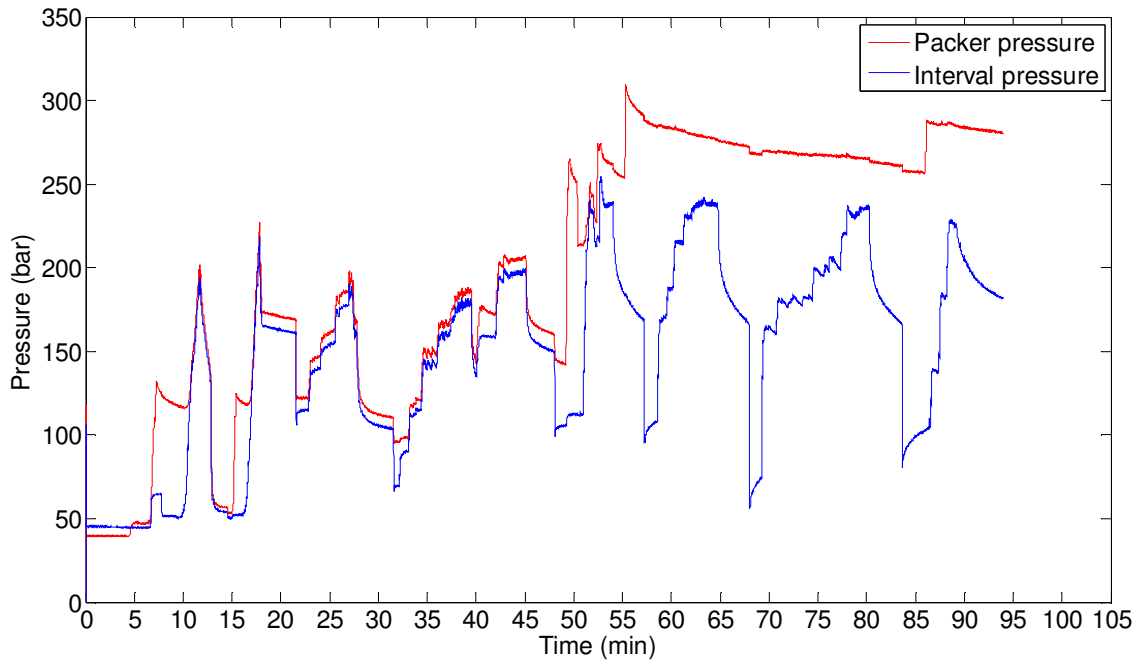


Test 12

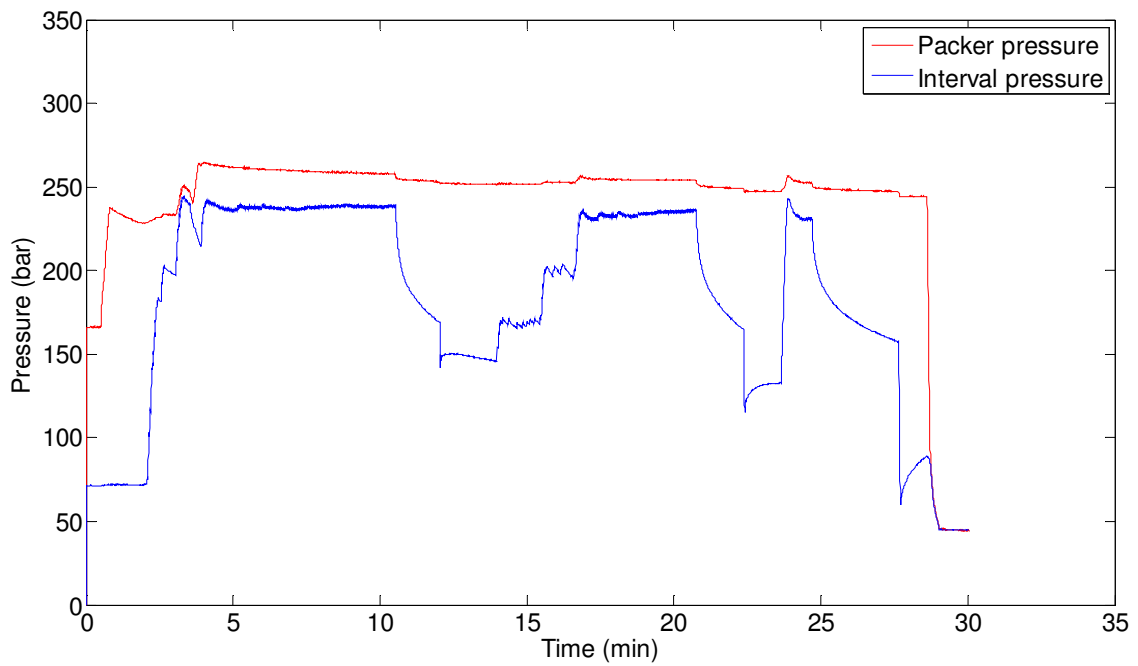


Borehole PD23

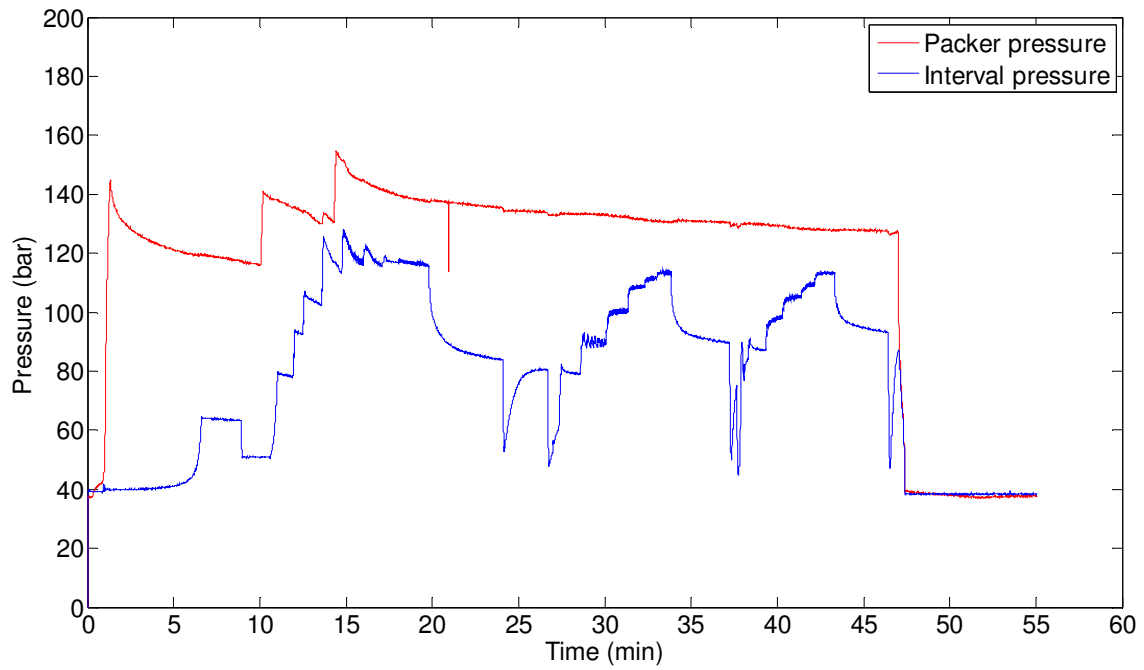
Test 1



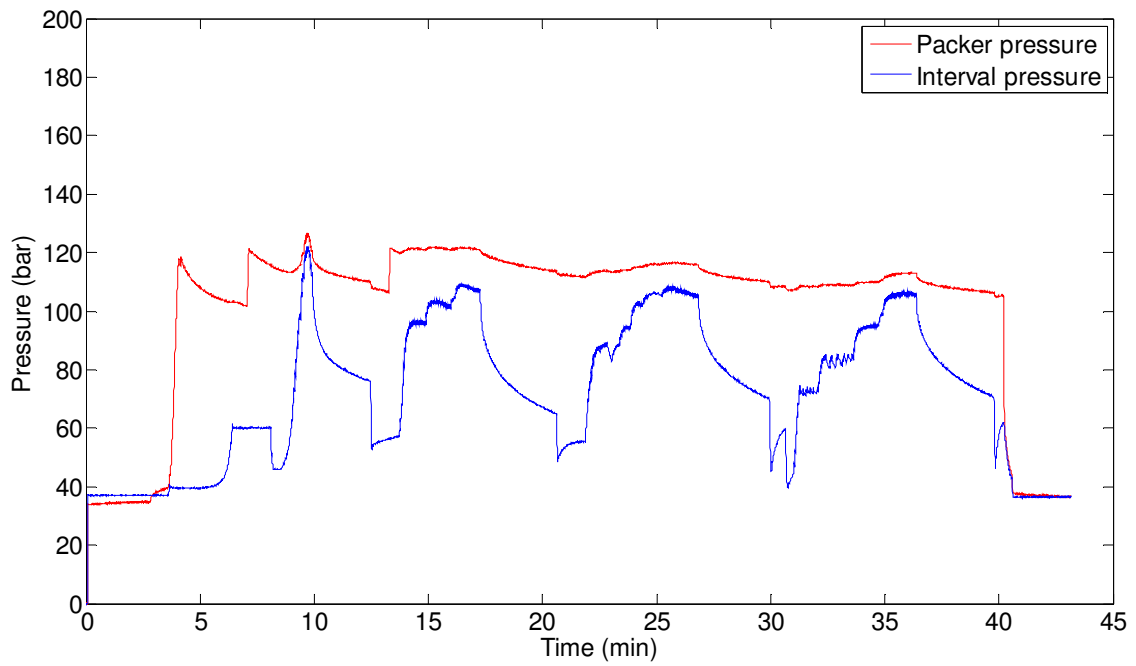
Test 1 (continuation)



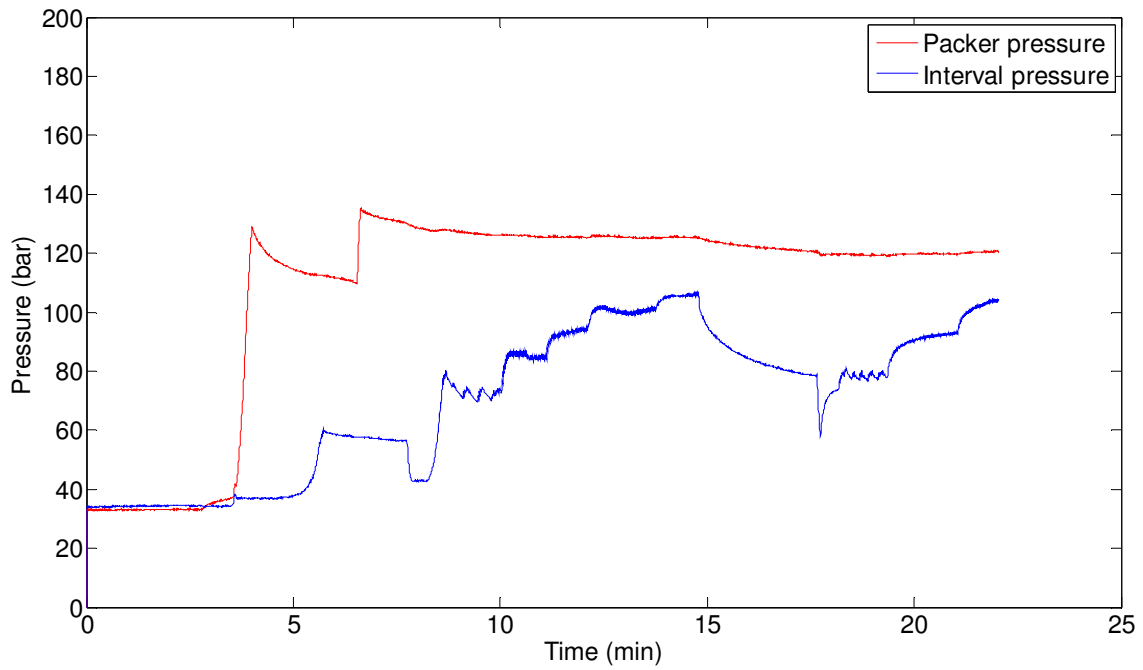
Test 2



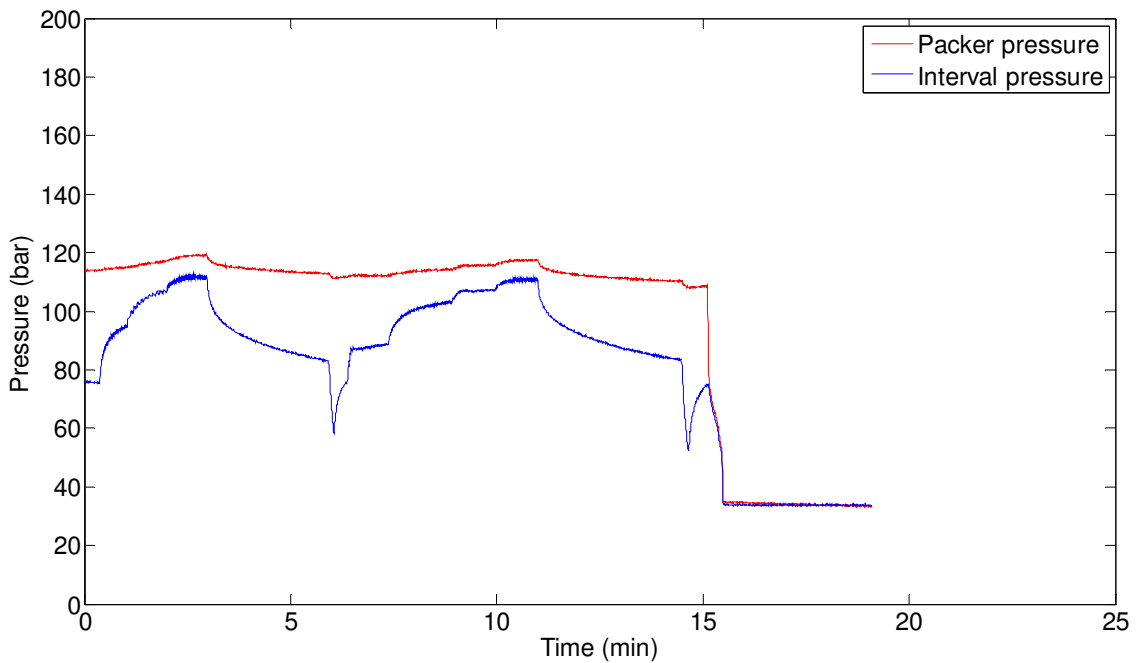
Test 3



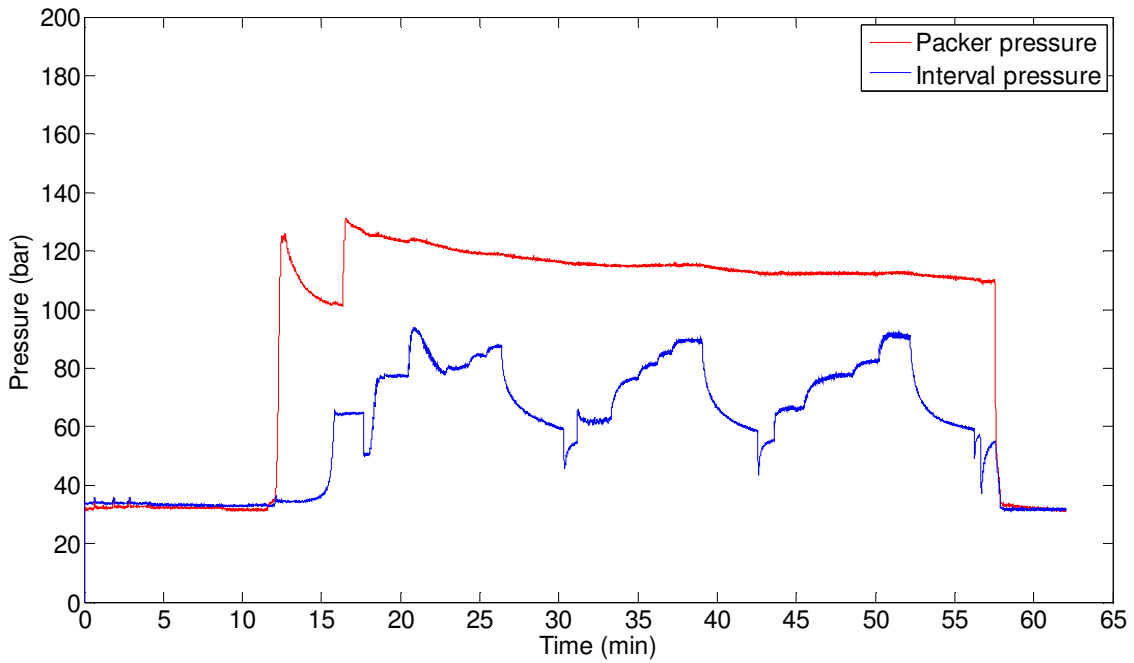
Test 4



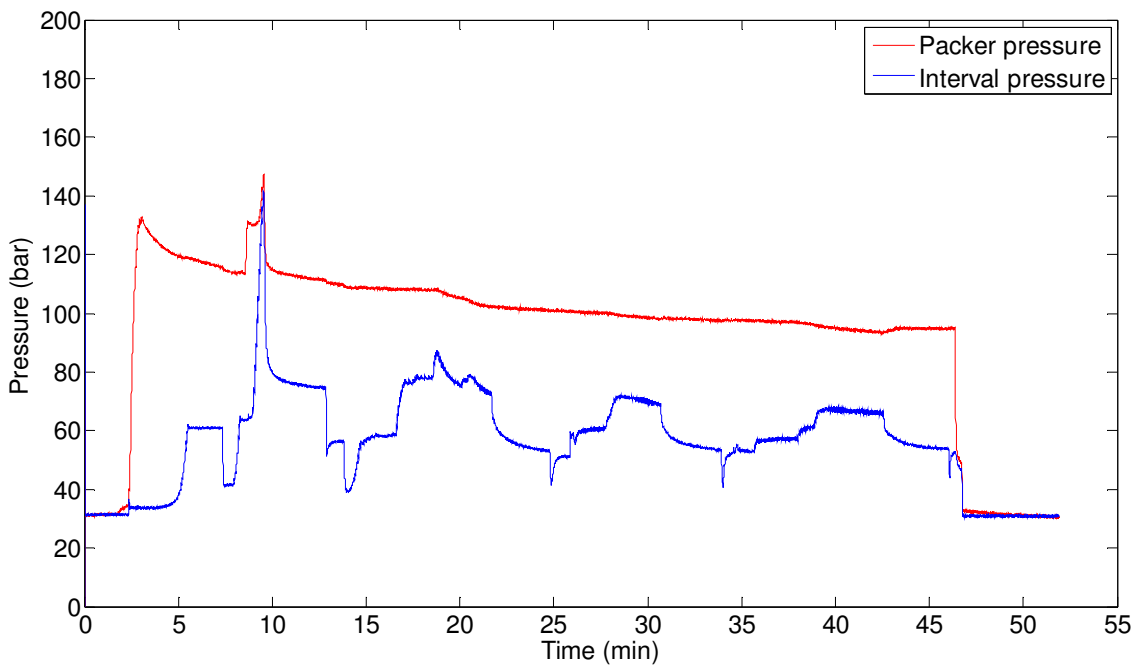
Test 4 (continuation)



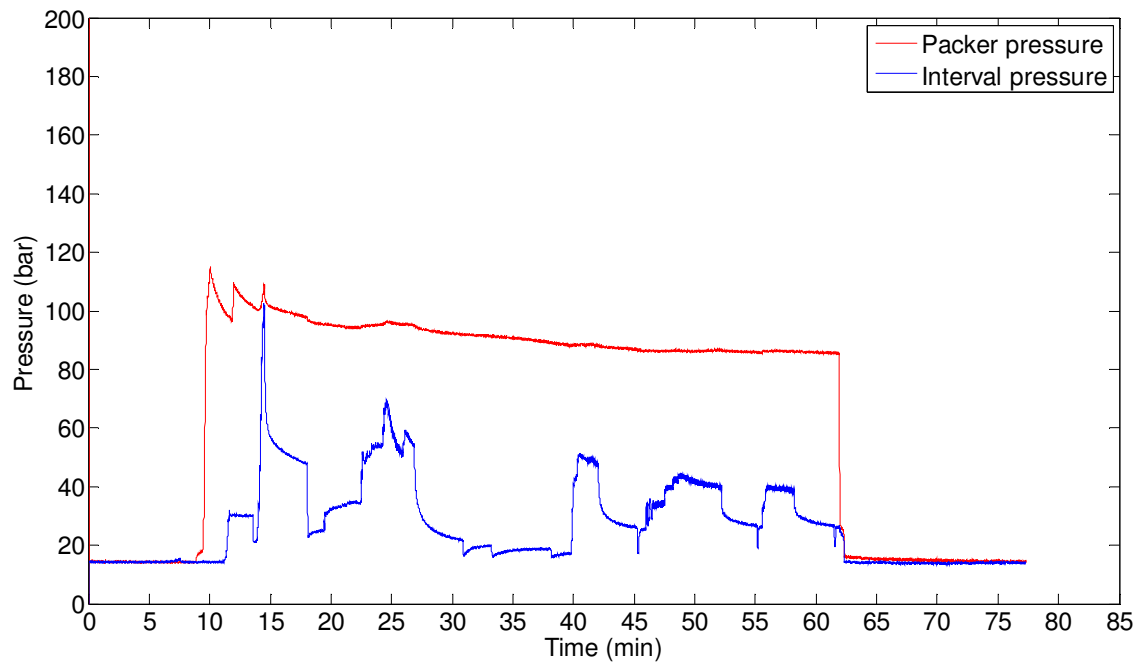
Test 5



Test 6



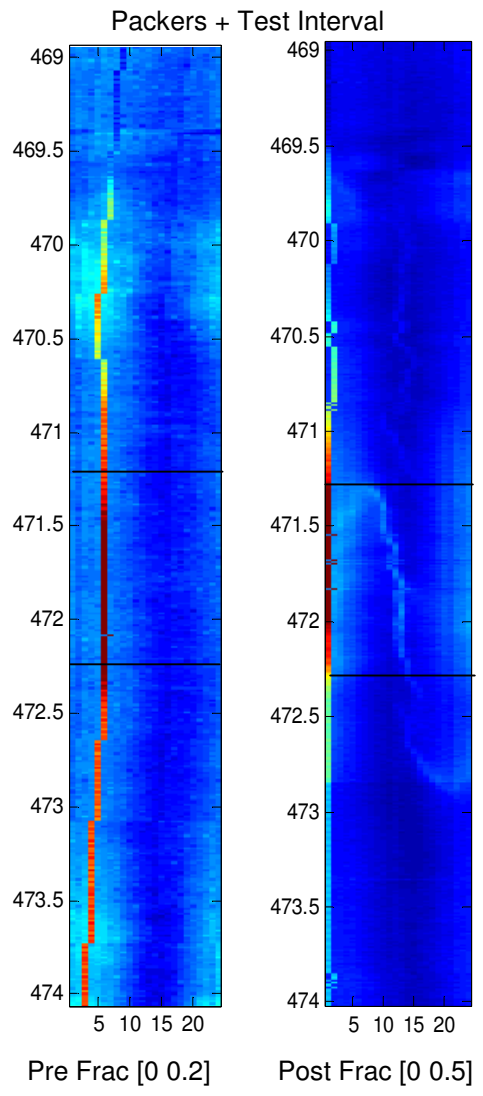
Test 7



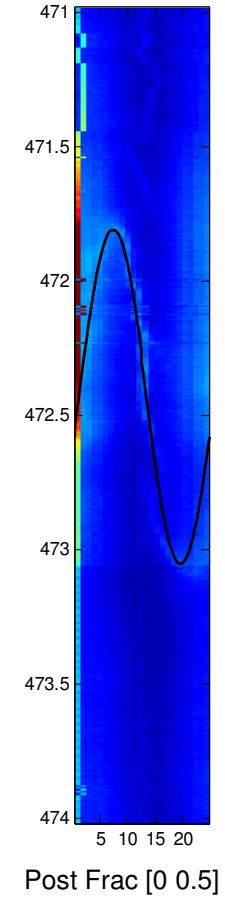
APPENDIX A2
Fracture orientation
determinations

Borehole PD19

Test 1

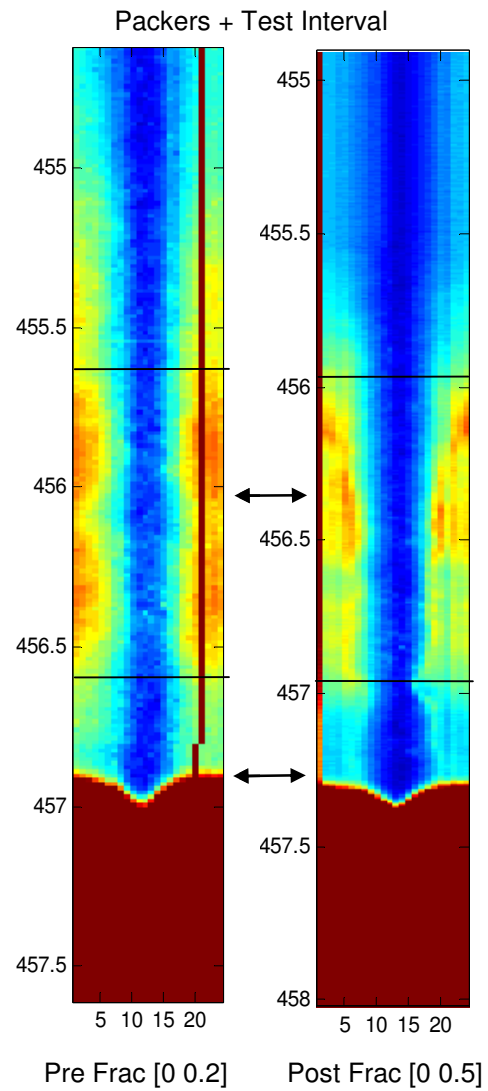


Fractures orientation determination

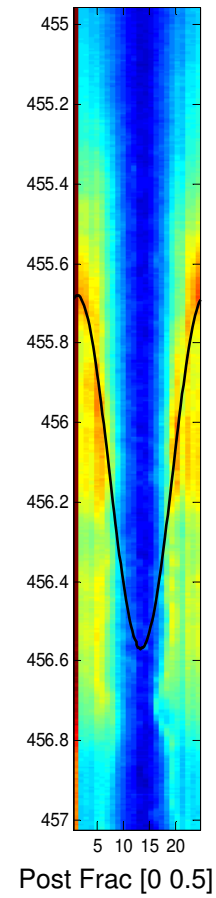


Corrected depth	Azimuth		Dip	
	ϕ ($^{\circ}$)	$\delta\phi$ ($^{\circ}$)	θ ($^{\circ}$)	$\delta\theta$ ($^{\circ}$)
471.8	108	4	87	2

Test 2

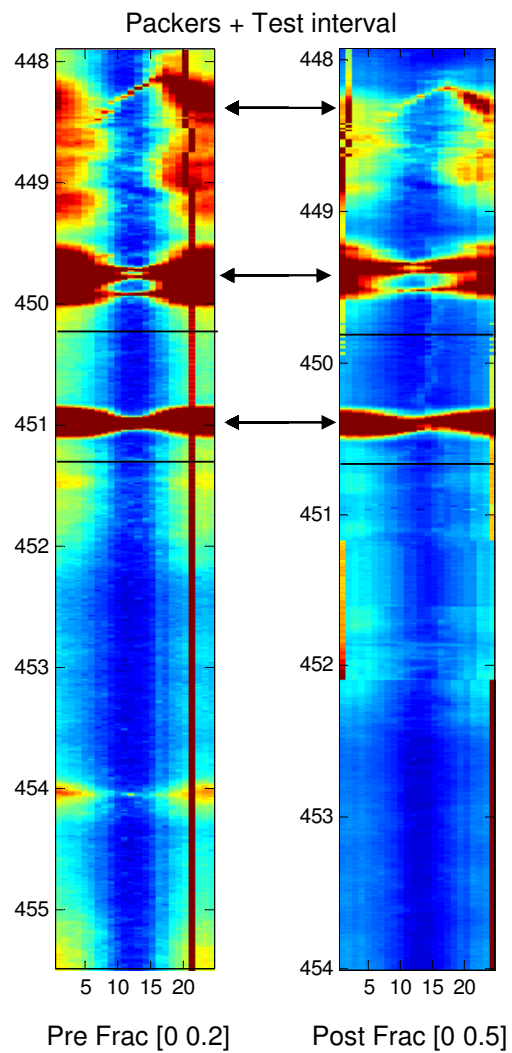


Fractures orientation determination

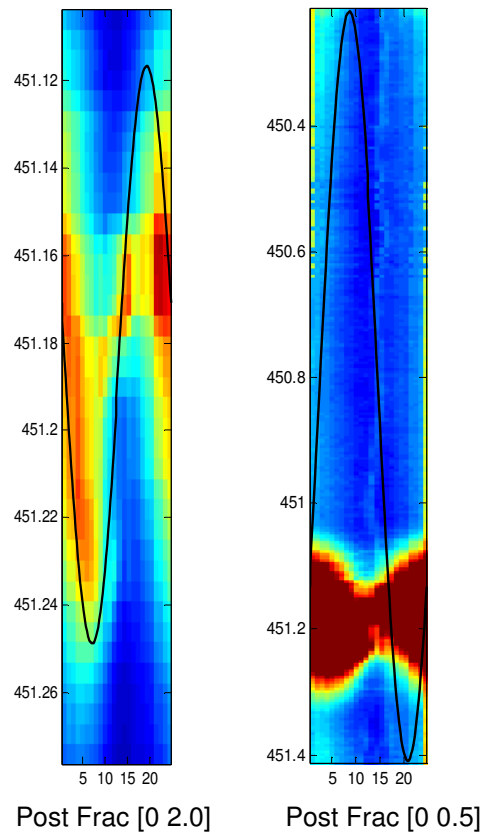


Corrected depth	Azimuth		Dip	
	ϕ (°)	$\delta\phi$ (°)	θ (°)	$\delta\theta$ (°)
455.5	18	7	90	2

Test 3

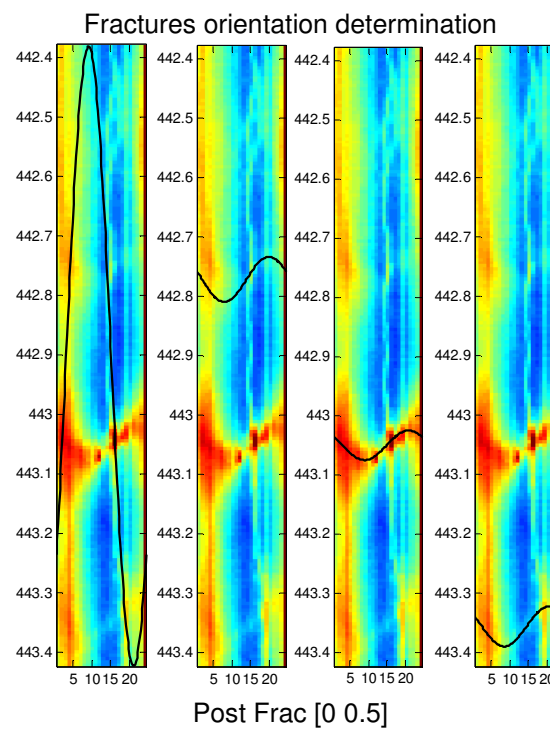
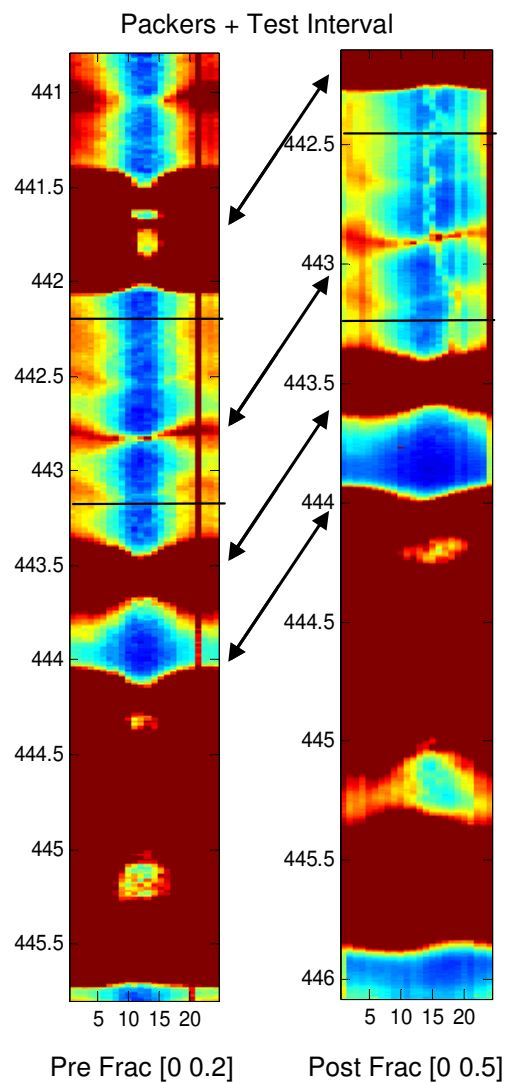


Fractures orientation determination



Corrected depth	Azimuth		Dip	
	ϕ ($^{\circ}$)	$\delta\phi$ ($^{\circ}$)	θ ($^{\circ}$)	$\delta\theta$ ($^{\circ}$)
450.1	126	5	90	2
450.4	281	6	60	1

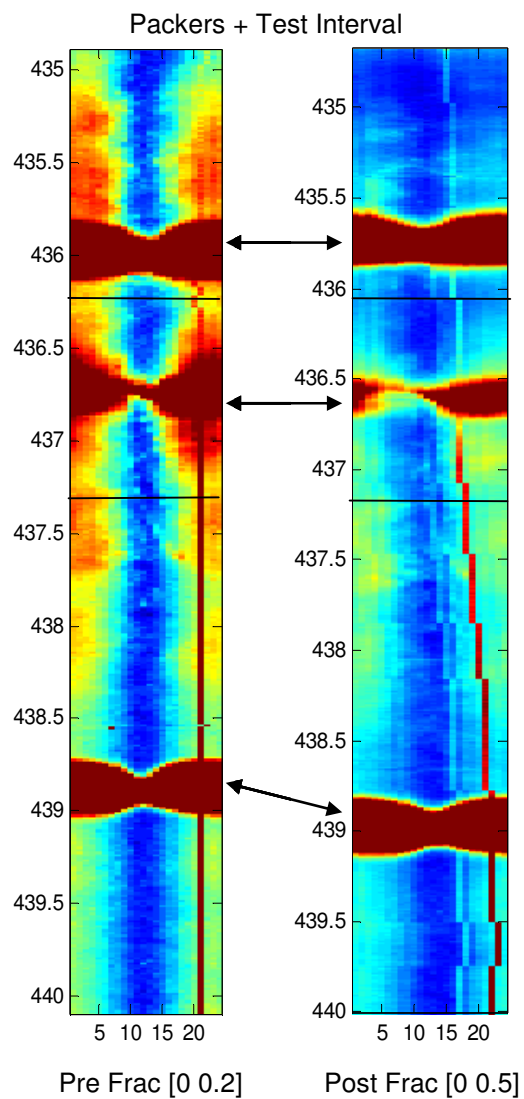
Test 4



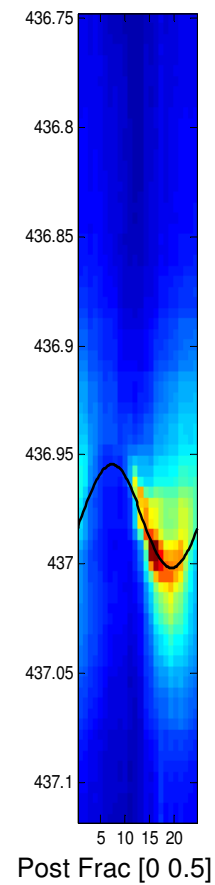
Corrected depth	Azimuth		Dip	
	ϕ (°)	$\delta\phi$ (°)	θ (°)	$\delta\theta$ (°)
442.1	133	5	90	2
442.0	301	5	49	2
442.1	306	5	38	2
442.6	301	5	40	2

Note: The mean value for the orientation of the parallel fractures was considered.

Test 5

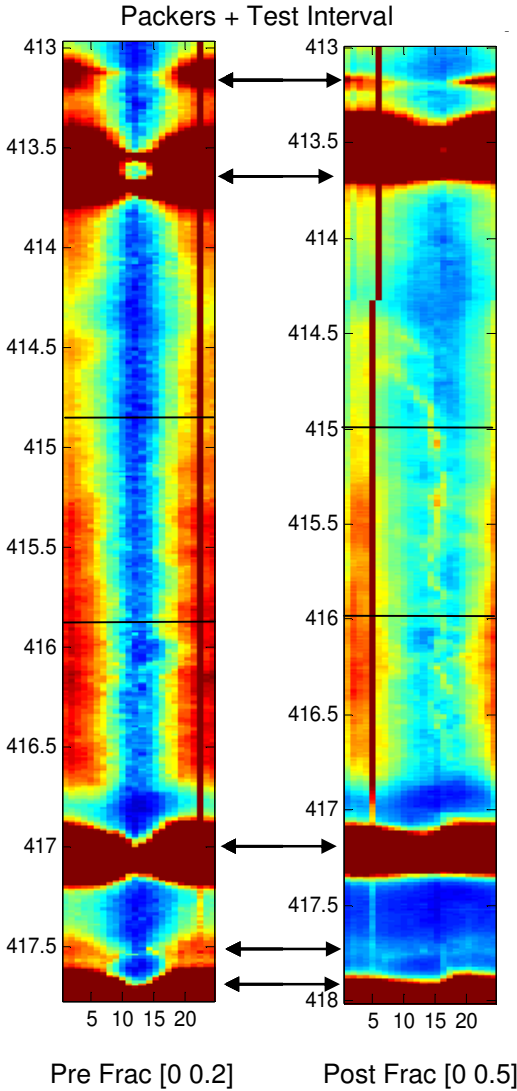


Fractures orientation determination

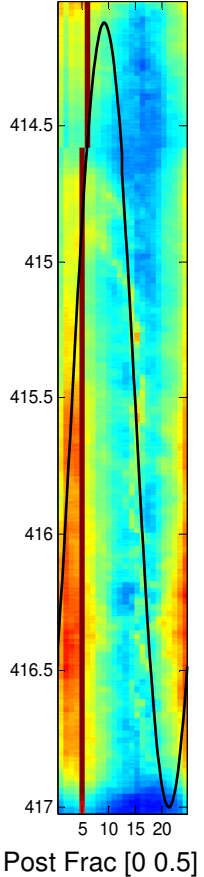


Corrected depth	Azimuth		Dip	
	ϕ ($^{\circ}$)	$\delta\phi$ ($^{\circ}$)	θ ($^{\circ}$)	$\delta\theta$ ($^{\circ}$)
436.3	108	6	32	2

Test 6

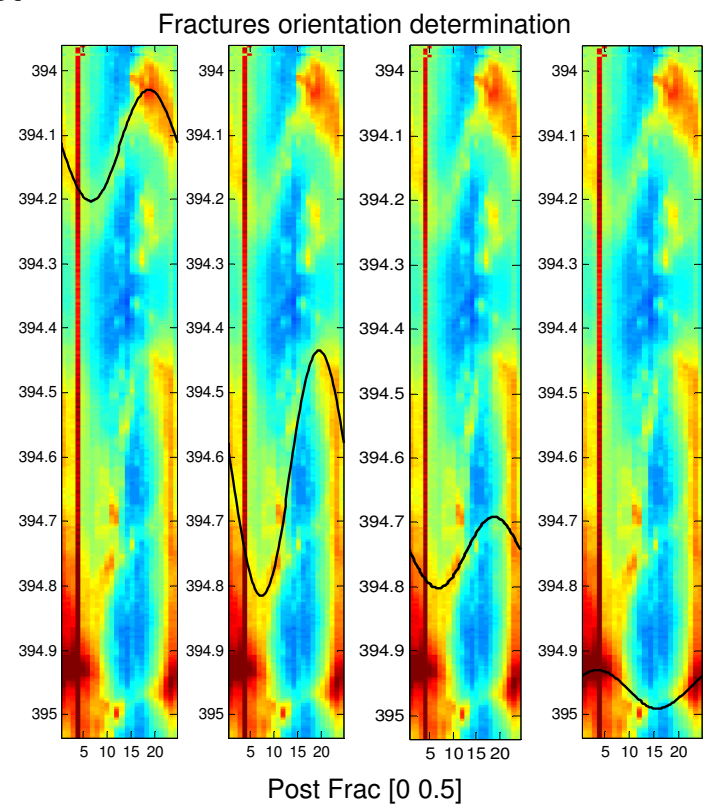
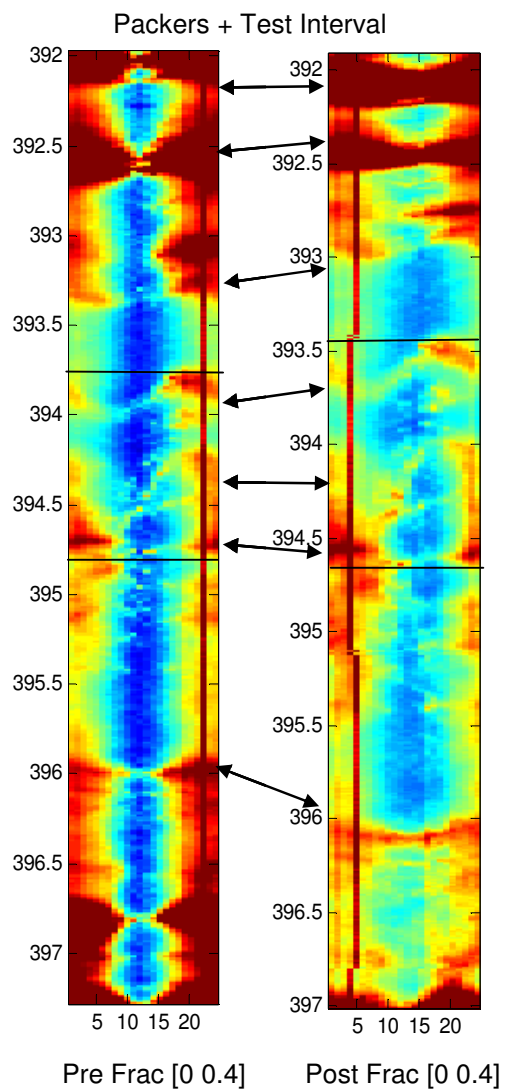


Fractures orientation determination



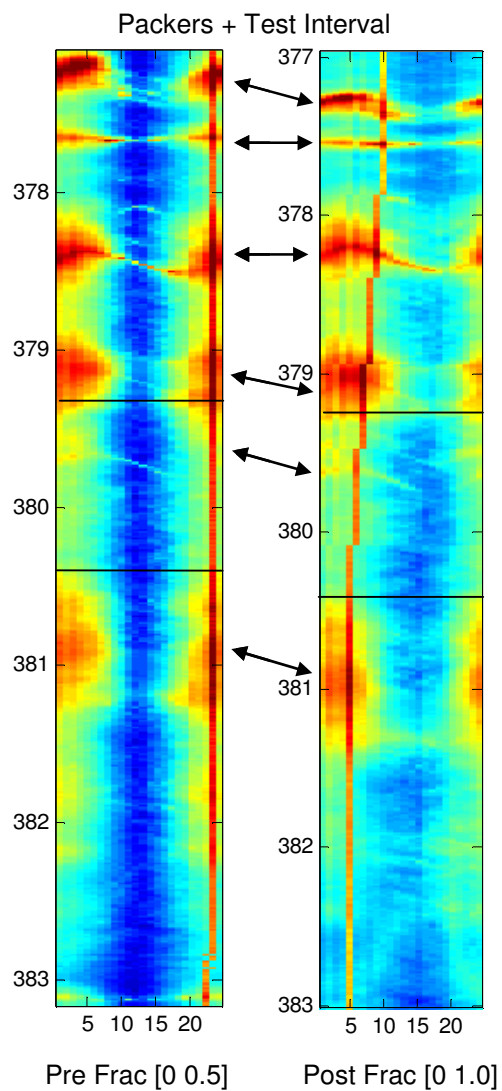
Corrected depth	Azimuth		Dip	
	ϕ (°)	$\delta\phi$ (°)	θ (°)	$\delta\theta$ (°)
414.9	133	4	90	2

Test 7

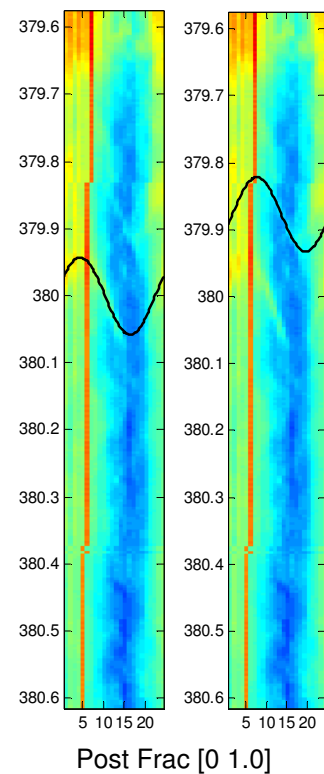


Corrected depth	Azimuth		Dip	
	ϕ ($^{\circ}$)	$\delta\phi$ ($^{\circ}$)	θ ($^{\circ}$)	$\delta\theta$ ($^{\circ}$)
393.4	270	4	66	2
393.9	284	3	79	2
394.1	277	5	52	2
394.3	50	5	38	2

Test 8



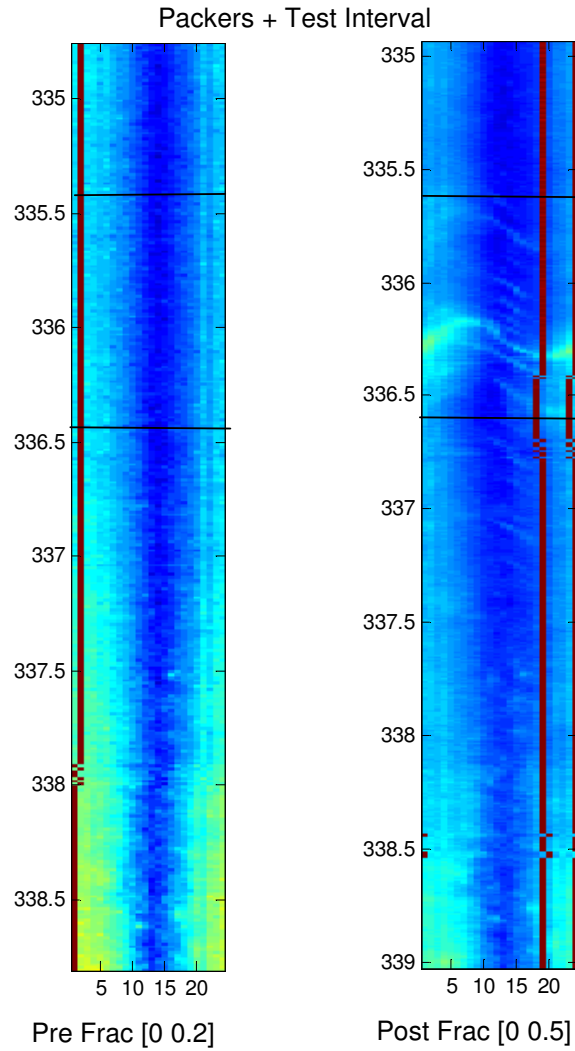
Fractures orientation determination



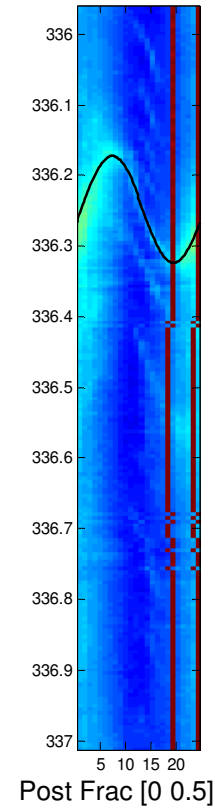
Corrected depth	Azimuth		Dip	
	ϕ ($^{\circ}$)	$\delta\phi$ ($^{\circ}$)	θ ($^{\circ}$)	$\delta\theta$ ($^{\circ}$)
379.2	82	3	57	2
379.1	94	3	56	2

Note: Two parallel fractures were identified in the electrical image obtained after the test. The mean value for their orientation was considered.

Test 9



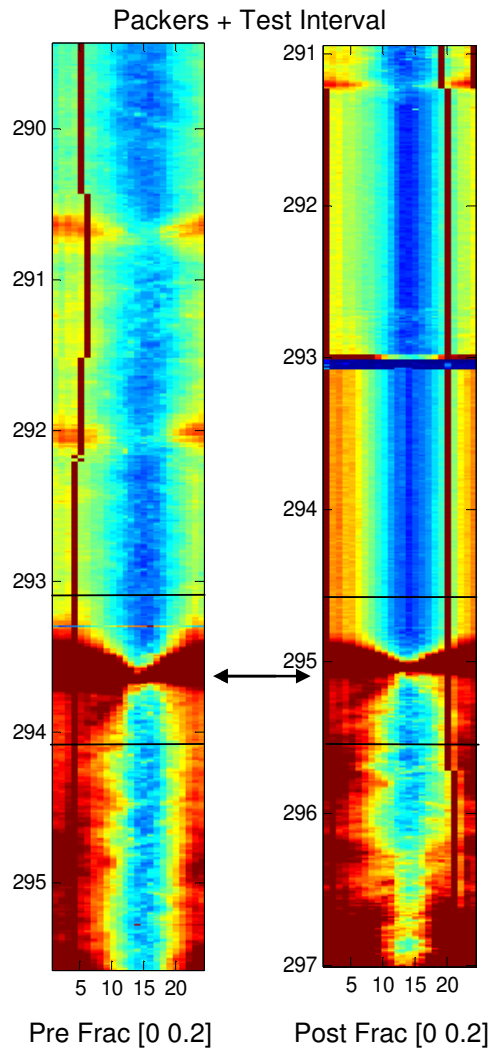
Fractures orientation determination



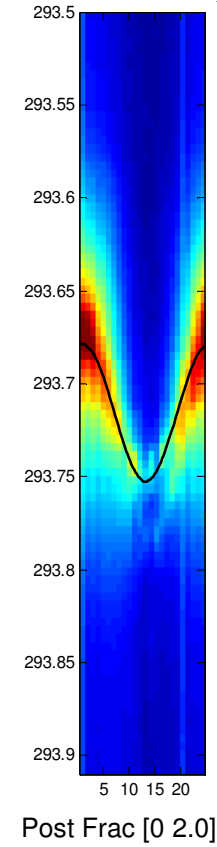
Corrected depth	Azimuth		Dip	
	ϕ ($^{\circ}$)	$\delta\phi$ ($^{\circ}$)	θ ($^{\circ}$)	$\delta\theta$ ($^{\circ}$)
335.6	119	3	61	2

Note: The mean value for the orientation of the inclined fractures was considered.

Test 10

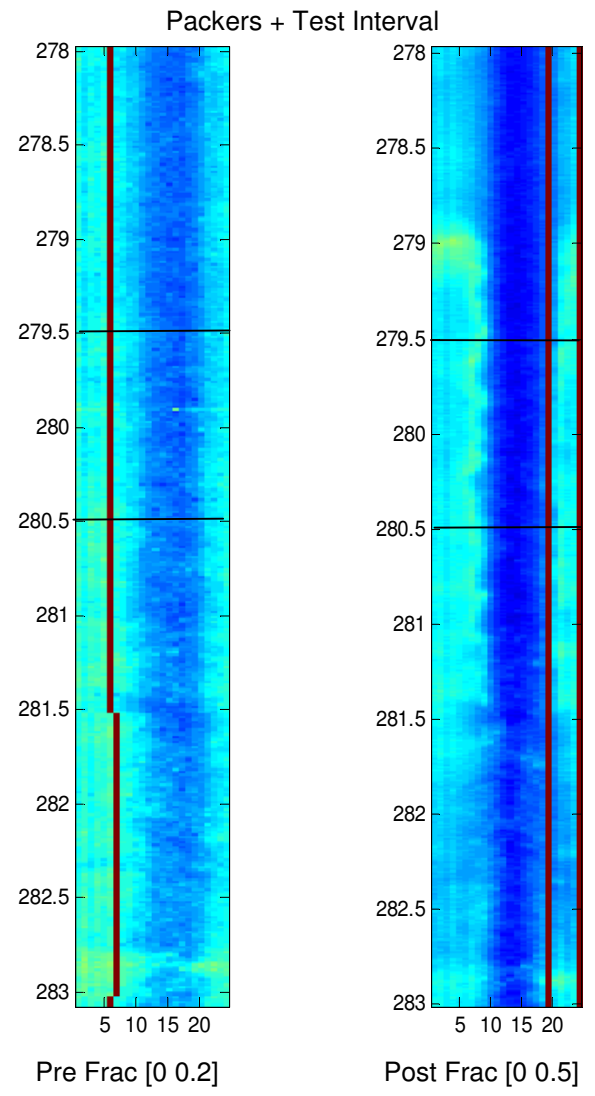


Fractures orientation determination

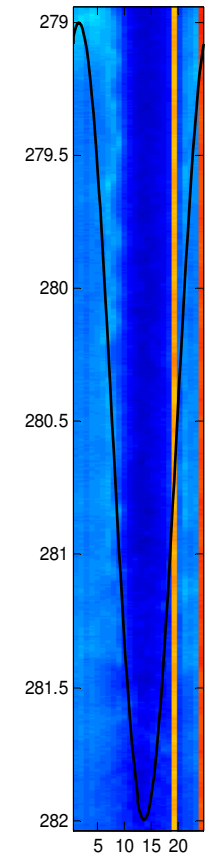


Corrected depth	Azimuth		Dip	
	ϕ ($^{\circ}$)	$\delta\phi$ ($^{\circ}$)	θ ($^{\circ}$)	$\delta\theta$ ($^{\circ}$)
293.1	14	2	44	3

Test 11



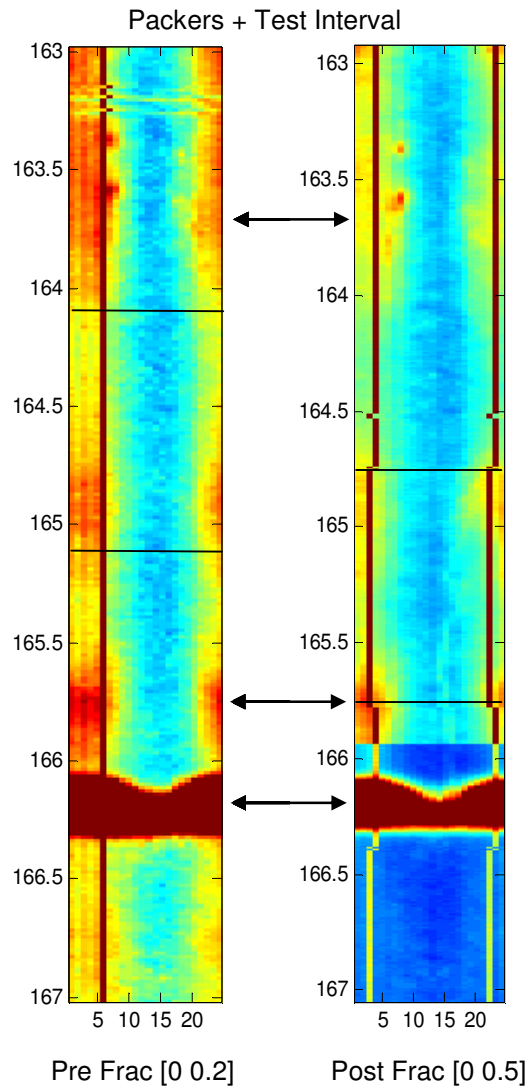
Fractures orientation determination



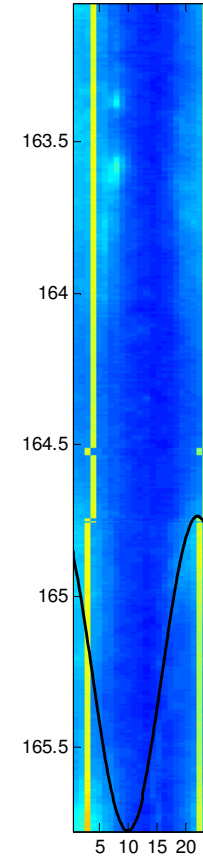
Post Frac [0 0.5]

Corrected depth	Azimuth		Dip	
	ϕ (°)	$\delta\phi$ (°)	θ (°)	$\delta\theta$ (°)
279.8	22	4	90	2

Test 12



Fractures orientation determination



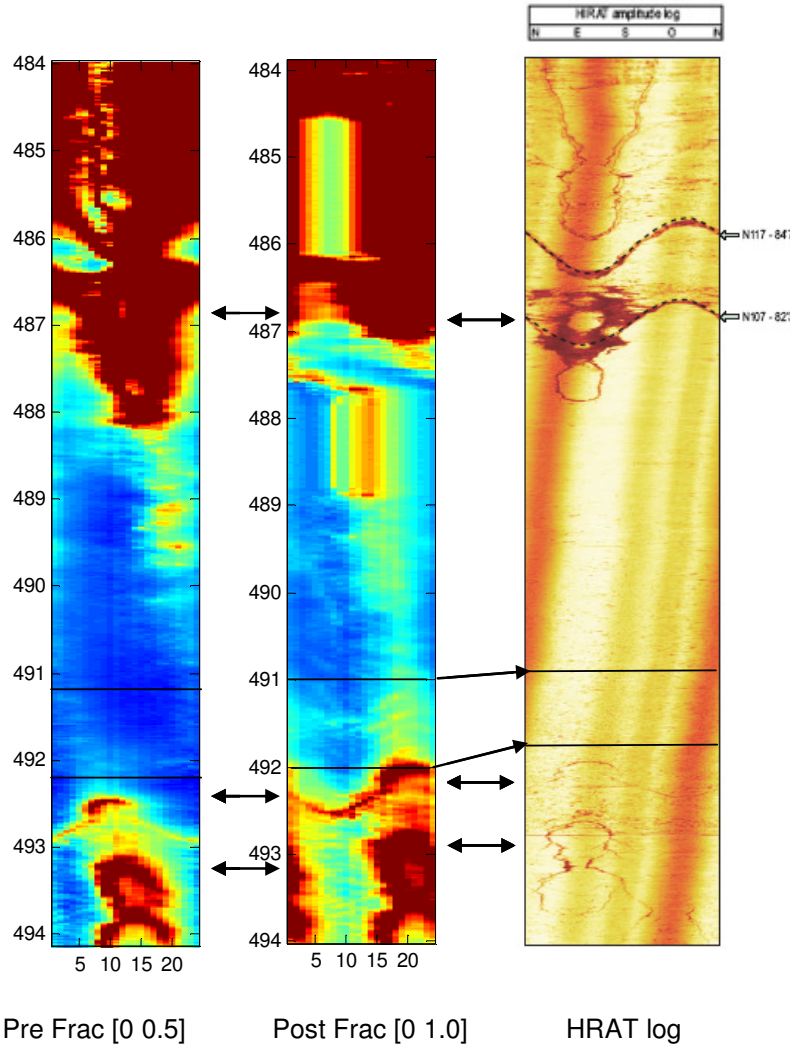
Post Frac [0 0.5]

Corrected depth	Azimuth		Dip	
	ϕ ($^{\circ}$)	$\delta\phi$ ($^{\circ}$)	θ ($^{\circ}$)	$\delta\theta$ ($^{\circ}$)
164.6	320	7	86	2

Borehole PD23

Test 1

Packers + Test interval

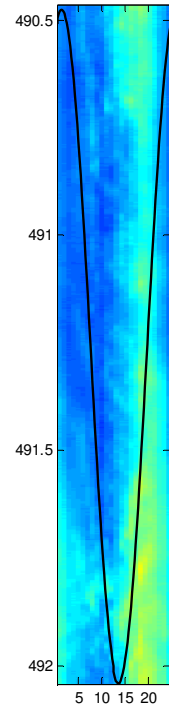


Fractures orientation determination

Main fractures:

Depth z (m)		Azimuth ϕ ($^\circ$)		Dip θ ($^\circ$)		Discrepancy Δ		
EI	HRAT	EI	HRAT	EI	HRAT	Δz (m)	$\Delta\phi$ ($^\circ$)	$\Delta\theta$ ($^\circ$)
492.3	491.3	295	112	82	83	-1.0	177	1

Note: This test was done 0.80 m above this main fracture. This value for the discrepancy between electrical and HRAT logs was considered ($\Delta\phi = 177^\circ$).



Post Frac [0 1.0]

Uncorrected orientations of the normal of the fracture plane:

Corrected depth	Azimuth		Dip	
	ϕ ($^\circ$)	$\delta\phi$ ($^\circ$)	θ ($^\circ$)	$\delta\theta$ ($^\circ$)
490.7	22	5	90	2

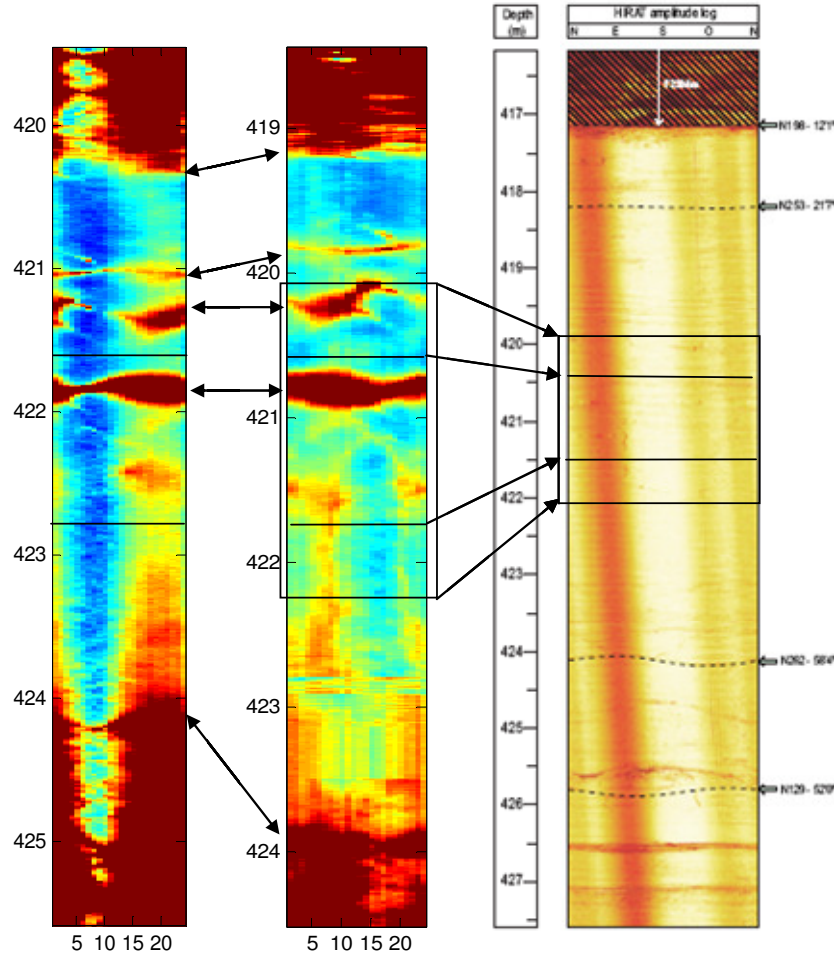
Corrected orientations of the normal of the fracture plane with respect to the HRAT log ($\Delta\phi = 177^\circ$):

Corrected depth	Azimuth		Dip	
	ϕ ($^\circ$)	$\delta\phi$ ($^\circ$)	θ ($^\circ$)	$\delta\theta$ ($^\circ$)
490.7	199	5	90	2

Note: This fracture is not visible in the HRAT log.

Test 2

Packers + Test Interval



Pre Frac [0 0.2]

Post Frac [0 0.4]

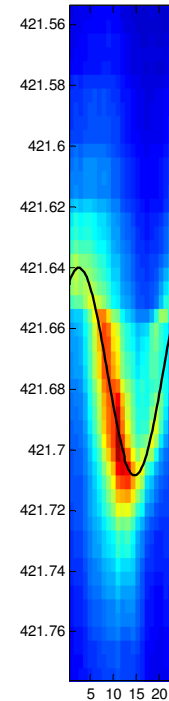
HRAT log

Fractures orientation determination

Main fractures:

Depth z (m)		Azimuth ϕ ($^\circ$)		Dip θ ($^\circ$)		Discrepancy Δ		
EI	HRAT	EI	HRAT	EI	HRAT	Δz (m)	$\Delta\phi$ ($^\circ$)	$\Delta\theta$ ($^\circ$)
422.5	421.5	22	23	90	90	-1	1	0
422.5	421.5	209	203	90	90	-1	-6	0

Note: The mean value for the discrepancy was considered ($\Delta\phi = -2.5^\circ$).



Post Frac [0 1.0]

Uncorrected orientations of the normal of the fracture plane:

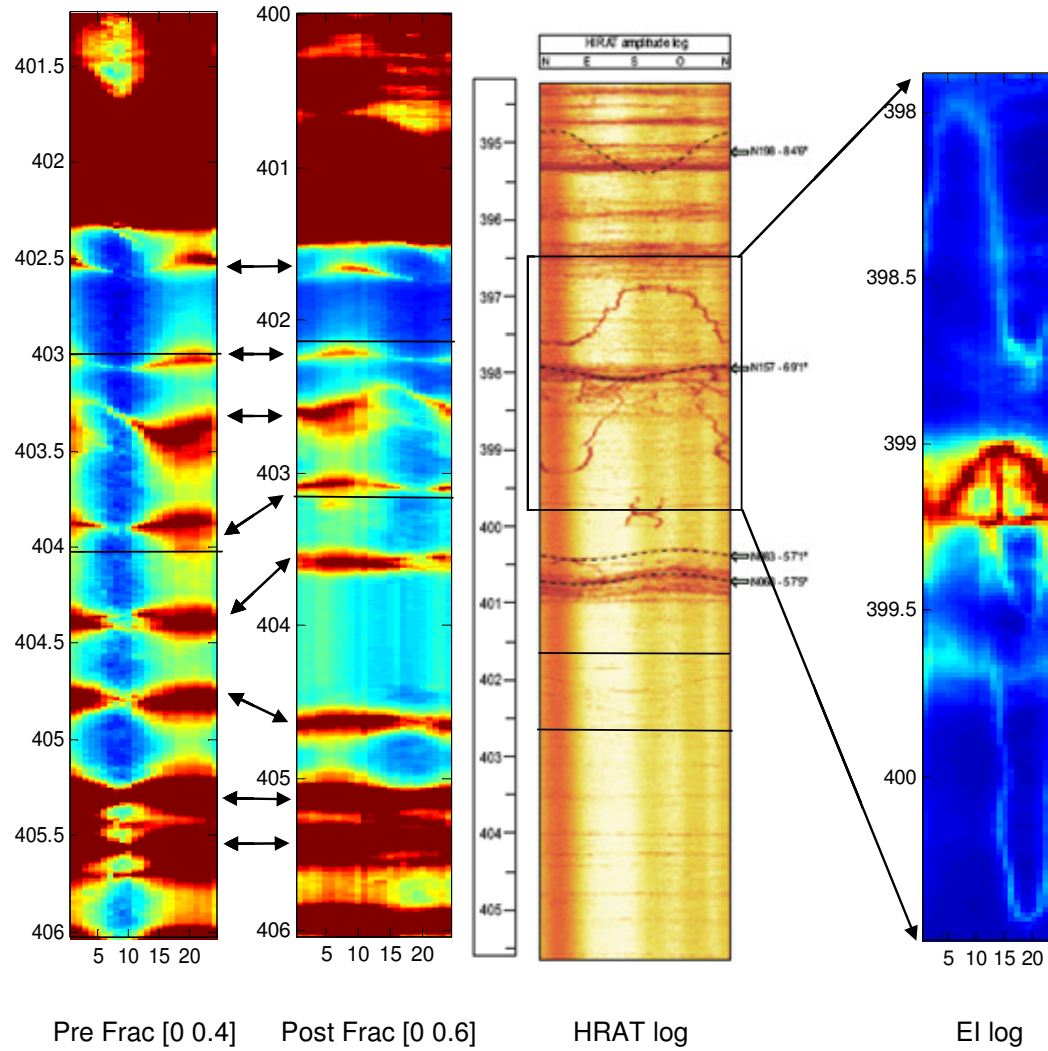
Corrected depth z (m)	Azimuth		Dip	
	ϕ ($^\circ$)	$\delta\phi$ ($^\circ$)	θ ($^\circ$)	$\delta\theta$ ($^\circ$)
421.8	22	5	90	2
420.9	36	5	42	2

Corrected orientations of the normal of the fracture plane with respect to the HRAT log ($\Delta\phi = -2.5^\circ$):

Corrected depth z (m)	Azimuth		Dip	
	ϕ ($^\circ$)	$\delta\phi$ ($^\circ$)	θ ($^\circ$)	$\delta\theta$ ($^\circ$)
421.8	19	5	90	2
420.9	33	5	42	2

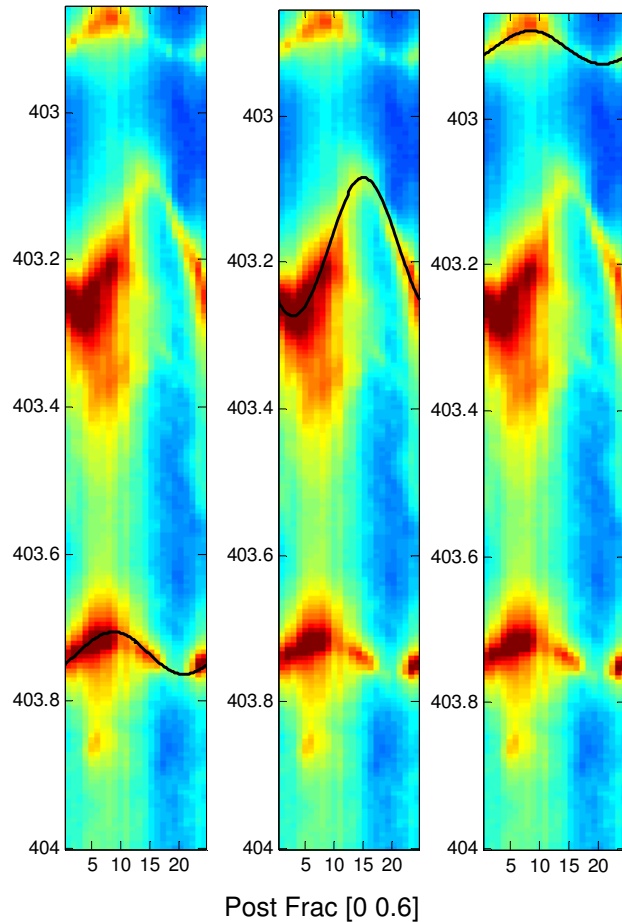
Note: These 2 fractures are identified in the HRAT log.

Test 3 Packers + Test Interval



Test 3 (continuation)

Fractures orientation determination



Main fractures:

Depth z (m)		Azimuth ϕ ($^\circ$)		Dip θ ($^\circ$)		Discrepancy Δ		
EI	HRAT	EI	HRAT	EI	HRAT	Δz (m)	$\Delta\phi$ ($^\circ$)	$\Delta\theta$ ($^\circ$)
399.1	397.9	209	337	69	69	-1.2	128	0

Note: This test was done 4.4 m below this main fracture. This value for the discrepancy between electrical and HRAT logs was considered ($\Delta\phi = 128^\circ$).

Uncorrected orientations of the normal of the fracture plane:

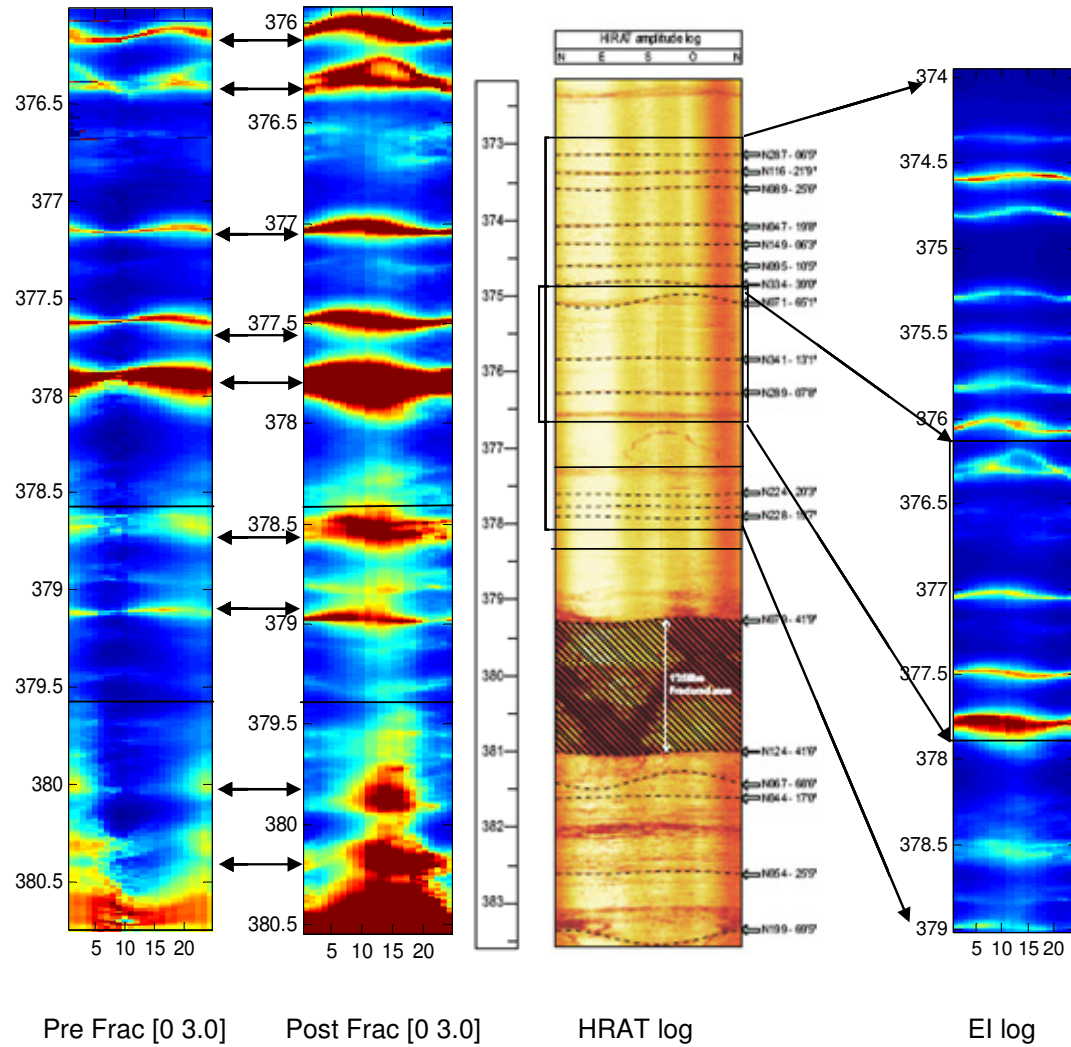
Corrected depth	Azimuth		Dip	
	ϕ ($^\circ$)	$\delta\phi$ ($^\circ$)	θ ($^\circ$)	$\delta\theta$ ($^\circ$)
402.9	126	5	37	3
402.4	220	5	68	2
402.1	122	5	31	3

Corrected orientations of the normal of the fracture plane with respect to the HRAT log ($\Delta\phi = 128^\circ$):

Corrected depth	Azimuth		Dip	
	ϕ ($^\circ$)	$\delta\phi$ ($^\circ$)	θ ($^\circ$)	$\delta\theta$ ($^\circ$)
402.9	254	5	37	3
402.4	348	5	68	2
402.1	250	5	31	3

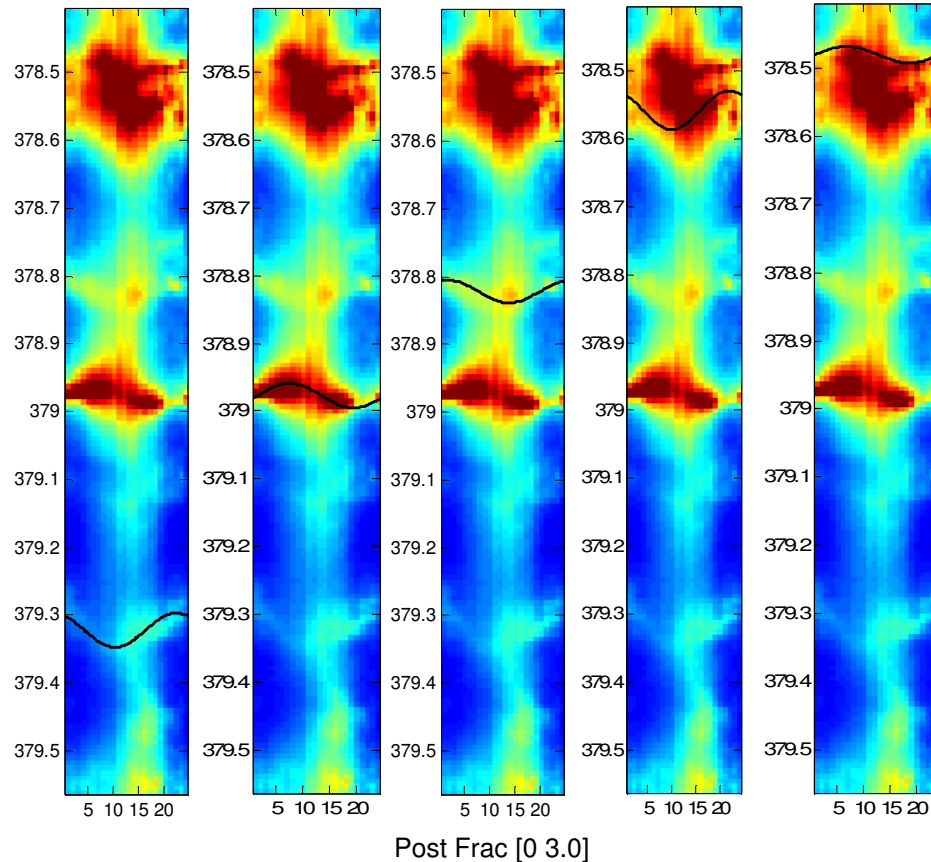
Note: These fractures are identified in the HRAT log. The mean value for the orientation of the two parallel fractures was considered.

Test 4 Packers + Test Interval



Test 4 (continuation)

Fractures orientation determination



Main fractures:

Depth z (m)		Azimuth ϕ ($^\circ$)		Dip θ ($^\circ$)		Discrepancy Δ		
EI	HRAT	EI	HRAT	EI	HRAT	Δz (m)	$\Delta\phi$ ($^\circ$)	$\Delta\theta$ ($^\circ$)
377.0	375.8	126	161	25	13	-1.2	35	-12
377.5	376.3	76	109	23	8	-1.2	33	-15

Note: The mean value for the discrepancy was considered ($\Delta\phi = 34$).

Uncorrected orientations of the normal of the fracture plane:

Corrected depth z (m)	Azimuth		Dip	
	ϕ ($^\circ$)	$\delta\phi$ ($^\circ$)	θ ($^\circ$)	$\delta\theta$ ($^\circ$)
378.4	328	5	35	2
378.1	108	5	25	2
377.9	25	5	24	2
377.7	324	10	37	2
377.6	97	5	18	2

Corrected orientations of the normal of the fracture plane with respect to the HRAT log ($\Delta\phi = 34^\circ$):

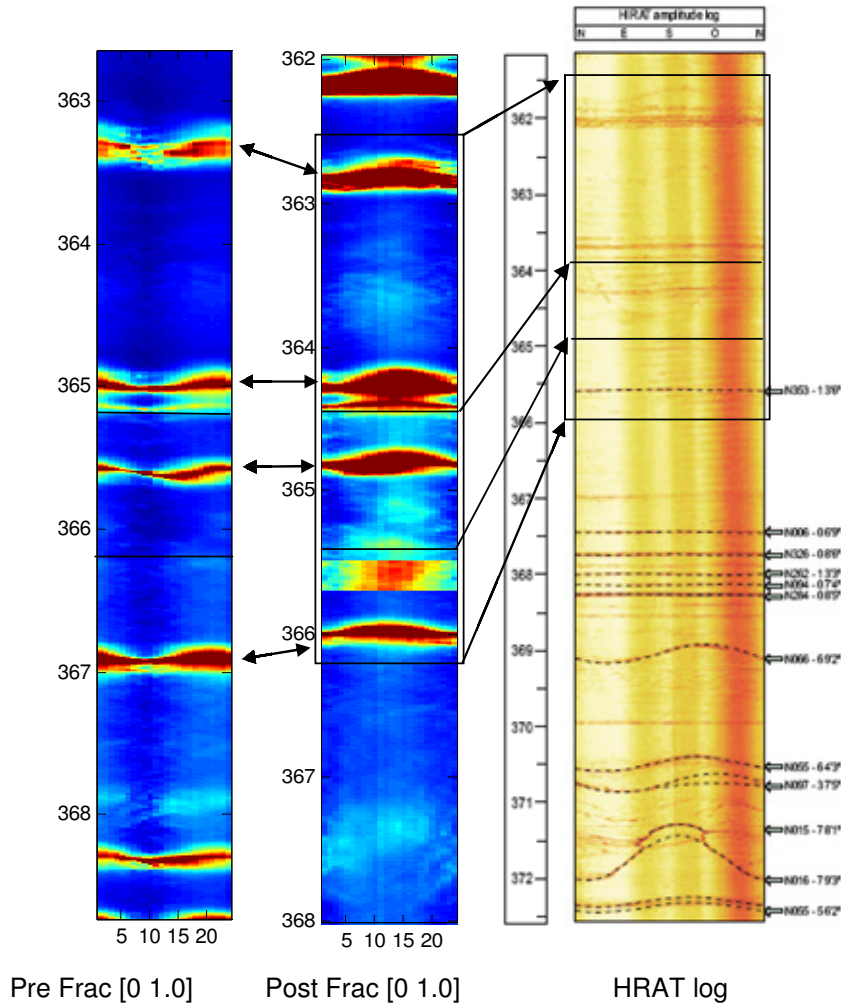
Corrected depth z (m)	Azimuth		Dip	
	ϕ ($^\circ$)	$\delta\phi$ ($^\circ$)	θ ($^\circ$)	$\delta\theta$ ($^\circ$)
378.4	2	5	35	2
378.1	142	5	25	2
377.9	59	5	24	2
377.7	358	10	37	2
377.6	131	5	18	2
377.4*	215	5	81	3
377.6*	44	5	20	3
377.8*	106	5	12	3
377.9*	48	5	20	3

*These fractures are identified only in the HRAT log.

Test 5

Packers + Test Interval

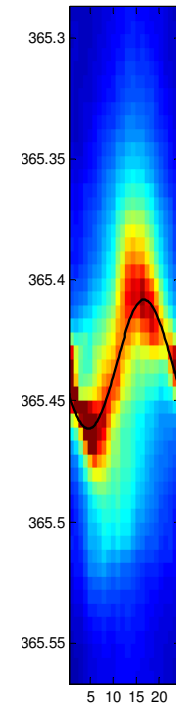
Fractures orientation determination



Main fractures:

Depth z (m)		Azimuth ϕ ($^{\circ}$)		Dip θ ($^{\circ}$)		Discrepancy Δ		
EI	HRAT	EI	HRAT	EI	HRAT	Δz (m)	$\Delta\phi$ ($^{\circ}$)	$\Delta\theta$ ($^{\circ}$)
366.8	365.6	166	173	19	14	-1.2	7	-5

Note: This test was done 1.3 m above this main fracture. This discrepancy between electrical and HRAT logs was considered ($\Delta\phi = 7^{\circ}$).



Uncorrected orientations of the normal of the fracture plane:

Corrected depth z (m)	Azimuth		Dip	
	ϕ ($^{\circ}$)	$\delta\phi$ ($^{\circ}$)	θ ($^{\circ}$)	$\delta\theta$ ($^{\circ}$)
364.6	245	5	35	2

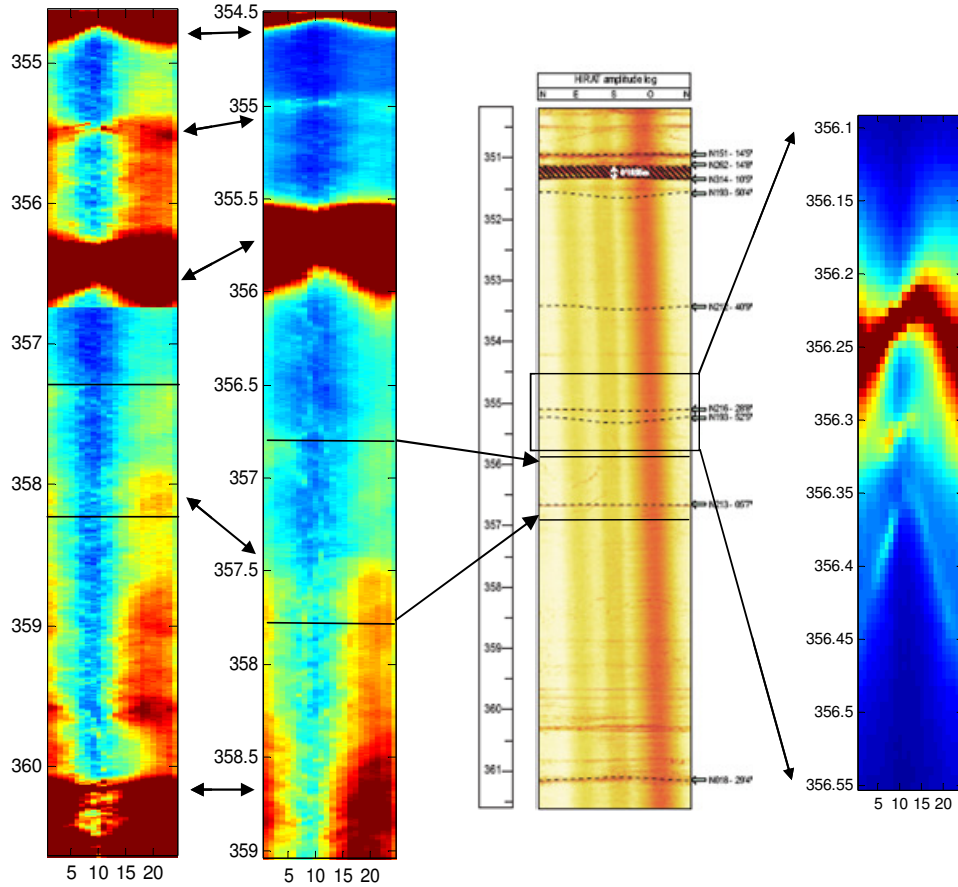
Corrected orientations of the normal of the fracture plane with respect to the HRAT log ($\Delta\phi = 7^{\circ}$):

Corrected depth z (m)	Azimuth		Dip	
	ϕ ($^{\circ}$)	$\delta\phi$ ($^{\circ}$)	θ ($^{\circ}$)	$\delta\theta$ ($^{\circ}$)
364.7*	325	5	81	3
364.6	252	5	35	2

* This fracture is identified only in the HRAT log.

Test 6

Packers + Test Interval



Pre Frac [0 0.2]

Post Frac [0 0.5]

HRAT log

EI

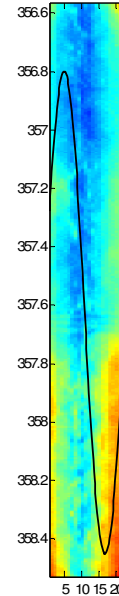
Post Frac [0 0.5]

Fractures orientation determination

Main fractures:

Depth z (m)		Azimuth ϕ ($^{\circ}$)		Dip θ ($^{\circ}$)		Discrepancy Δ		
EI	HRAT	EI	HRAT	EI	HRAT	Δz (m)	$\Delta\phi$ ($^{\circ}$)	$\Delta\theta$ ($^{\circ}$)
356.3	355.1	198	36	29	29	-1.2	198	0
356.4	355.3	169	13	50	53	-1.1	204	3

Note: This test was done 1.2 m below these two main fractures. The mean discrepancy between electrical and HRAT logs obtained from these two fractures was considered ($\Delta\phi = 201^{\circ}$).



Uncorrected orientations of the normal of the fracture plane:

Corrected depth	Azimuth		Dip	
	ϕ ($^{\circ}$)	$\delta\phi$ ($^{\circ}$)	θ ($^{\circ}$)	$\delta\theta$ ($^{\circ}$)
z (m)				
356.8	68	4	90	2

Corrected orientations of the normal of the fracture plane with respect to the HRAT log ($\Delta\phi = 204^{\circ}$):

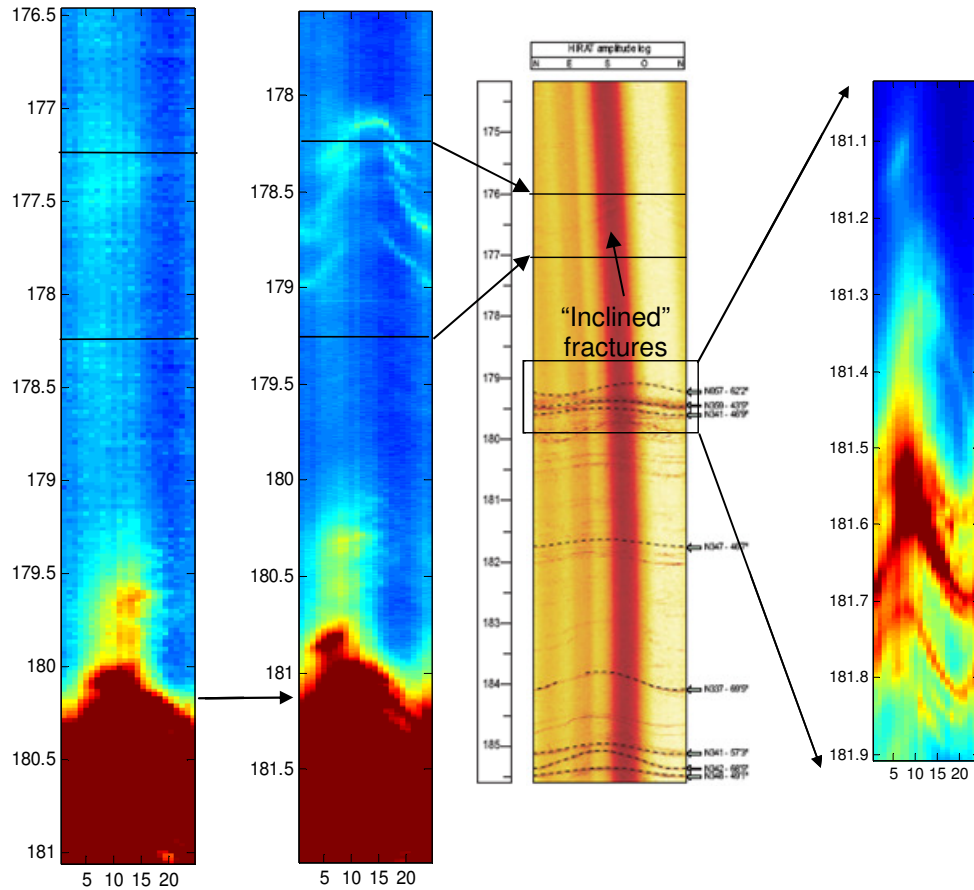
Corrected depth	Azimuth		Dip	
	ϕ ($^{\circ}$)	$\delta\phi$ ($^{\circ}$)	θ ($^{\circ}$)	$\delta\theta$ ($^{\circ}$)
z (m)				
356.8*	269	4	90	2
357.0**	33	5	6	3

* This fracture is identified in the HRAT log.

** This fracture is sub horizontal and is identified only in the HRAT log.

Test 7

Packers + Test Interval



Pre Frac [0 0.2]

Post Frac [0 0.5]

HRAT log

EI log

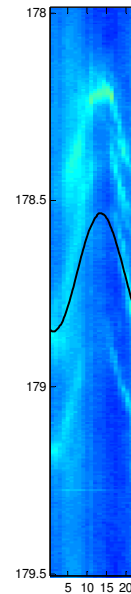
Post Frac [0 0.5]

Fractures orientation determination

Main fractures:

Depth z (m)		Azimuth ϕ (°)		Dip θ (°)		Discrepancy Δ		
EI	HRAT	EI	HRAT	EI	HRAT	Δz (m)	$\Delta\phi$ (°)	$\Delta\theta$ (°)
181.4	179.2	180	237	66	62	-2.2	57	-4
181.7	179.4	133	179	55	44	-2.3	46	-11
181.8	179.6	112	161	53	47	-2.2	49	-6

Note: This test was done 3.0 m below these main fractures. The mean discrepancy between electrical and HRAT logs obtained from these three fractures was considered ($\Delta\phi = 51^\circ$).



Uncorrected orientations of the normal of the fracture plane:

Corrected depth	Azimuth		Dip	
	z (m)	ϕ (°)	θ (°)	$\delta\theta$ (°)
176.6	192	3	78	2

Note: The mean value for the orientation of the inclined fractures was considered.

Corrected orientations of the normal of the fracture plane with respect to the HRAT log ($\Delta\phi = 51^\circ$):

Corrected depth	Azimuth		Dip	
	z (m)	ϕ (°)	θ (°)	$\delta\theta$ (°)
176.6	243	3	77	2

Note: The *inclined* fractures are identified in the HRAT log.

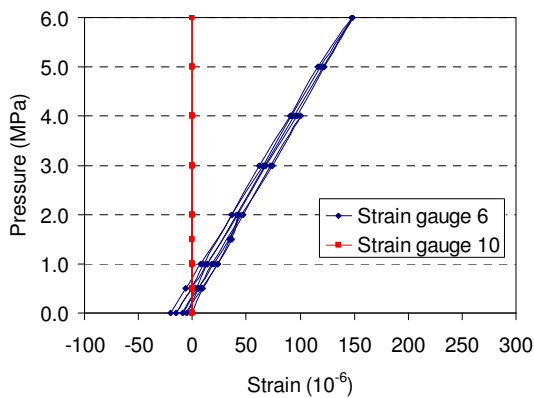
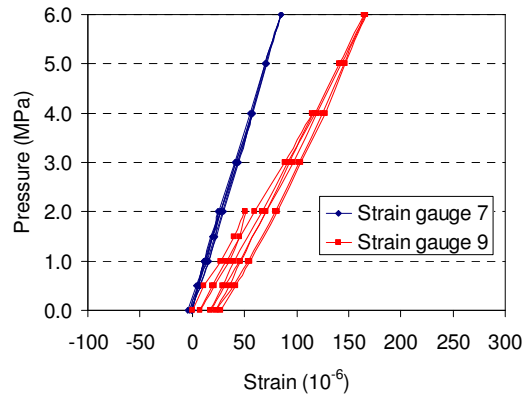
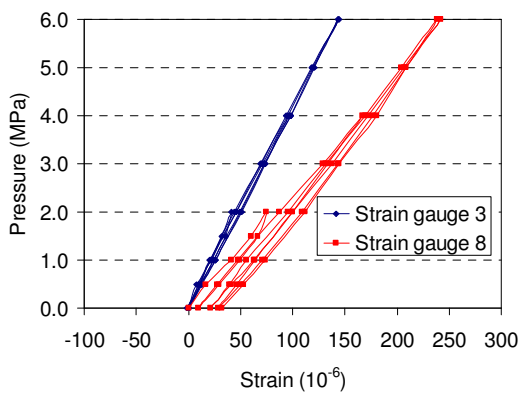
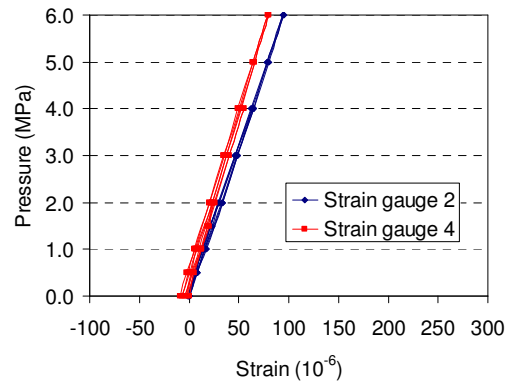
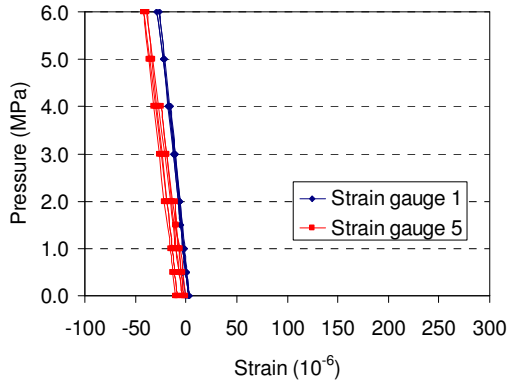
APPENDIX B

Overcoming test results

Borehole PD1

Test 1

Results of the biaxial test



Unit strains ($10^{-6}/\text{MPa}$) for $p = 6.0 \text{ MPa}$	ϵ_1	ϵ_2	ϵ_3	ϵ_4	ϵ_5	ϵ_6	ϵ_7	ϵ_8	ϵ_9	ϵ_{10}
Measured	-5	16	24	15	-5	27	15	35	24	0
Calculated	-7	18	28	18	-7	34	18	28	18	34

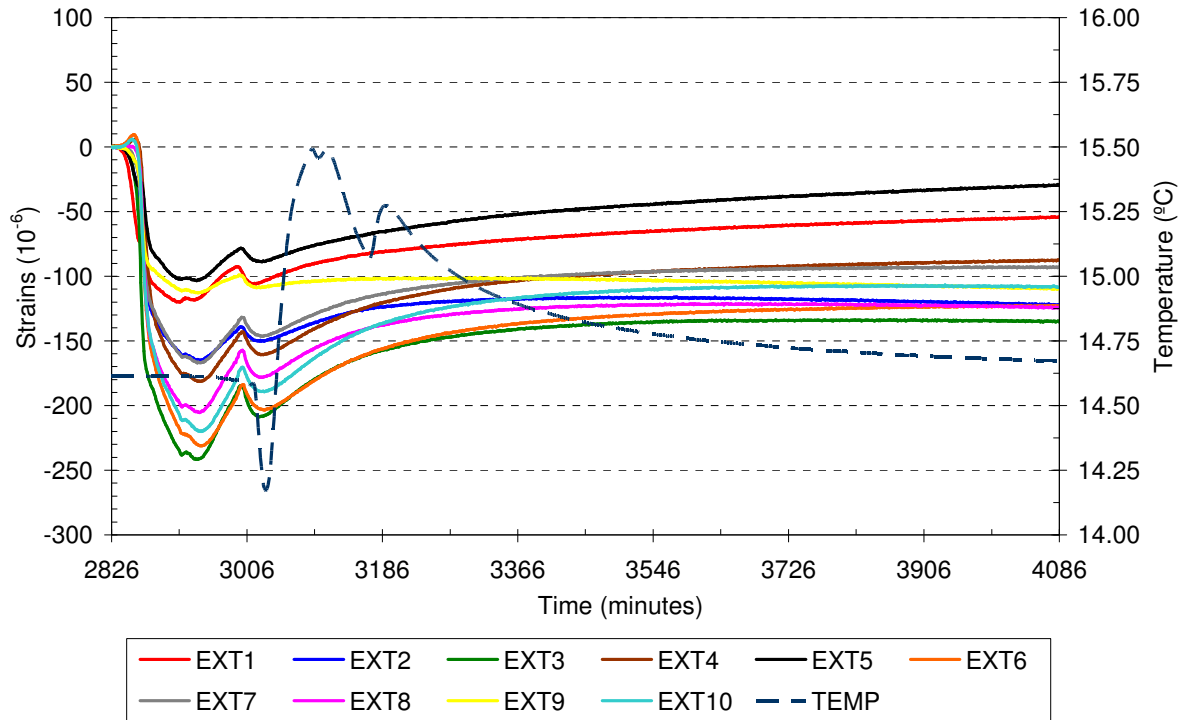
Calculated values

$E = 74 \text{ GPa}$

$\nu = 0.39$

Test 1

Results of the overcoring test



Strains (10^{-6})	ϵ_1	ϵ_2	ϵ_3	ϵ_4	ϵ_5	ϵ_6	ϵ_7	ϵ_8	ϵ_9	ϵ_{10}
Measured	48	129	139	84	22	124	96	131	114	113
Calculated	54	123	141	81	24	129	90	137	106	116

Elastic constants

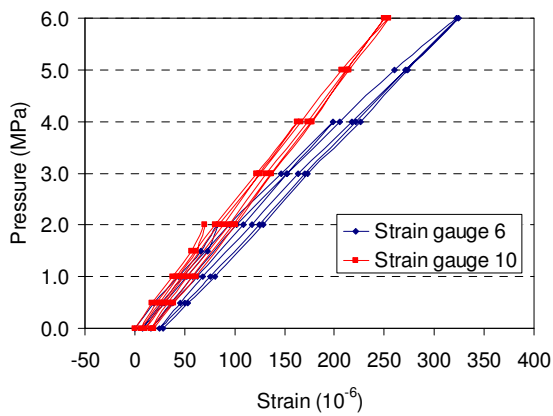
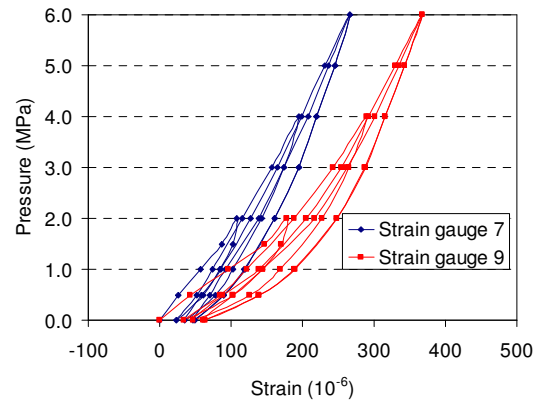
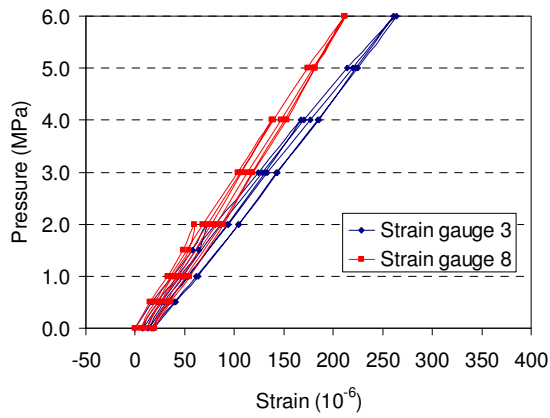
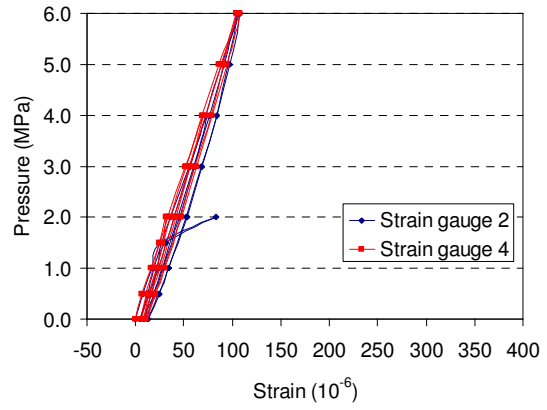
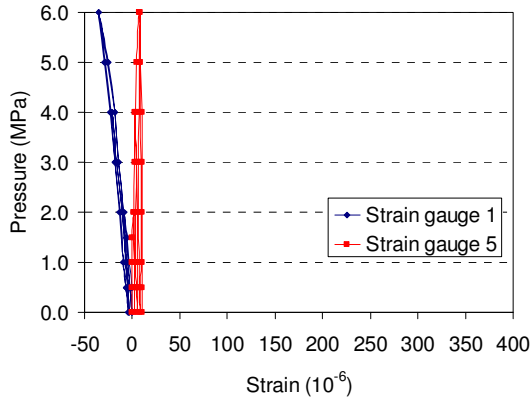
$E = 74 \text{ GPa}$

$\nu = 0.39$

Stresses in the local axis of the STT (MPa)					
σ_{xx}	σ_{yy}	σ_{zz}	τ_{xy}	τ_{yz}	τ_{xz}
5.63	4.95	6.13	-0.17	0.53	-0.07

Test 2

Results of the biaxial test



Unit strains ($10^{-6}/\text{MPa}$) for $p = 6.0 \text{ MPa}$	ϵ_1	ϵ_2	ϵ_3	ϵ_4	ϵ_5	ϵ_6	ϵ_7	ϵ_8	ϵ_9	ϵ_{10}
Measured	-5	16	41	16	0	50	21	33	26	39
Calculated	-6	24	36	24	-6	43	24	36	24	43

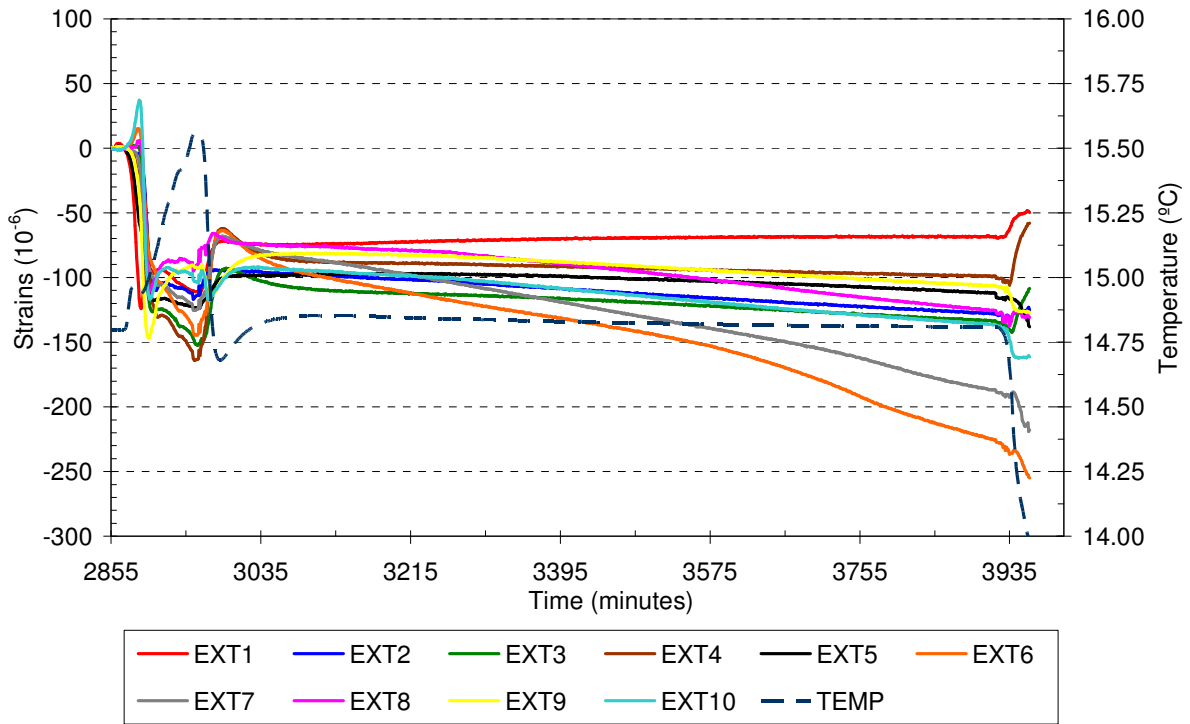
Calculated values

$E = 57 \text{ GPa}$

$\nu = 0.34$

Test 2

Results of the overcoring test



Strains (10^{-6})	ϵ_1	ϵ_2	ϵ_3	ϵ_4	ϵ_5	ϵ_6	ϵ_7	ϵ_8	ϵ_9	ϵ_{10}
Measured	74	99	110	88	98	102	89	77	82	96
Calculated	81	100	101	99	88	101	90	84	76	94

Elastic constants

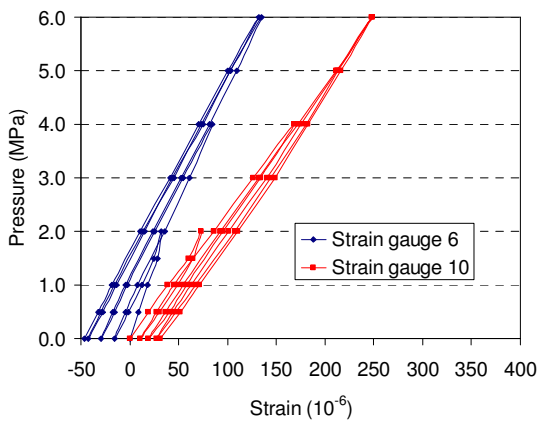
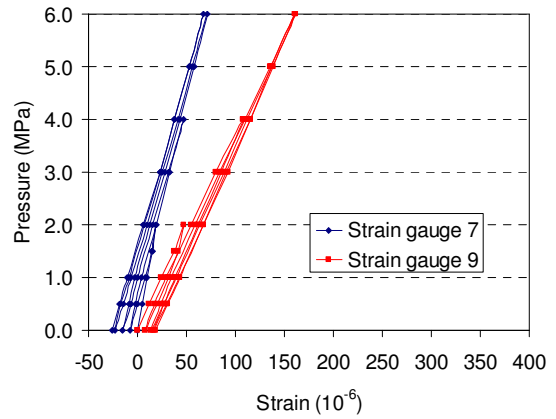
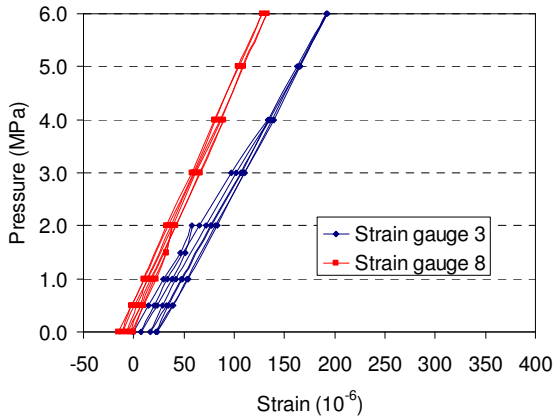
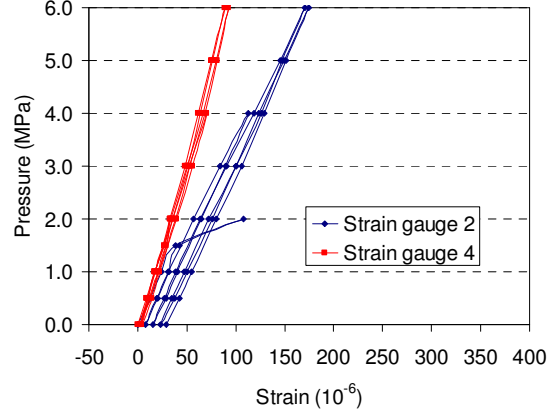
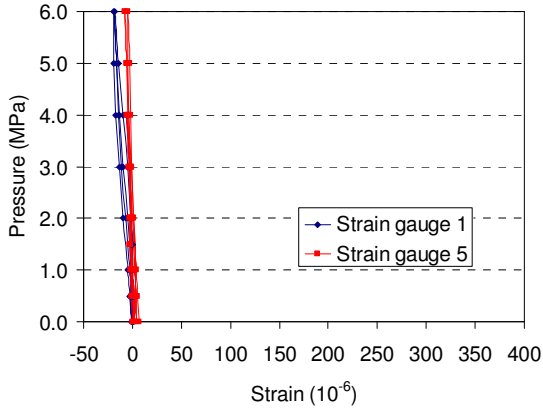
$E = 57 \text{ GPa}$

$\nu = 0.34$

Stresses in the local axis of the STT (MPa)					
σ_{xx}	σ_{yy}	σ_{zz}	τ_{xy}	τ_{yz}	τ_{xz}
3.26	3.32	6.95	-0.08	-0.09	-0.24

Test 3

Results of the biaxial test



Unit strains ($10^{-6}/\text{MPa}$) for $p = 6.0 \text{ MPa}$	ϵ_1	ϵ_2	ϵ_3	ϵ_4	ϵ_5	ϵ_6	ϵ_7	ϵ_8	ϵ_9	ϵ_{10}
Measured	-3	25	28	15	-2	29	15	24	24	37
Calculated	-3	20	28	20	-3	33	20	28	20	33

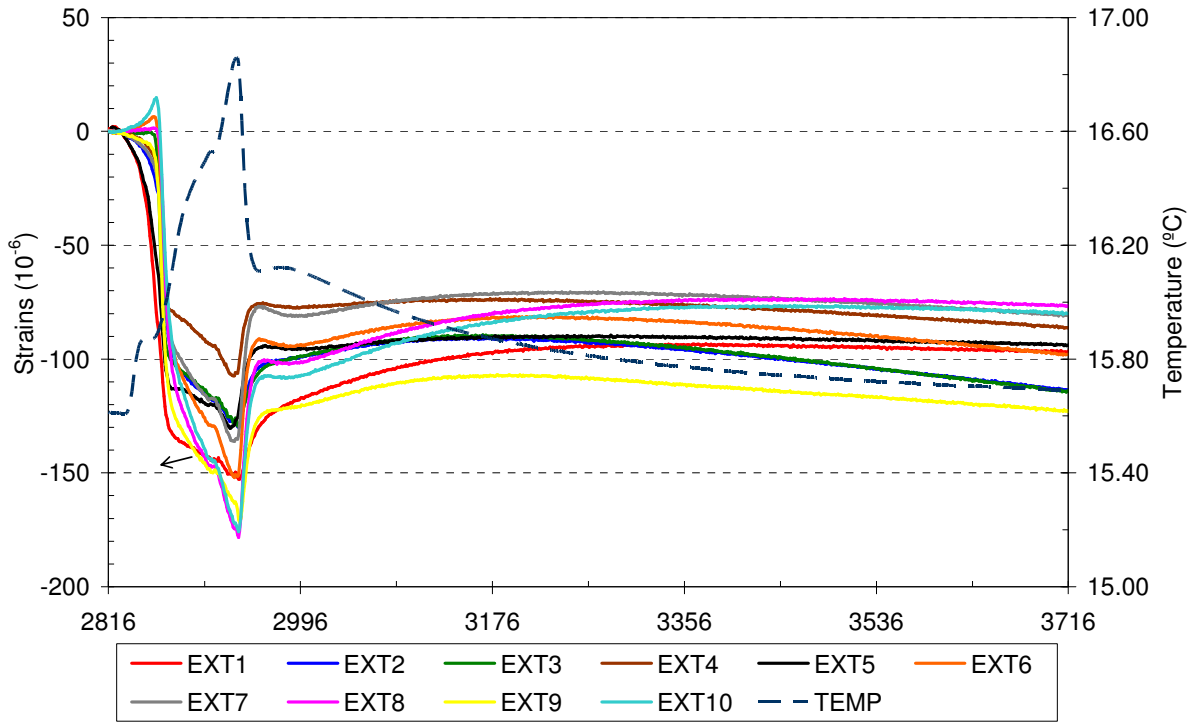
Calculated values

$E = 73 \text{ GPa}$

$\nu = 0.26$

Test 3

Results of the overcoring test



Strains (10^{-6})	ϵ_1	ϵ_2	ϵ_3	ϵ_4	ϵ_5	ϵ_6	ϵ_7	ϵ_8	ϵ_9	ϵ_{10}
Measured	95	92	91	74	90	82	71	77	108	80
Calculated	103	93	84	79	82	78	73	84	99	84

Elastic constants

$E = 73 \text{ GPa}$

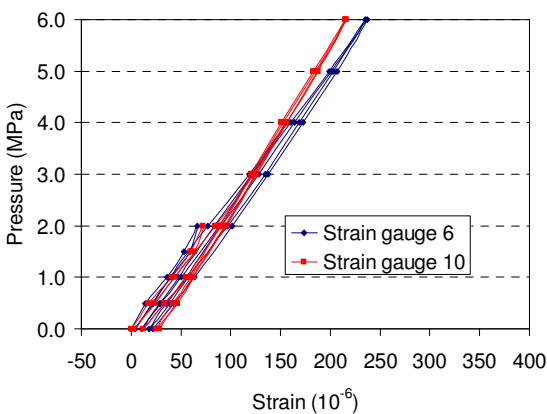
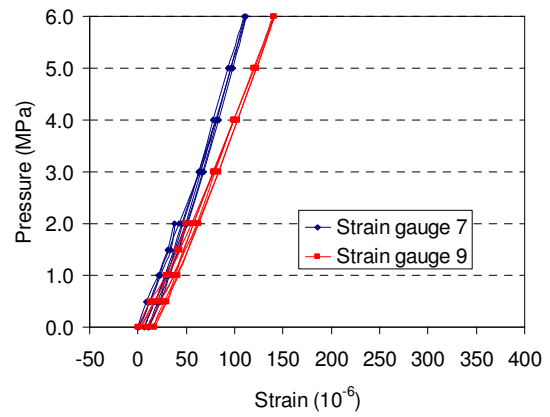
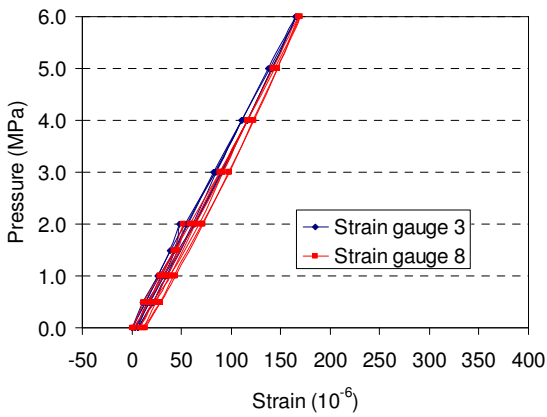
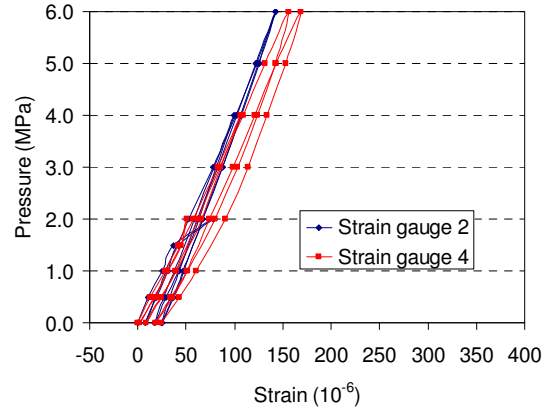
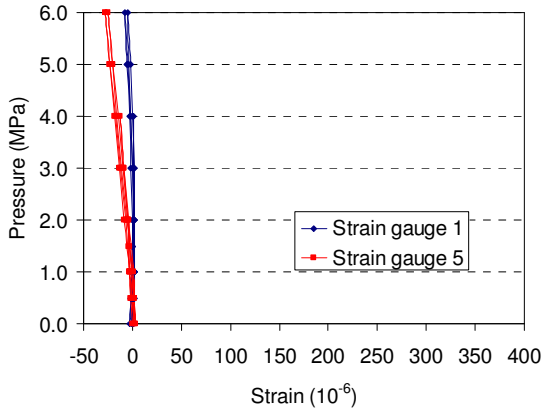
$\nu = 0.26$

Stresses in the local axis of the STT (MPa)

σ_{xx}	σ_{yy}	σ_{zz}	τ_{xy}	τ_{yz}	τ_{xz}
3.39	3.36	8.64	0.07	0.39	-0.01

Test 4

Results of the biaxial test



Unit strains ($10^{-6}/\text{MPa}$) for $p = 6.0 \text{ MPa}$	ϵ_1	ϵ_2	ϵ_3	ϵ_4	ϵ_5	ϵ_6	ϵ_7	ϵ_8	ϵ_9	ϵ_{10}
Measured	-1	20	27	24	-5	36	17	26	21	32
Calculated	-3	20	28	20	-3	34	20	28	20	34

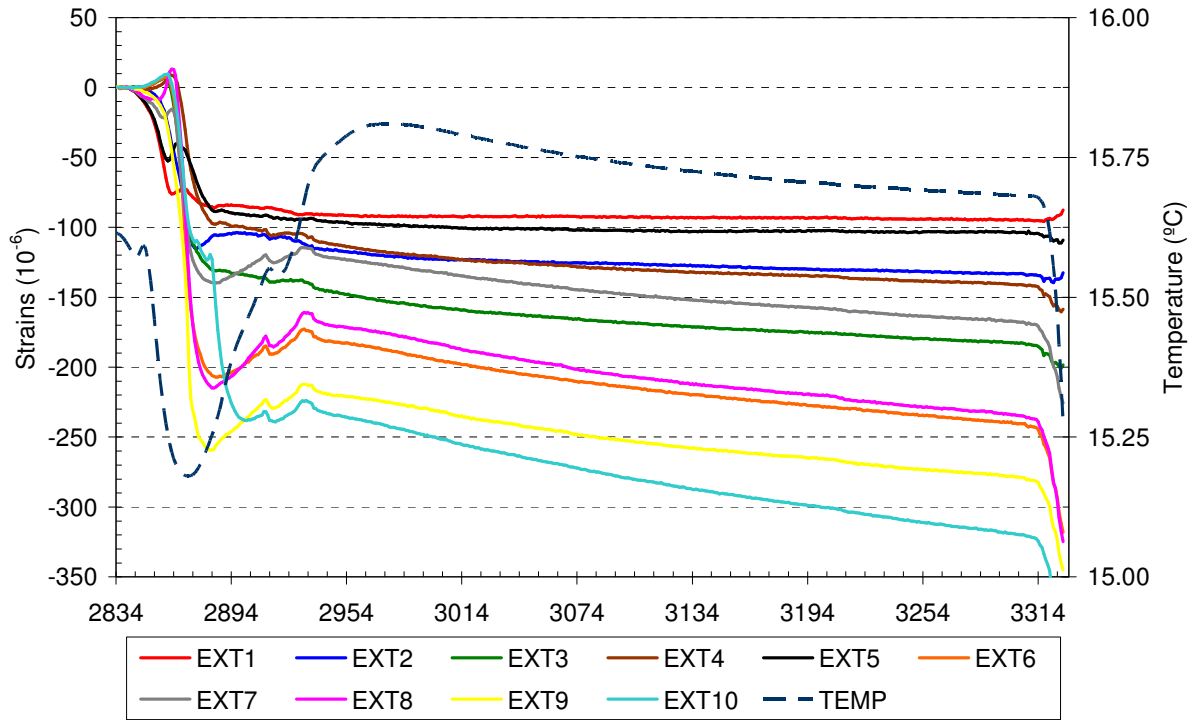
Calculated values

$E = 71 \text{ GPa}$

$\nu = 0.28$

Test 4

Results of the overcoring test



Strains (10^{-6})	ϵ_1	ϵ_2	ϵ_3	ϵ_4	ϵ_5	ϵ_6	ϵ_7	ϵ_8	ϵ_9	ϵ_{10}
Measured	92	117	148	114	96	183	123	171	221	236
Calculated	106	119	133	136	74	180	132	178	213	230

Elastic constants

$E = 71 \text{ GPa}$

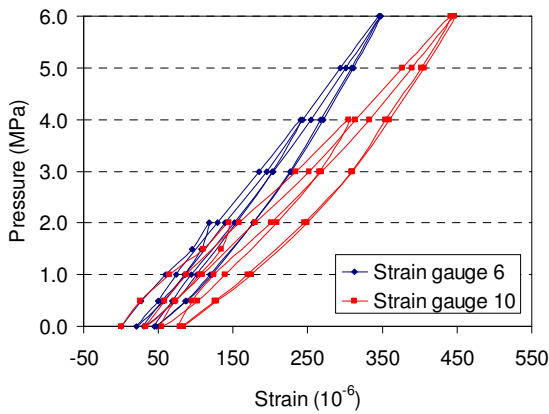
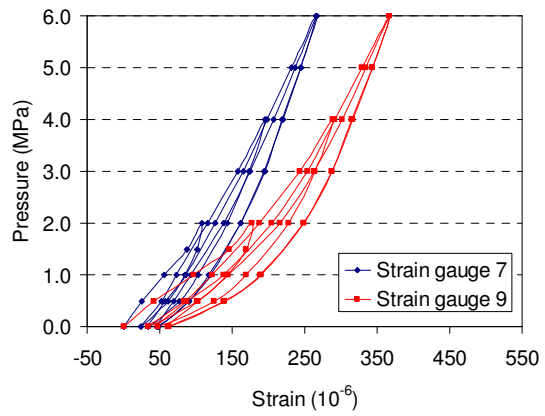
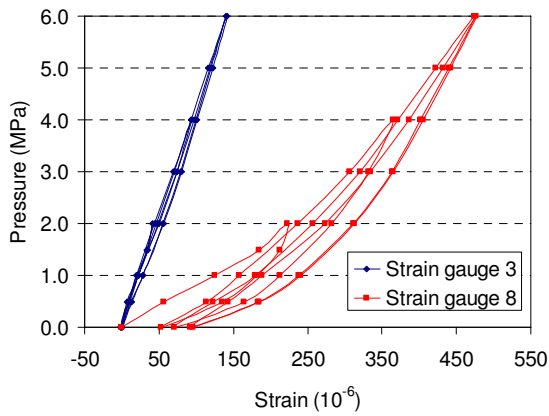
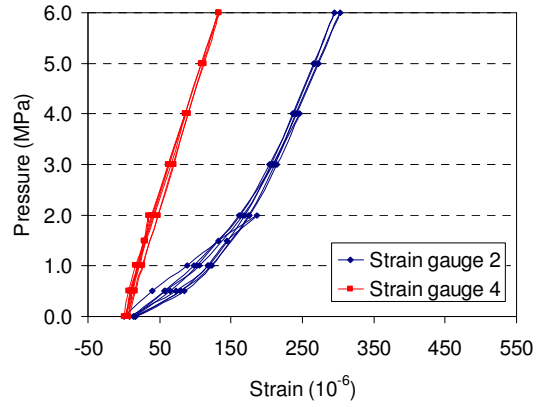
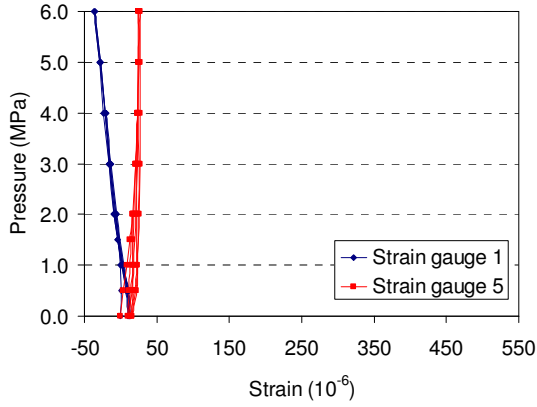
$\nu = 0.28$

Stresses in the local axis of the STT (MPa)

σ_{xx}	σ_{yy}	σ_{zz}	τ_{xy}	τ_{yz}	τ_{xz}
6.27	6.94	8.80	0.58	0.60	0.85

Test 5

Results of the biaxial test



Unit strains ($10^{-6}/\text{MPa}$) for $p = 6.0 \text{ MPa}$	ϵ_1	ϵ_2	ϵ_3	ϵ_4	ϵ_5	ϵ_6	ϵ_7	ϵ_8	ϵ_9	ϵ_{10}
Measured	-7	33	22	22	1	46	29	46	34	55
Calculated	-5	29	42	29	-5	50	29	42	29	50

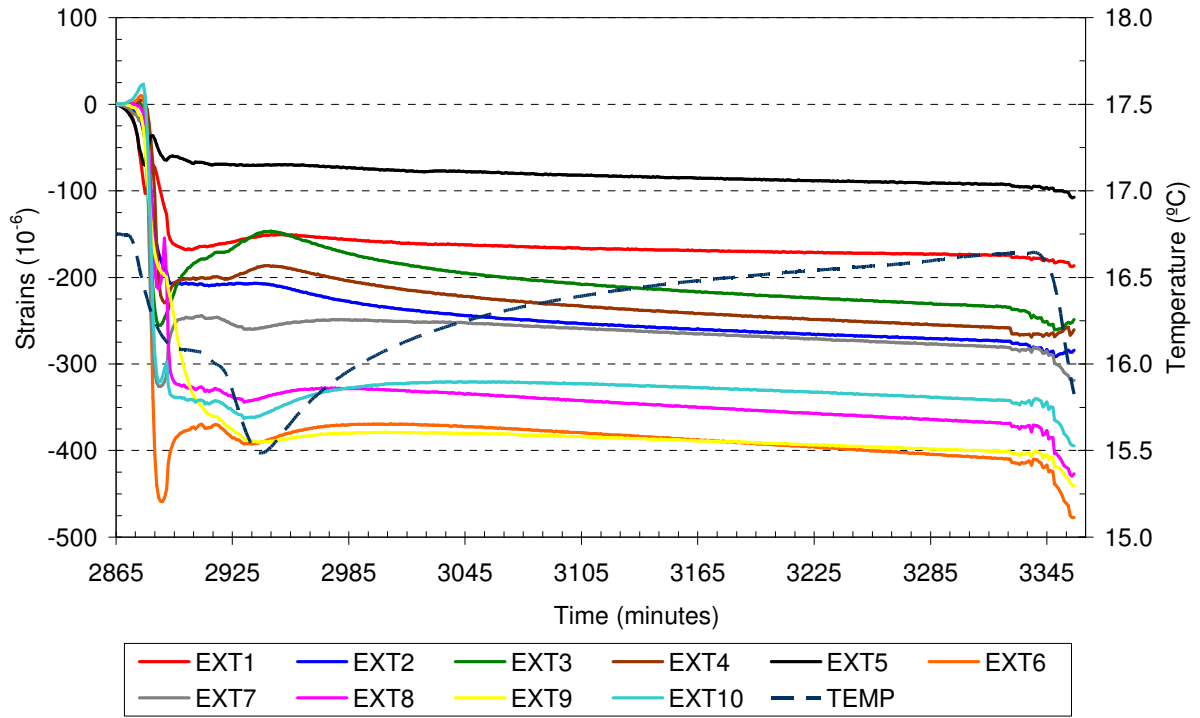
Calculated values

$E = 50 \text{ GPa}$

$\nu = 0.26$

Test 5

Results of the overcoring test



Strains (10^{-6})	ϵ_1	ϵ_2	ϵ_3	ϵ_4	ϵ_5	ϵ_6	ϵ_7	ϵ_8	ϵ_9	ϵ_{10}
Measured	167	253	208	233	82	379	259	342	384	323
Calculated	175	245	239	184	99	356	265	336	358	372

Elastic constants

$E = 50 \text{ GPa}$

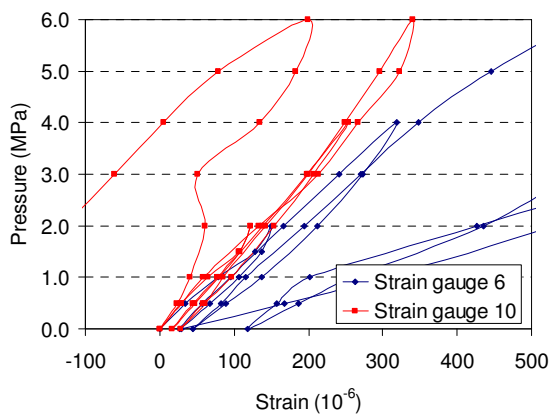
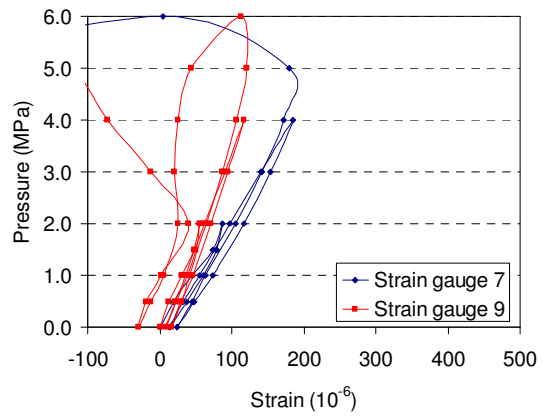
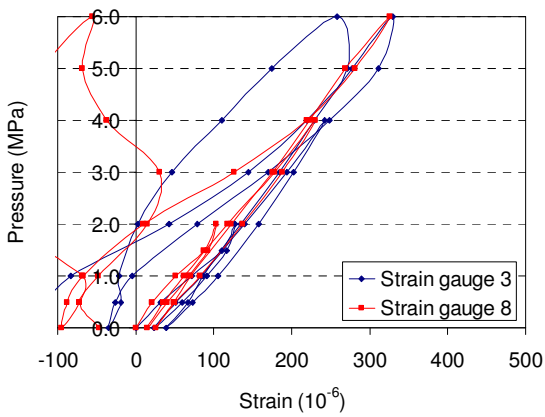
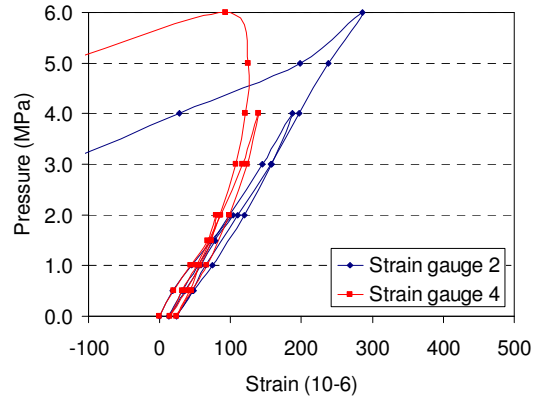
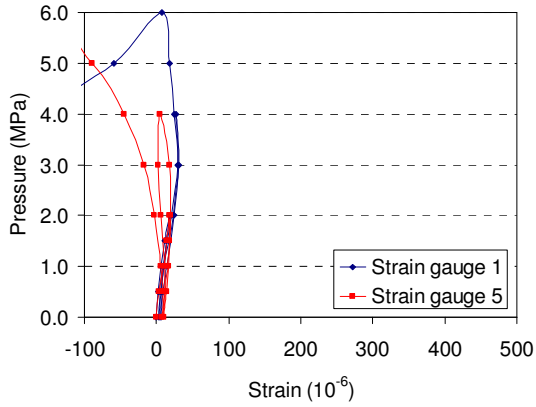
$\nu = 0.26$

Stresses in the local axis of the STT (MPa)

σ_{xx}	σ_{yy}	σ_{zz}	τ_{xy}	τ_{yz}	τ_{xz}
7.89	8.51	9.40	0.13	1.04	1.31

Test 6

Results of the biaxial test



Unit strains ($10^{-6}/\text{MPa}$) for $p = 6.0 \text{ MPa}$	ϵ_1	ϵ_2	ϵ_3	ϵ_4	ϵ_5	ϵ_6	ϵ_7	ϵ_8	ϵ_9	ϵ_{10}
Measured	5	42	49	26	-7	72	39	50	24	56
Calculated	-5	36	52	36	-5	62	36	52	36	62

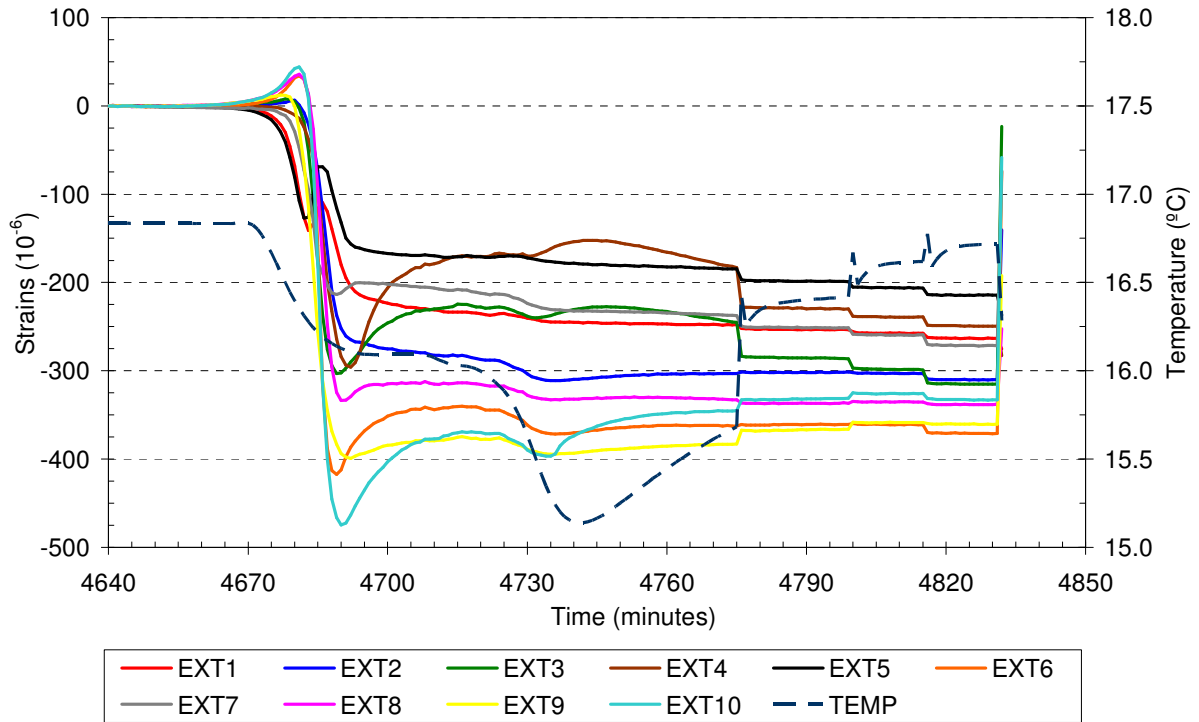
Calculated values

$E = 40 \text{ GPa}$

$\nu = 0.25$

Test 6

Results of the overcoring test



Strains (10^{-6})	ϵ_1	ϵ_2	ϵ_3	ϵ_4	ϵ_5	ϵ_6	ϵ_7	ϵ_8	ϵ_9	ϵ_{10}
Measured	248	303	245	182	185	362	237	333	383	346
Calculated	267	299	247	191	157	349	263	322	376	351

Elastic constants

$E = 40 \text{ GPa}$

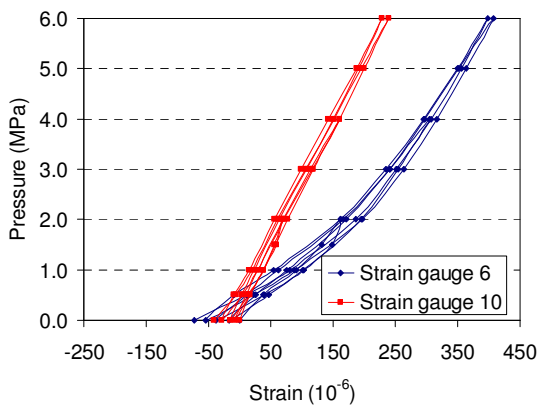
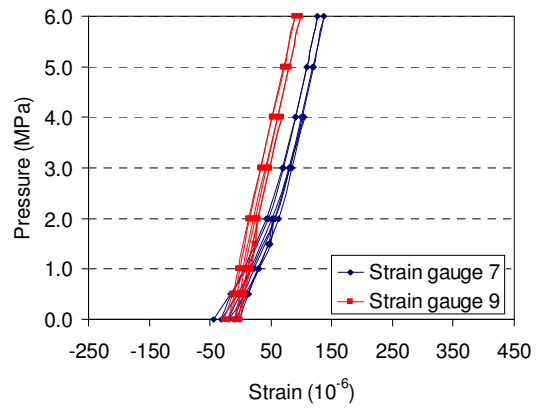
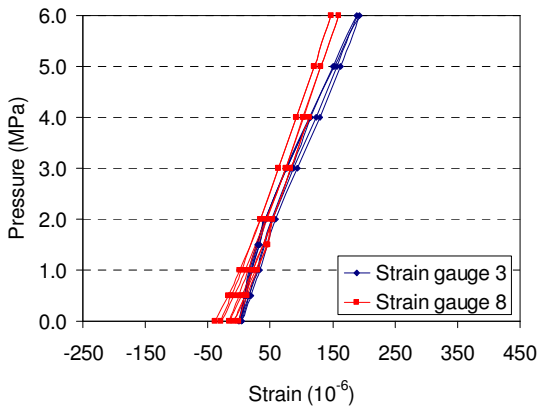
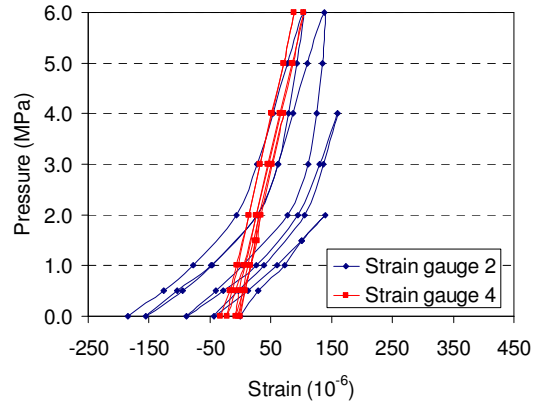
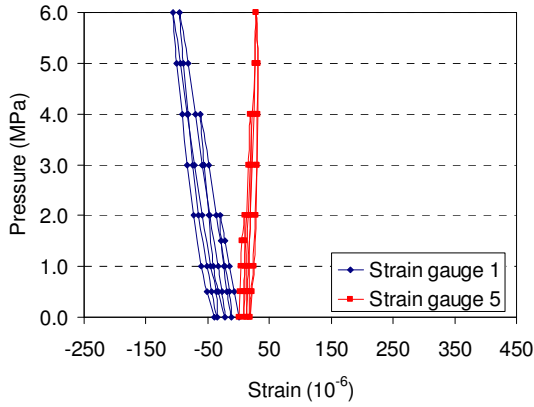
$\nu = 0.25$

Stresses in the local axis of the STT (MPa)					
σ_{xx}	σ_{yy}	σ_{zz}	τ_{xy}	τ_{yz}	τ_{xz}
6.25	6.76	10.86	0.02	1.18	0.80

Borehole PD2

Test 1

Results of the biaxial test



Unit strains ($10^{-6}/\text{MPa}$) for $p = 6.0 \text{ MPa}$	ϵ_1	ϵ_2	ϵ_3	ϵ_4	ϵ_5	ϵ_6	ϵ_7	ϵ_8	ϵ_9	ϵ_{10}
Measured	-9	23	35	19	1	56	21	29	19	43
Calculated	-8	24	37	24	-8	44	24	37	24	44

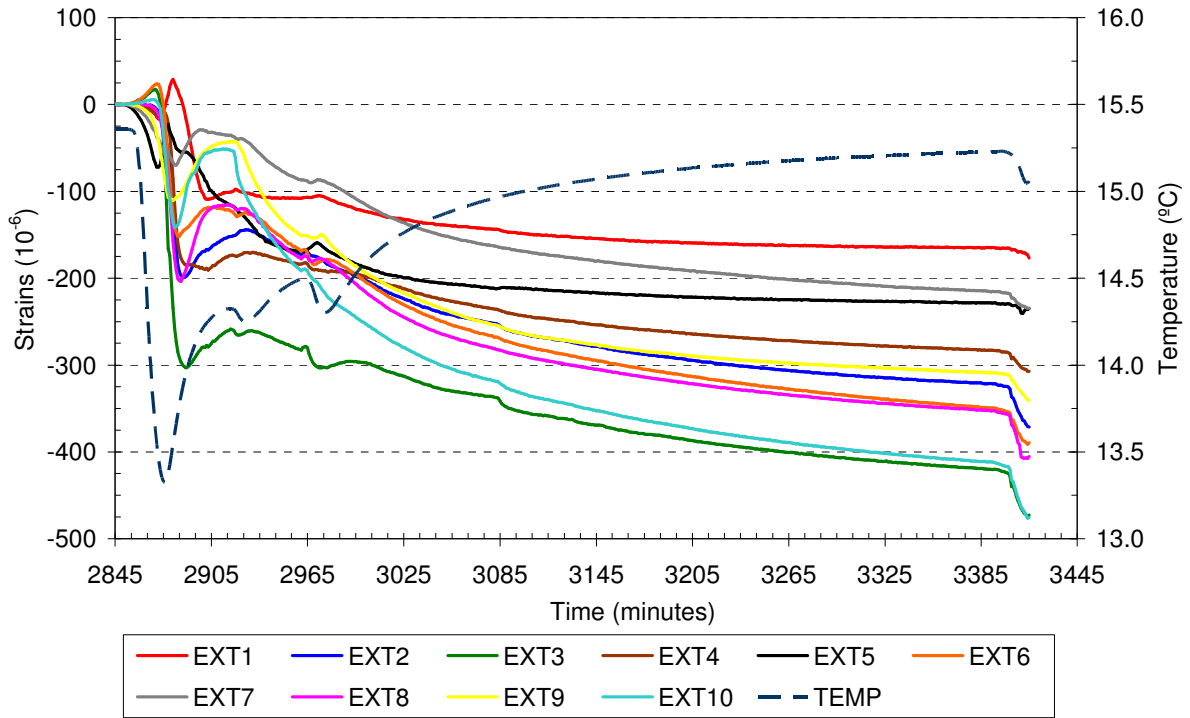
Calculated values

$E = 55 \text{ GPa}$

$\nu = 0.40$

Test 1

Results of the overcoring test



Strains (10^{-6})	ϵ_1	ϵ_2	ϵ_3	ϵ_4	ϵ_5	ϵ_6	ϵ_7	ϵ_8	ϵ_9	ϵ_{10}
Measured	106	169	280	184	167	171	88	175	151	191
Calculated	121	187	250	223	125	151	117	177	146	184

Elastic constants

$E = 55 \text{ GPa}$

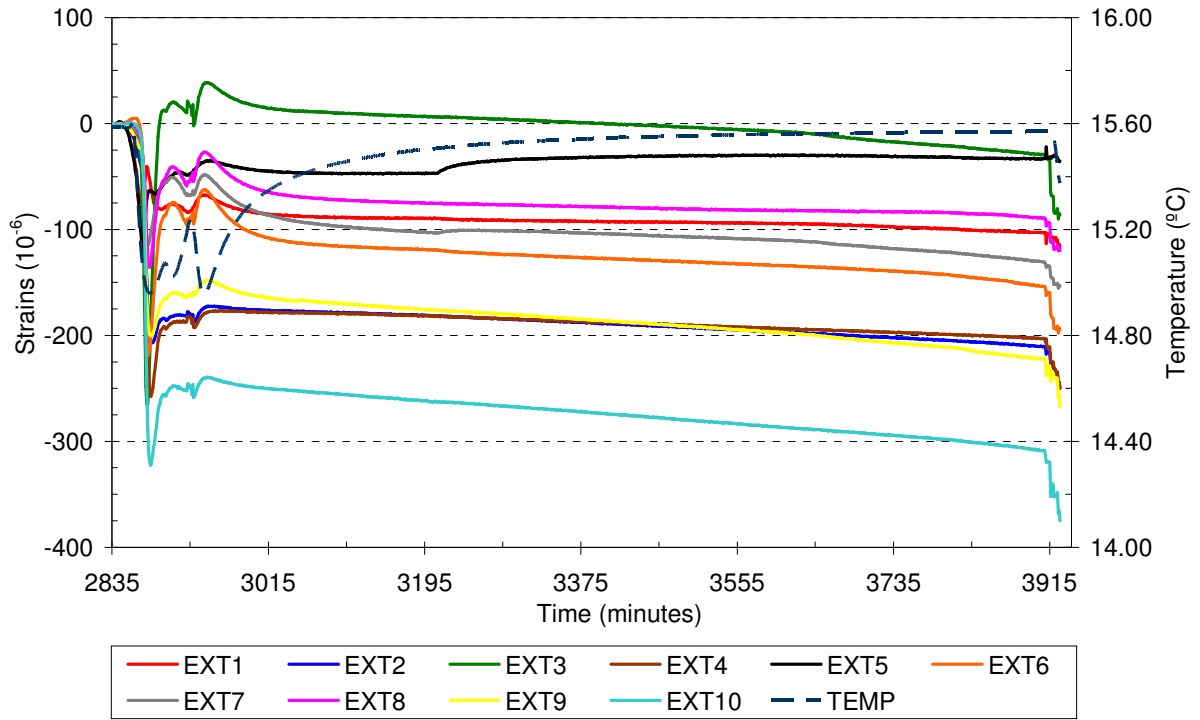
$\nu = 0.40$

Stresses in the local axis of the STT (MPa)

σ_{xx}	σ_{yy}	σ_{zz}	τ_{xy}	τ_{yz}	τ_{xz}
6.98	6.05	11.68	0.32	-0.05	-0.98

Test 2

Results of the overcoring test



Strains (10^{-6})	ϵ_1	ϵ_2	ϵ_3	ϵ_4	ϵ_5	ϵ_6	ϵ_7	ϵ_8	ϵ_9	ϵ_{10}
Measured	89	179	-8	180	47	117	100	74	172	258
Calculated	101	149	158	183	63	165	54	101	163	237

Elastic constants

$E = 55 \text{ GPa}$

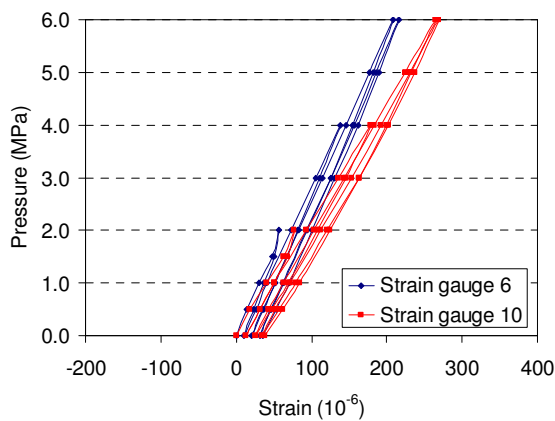
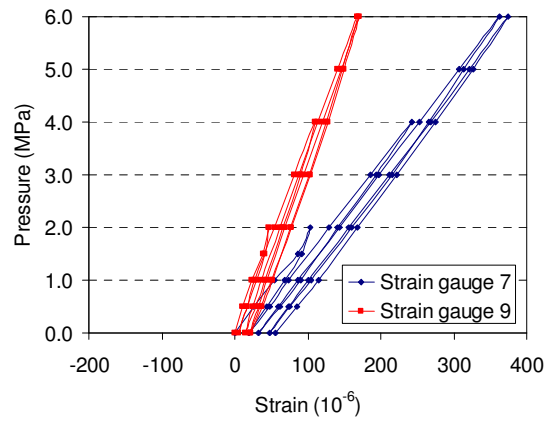
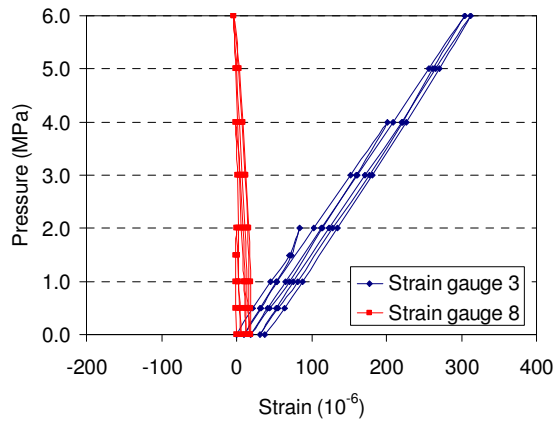
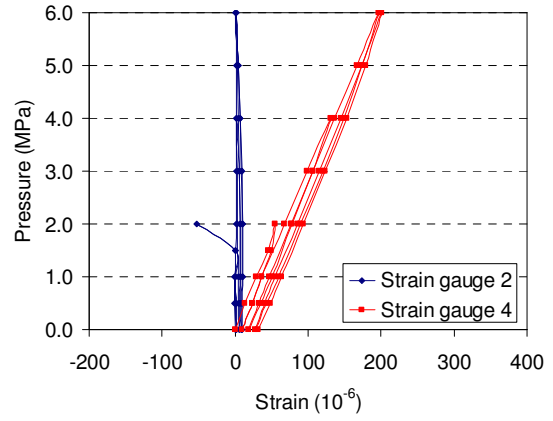
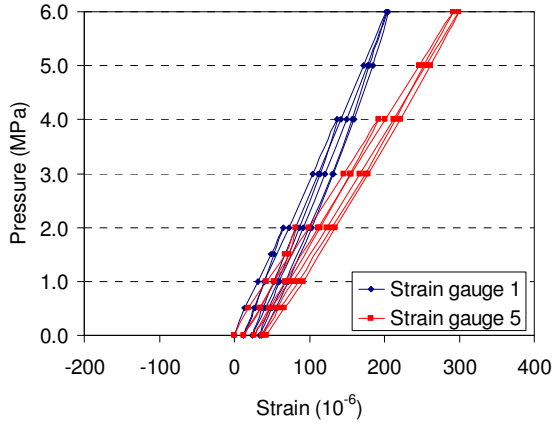
$\nu = 0.40$

Stresses in the local axis of the STT (MPa)

σ_{xx}	σ_{yy}	σ_{zz}	τ_{xy}	τ_{yz}	τ_{xz}
4.94	5.89	7.78	0.71	0.50	-0.77

Test 3

Results of the biaxial test



Unit strains ($10^{-6}/\text{MPa}$) for $p = 6.0 \text{ MPa}$	ϵ_1	ϵ_2	ϵ_3	ϵ_4	ϵ_5	ϵ_6	ϵ_7	ϵ_8	ϵ_9	ϵ_{10}
Measured	28	-1	46	29	43	30	53	-4	25	39
Calculated	0	34	47	34	0	55	34	47	34	55

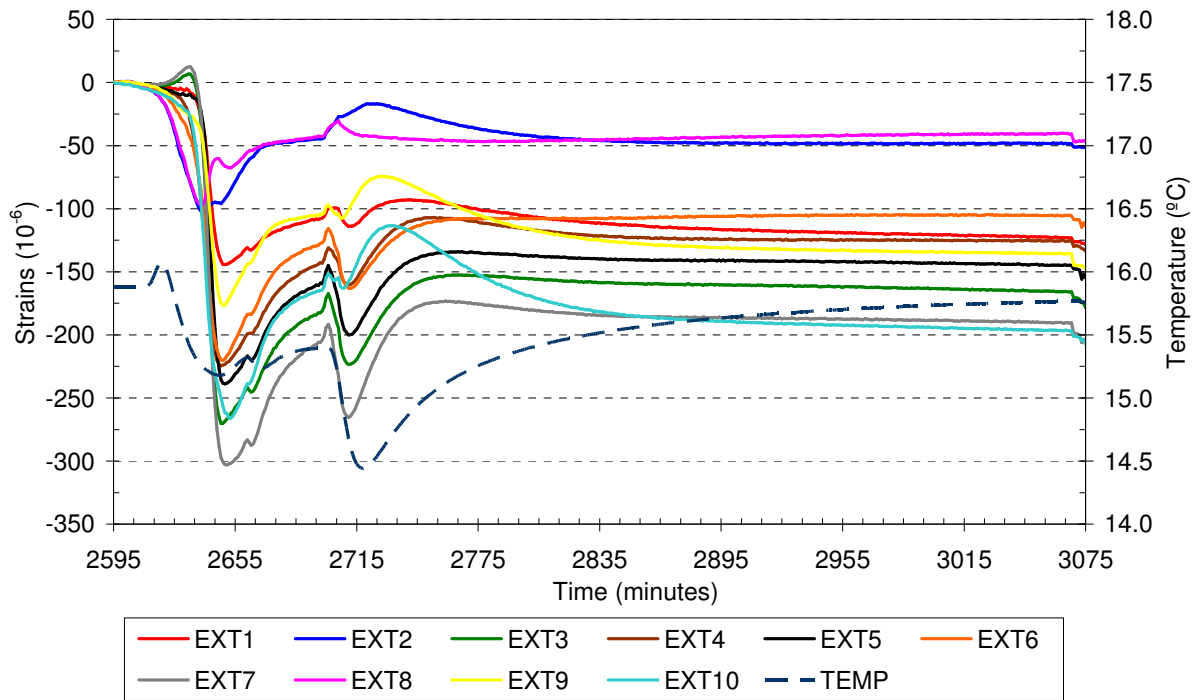
Calculated values

$E = 43 \text{ GPa}$

$\nu = 0.17$

Test 3

Results of the overcoring test



Strains (10^{-6})	ϵ_1	ϵ_2	ϵ_3	ϵ_4	ϵ_5	ϵ_6	ϵ_7	ϵ_8	ϵ_9	ϵ_{10}
Measured	111	46	159	122	140	108	184	46	125	182
Calculated	96	75	95	160	151	128	139	105	114	158

Elastic constants

$E = 43 \text{ GPa}$

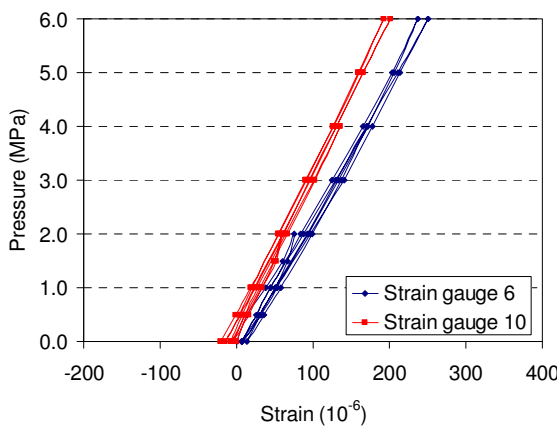
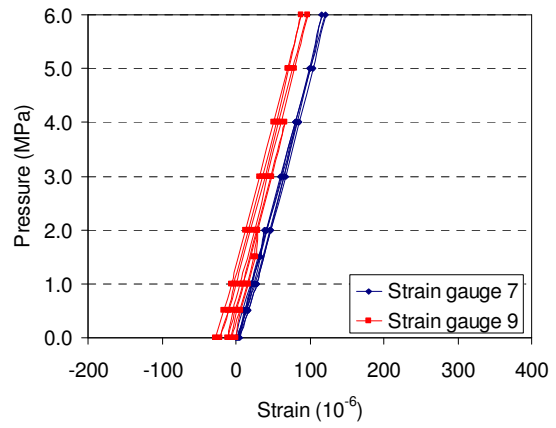
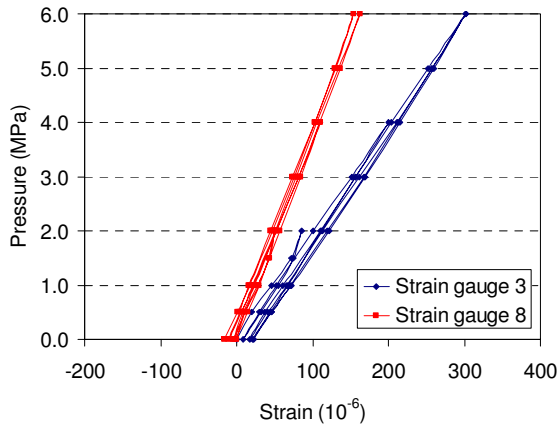
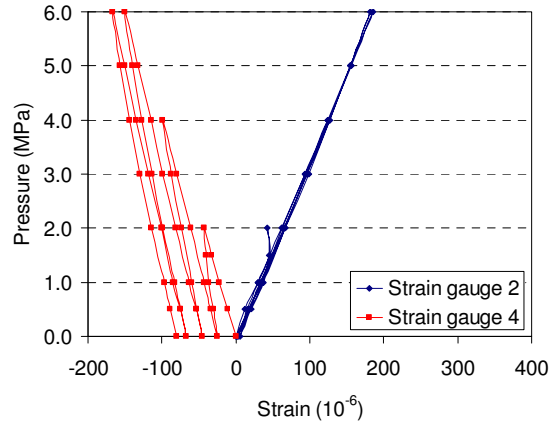
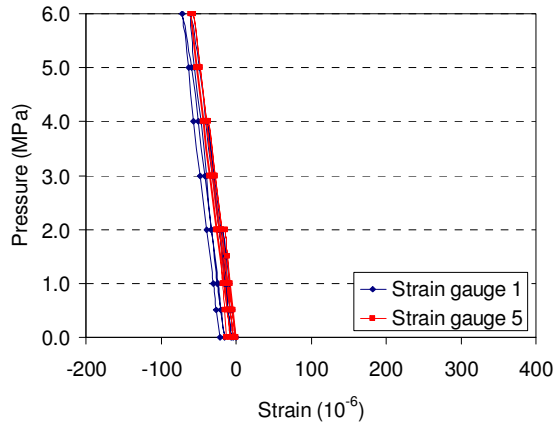
$\nu = 0.17$

Stresses in the local axis of the STT (MPa)

σ_{xx}	σ_{yy}	σ_{zz}	τ_{xy}	τ_{yz}	τ_{xz}
2.31	2.78	6.04	0.20	-0.68	0.12

Test 4

Results of the biaxial test



Unit strains ($10^{-6}/\text{MPa}$) for $p = 6.0 \text{ MPa}$	ϵ_1	ϵ_2	ϵ_3	ϵ_4	ϵ_5	ϵ_6	ϵ_7	ϵ_8	ϵ_9	ϵ_{10}
Measured	-8	30	47	-15	-9	39	19	28	19	35
Calculated	-13	22	35	22	-13	43	22	35	22	43

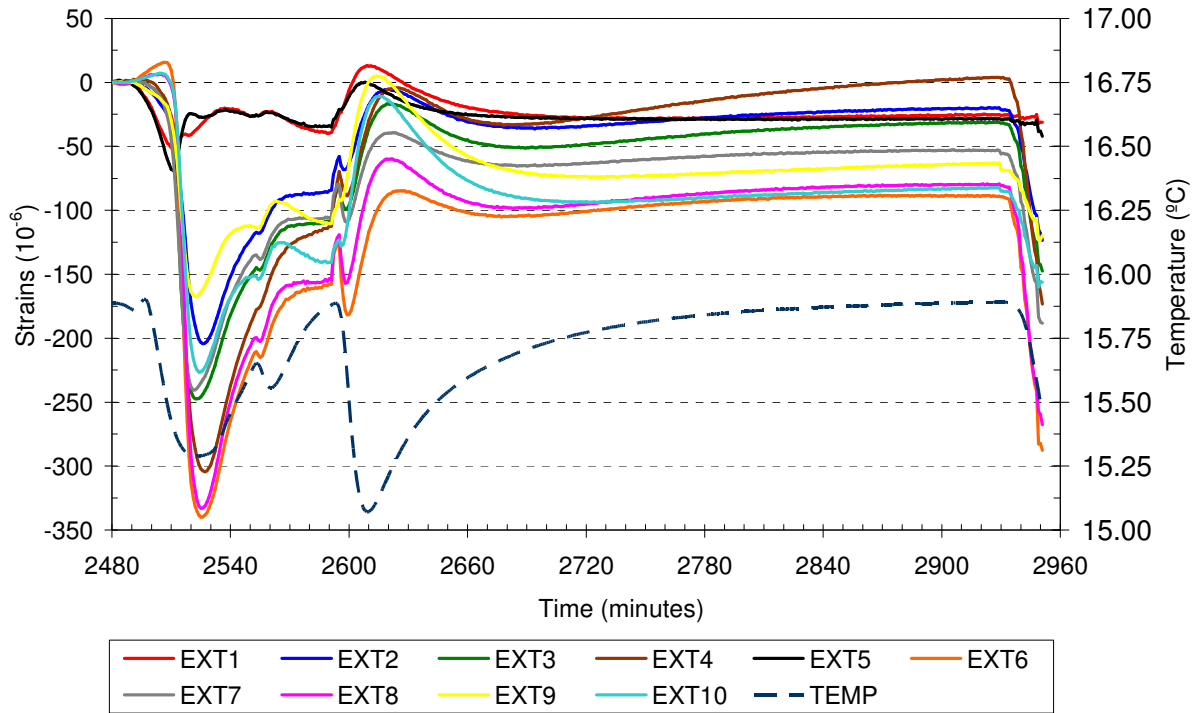
Calculated values

$E = 57 \text{ GPa}$

$\nu = 0.42$

Test 4

Results of the overcoring test



Strains (10^{-6})	ϵ_1	ϵ_2	ϵ_3	ϵ_4	ϵ_5	ϵ_6	ϵ_7	ϵ_8	ϵ_9	ϵ_{10}
Measured	39	85	109	114	34	159	106	154	110	140
Calculated	32	89	120	100	39	146	116	141	114	151

Elastic constants

$E = 57 \text{ GPa}$

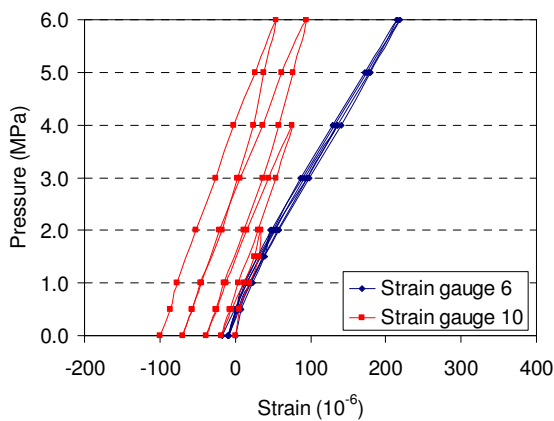
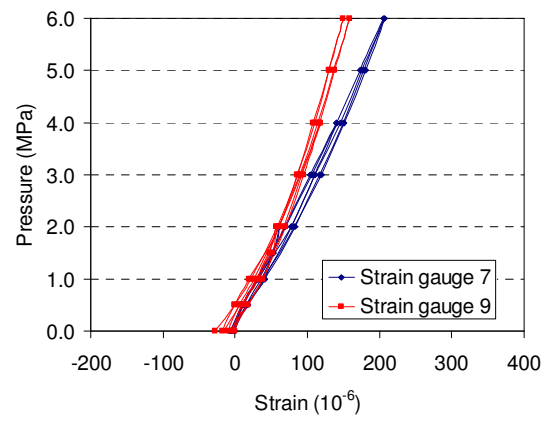
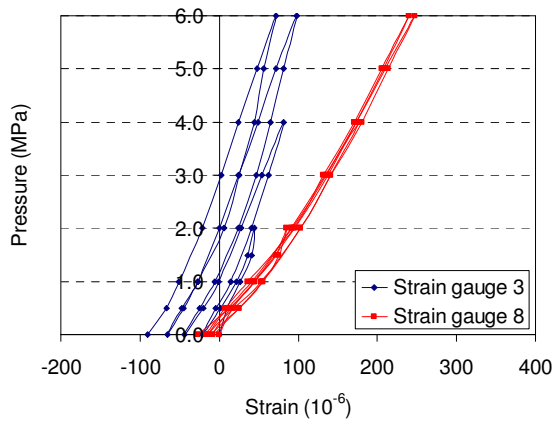
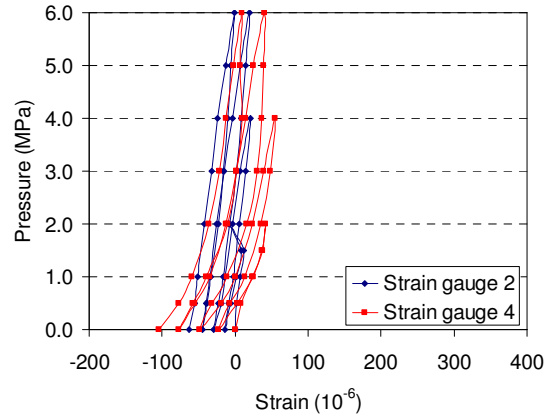
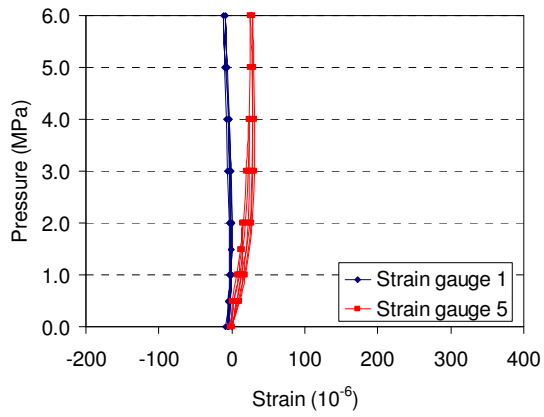
$\nu = 0.42$

Stresses in the local axis of the STT (MPa)

σ_{xx}	σ_{yy}	σ_{zz}	τ_{xy}	τ_{yz}	τ_{xz}
4.50	4.53	4.92	0.05	-0.09	0.28

Test 5

Results of the biaxial test



Unit strains ($10^{-6}/\text{MPa}$) for $p = 6.0 \text{ MPa}$	ϵ_1	ϵ_2	ϵ_3	ϵ_4	ϵ_5	ϵ_6	ϵ_7	ϵ_8	ϵ_9	ϵ_{10}
Measured	-2	-9	21	9	0	41	32	36	23	23
Calculated	-5	21	31	21	-5	37	21	31	21	37

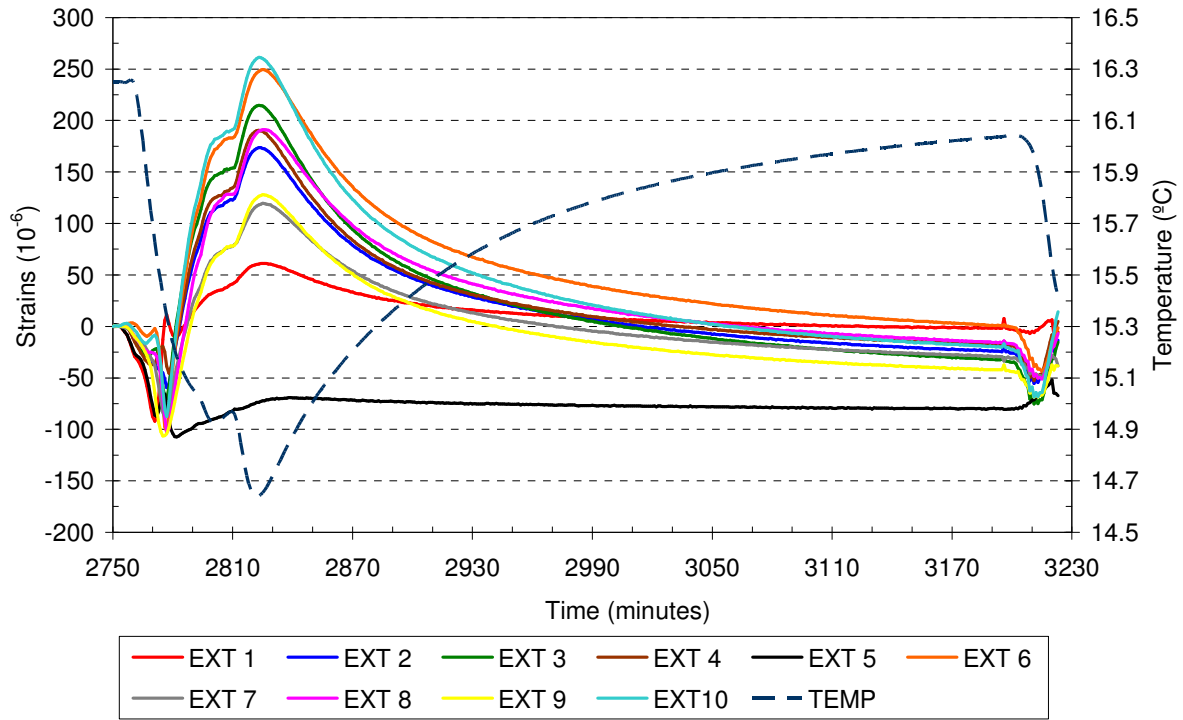
Calculated values

$E = 75 \text{ GPa}$

$\nu = 0.24$

Test 5

Results of the overcoring test



Strains (10^{-6})	ϵ_1	ϵ_2	ϵ_3	ϵ_4	ϵ_5	ϵ_6	ϵ_7	ϵ_8	ϵ_9	ϵ_{10}
Measured	-34	-79	-94	-83	72	-136	-54	-98	-51	-123
Calculated	-20	-89	-98	-83	-17	-125	-68	-81	-68	-121

Elastic constants

$E = 75 \text{ GPa}$

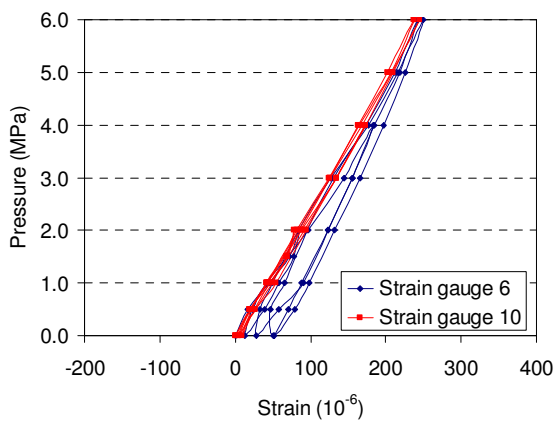
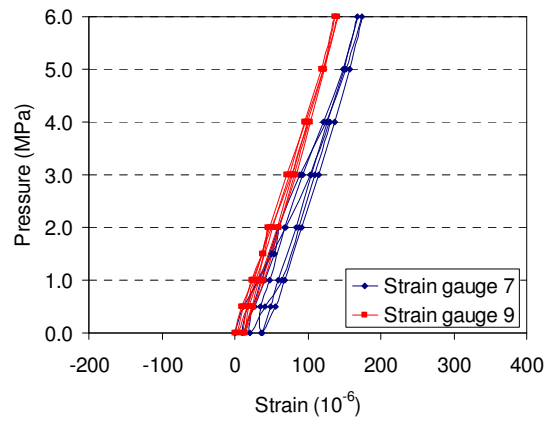
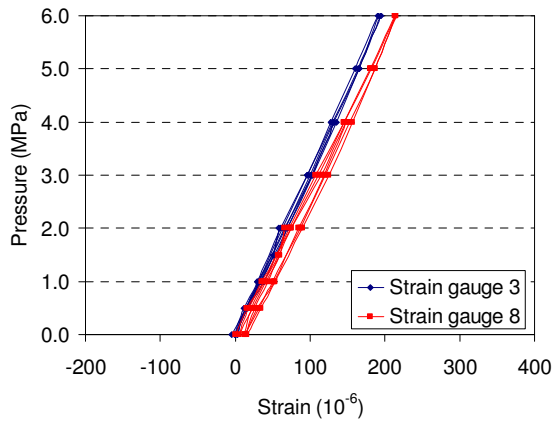
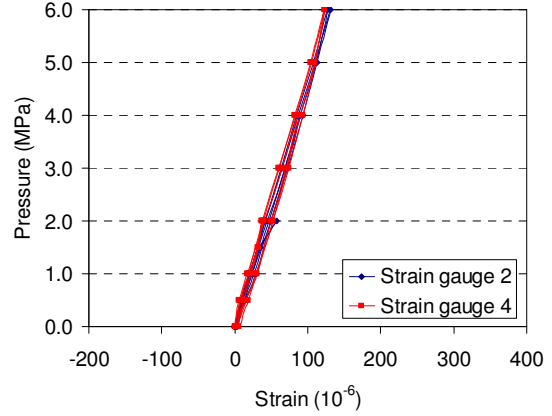
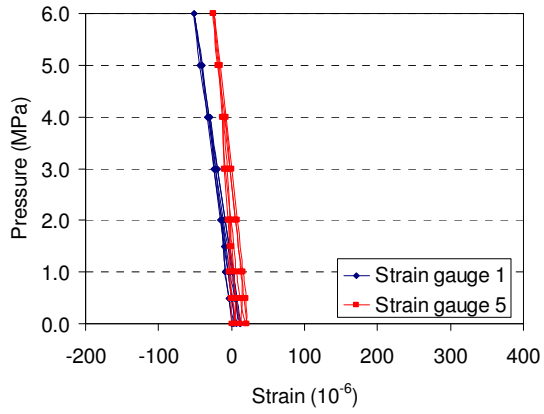
$\nu = 0.24$

Stresses in the local axis of the STT (MPa)

σ_{xx}	σ_{yy}	σ_{zz}	τ_{xy}	τ_{yz}	τ_{xz}
-3.57	-3.96	-2.03	0.04	-0.06	0.36

Test 6

Results of the biaxial test



Unit strains ($10^{-6}/\text{MPa}$) for $p = 6.0 \text{ MPa}$	ϵ_1	ϵ_2	ϵ_3	ϵ_4	ϵ_5	ϵ_6	ϵ_7	ϵ_8	ϵ_9	ϵ_{10}
Measured	-10	21	32	20	-8	33	22	33	21	39
Calculated	-9	20	32	20	-9	38	20	32	20	38

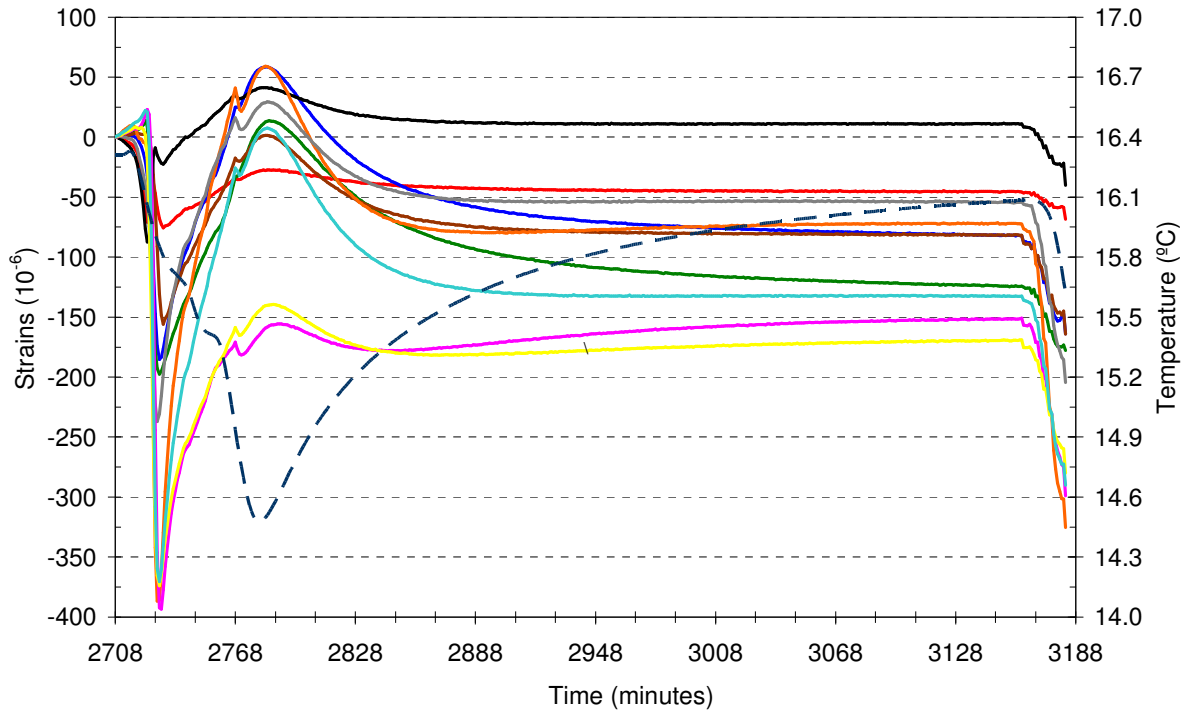
Calculated values

$$E = 61 \text{ GPa}$$

$$\nu = 0.46$$

Test 6

Results of the overcoring test



Strains (10^{-6})	ϵ_1	ϵ_2	ϵ_3	ϵ_4	ϵ_5	ϵ_6	ϵ_7	ϵ_8	ϵ_9	ϵ_{10}
Measured	44	71	109	79	-11	77	54	164	178	132
Calculated	51	64	117	72	-4	77	55	162	171	139

Elastic constants

$E = 61 \text{ GPa}$

$\nu = 0.46$

Stresses in the local axis of the STT (MPa)

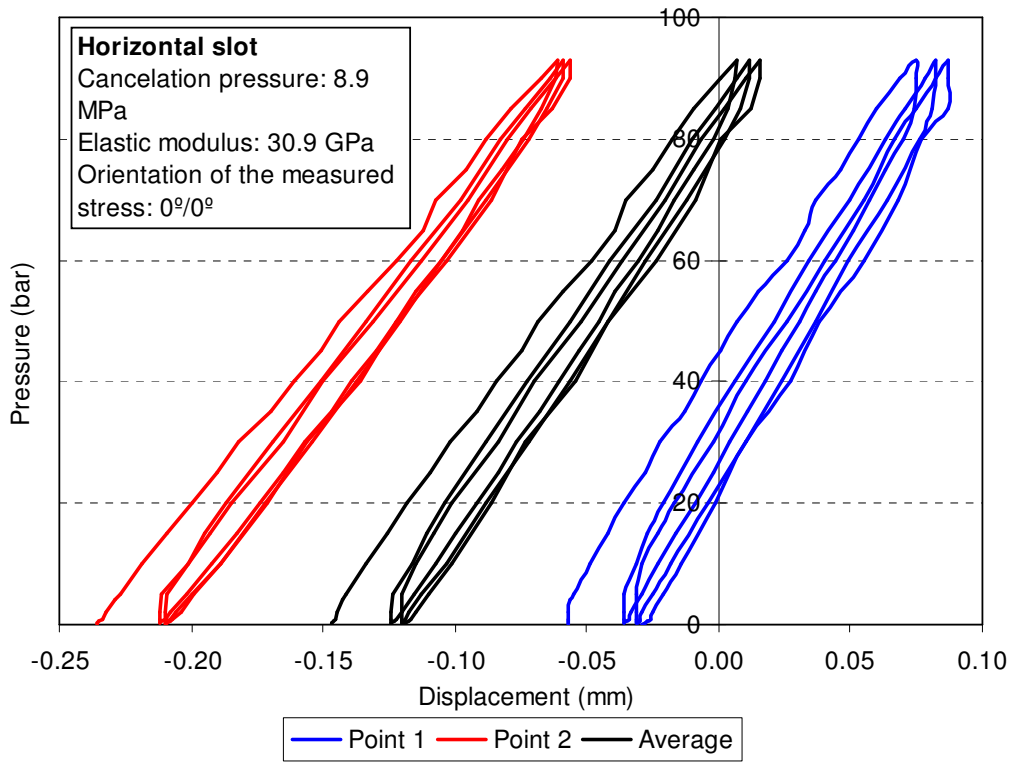
σ_{xx}	σ_{yy}	σ_{zz}	τ_{xy}	τ_{yz}	τ_{xz}
4.84	3.92	4.79	0.75	0.77	0.65

APPENDIX C

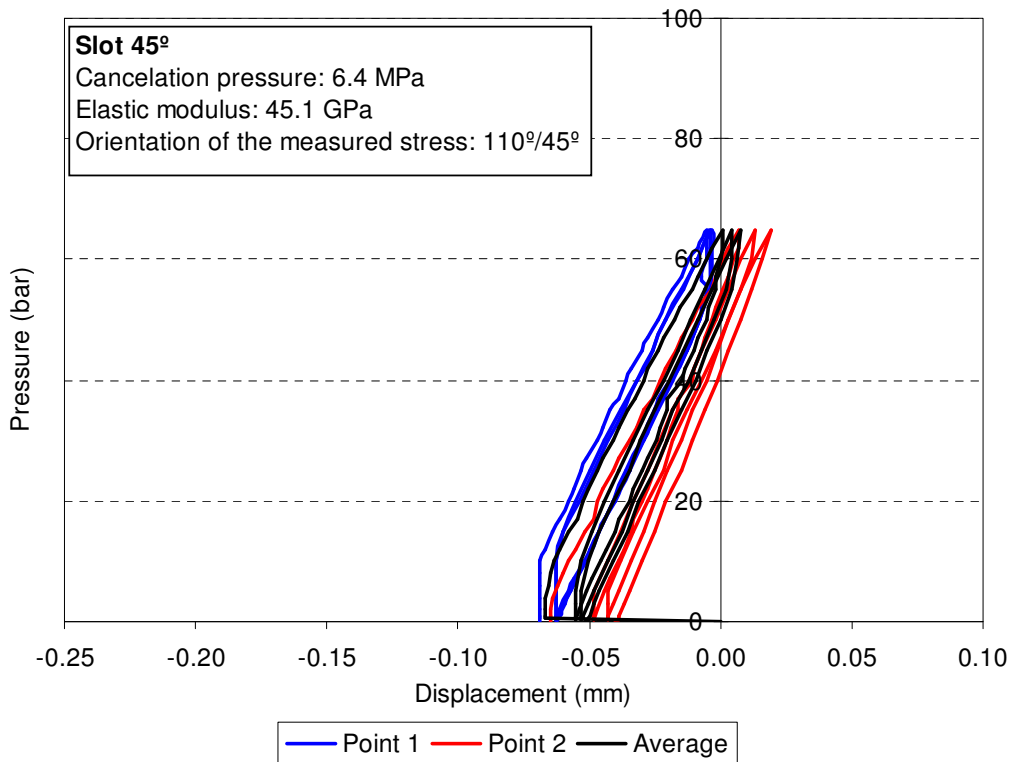
Small flat jack test results

Location SFJ1

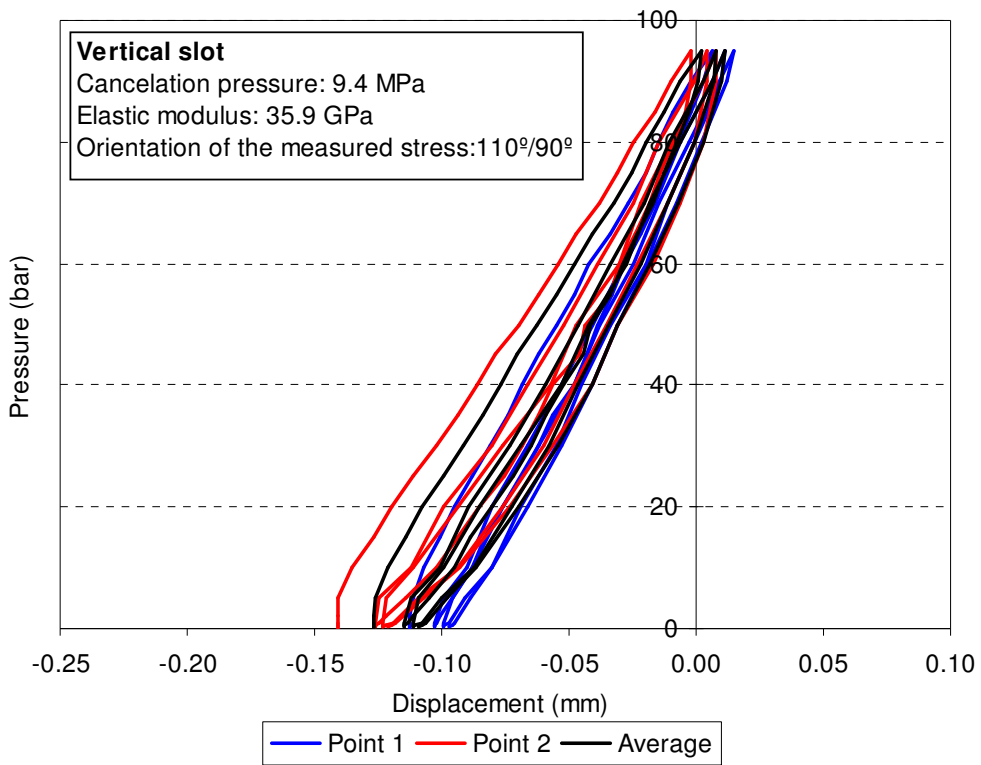
Test 1



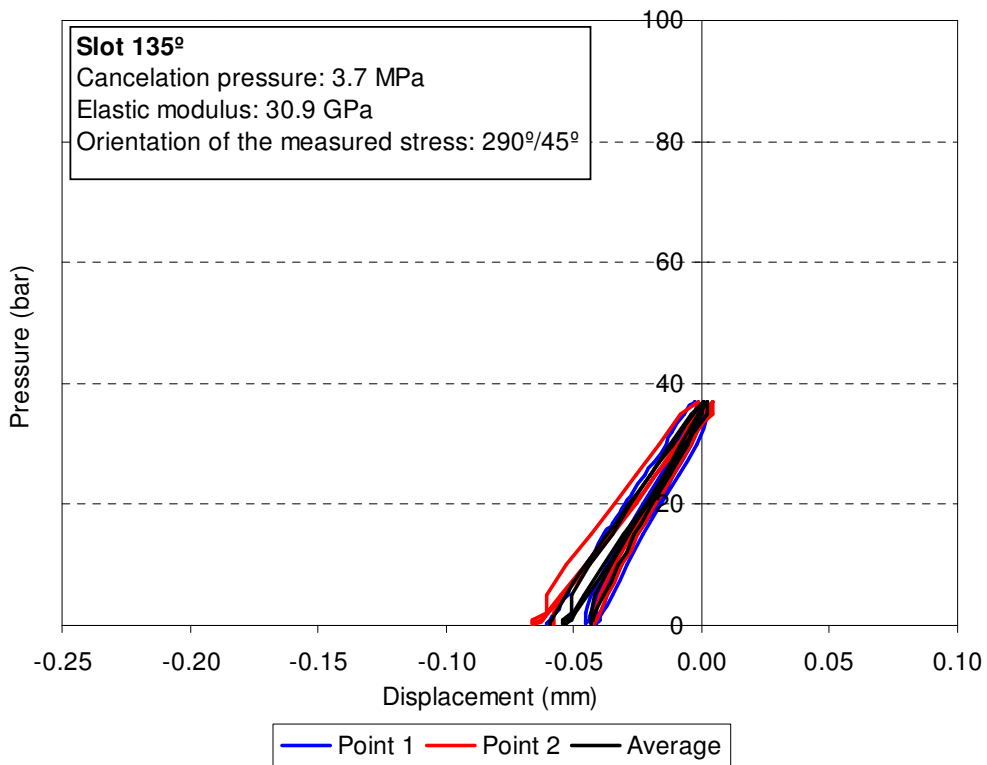
Test 2



Test 3

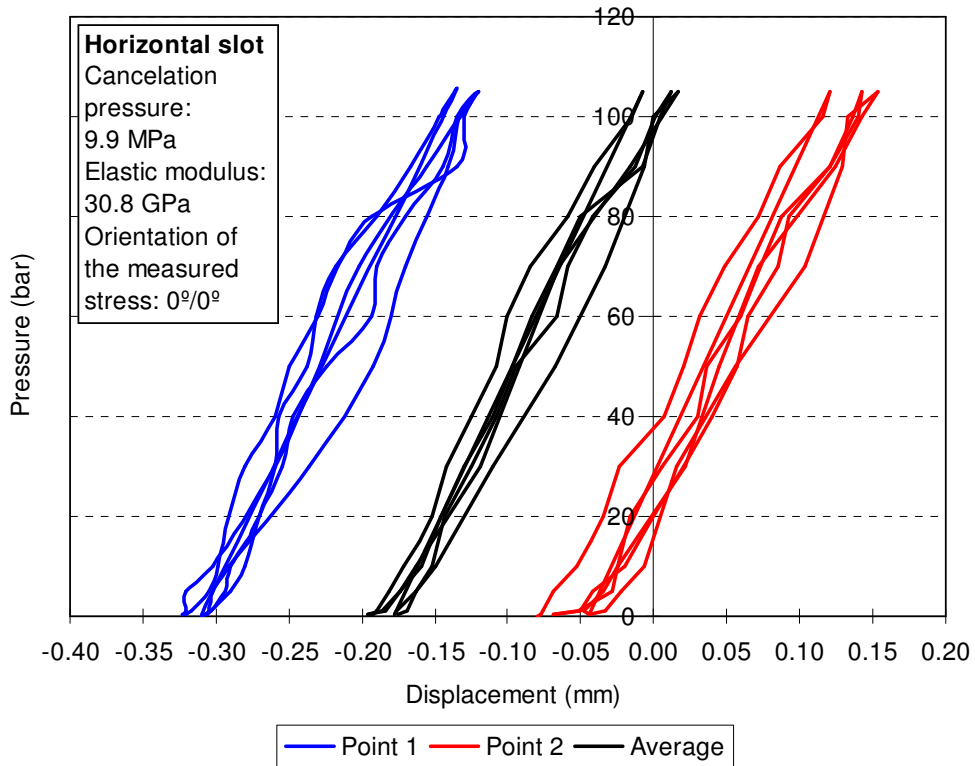


Test 4

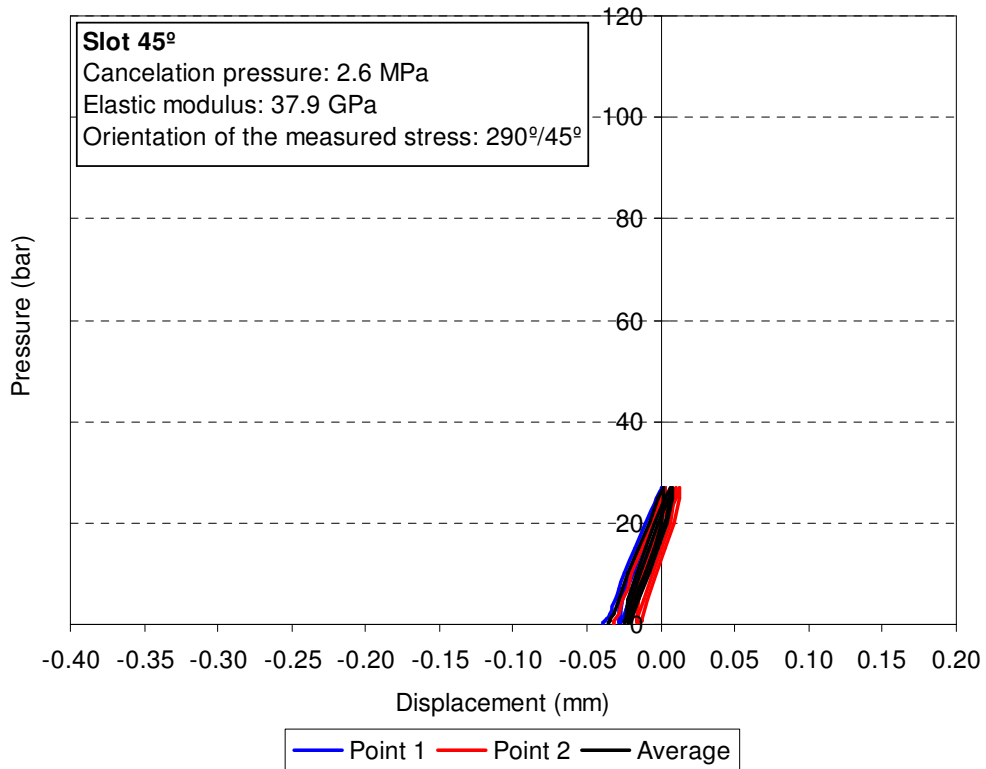


Location SFJ2

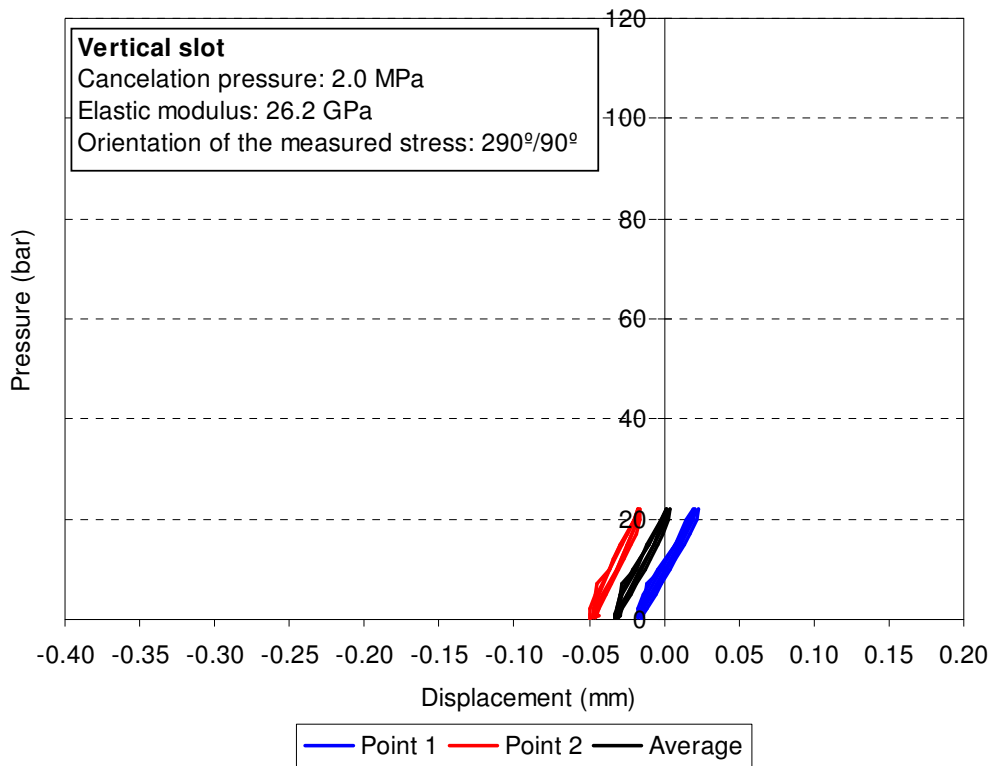
Test 1



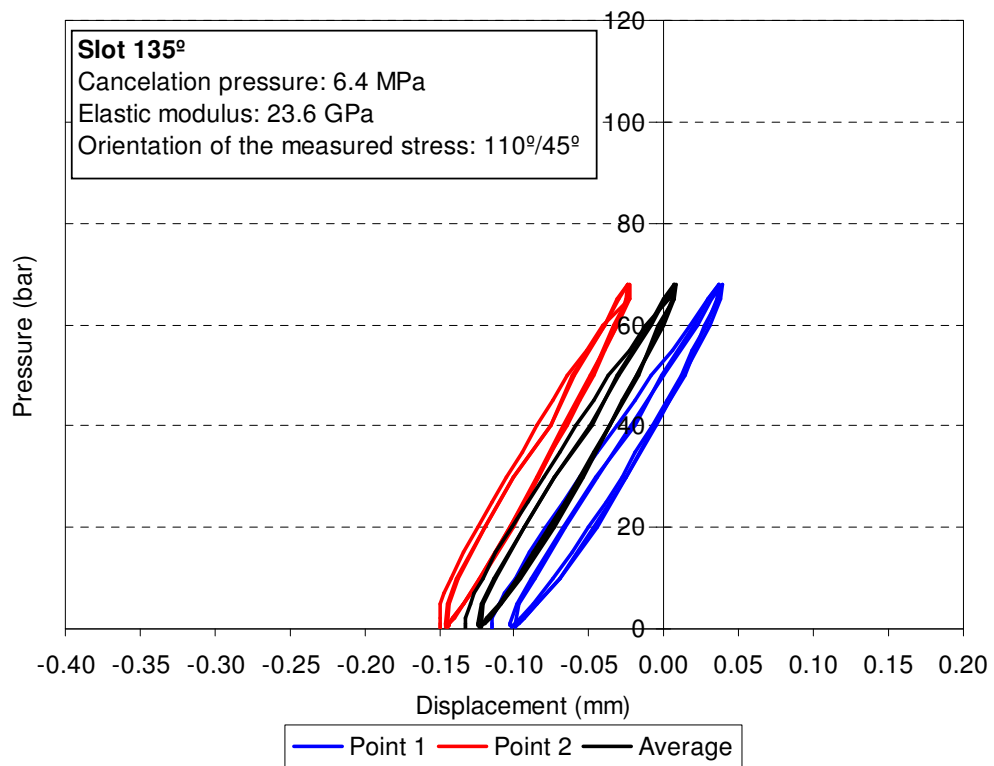
Test 2



Test 3

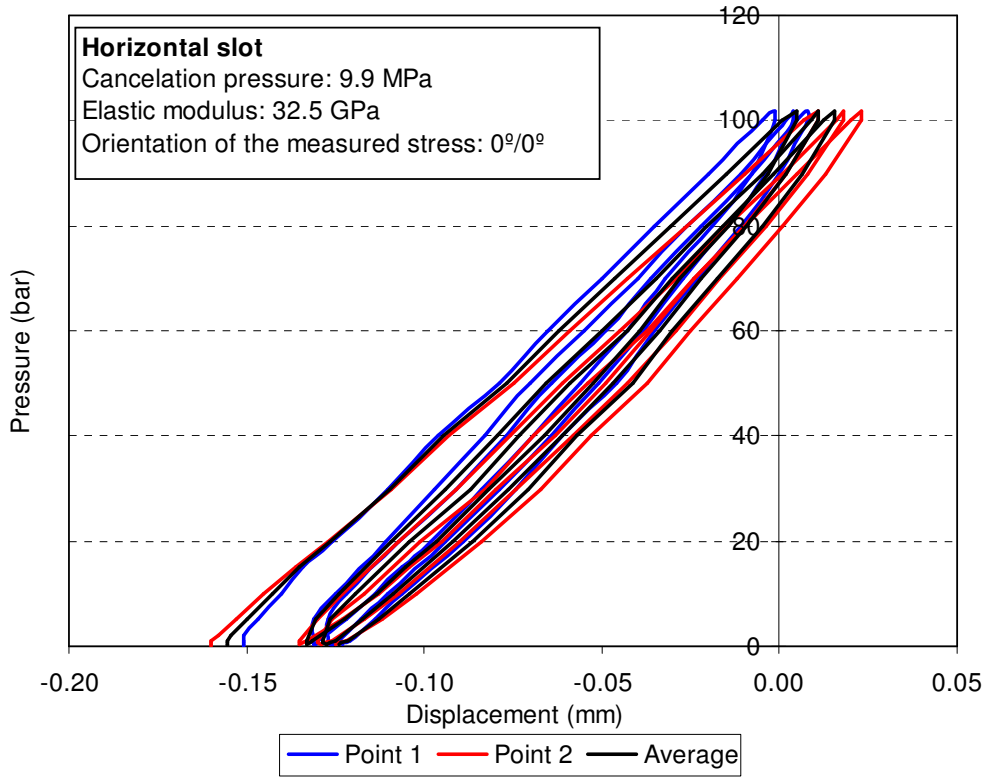


Test 4

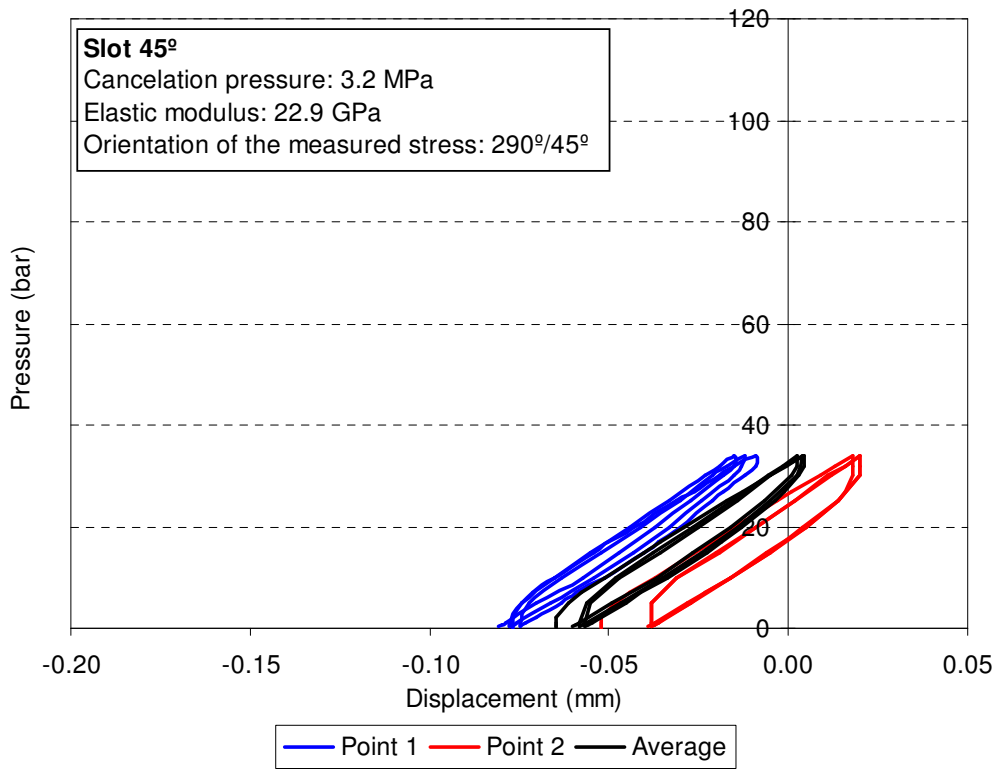


Location SFJ3

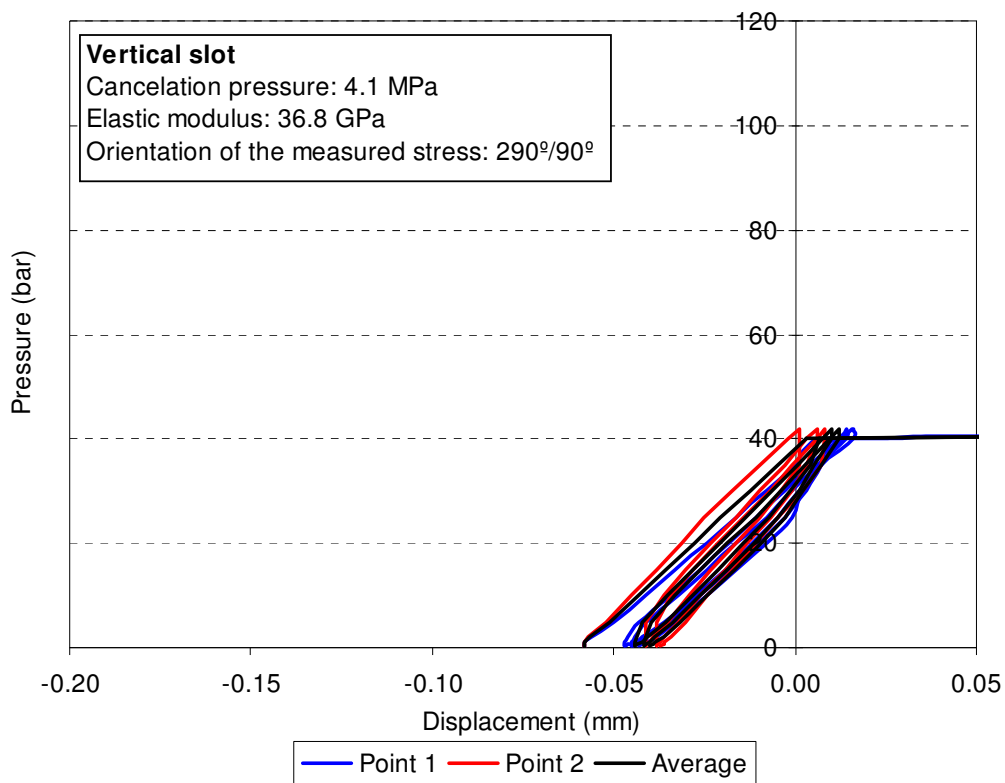
Test 1



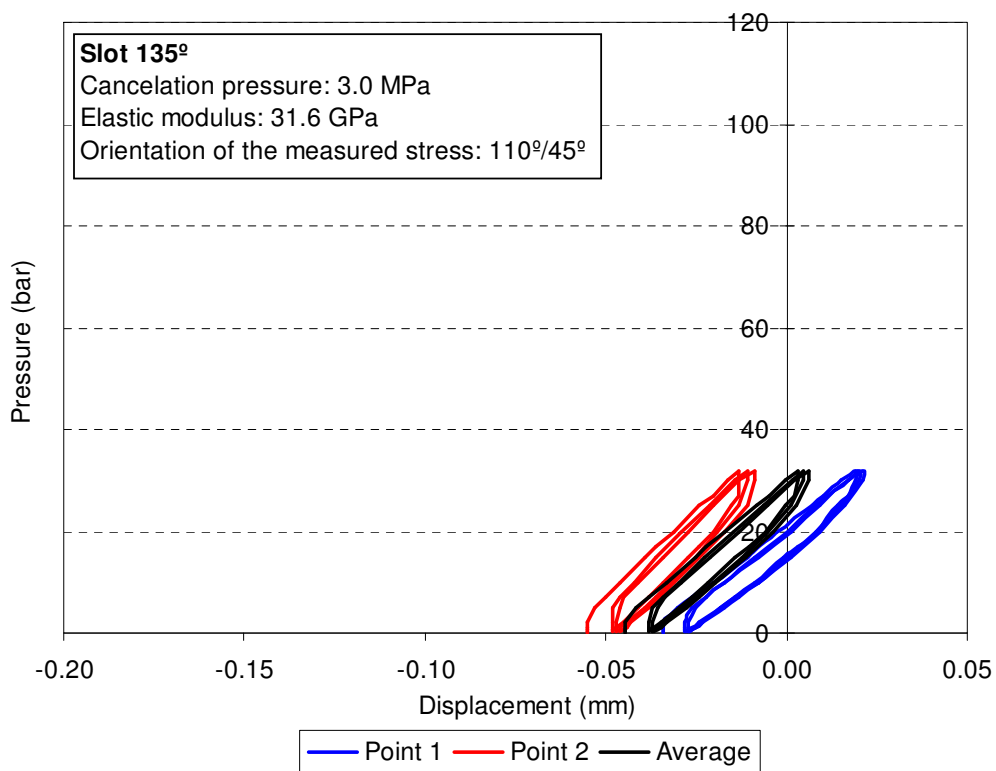
Test 2



Test 3



Test 4



PAPER 1

Effect of topography on *in situ* stresses distribution due to gravity and tectonic loadings at Paradela site

Figueiredo, B., Cornet, F.H., Lamas, L., Muralha, J. (2012)

Effect of topography on the distribution of *in situ* stresses due to gravity and tectonic loadings at Paradela site (Portugal)

B. Figueiredo¹, F. H. Cornet², L. Lamas¹ & J. Muralha¹

¹ National Laboratory for Civil Engineering – LNEC, Portugal

² Institute de Physique du Globe de Strasbourg – IPGS, Strasbourg

Abstract: A methodology is proposed for dealing with the unbalanced stresses that arise from numerical models due to topography effects when horizontal stresses are applied at the vertical boundaries. The proposed methodology is used for understanding the role of topography on the distribution of *in situ* stresses due to both gravity and tectonic loadings. In particular, the influence of Poisson's ratio on the orientation of principal stresses is illustrated for the case where only gravity loading is introduced. This approach is applied to the Paradela site, in Portugal, where a large underground repowering scheme is underway.

Theme: Geological site characterization.

Keywords: Topography, tectonic and gravitational stresses, numerical model, boundary conditions.

1 INTRODUCTION

Paradela site refers to the location of the re-powering scheme of Paradela dam located on the Cávado River in the North of Portugal. Figure 1 shows the location of Paradela site and the orientations of the regional maximum horizontal compressive stresses taken from the World Stress Map (Heidbach et al., 2008). The re-powering scheme includes a new 10 km long hydraulic circuit and a powerhouse complex placed about halfway in the circuit and comprising a new powerhouse cavern, a valves chamber and a large surge chamber with several adits located 500 m below ground surface (Fig. 2). The water intake is placed at Paradela dam (bottom right corner of the figure), which is a concrete face rockfill dam built in the 50's. The circuit will run approximately along the Cávado River exiting near the confluence of the Rabagão River (a left bank tributary). It will cross the flank of Serra do Gerês that corresponds essentially to an outcrop of the Gerês granite, which is a post-tectonic biotite granite with calcite plagioclase of medium size with porphyritic trends.

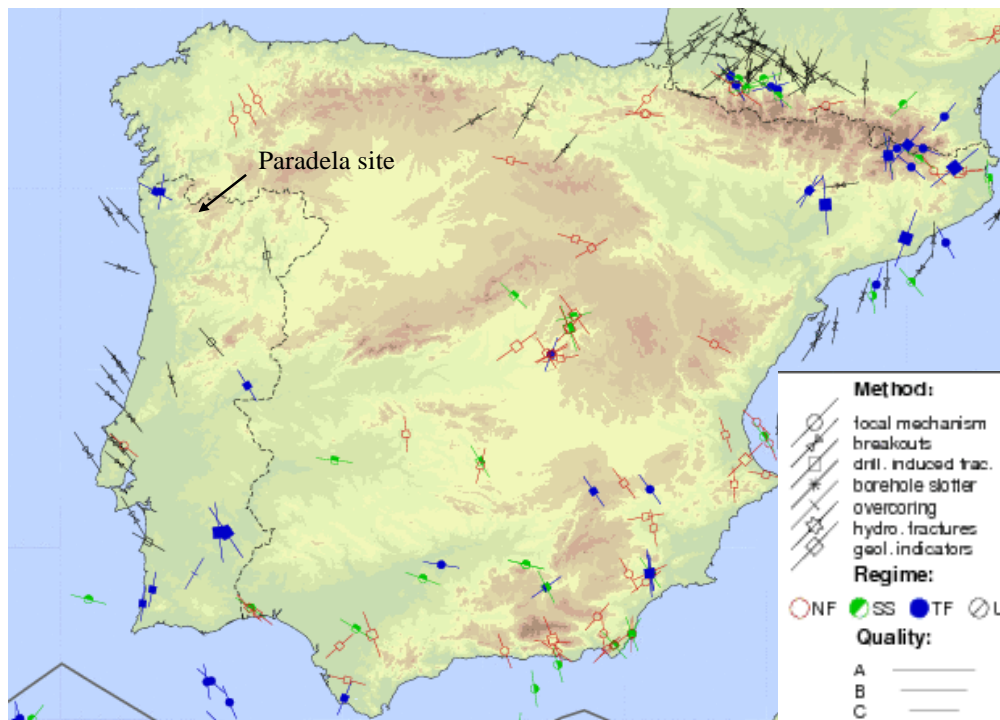


Figure 1. Location of Paradela site and orientations of the regional tectonic maximum horizontal compressive stress from the World Stress Map (Heidbach et al., 2008).

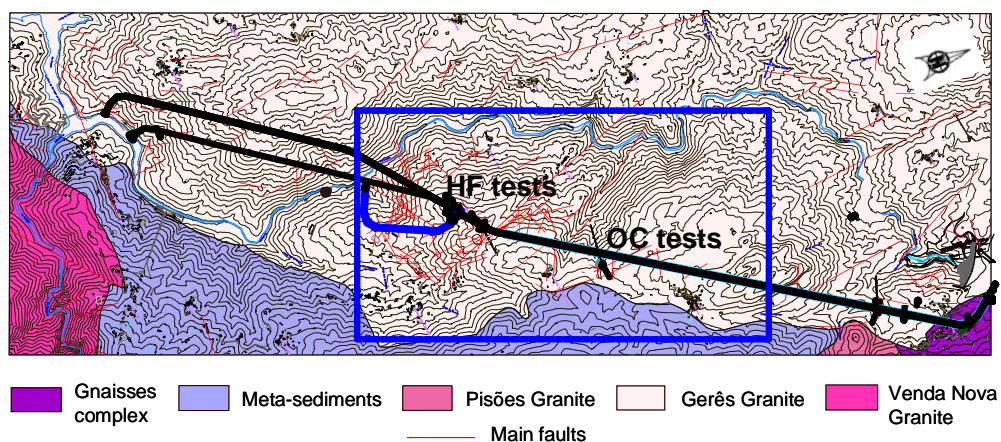


Figure 2. Top view of the hydropower circuit at Paradela (adapted from a drawing provided by EDP).

The design of Paradela re-powering scheme requires a sound understanding of the regional stress field, since the state of stress is frequently the main load to be considered in the design of underground works in rock masses. The determination of rock stresses is a great challenge, due to its spatial variability and the many factors that influence it.

Overcoring tests (OC), hydraulic fracturing tests (HF), and hydraulic tests in pre-existing fractures (HTPF) were carried out in order to characterize *in situ* stresses at the locations of the new hydraulic circuit and powerhouse. Overcoring tests were performed in two parallel 60 m deep vertical boreholes (PD1 and PD2), 150 m apart. They were drilled 160 m below ground surface inside an existing adit located approximately 4550 m downstream from the water intake and 1650 m upstream from the future powerhouse cavern (Fig. 2). The adit is located 640 m above sea level and 170 m above the future hydraulic circuit. HF and HTPF were carried out in two 500 m deep vertical boreholes (PD19 and PD23), 100 m apart, located 1650 m downstream from the PD1 and PD2 boreholes (Fig. 2). The boreholes were drilled at an elevation of 730 m above sea level. Data from both measurement techniques is being analyzed separately in order to determine stresses in the rock mass at both locations.

A three dimensional model, including the locations where overcoring and hydraulic tests were carried out, has been developed for the interpretation of the tests results. Since topography plays an important role on the distribution of *in situ* stresses at Paradela site, a sensitivity analysis regarding the dimensions of the area to be considered in the numerical model was undertaken. This analysis concluded that the region delimited by the window shown in Figure 2 is large enough for obtaining reliable estimates of the stress field associated with gravity and tectonic loadings at the locations of the *in situ* tests. The detailed elevation of the simulated area together with the position of the test boreholes is shown in Figure 3. The figure shows that the maximum difference in elevation is about 600 m.

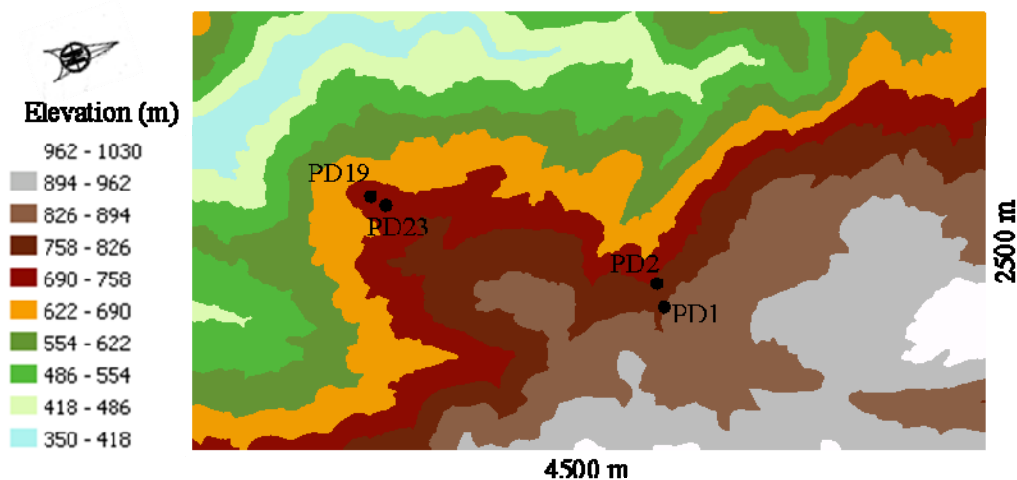


Figure 3. Elevation of the region considered in the three dimensional numerical model.

2 CONSIDERATION OF THE TECTONIC STRESSES IN NUMERICAL MODELS

Numerical modelling is a useful tool for estimating the influence of various factors on the stress field, such as the constitutive models for the rock mass constituents, the loading history, the geological structures, or the role of heterogeneity and of topography (Hart, 2003). However, without stress measurements data for validating the numerical models, such modelling is only of academic interest. Numerical models and stress measurements data must always be combined in order to contribute to a better understanding of the stress field at a given site.

It is common practice to divide the stress field in the earth's crust into vertical and horizontal components. The vertical component is generally equal to the weight of the overlying material and is of gravitational origin. For this component of the gravity loading it is also common practice to assume that lateral confinement results from preventing the normal displacements at the boundaries of numerical models.

For the tectonic loading it is usually assumed that the tectonic stresses act entirely upon the vertical boundaries of the models.

To estimate the tectonic boundary stresses to be considered in the numerical models from stress measurements data the following methodology is commonly used. Unit normal and shear stresses are applied to the model boundaries and the response is computed at the location of the stress measurements. For analysis purposes, it is assumed that the tectonic components of the far field stress tensor can be considered as constant plus a vertical gradient with depth. Then, an optimization procedure is used to compute the proportions of each tectonic stress component that is required, in addition to the gravitational stresses, to reproduce the state of stress at the location of the stress measurements (Li et al. 2009, McKinnon 2001, Tonon et al. 2001).

The main drawback of this technique is that the unit stress components can be applied only at the boundaries of models that simulate rock masses at a scale large enough so that topography effect is negligible when compared with the length assigned to the vertical direction of the model. Otherwise, without assuming certain artificial boundary conditions, such as prescribed displacement boundary conditions or prescribed stress boundaries, unbalanced stresses occur due to topography effects. Furthermore, in this approach the influence of topography on the distribution of the horizontal stresses at the lateral boundaries of the model is neglected.

Let us consider the following example of a unit and uniform compressive stress distribution S_{xx} applied at the lateral boundaries of the numerical model (Fig. 4a). Due to the topography effect, an unbalanced stress state ($F_{res} \neq 0$) occurs when this loading condition is applied.

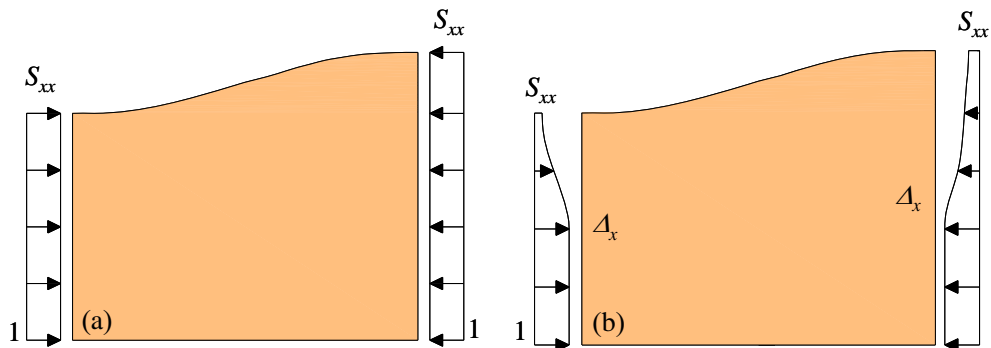


Figure 4. (a) Unbalanced stress state due to the effect of topography when a uniform stress S_{xx} distribution is applied at the boundaries of the numerical model (b) Uniform normal displacement Δ_x applied at the boundaries to induce a horizontal unit stress σ_{xx} at the bottom boundary of the model.

In this paper a new numerical technique for dealing with the unbalanced stress state problem in order to estimate the role of topography when both tectonic and gravity forces are active is presented. It consists in applying a uniform normal displacement Δ_x at the lateral boundaries of the numerical model that yields a unit horizontal stress at the elements of the bottom boundary of the model (Fig. 4b). For this method to be successful, it is necessary that the stresses at the bottom boundary of the model are not influenced by topography which may be achieved by extending the model in the vertical direction. In this approach, non-uniform distributions are generated at the lateral boundaries of the model. These stress distributions are balanced ($F_{res} = 0$) and take into account the effect of topography.

An equivalent procedure would be to apply unit stress components in all elements of the model and preventing boundary displacements. However, for those models that aim to simulate the poor quality of the rock mass near the surface by decreasing the local elastic modulus, this loading condition is not effective, since it leads to stress distributions that are unaffected by the variability of the elastic modulus.

3 APPLICATION TO PARADELA SITE TOPOGRAPHY

3.1 Numerical model

A three dimensional model has been developed for Paradela site using the software FLAC 3D (Itasca, 2009). The model includes the location of the overcoring and hydraulic tests (HF/HTPF) (Fig. 5) and the terrain topography of the region shown in Figure 3. Since the data analysis is not completed yet, directions of the principal stresses are not known. The x axis of the numerical model is oriented to N30°E, so that it is approximately aligned with the direction of the regional (tectonic) minimum principal stresses suggested by the World Stress Map (Heidbach et al., 2008). The introduction of tectonic shear stresses S_{xy} enables to simulate other principal stress orientations, yet using the same grid.

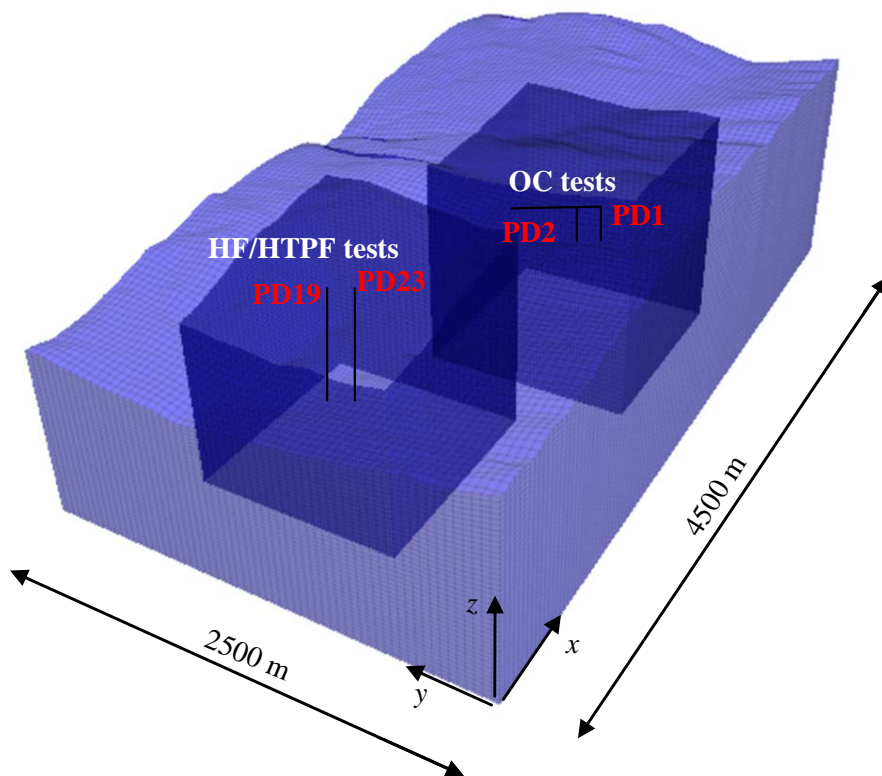


Figure 5. Three dimensional numerical model for Paradela site.

In the dark blue region of Figure 5, the mesh is composed by 25 m side cubes, and in the light blue region by 50 m side cubes. A large vertical extension has been considered so that topography effects do not influence the stress distribution at the bottom of the model. Hence, the bottom boundary of the model has been placed 2500 m below sea level.

In this analysis, a linear elastic, isotropic behavior for the rock mass has been assumed. Results from laboratory tests conducted on the cores extracted from Paradela

provided average values of 45 GPa for the Young's modulus, 0.25 for the Poisson's ratio, and 2650 kg/m³ for the rock mass density.

3.2 Influence of topography on the distribution of *in situ* stresses due to tectonic and gravity loadings

The model has been used for assessing the variation of magnitude and orientation of the principal stresses along the boreholes where tests have been carried out.

First, the influence of topography on the distribution of the stress tensor components due to unit tectonic S_{yy} and S_{xy} components at the location of the boreholes was analyzed. Figure 6 shows the variation with depth of all stress tensor components at the location of the boreholes. They have been obtained for a unit horizontal stress component S_{yy} . Figure 7 shows the variation with depth of the stress tensor components at the same locations for a unit tectonic shear stress S_{xy} component introduced in the numerical model. These figures clearly show the effect of topography, since stress profiles are quite different at the locations of overcoring and hydraulic tests. The stresses displayed in both figures are compared with those that would be the result of the same unit stress loading considering a horizontal ground surface.

Figure 6 shows that the stresses σ_{yy} vary 45% along a 1000 m depth range at the location of the overcoring tests. At the location of boreholes PD19 and PD23 variations of 80% and 60% along a 1000 m depth range are exhibited, respectively. Variations of the horizontal stresses σ_{xx} and vertical stresses σ_{zz} that reach maximums of 10% and 5%, respectively, are also seen. The shear stresses σ_{xy} , σ_{yz} and σ_{xz} exhibit variations that reach a maximum of 10%, 15% and 5%, respectively. This analysis also concludes that the effect of topography at 1000 m depth is higher at the location of overcoring data.

Figure 7 shows that the horizontal stresses σ_{xx} exhibit a 20% variation along a 1000 m depth range at the location of boreholes PD1 and PD19 and a 40% variation at the location of boreholes PD2 and PD23. The horizontal stresses σ_{yy} exhibit a variation that reach an average of 40% at the location of overcoring data. The shear stresses σ_{xy} also displays a variation along the same depth range that can reach maximums of 20% and 60% at the location of overcoring and hydraulic data, respectively. From 500 m below ground surface, the influence of topography on this stress tensor component is negligible at the two locations. The shear stresses σ_{xz} exhibits a variation that reaches a maximum of 20% at the location of the borehole PD2.

Next, the influence of the tectonic loading S_{yy} component on the results obtained for the gravity loading G was analyzed. Three values were considered for the S_{yy} tectonic component: S_{yy1} , S_{yy2} and S_{yy3} equal to 1, 5 and 10 MPa, respectively. After data processing, if the directions of the principal stresses do not coincide with the directions of the model axis, a shear tectonic stress S_{xy} component may be introduced to better fit the data.

Figures 8 and 10 show the orientation of the principal stresses directions with depth at the locations of boreholes PD1 and PD19, respectively, obtained for the gravity loading G and for the combined effect of the gravity and tectonic S_{yy1} , S_{yy2} and S_{yy3} loadings. The orientations of the principal stresses are shown in a lower hemisphere stereographic projection in which the direction of the x axis of the numerical model is shown. Figures 9 and 11 show the magnitudes of the principal stresses with depth at the location of boreholes PD1 and PD19, respectively.

The results for the magnitude and orientation of the principal stresses at the location of the boreholes PD2 and PD23 are not presented in the paper since they are very similar to the results obtained at the location of the boreholes PD1 and PD19, respectively.

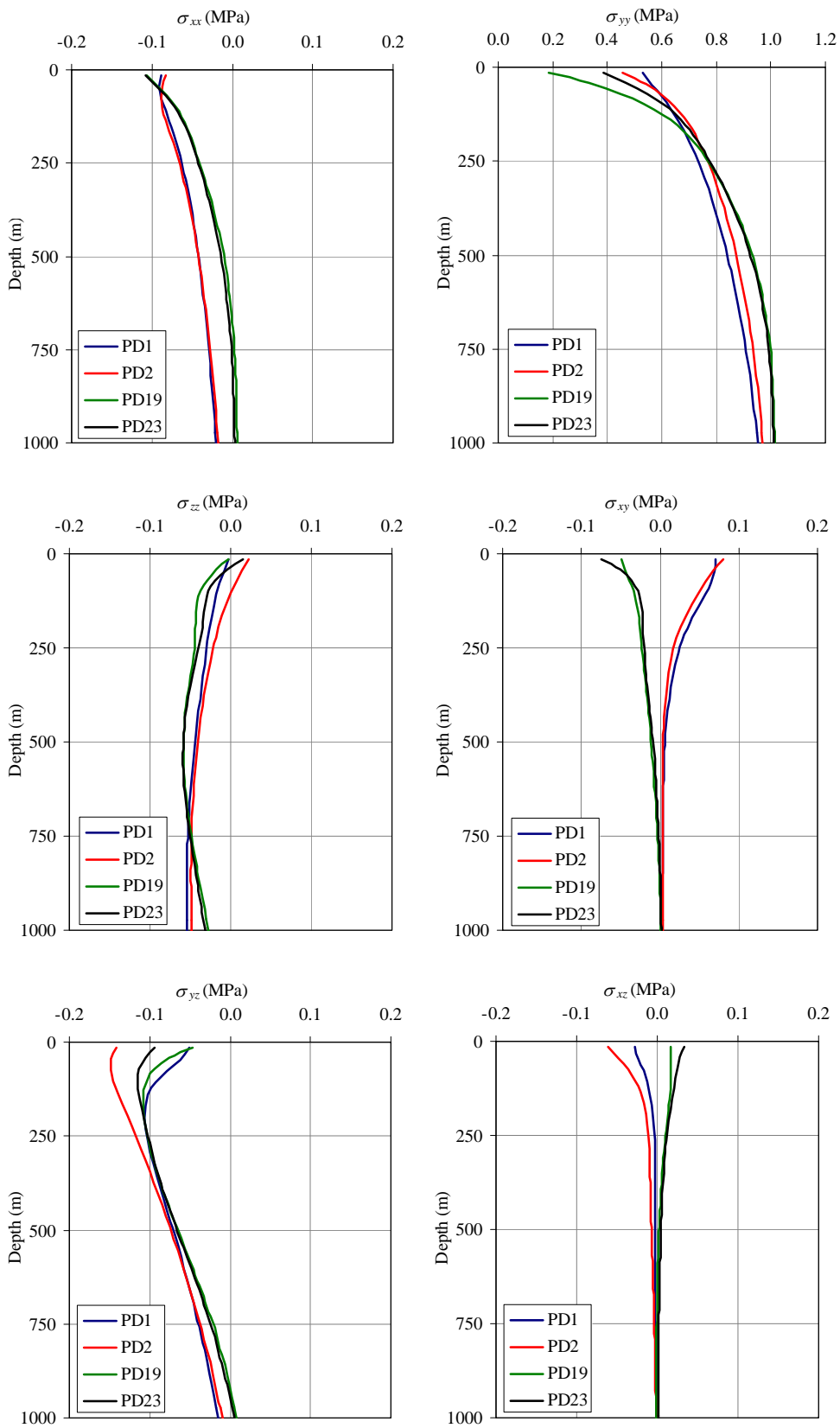


Figure 6. Variation of the stress tensor components for a unit tectonic stress S_{yy} .

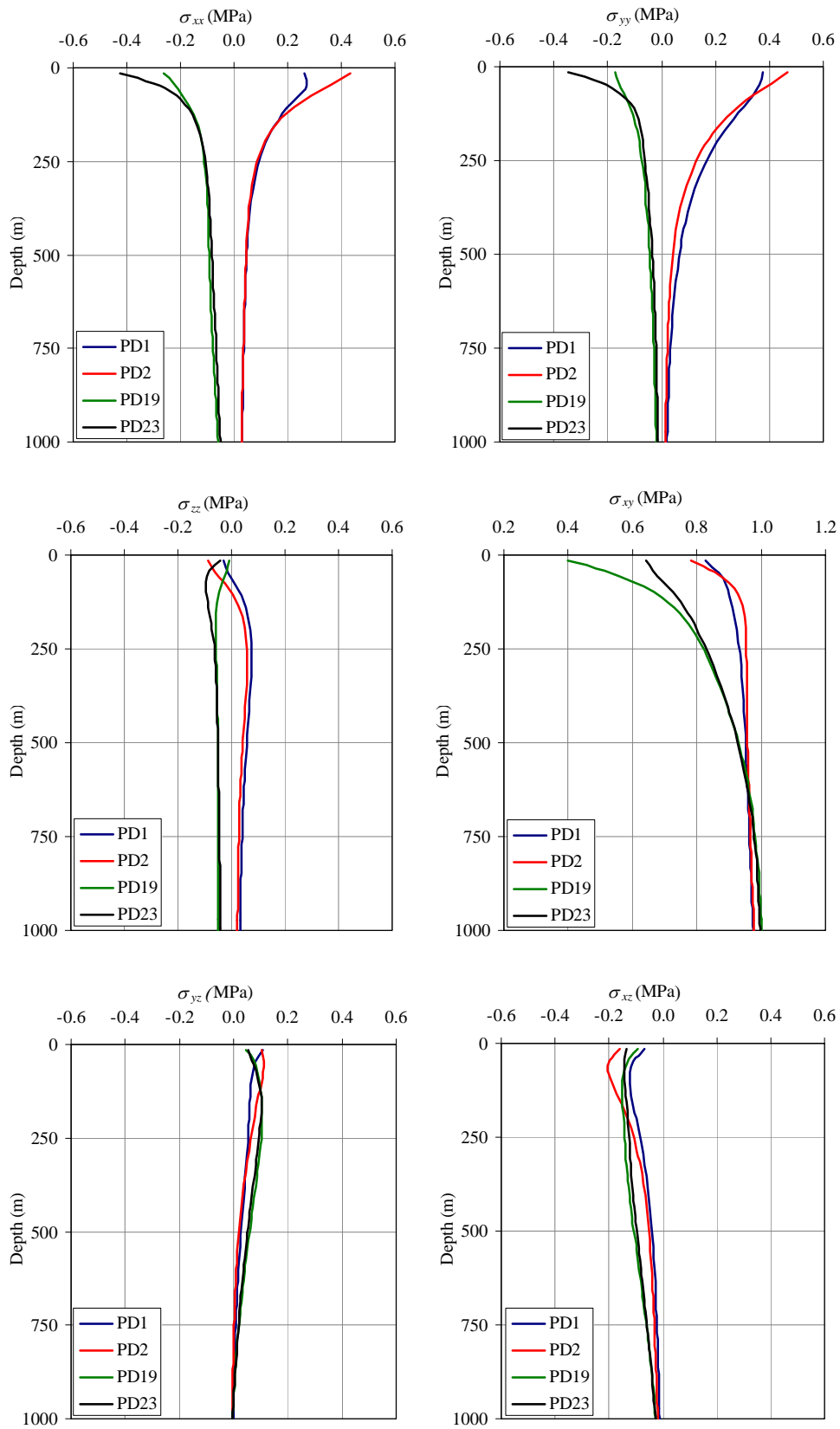


Figure 7. Variation of the stress tensor components for a unit shear stress S_{xy} .

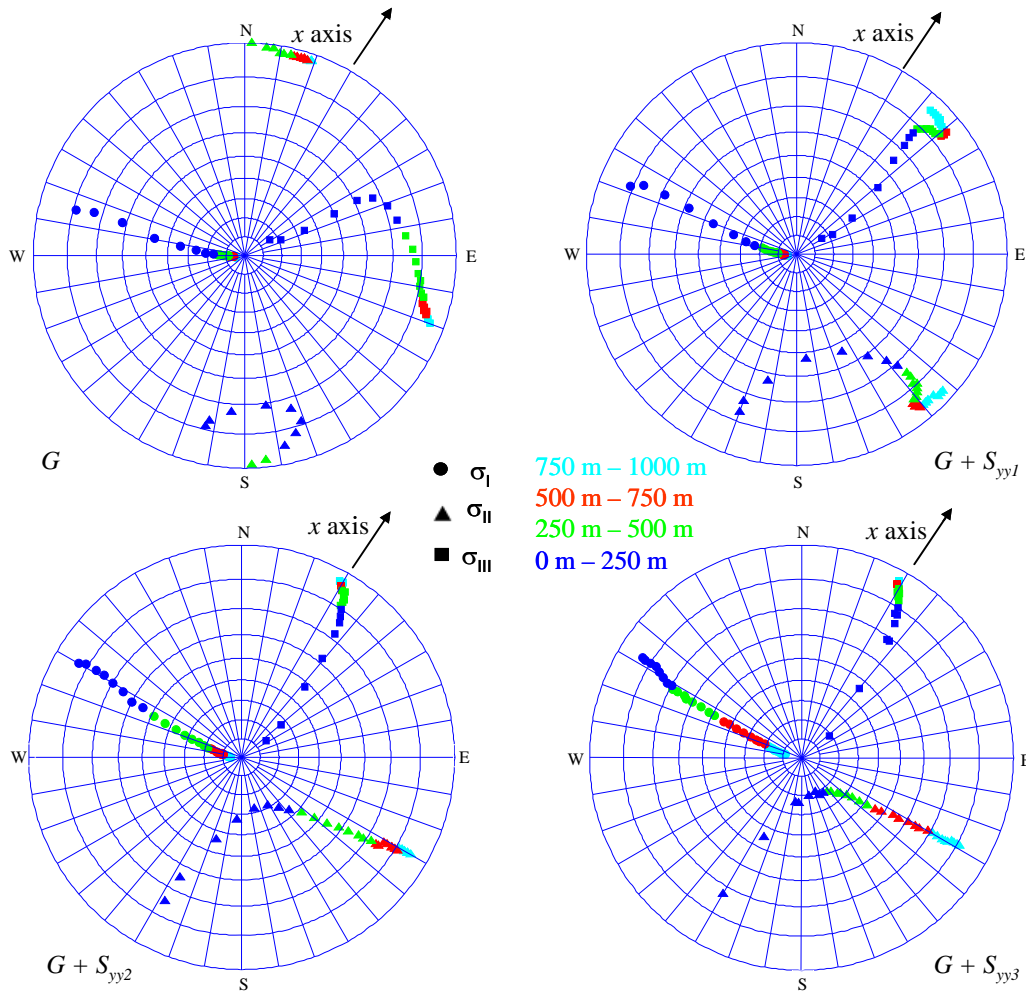


Figure 8. Orientation of the principal stresses obtained at the location of the borehole PD1 for the combined effect of gravity G and tectonic S_{yy} loadings.

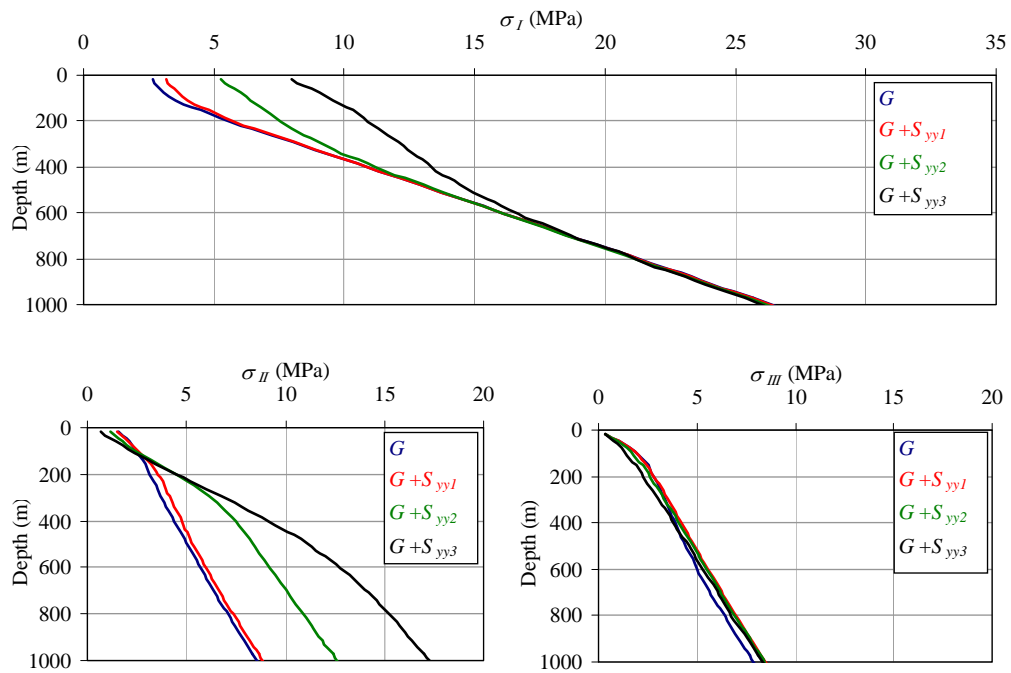


Figure 9. Magnitudes of the principal stresses obtained at the location of the borehole PD1 for the combined effect of gravity G and tectonic S_{yy} loadings.

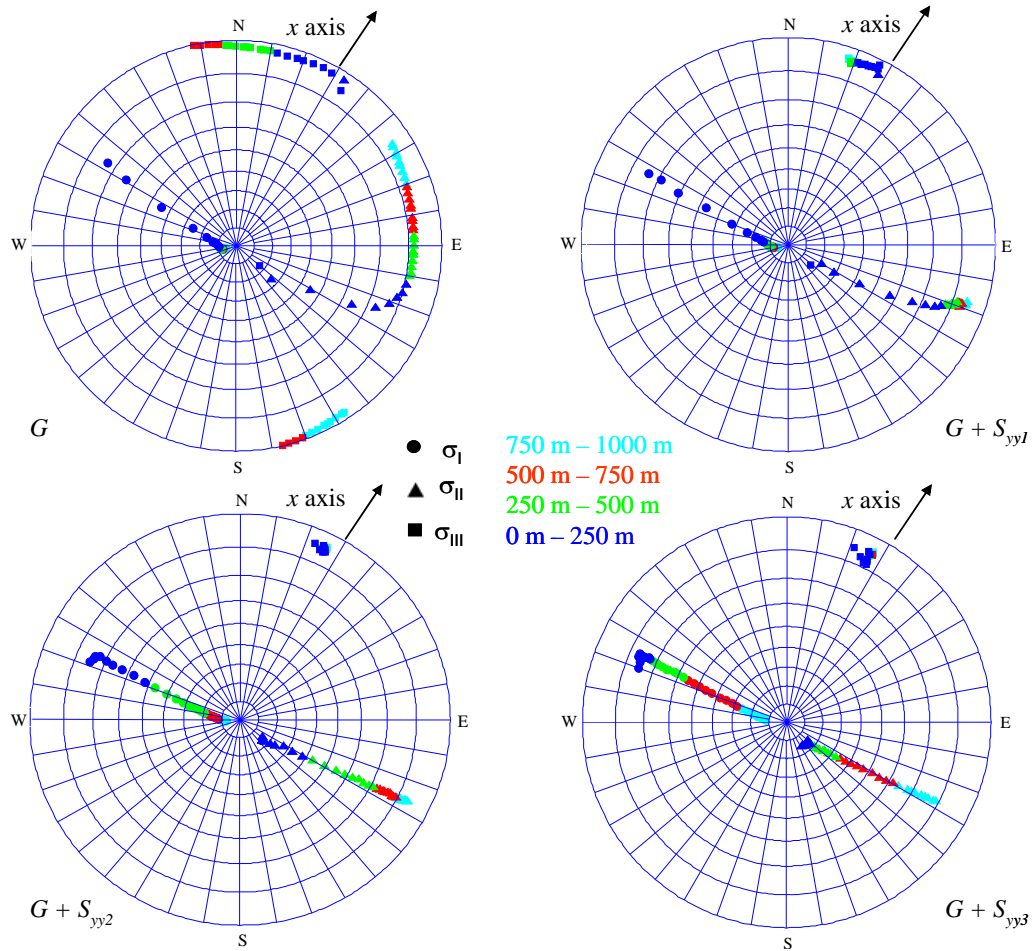


Figure 10. Orientation of the principal stresses obtained at the location of the borehole PD19 for the combined effect of gravity G and tectonic S_{yy} loadings.

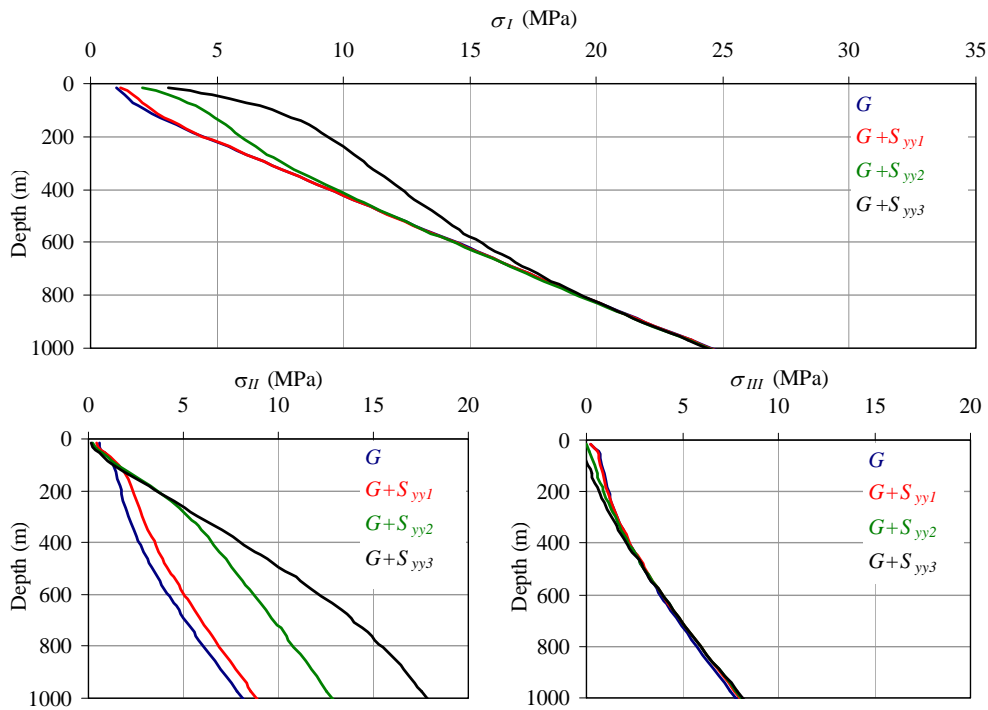


Figure 11. Magnitudes of the principal stresses obtained at the location of the borehole PD19 for the combined effect of gravity G and tectonic S_{yy} loadings.

For the gravity loading, at the location of the borehole PD1 the direction of the minimum principal stress (σ_{III}) is approximately constant (N 65° E) down to 200 m below the surface. From this depth down to 1000 m this direction rotates about 45°. Because, the two sub-horizontal stress components are of similar magnitude, the rotation of their directions with increasing depth is meaningless.

For the combined effect of gravity G loading and a unit horizontal stress applied in the y axis direction of the model, the minimum principal stress is orientated N 40°E at 1000 m depth and rotates about 20° till the ground surface. As the tectonic loading increases, the rotation of the minimum and intermediate principal stress directions with depth decreases and these components get aligned with the x and y axis of the model, respectively. The direction of the maximum principal stress (σ_I) is not influenced as much by the tectonic loading as the direction of the minimum principal stress, since it rotates between 5° and 50° when a tectonic loading S_{yy} is applied. This principal stress component is practically aligned with the y axis of the numerical model.

At the location of borehole PD19, the minimum principal stress (σ_{III}) remains sub-horizontal with depth for the considered loading conditions. For the gravity loading its direction rotates about 70° with depth, which is not significant because the sub-horizontal stresses are of similar magnitude.

For the combined effect of gravity and tectonic loadings the direction of this principal stress component only rotates about 10° and is practically aligned with the x axis of the model. The maximum principal stress (σ_I) is sub-vertical for depths greater than 200 m below the surface when the gravity loading alone is applied. However, its inclination varies substantially with depth when the tectonic loading is introduced in the model. The direction of this principal stress component is practically constant with depth for all loading conditions and is practically aligned with the y axis of the model.

At depths greater than 200 m below the surface, the magnitude of the sub-horizontal stresses in borehole PD1 is about 1 MPa larger than in borehole PD19. For the vertical stress component, this difference is about 1.5 MPa.

The magnitude of the minimum principal stress is practically unaffected by the tectonic loading. The magnitude of the maximum principal stress obtained for the gravity loading at the locations of the boreholes PD1 and PD19 is not influenced in a range from 600 m and 700 m, respectively, when a tectonic loading is applied. In this way, for greater depths the magnitude of the maximum principal stress is controlled by the gravity loading.

Several steps are being taken to integrate the three dimensional numerical model with the results from *in situ* stress measurements in order to estimate the regional stress field at Paradela site. The main goal consists in fitting the results from stress measurements with those computed with the numerical model at the same locations by adjusting the horizontal stress components that must be applied to the model boundaries. In this analysis, it is assumed that the rock mass has a linear, elastic and isotropic behaviour and the tectonic stress field can be described as a linear combination of the stress tensors calculated for unit tectonic S_{xx} , S_{yy} and S_{xy} components applied at the boundaries of the numerical model.

However, if the rock mass does not exhibit a linearly elastic behaviour such an analysis is not correct. A viscoelastic model taking into account the influence of time on the distribution of *in situ* stresses may be considered by adjusting the values of the elastic parameters of the rock mass.

As a matter of fact, the values of the elastic parameters obtained from tests of the cores extracted from the rock mass are unrealistic when the aim is the simulation of the behaviour of the rock mass at a large scale. To understand the influence of the elastic parameters in the stress field, different values of the Poisson's ratio (0.30 and

0.35) were used in the numerical model, since changing the Young's modulus does not induce variations in the results.

A comparison between the principal stress directions obtained with Poisson's ratios equal to 0.25 and to 0.35 has been conducted. Results obtained along the axis of borehole PD19 for the gravity loading show that they differ by about 25° (Fig. 12). Increases of the Poisson's ratio of 0.05 and 0.10 yield increases of about 35% and 75%, respectively, for the magnitude of the intermediate and minimum principal stresses at 500 m depth below ground surface. The magnitude of the maximum principal stress is not influenced by the Poisson's ratio because this stress component is sub-vertical. (Fig. 13).

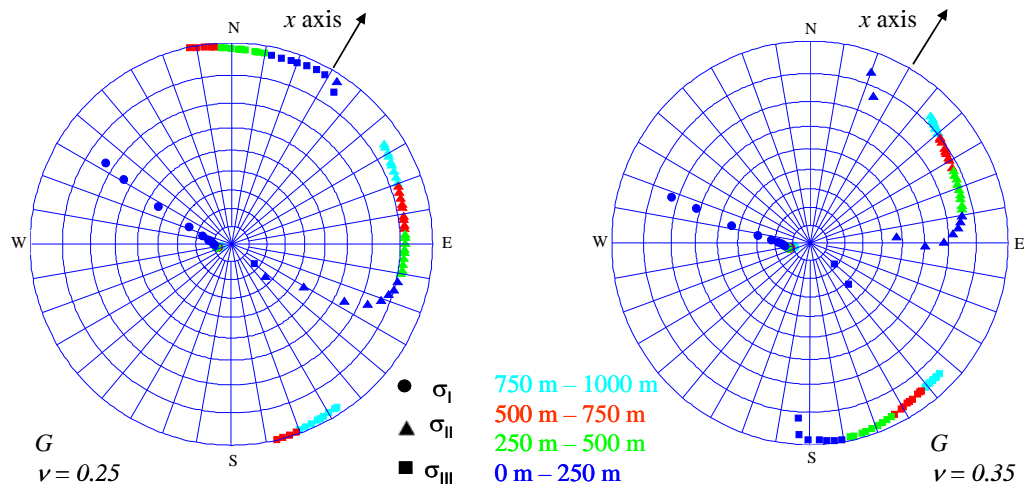


Figure 12. Orientations of the principal stresses obtained at the location of the borehole PD19 for the gravity loading with the values of 0.25 and 0.35 for the Poisson's ratio.

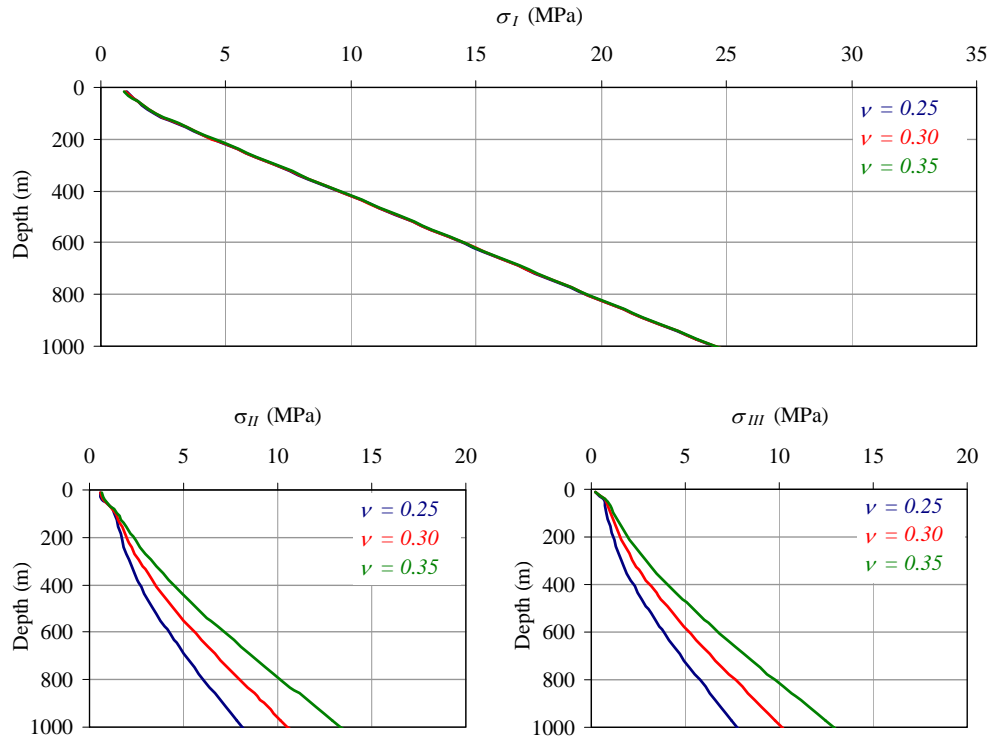


Figure 13. Comparison of the magnitudes of the principal stresses obtained at the location of the borehole PD19 for the gravity loading, with the values of 0.25, 0.30 and 0.35 for the Poisson's ratio.

4 CONCLUSIONS

The design of Paradela hydroelectric re-powering scheme required a set of overcoring and hydraulic *in situ* tests in order to characterize the stress field at the location of the new hydraulic circuit and powerhouse.

A three dimensional numerical model including the location of the *in situ* tests has been developed. A methodology for dealing with the unbalanced stresses due to effect of topography when horizontal stresses are applied at the boundaries of numerical models has been developed. This technique was used to understand the role of topography on the distribution of *in situ* stresses resulting from gravity G and tectonic loadings S_{yy} at the location of the tests. A tectonic shear stress component S_{xy} enables to consider different directions of the principal stresses, yet using the same grid.

The analysis concludes that due to gravity loading the influence of topography on the distribution of *in situ* stresses is significantly different at the two test locations. At the location of the hydraulic tests the principal stresses σ_{II} and σ_{III} are sub-horizontal down to a 150 meter depth, while at the location of the overcoring tests are sub-horizontal only down to a 250 meter depth. The orientation of the minimum principal stress changes significantly when tectonic stresses S_{yy} are considered. As the magnitude of this tectonic component increases, rotation of the minimum principal stress with depth decreases. The analysis also concludes that the stresses are controlled by gravity effects at the location of the overcoring tests, while in the boreholes where the hydraulic tests have been conducted, stresses may also be influenced by tectonic stresses.

Assuming a linear and elastic behaviour for the rock mass, the tectonic stress tensor at any given point may be described as a linear combination of the stress tensors calculated for horizontal unit far field stress components (two normal and one shear components). In this way, six model parameters are required for describing the tectonic far field stress (three components at a given depth plus their vertical gradients) and three model parameters for describing the rock mass properties (elastic modulus, Poisson's ratio and density), accounting a total of nine model parameters.

In order to consider that the rock mass may not be linearly-elastic, visco-elasticity may be assumed for taking into account some relaxation in the rock mass. Indeed, the elastic properties of the rock mass obtained from the extracted cores might not be realistic for a simulation of its behaviour at a large time scale. Visco-elastic effects can be considered in the model by performing an elastic analysis but with relaxed elastic properties.

A first trial of relaxation was performed by investigating the influence of Poisson's ratio on the magnitude and orientation of the principal stresses at the location of borehole PD19. This analysis concludes that it may not be simple to separate visco-elastic effects from tectonic effects, when only stress measurements at isolated locations are considered. However, the availability of vertical stress profiles provides data that may enable separating both effects more efficiently.

5 ACKNOWLEDGEMENTS

The work presented in this paper has been funded by the fellowship SFRH/BD/68322/2010 from the Portuguese Foundation for Science and Technology (FCT).

The authors thank EDP – Energias de Portugal, S.A. for authorizing to publish the information regarding Paradela II hydroelectric scheme.

6 REFERENCES

- Hart, R. 2003. Enhancing rock stress understanding through numerical analysis. *International Journal of Rock Mechanics & Mining Sciences*, 40: 1089-1097.
- Heidbach, O., Tingay, M., Barth, A., Reinecker, J., Kurfeß, D. & Müller, B. 2008. The release of the World Stress Map (available online at www.world-stress-map.org)
- Itasca Consulting Group, Inc. 2009. *FLAC3D, Version 4.0 User's Manual*. Minneapolis: Itasca.
- Li, G., Mizuta, Y., Ishida, Li, H., Nakama, S. & Sato, T. 2009. Stress field determination from local stress measurements by numerical modelling. *International Journal of Rock Mechanics & Mining Sciences*, 46: 138-147.
- McKinnon, S. D. 2001. Analysis of stress measurements using a numerical model methodology. *International Journal of Rock Mechanics & Mining Sciences*, 38: 699-709.
- Tonon, F., Amadei, B., Pan, E. & Frangopol, D.M. 2001. Bayesian estimation of rock mass boundary conditions with applications to the AECL underground research laboratory. *International Journal of Rock Mechanics & Mining Sciences*, 38: 995-1027.

PAPER 2

Determination of the stress field in a granite rock mass Part I: *in situ* measurements

Figueiredo, B., Cornet, F.H., Lamas, L., Muralha, J. (2013)

Submitted for publication in
International Journal of Rock Mechanics and Mining Sciences in June 2013

Determination of the stress field in a granite rock mass

Part I: *in situ* measurements

B. Figueiredo¹, F.H. Cornet², L. Lamas¹ & J. Muralha¹

¹ Portuguese Laboratory for Civil Engineering (LNEC), Avenida do Brasil, 101, Lisbon, Portugal

e-mail: brunof@lnec.pt

Phone number: +351218443391

² Institut de Physique du Globe de Strasbourg (IPG-S-CNRS), 5 rue René Descartes, Strasbourg, France

e-mail: Francois.Cornet@unistra.fr

Phone number: +33368850344

ABSTRACT: The design of an underground hydroelectric power scheme that includes a large powerhouse cavern and a hydraulic pressure tunnel required the characterisation of the regional stress field. This characterisation involved a set of *in situ* stress measurements that are presented in part I of this paper. Measurements were taken at different locations where the stress field is most likely to be significantly influenced by topography effects. The measurements included hydraulic tests, small flat jack tests and overcoring tests. Hydraulic testing provided the means to determine the complete stress profile in two 500 m deep vertical boreholes that reached the location of the future powerhouse cavern. Overcoring tests conducted in two 60 m deep vertical boreholes drilled from an existing adit some 160 m below ground surface provided information about a site located approximately 1.7 km away from the location of the hydraulic tests. Small flat jack tests performed near the location of overcoring tests provided further information on the stress state in the immediate vicinity of the adit. The results of these various measurements revealed the existence of local stress heterogeneity, spatial variability in the rock mass properties, non-elastic behaviour of the rock mass for low stress levels and non-elastic stress variations close to the existing adit. A comparison between the results of the hydraulic and overcoring tests shows that the stresses estimated by both techniques are of similar magnitude. But a comparison between the results of the small flat jack tests and the overcoring tests conducted at approximately the same location outlines a significant discrepancy between the stress field close to the adit and that observed away from it. A simple rheological model is proposed in part II of this paper for modelling the data gathered away from the adit.

KEYWORDS: *In situ* stress measurements, topography, hydraulic tests, overcoring tests, flat jack tests

1 INTRODUCTION

In situ tests are essential for characterising the natural stresses that exist in a rock mass and such a characterisation is required for designing deep underground structures, such as caverns or tunnels. However, due to the various factors that influence rock stresses, such as rock heterogeneity or

existing geological structures and the correlated spatial variability of rock mass properties, *in situ* tests provide information on the stresses only at the location where they have been performed. The results of these various types of measurements must be integrated later into a simple model to extrapolate them to the volume of interest for the design of the underground structures of concern.

When different types of measurement techniques are used at the same location, the results must be combined into a single inversion scheme to determine the stress field that best fits all the data. Such integration schemes have already been presented by several authors, including the following: hydraulic fracturing (HF) tests and hydraulic tests on pre-existing fractures (HTPF) (Cornet and Valette [1]), hydraulic tests (HF and HTPF) and flat jacks (Cornet [2]), hydraulic tests and focal mechanisms of induced seismicity (Cornet and Yin [3]), hydraulic tests and overcoring tests (Ask [4]) and overcoring and flat jack tests (Lamas *et al.* [5]).

Numerical models are then sometimes developed to integrate all the tests results within a single model that is used to determine the most probable stress state in the volume of interest (Hart [6], Lamas *et al.* [5], Matsuki *et al.* [7], Muralha *et al.* [8], Sousa *et al.* [9]). In mountainous regions, these models are an essential tool for evaluating the influence of topography on the stress field.

Here, a case is considered in which the data produced by different techniques (hydraulic tests, overcoring tests and small flat jack tests) were gathered from various locations within a rock mass in which there are most likely significant topography effects.

Measurements were performed for the design of the re-powering scheme of the Paradelas hydroelectric scheme located on the Cávado River in the North of Portugal. The Paradelas II scheme includes a new 10 km hydraulic conduit and a powerhouse complex placed about halfway in the conduit (Figure 1) that will primarily be excavated in granite. It includes a new powerhouse cavern, a valves chamber and a large surge chamber with several adits located 500 m below ground level.

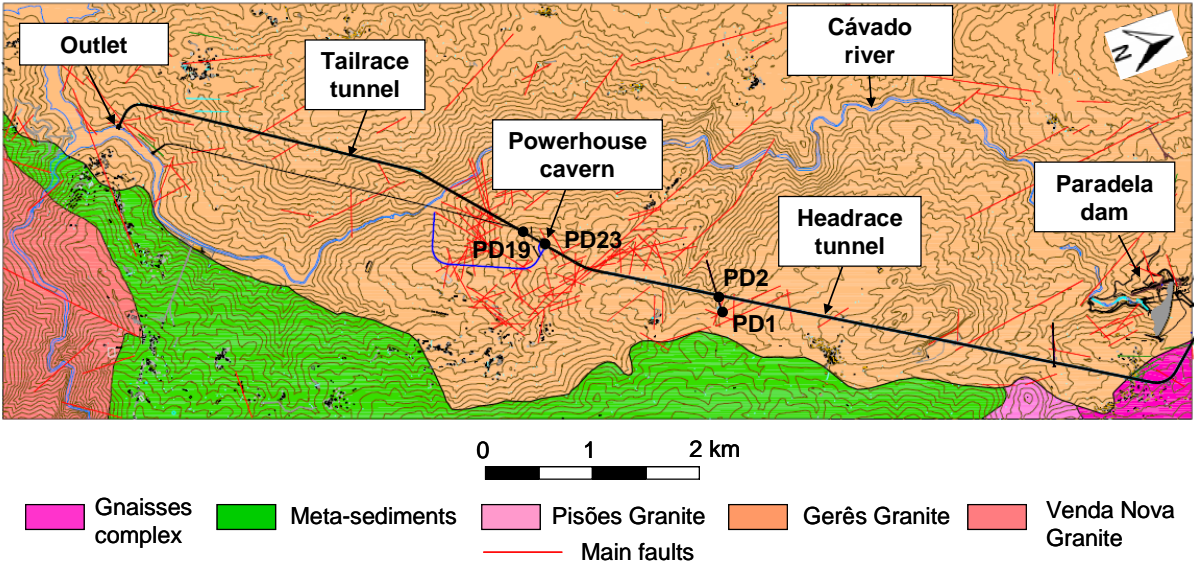


Figure 1: Layout of the Paradelas II hydroelectric repowering scheme (courtesy of Energy of Portugal-EDP).

Hydraulic tests provided the means to determine the natural stress profiles in two vertical 500 m deep boreholes (PD19 and PD23; Figure 2a). These two boreholes are separated by 100 m and reach the location of the future powerhouse cavern. The tests were conducted between 200 m and 500 m below ground surface, i.e., above and below the altitude of the nearby river bed.

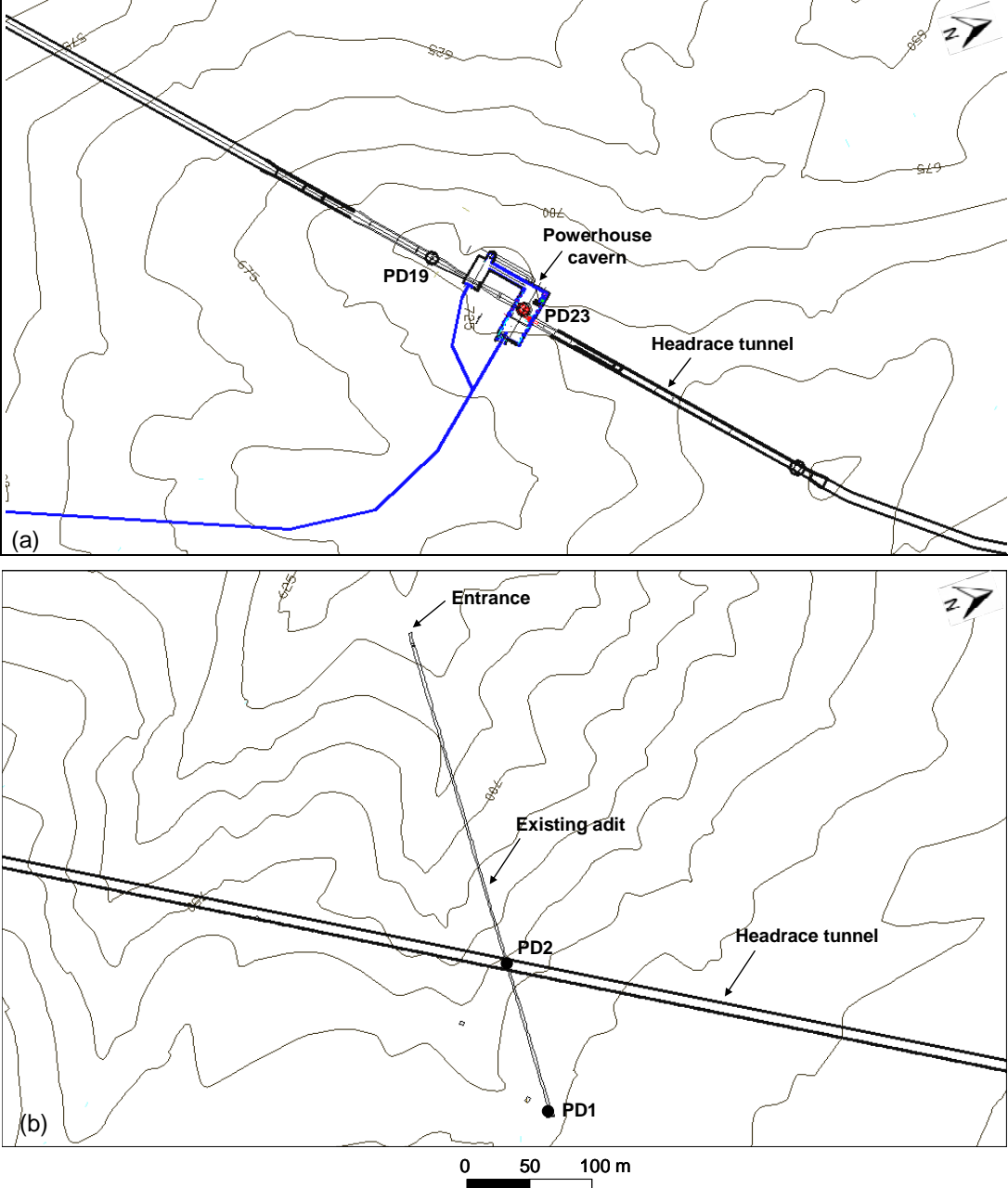


Figure 2: Location of the (a) hydraulic tests and (b) overcoring tests.

In another location, approximately 1.7 km away from the hydraulic test site, OverCoring (OC) and Small Flat Jack (SFJ) tests were performed. Overcoring tests were conducted to determine the complete stress tensor at six different depths in two 60 m deep vertical boreholes (PD1 and PD2; Figure 2b), located approximately 4550 m downstream from the water intake. These boreholes are separated by 150 m and were drilled from an existing adit located 160 m below ground level. In

borehole PD1, tests were conducted at depths between 205 m and 251 m below ground level. In borehole PD2, tests were conducted at depths between 163 m and 202 m below ground surface. Two tests were performed at approximately the same depth in each borehole. All of the tests were conducted above the river bed.

Small flat jack tests were performed to determine the stresses normal to various planes perpendicular to the walls of the existing adit near the boreholes where the overcoring tests were performed. Four tests were performed at a site (SFJ1) located within 3 m of borehole PD1, and eight tests were performed at sites (SFJ2 and SFJ3) located within 50 m of borehole PD2. Figure 3 presents a vertical cross section along the axis of the adit, along with the location of the overcoring and small flat jack tests.

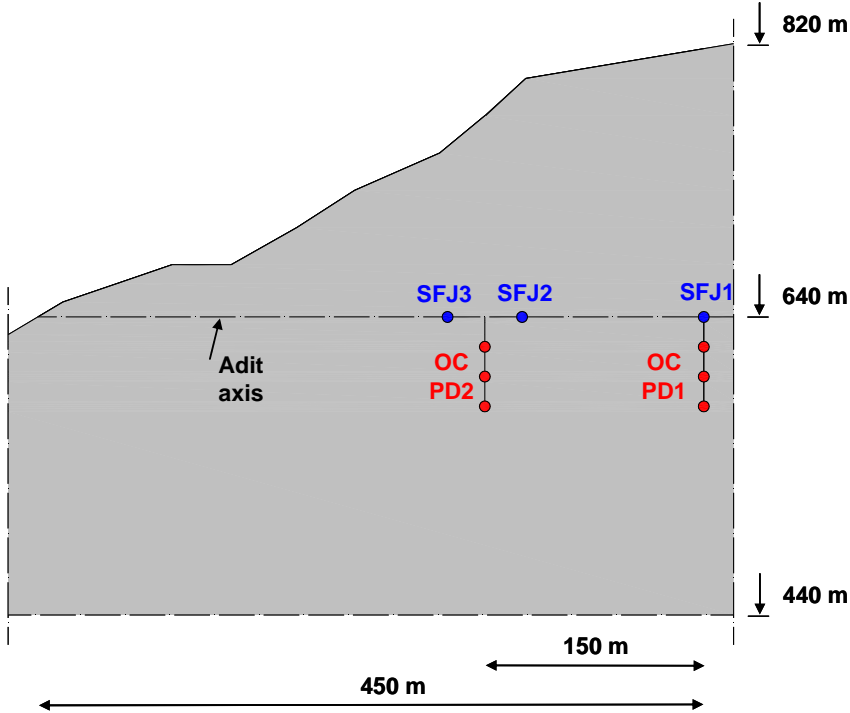


Figure 3: Vertical cutting plane along the adit axis showing the location of the overcoring and small flat jack tests.

The work reported here required the development of an integrated methodology for extrapolating the results of the various *in situ* tests to the rock mass volume of interest for the design of the underground hydroelectric power scheme. This work is presented in two parts.

In Part I, is discussed the collection and preliminary interpretation of the data. First, is described how hydraulic tests help determine the vertical stress profile. The overcoring tests are then described, and the results are combined in an inversion scheme to constrain the stress tensor at their location. Finally, the small flat jack tests are discussed, and their results are compared to those of the overcoring tests that were conducted at almost the same location. Part II of this paper presents the integrated approach that was developed to assess the regional stress field at the Paradela II site. The results of this model are then discussed to ascertain the long-term rheological characteristics of the equivalent geomaterial.

2 HYDRAULIC TESTS

Hydraulic testing has involved two different techniques, Hydraulic Fracturing and Hydraulic Testing of Pre-existing Fractures, following the procedures described by Haimson and Cornet [10].

HF tests involve the pressurisation of a 1 m-long intact borehole section, sealed with two packers, until the borehole wall fractures. During these measurements, the interval pressure *versus* time is recorded (Figure 4). The pressure required to induce fractures is called the breakdown pressure P_b .

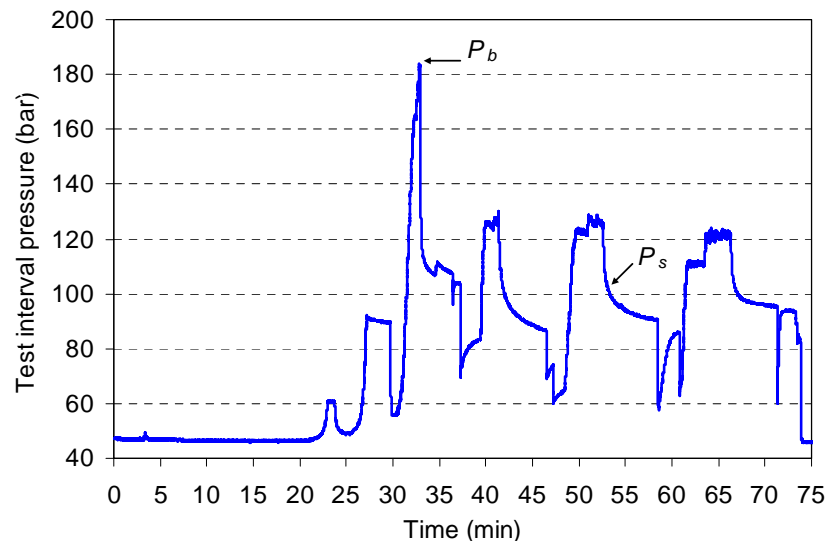


Figure 4: Actual record of test interval pressure *versus* time in a hydraulic fracturing test.

The fracture propagates in the direction that offers the least resistance, which is usually the direction perpendicular to the minimum *in situ* principal stress. When the injection stops and the hydraulic system remains sealed, the pressure immediately decreases. The pressure first decreases very rapidly as the fluid chases the still-extending fracture tip, and then it decreases much more slowly as the fracture closes. The pressure at which the fracture closes is called the shut-in pressure P_s . The shut-in pressure is the transition between fast and slow pressure decay, and it is considered to be equal to the normal stress component acting on the fracture plane (i.e., the minimum principal stress component for true hydraulic fractures). These pressurisation cycles are repeated several times to obtain some redundancy in determining the shut-in pressure.

HTPF provides measurements of the normal stress component supported by the corresponding pre-existing tested fracture (Cornet [11], Cornet and Valette [1]).

The hydraulic testing equipment that was used in these measurements includes two inflatable steel-reinforced packer elements that are used to create or to reopen pre-existing fractures and an electrical imaging device (Mosnier and Cornet [12]), which is used first to log the borehole and to identify the optimum location of test intervals (homogeneous rock formation for HF, single isolated fractures for HTPF).

The hydraulic data analysis consists of determining the stresses normal to the tested fracture planes, their depths below the surface and their orientations with respect to the North.

The depths of the tested fracture planes are determined through a comparison of the electrical imaging data and the rock cores extracted from boreholes PD19 and PD23, where the hydraulic tests were performed. In this way, a few characteristic and unambiguous fracture sets on both logs can be identified, and a rule for depth correspondence is defined. Based on this comparison, the corresponding maximum standard deviation associated with depth measurements has been evaluated at 0.5 m.

The stress normal to a tested fracture plane is directly related to the shut-in pressure measured in each test cycle. Aamodt and Kuriyagawa's method (Aamodt and Kuriyagawa [13]) was applied in each test cycle to identify the maximum borehole pressure for which the fracture is completely closed such that the flow obeys Darcy law. This pressure value is an underestimate of the normal stress supported by the fracture. Hayashi and Haimson's method (Hayashi and Haimson [14]) was applied in each test cycle to determine the pressure at the end of the fracture propagation, which is an overestimate of the normal stress supported by the fracture. For each test sequence (three or more shut-in readings), the minimum value obtained with the Aamodt and Kuriyagawa method and the maximum value obtained with Hayashi and Haimson's method were used to define the 99% confidence limit interval for the normal stress, characterised by six standard deviations, if one assumes that the errors obey a normal distribution.

The geometry and orientation of the tested fracture planes are determined through a comparison between the orientated electrical images obtained before and after the hydraulic tests. The fracture planes are recognised as sinusoids on electrical imaging logs. Two sinusoidal curves that completely cover the extent of the identified fracture plane in the electrical imaging logs were drawn to identify extreme values for the azimuth of the normal to the tested fracture planes and its inclination with respect to the vertical direction. From the scatter described by the two sinusoidal curves, a 99% confidence limit interval is defined for the two angles, which corresponds to six standard deviations, if one assumes that the errors obey a normal distribution. In borehole PD23, a technical difficulty prevented the determination of the tool orientation during logging. This difficulty was overcome by running a properly oriented high-resolution acoustic televiewer (HRAT) log. A comparison with the electrical log provided the proper orientation of all the hydraulically tested fractures for this borehole.

Figure 5 shows a comparison of electrical imaging logs along with the location of the test interval obtained before and after a hydraulic fracturing test (a) and the adjustment of the fracture plane located in the test interval with a sinusoidal curve (b). This figure also shows a comparison between the electrical imaging and HRAT logs (c), in which the main fractures located near the tested fractures are identified in both logs.

Tables 1 and 2 present a summary of the hydraulic test results. In these tables, z is the depth of the tests, ϕ is the azimuth of the normal to the fracture plane with respect to the North (positive eastward), θ is the inclination angle of the normal to the fracture plane with respect to the vertical direction, and σ_n is the normal stress measurement for the corresponding depth interval. The standard deviations associated with z , ϕ , θ and σ_n are δz , $\delta\phi$, $\delta\theta$ and $\delta\sigma_n$, respectively. In Table 2, the orientations marked with * were only obtained with the HRAT log. The tables show that eight tests are ambiguous because two or more fracture planes were observed in the test interval.

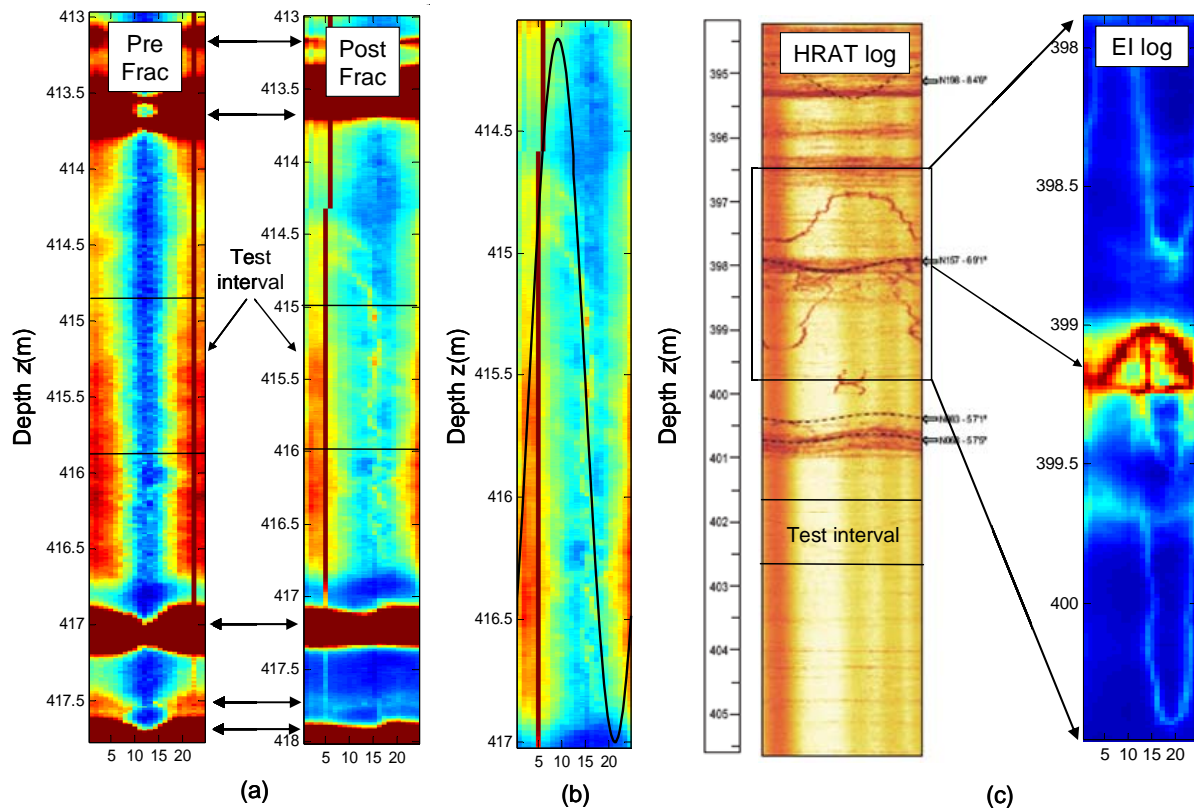


Figure 5: (a) Comparison between electrical imaging (EI) logs obtained before (Pre Frac) and after (Post Frac) a hydraulic fracturing test; (b) adjustment of the fracture plane with a sinusoidal curve; and (c) identification of the main fracture planes in the electrical imaging and HRAT logs.

The inversion of the hydraulic data was conducted to determine the complete stress field along the axes of the boreholes that fits with the normal stress measurements associated with the tested fracture planes. Before determining the stress field, a preliminary analysis of the results shown in Tables 1 and 2 is performed.

Figure 6 shows the variation of the normal stress magnitudes obtained from HF and HTPF as a function of depth. Figure 7 shows the variation of the azimuth of the normal to the fracture planes obtained from the HF tests only as a function of depth. In these tests, the fracture planes are parallel to the axes of the boreholes. Two different groups are noted. The solid line represents the azimuth of the fractures observed when the measured normal stress is close to the expected minimum stress magnitude at the correlative depth. The dashed line represents a perpendicular set of azimuths.

The analysis shown in Figure 6 indicates that most of the values are included in a domain delimited by two straight lines, the slope of which are respectively 0.0165 MPa/m and 0.0255 MPa/m, which may be assumed to correspond to the gradients of the minimum and the maximum principal stress magnitudes, respectively.

Two tests yielded results that were different from the regional trend: test number 1 in borehole PD23 and test number 8 in borehole PD19. These results were not included in the stress inversion procedure.

Table 1: Summary of the hydraulic test results obtained from borehole PD19.

Test	Depth		Azimuth		Dip		Normal stress	
	z (m)	δz (m)	ϕ ($^{\circ}$)	$\delta\phi$ ($^{\circ}$)	θ ($^{\circ}$)	$\delta\theta$ ($^{\circ}$)	σ_n (MPa)	$\delta\sigma_n$ (MPa)
1	471.8	0.5	108	4	87	2	10.3	0.4
2	455.5	0.5	18	7	90	2	9.0	0.2
3	450.1	0.5	126	5	90	2	7.8	0.2
	450.4	0.5	281	6	60	1		
4	442.1	0.5	133	5	90	2	9.0	0.2
	442.2	0.5	303	5	42	2		
5	436.3	0.5	108	6	32	2	8.9	0.2
6	414.9	0.5	133	4	90	2	7.1	0.1
7	393.4	0.5	270	4	66	2	7.3	0.3
	393.9	0.5	284	3	79	2		
	394.1	0.5	277	5	52	2		
	394.3	0.5	50	5	38	2		
8	379.3	0.5	88	3	57	2	5.6	0.2
9	335.6	0.5	119	3	61	2	6.7	0.1
10	293.1	0.5	14	2	44	3	7.5	0.3
11	279.8	0.5	22	4	90	2	5.8	0.1
12	164.6	0.5	320	7	86	2	2.6	0.3

Table 2: Summary of the hydraulic test results obtained from borehole PD23.

Test	Depth		Azimuth		Dip		Normal stress	
	z (m)	δz (m)	ϕ ($^{\circ}$)	$\delta\phi$ ($^{\circ}$)	θ ($^{\circ}$)	$\delta\theta$ ($^{\circ}$)	σ_n (MPa)	$\delta\sigma_n$ (MPa)
1	490.7	0.5	199	5	90	2	20.2	0.5
2	421.8	0.5	19	5	90	2	9.9	0.2
	420.9		33	5	42	2		
3	402.4	0.5	348	5	68	2	8.9	0.2
	402.5		252	5	34	3		
4	377.4*	0.5	215*	5*	81*	3*	9.7	0.2
	377.8*		106*	5*	12*	3*		
	377.8*		46*	5*	20*	3*		
	378.4		2	5	35	2		
	377.9		137	5	22	2		
	377.9		59	5	24	2		
	377.7		358	10	37	2		
5	364.7*	0.5	325*	5*	81*	3*	7.0	0.2
	364.6		252	5	35	2		
6	356.8	0.5	269	4	90	2	5.9	0.1
	357.0*		33*	5*	6*	3*		
7	176.6	0.5	243	3	77	2	3.2	0.2

* orientation obtained from the re-orientation of the electrical logs by using the HRAT log

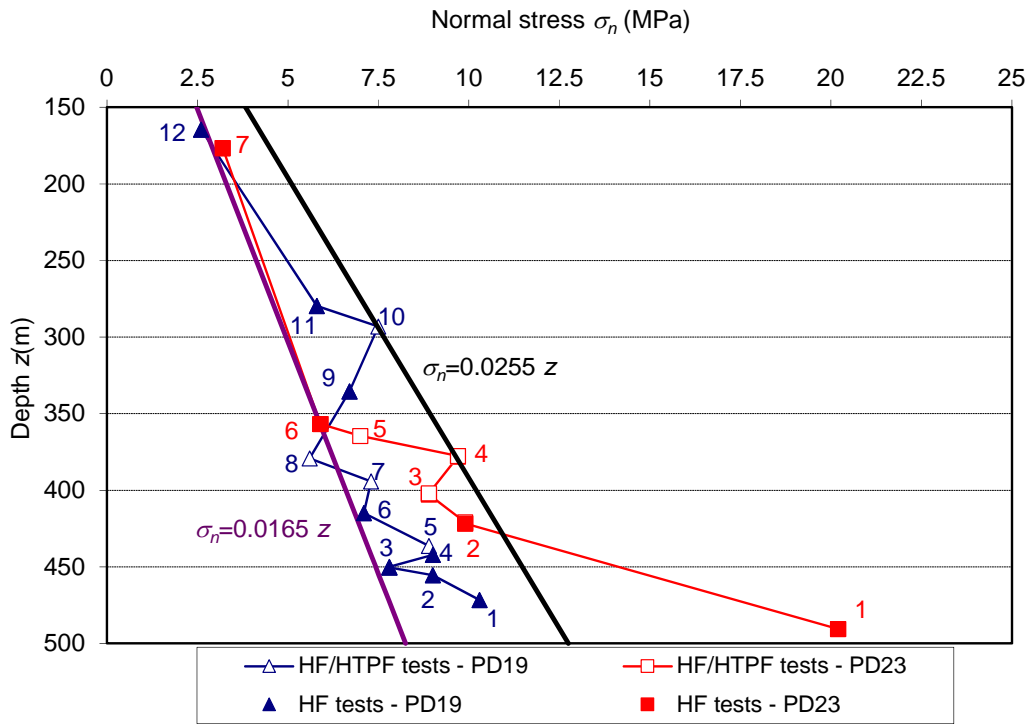


Figure 6: Variation of the normal stress σ_n magnitudes as a function of depth.

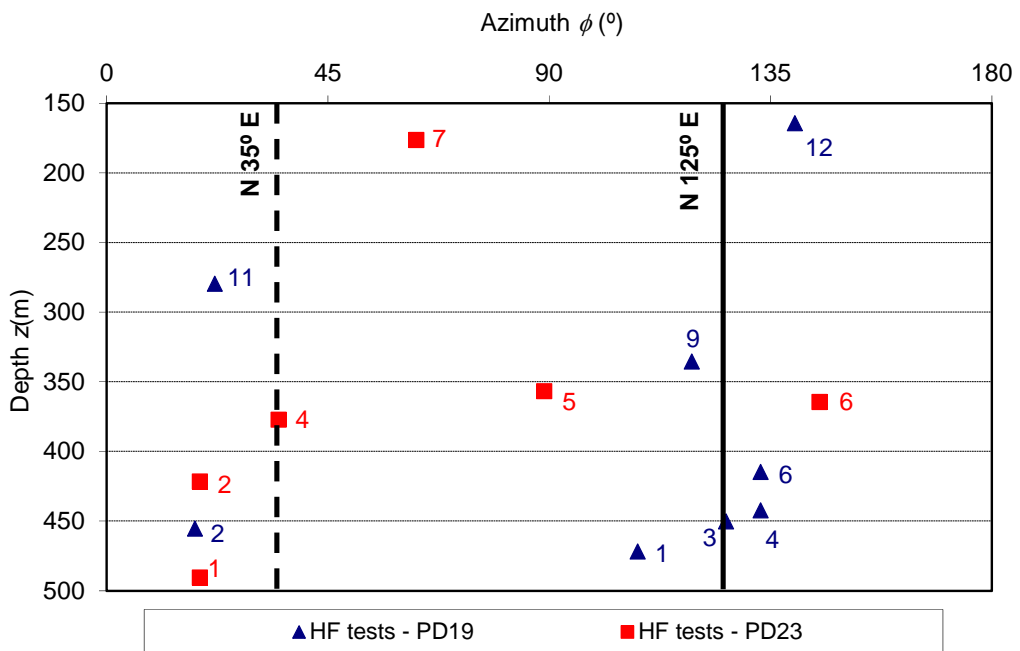


Figure 7: Variation of the azimuth ϕ of the normal to the fracture planes obtained in hydraulic fracturing tests as a function of depth.

For test number 1 in borehole PD23, the normal stress magnitude is significantly larger than all the other values by more than 10 MPa. However, the measurement is reproducible and satisfies all the prerequisite conditions of validity. It is important to determine whether the measurement is meaningful or whether it results from a specific local condition, in which case the test has no relevance to the stress determination. A detailed examination of both the electrical and the HRAT images shows a clear inclined fracture below the lower packer. In comparison to other post-fracture images, no other fracture is observed within the tested interval. This result strongly suggests that flow occurred within the inclined fracture below the packer. In such conditions, the pressure applied by the packer is also applied on some parts of the inclined fracture such that its opening remains very limited in azimuth. The stress analysis for such fractures has been discussed by Cornet *et al.* [15], who showed that the shut-in pressures in such configurations do not yield the far-field normal stress value. Therefore, it is concluded that because of the specific geometric conditions, this test does not yield any information on the normal stress supported by the plane.

For test number 8 conducted in borehole PD19, the measured normal stress is more than three standard deviations smaller than the expected trend. This test satisfies all prerequisite conditions. The pre-existing fracture is clearly identified. The pressure tests are fully satisfactory. It is considered a valid test for a stress evaluation. However, approximately 20 m above the test location, a strongly altered zone was observed in the electrical imaging log. This zone dips steeply and is therefore not very far from the tested fracture. It seems reasonable to assume that it is the cause for the local low stress value. This test result shows the limits of large scale stress evaluation campaigns. Rocks always exhibit some heterogeneity, and therefore, stress components may vary from those predicted by an ideal homogeneous model. This is further discussed in part II of this paper.

Additionally, test number 7 in borehole PD19 and test number 4 in borehole PD23 resulted in four and seven different fractures observed within the tested interval, respectively. These results were not included in the database, and only a total of 15 tests were considered for the determination of the stress field.

The analysis shown in Figures 6 and 7 reveals that the normal stress magnitudes measured for sub-vertical fractures that are nearly perpendicular to each other are very similar. This result suggests that differences between the maximum and minimum principal horizontal stress magnitudes are likely to be fairly small. Another possibility is that some strong stress heterogeneity exists in the rock mass due to the effects of local faults and fractures. This local heterogeneity is suggested by the inclined fractures with respect to the borehole axis in the hydraulic fracturing tests. This type of fracture was observed in two of the tests: test number 9 in borehole PD19 and test number 7 in borehole PD23.

In the inversion of the hydraulic data, the following assumptions are considered: (i) the linear stress variation holds over the complete domain of investigation, as suggested by Figure 6; (ii) the vertical direction is a principal direction in most of the domain that was tested, which is justified because most fractures in hydraulic fracturing tests are sub-vertical; and (iii) the horizontal gradient of the stresses between the two boreholes (PD19 and PD23) is negligible, which is justified by their close proximity.

Due to the influence of topography effects on the *in situ* stress distribution, a linear stress variation with depth may not be reasonable in regions close to ground level. Because these effects are not as

significant in the depth range between 280 m and 490 m below the surface, where the majority of measurements were performed, the hydraulic data was inverted by considering an 8-parameter model (Cornet [11]). Four parameters are associated with the stress tensor $\sigma(z_c)$ at the centre z_c of the measurements located 385 m below the surface, and four of them are associated with the stress gradient tensor α along the boreholes axis. In this model, S_1 , S_2 and S_3 are the maximum and minimum horizontal stresses and the vertical stress at the centre of the measurements, respectively, and λ is the direction of the maximum horizontal principal stress with respect to the North. α_1 , α_2 , and α_3 are the nonzero eigenvalues of the vertical gradient of the stress tensor α , and η is the orientation of the eigenvector α_1 with respect to the S_1 eigenvector.

For the m^{th} hydraulic test, the following error function defined from the measured and calculated stresses was used (Cornet [11]):

$$\sigma_n^m - (S_3 + \alpha_3(z_m - z_c))\cos^2 \theta_m - \frac{1}{2}\sin^2 \theta_m \left\{ \begin{array}{l} S_1 + S_2 + (\alpha_1 + \alpha_2)(z_m - z_c) + \\ (S_1 - S_2)\cos 2(\phi_m - \lambda) + \\ + (\alpha_1 - \alpha_2)(z_m - z_c)\cos 2[\phi_m - (\lambda + \eta)] \end{array} \right\} = 0, \quad [1]$$

where σ_n^m is the normal stress measured on the m^{th} fracture plane, z_m and z_c are the depths below the surface of the m^{th} test and of the centre of the measurements, respectively, ϕ_m is the azimuth of the normal to the m^{th} fracture plane with respect to the North, and θ_m is its inclination with respect to the vertical direction.

To solve the inverse problem presented in equation [1], the iterative method developed by Cornet and Valette [1] based on the least squares criterion (Tarantola and Valette [16]) was used. In this algorithm, the *a priori* values for the principal stresses S_1 , S_2 and S_3 were set to 10 MPa with associated large *a priori* standard deviations (10 MPa). The direction λ of the maximum horizontal principal stress was set to N43°E (the direction of the maximum horizontal principal stress at approximately 450 m) with no rotation η with depth. A small *a priori* standard deviation (5°) was set for these two angles. The vertical gradient of the minimum horizontal principal stress (α_2) was chosen as 0.0165 MPa/m, as suggested by Figure 6. Based on this figure, the vertical gradients of the maximum horizontal principal stress (α_1) and vertical stress (α_3) were set to 0.0255 MPa. The *a priori* standard deviation values associated with the gradients of the principal stresses were set to 0.02 MPa/m.

In general, the modelling proceeds as follows. First, an inversion of the results from the nine tests for which only one fracture plane had been observed is run. Next, the inversion is undertaken by considering the complete set of fifteen tests, which includes the tests with two possible fracture planes. All 64 possible combinations of fracture planes are considered. For each fracture plane combination, the stress field solution is calculated according to the least squares procedure (Tarantola and Valette [16]). The misfit for the i^{th} test ($i = 1, \dots, 15$) is defined as the absolute value of the difference between the measured normal stresses ($\sigma_{n,mes}$) and calculated normal stresses ($\sigma_{n,calc}$) associated with the stress field solution. The quality of the solution is characterised by the sum of the fifteen misfits. The set of fracture planes that yields the smallest value of the misfit is identified. The

solution associated with it is defined as the solution of the inversion of the set of fifteen tests. Table 3 shows the *a priori* values (p_0) and the *a posteriori* values (p) of the far-field stress parameters that were obtained by applying this procedure to hydraulic data.

Table 3: *A priori* values (p_0) and *a posteriori* values (p) for the far-field stress parameters.

Parameter	<i>A priori</i> values p_0	<i>A posteriori</i> values p	
		9 tests	15 tests
S_1 (MPa)	10.0	9.9	8.8
S_2 (MPa)	10.0	6.3	6.2
S_3 (MPa)	10.0	8.7	9.4
λ ($^\circ$)	43	60	4
α_1 (MPa/m)	0.0255	0.0319	0.0276
α_2 (MPa/m)	0.0165	0.0156	0.0152
α_3 (MPa/m)	0.0255	0.0242	0.0244
η ($^\circ$)	0	3	-3

This model yields the stress field at 475 m below the surface, as shown in Table 4. In this table, $\delta\sigma_H$, $\delta\sigma_h$, $\delta\sigma_v$ and $\delta\omega_H$ are the *a posteriori* standard deviations on the maximum horizontal (σ_H), minimum horizontal (σ_h) and vertical (σ_v) stresses, and the orientation (ω_H) of the maximum horizontal stress, respectively.

Table 4: Results of the stress field at 475 m below the surface.

Number of tests	σ_H (MPa)	$\delta\sigma_H$ (MPa)	σ_h (MPa)	$\delta\sigma_h$ (MPa)	σ_v (MPa)	$\delta\sigma_v$ (MPa)	ω_H ($^\circ$)	$\delta\omega_H$ ($^\circ$)
9	12.8	1.0	7.7	0.3	10.9	0.4	62	4
15	11.3	0.3	7.6	0.2	11.6	0.3	2	2

Table 4 shows that the magnitudes of the vertical and horizontal stresses are well constrained. In fact, the *a posteriori* standard deviations associated with these stress components are less than 10% of the expected values.

The *a posteriori* value for the gradient of the vertical stress is less than the density of the rock mass (2650 kg/m³). This result is consistent with the fact that in mountainous areas, the principal stress directions are not vertical for locations close to the ground surface.

Using the stress field solutions shown in Table 3, the *a posteriori* values for normal stresses on the fracture planes were calculated. The comparison between the *a priori* and *a posteriori* values for the normal stresses (σ_n and σ_{nc} , respectively) is shown in Table 5.

An average misfit of 0.3 MPa and a largest misfit of 1.3 MPa are observed for the solution identified with results from nine tests. These values are 0.3 MPa and 2.1 MPa for the set of fifteen tests. The sum of the misfits is 2.4 and 5.1 MPa for the sets of nine and fifteen tests, respectively. For both

cases, only one test has a *posteriori* value for the normal stress that differs from the *a priori* value by more than 3 standard deviations of the measurements.

Table 5: Comparison between the *a priori* values (σ_n) and *a posteriori* values (σ_{nc}) for the normal stresses.

Borehole	Test	Number of tests			
		9 tests		15 tests	
		σ_n (MPa)	σ_{nc} (MPa)	σ_n (MPa)	σ_{nc} (MPa)
PD19	1	10.3	10.1	10.3	8.2
	2	9.0	9.1	9.0	9.3
	3	-	-	7.8	8.0
	4	-	-	9.0	8.8
	5	8.9	9.5	8.9	9.5
	6	7.1	7.1	7.1	7.3
	9	6.7	6.6	6.7	6.5
	10	7.5	6.2	7.5	6.7
	11	5.8	5.8	5.8	5.8
	12	2.6	2.8	2.6	2.7
PD23	2	-	-	9.9	9.7
	3	-	-	8.9	8.9
	5	-	-	7.0	7.2
	6	-	-	5.9	5.8
	7	3.2	3.2	3.2	3.3

A search for other solutions was conducted by relaxing the *a priori* standard deviation on the direction of the maximum horizontal principal stress at the centre of the measurements and its rotation with depth. The model has been used to calculate the range of possible solutions at a depth of 475 m by considering the set of fifteen tests. From the range of possible solutions for the maximum and minimum horizontal stresses, vertical stress and orientation of the maximum horizontal stress, the following 99% confidence intervals were obtained:

$$9.9 \text{ MPa} \leq \sigma_H \leq 12.7 \text{ MPa}$$

$$7.1 \text{ MPa} \leq \sigma_h \leq 9.7 \text{ MPa}$$

$$10.2 \text{ MPa} \leq \sigma_v \leq 12.5 \text{ MPa}$$

$$N0^\circ E \leq \omega_H \leq N70^\circ E$$

The large uncertainty in the orientation of the maximum horizontal stress results from the fact that both horizontal principal stress magnitudes are not very different from each other; therefore, their orientation is strongly influenced by local heterogeneities.

3 OVERCORING TESTS

The Stress Tensor Tube (STT) test initially developed by Rocha and Silverio [17] basically corresponds to an overcoring test. The overcoring method is based on the stress relief around a borehole and yields the complete stress state at the corresponding location through a single overcoring operation.

The STT strain measurement device is a hollow epoxy resin cylinder with an outer diameter of 35 mm, an approximate length of 20 cm, and a thickness of 2 mm. The cell has 10 electrical resistance strain gauges embedded in positions normal to the faces of a regular icosahedron, which enables an equal sampling of the stress states in all directions (Pinto and Cunha [18]). The cell includes a metal capsule in which a small data acquisition unit is located. The cell also includes a thermocouple such that readings of all strain gauges and the temperature are conducted at fixed time intervals, and these readings are stored in local memory.

A test consists of the following: (1) drilling a borehole with a diameter of 140 mm to the depth of interest; (2) drilling a concentric 37 mm diameter borehole from the bottom of the large diameter borehole in which a STT cell is inserted and glued against the walls using an epoxy resin; and (3) resuming the drilling of the large diameter borehole to a depth compatible with a complete stress release around the STT cell.

After the overcoring, the core with the strain measurement device is recovered, and the content of the memory (strains, temperatures and times) is transferred to a computer. In Figure 8, the variation of the strains with time at the location of the ten strain gauges obtained during an overcoring test is shown. The dashed line represents the variation of the temperature with time. Strain readings are taken before and after overcoring when the temperature is stabilised. The difference between these values is calculated, which corresponds to the strains that result from the overcoring.

To determine the elastic constants of the overcored cores, they are placed inside a biaxial chamber in which a radial hydraulic pressure p is applied. Three loading and unloading cycles were performed. The first cycle achieves a maximum pressure of 2 MPa. In the other two cycles, a maximum pressure of 6 MPa is applied. The deformation at the location of the ten strain gauges that results from the applied pressure is measured.

In the majority of biaxial tests, the obtained pressure *versus* strains curves show a linear and elastic behaviour (Figure 9a). In these cases, the calculation of the elastic constants is performed by considering the strains measured by the ten strain gauges associated with the average of the first unloading cycle at 6.0 MPa and the second loading cycle at the same pressure. However, in some cases, the behaviour of the rock core is non-linear and non-elastic for small pressures (in the 0 MPa to 2 MPa range, Figure 9b). This may indicate the closure of existing microfissures when the biaxial

loading is applied. In these cases, the calculation of the elastic constants is made by neglecting the pressure *versus* strain curves obtained between 0 MPa and 2 MPa.

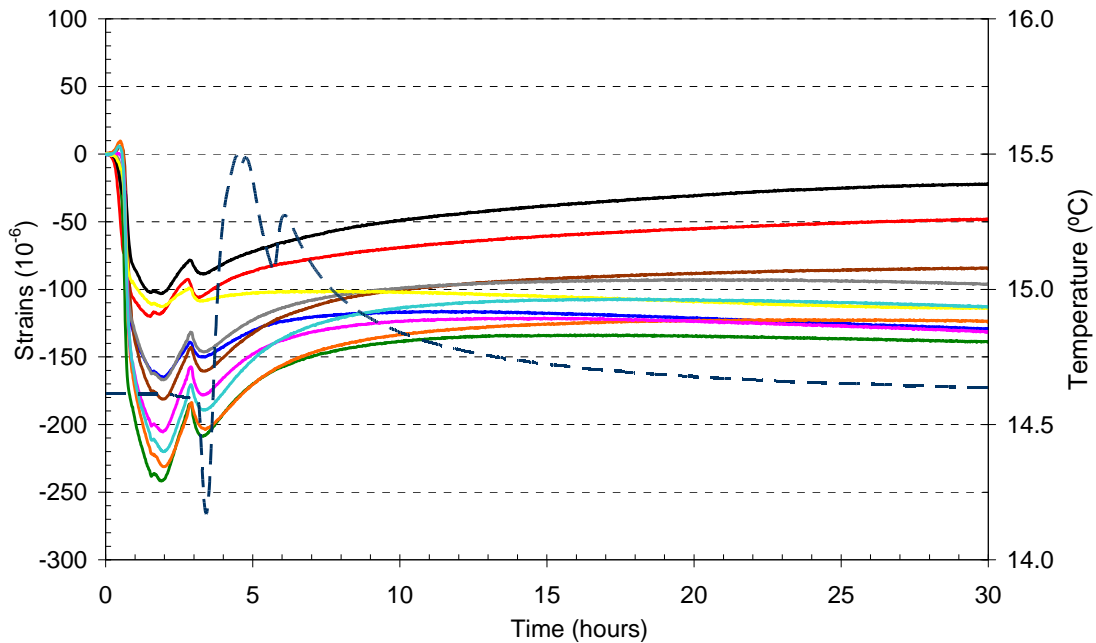


Figure 8: Strain *versus* time curves obtained during an overcoring test.

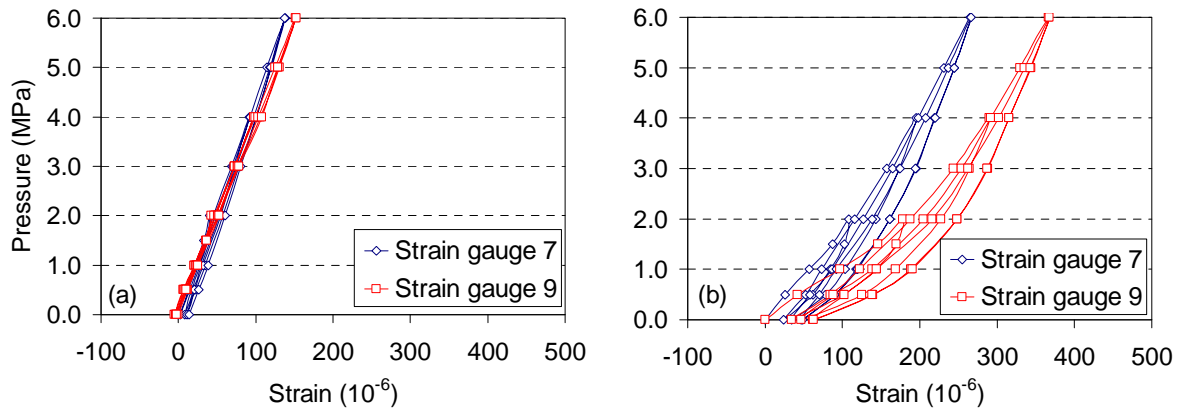


Figure 9: Pressure *versus* displacement curves obtained in biaxial tests performed in overcored cores. (a) linear and elastic behaviour; (b) non-linear and non-elastic behaviour.

The model used for interpreting the STT tests results assumes that the rock is homogeneous, linear, elastic and isotropic; that the relationship between the length and diameter of the cell is high; and that the stiffness of the hollow cylinder is significantly less than the stiffness of the rock. In this model, given the arrangement of the strain gauges, the strains ε_i at the location of the strain gauge i ($i = 1, \dots, 10$) are related to the components of the *in situ* stresses σ_j ($j = 1, \dots, 6$) through the following matrix equation:

$$\varepsilon_i = a_{ij}\sigma_j, \quad [2]$$

where a_{ij} is a matrix with ten rows and six columns that depends on the elastic parameters (elastic modulus E and Poisson's ratio ν) of the overcored core (Pinto and Cunha [18]).

With the measured ten strains that result from a biaxial loading ($\sigma_1 = \sigma_2 = p$ and $\sigma_3 = \sigma_4 = \sigma_5 = \sigma_6 = 0$), the least squares method is applied to solve the matrix equation [2] and consequently determine the elastic constants. Once the strains resulting from the overcoring are measured and the elastic constants are determined, the least squares method is applied to determine the six components of the stress state in the co-ordinate system associated with the STT cell.

The obtained elastic constants are shown in Table 6. By considering the set of six biaxial tests obtained in each borehole, the following average (E and ν) and standard deviation (δE and $\delta \nu$) values for the elastic constants were obtained:

Borehole PD1: $E = 60.8$ GPa, $\delta E = 12.9$ GPa, $\nu = 0.30$, $\delta \nu = 0.05$

Borehole PD2: $E = 57.7$ GPa, $\delta E = 9.5$ GPa, $\nu = 0.35$, $\delta \nu = 0.11$

Table 6: Biaxial test results.

Borehole	Test	Depth z (m)	E (GPa)	ν
PD1	1	202.8	74	0.39
	2	206.5	57	0.34
	3	221.5	73	0.26
	4	222.2	71	0.28
	5	250.9	50	0.26
	6	251.7	40	0.25
PD2	1	162.5	55	0.40
	2	164.1	55	0.40
	3	183.5	43	0.17
	4	184.1	57	0.42
	5	201.5	75	0.24
	6	202.9	61	0.46

The standard deviations of the elastic modulus are approximately 21% and 16% of the average values, whereas the standard deviations for Poisson's ratio are approximately 17% and 31% of the average values for boreholes PD1 and PD2, respectively. This analysis outlines a significant dispersion of the elastic parameters around their average values. Comparing these results with those obtained from uniaxial compression tests conducted in cores, the following values were obtained:

$$E = 44.6 \text{ GPa}, \delta E = 9.0 \text{ GPa}, \nu = 0.25, \delta \nu = 0.06$$

The standard deviations of the elastic modulus and Poisson's ratio are approximately 20% and 24% of the average values, respectively. The values of Poisson's ratio determined from biaxial testing are considerably greater than those obtained from uniaxial tests, which may be explained due to the development of microcracks normal to the axes of the cores and consequent tensile strains in this direction during biaxial testing.

The magnitude and orientation of the principal stresses (σ_I , σ_{II} , σ_{III}) obtained in each test are presented in Table 7. In this table, the orientations are described by two angles; the first angle is the direction of the principal stress component with respect to the North, and the second angle is the inclination with respect to the horizontal plane.

Table 7: Principal stress (σ_I , σ_{II} , σ_{III}) magnitudes and orientations obtained from interpreting the overcoring tests.

Borehole	Test	Depth z (m)	Principal stress magnitudes (MPa)			Principal stress orientations (°)		
			σ_I	σ_{II}	σ_{III}	σ_I	σ_{II}	σ_{III}
PD1	1	202.8	6.4	5.6	4.7	325/66	85/12	179/20
	2	206.5	7.0	3.4	3.2	249/86	147/1	56/4
	3	221.5	8.7	3.4	3.3	354/86	231/2	141/4
	4	222.2	9.3	6.9	5.9	36/64	188/23	283/11
	5	250.9	10.6	8.2	7.0	94/54	200/11	298/34
	6	251.7	11.3	6.5	6.0	26/73	150/10	242/14
	Inversion	225.9	9.7	6.0	5.9	48/78	184/8	275/8
PD2	1	162.5	11.9	6.9	5.9	94/79	260/11	350/3
	2	164.1	8.0	6.3	4.3	328/75	229/2	139/15
	3	183.5	6.2	2.8	2.0	324/79	177/10	86/6
	4	184.4	5.1	4.6	4.3	285/63	24/5	116/26
	5	201.5	-1.9	-3.6	-4.0	267/77	69/12	160/4
	6	202.9	6.0	4.2	3.4	289/39	147/45	36/20
	Inversion	190.3	4.4	3.4	3.1	301/62	193/13	94/25

All the overcoring data obtained in each borehole are considered in matrix equation [2] to calculate the stress tensor that fits best with all the overcoring stress measurements at the centre of each tested rock mass volume. In this global inversion of the overcoring data obtained in each borehole, the following assumptions are made: (i) the rock mass exhibits an isotropic, linear, elastic behaviour; (ii) the influence of topography on the overcoring tests results is negligible (which is reasonable given that at the depth of the tests, one of the principal stresses is practically sub-vertical); (iii) the vertical gradient of the stress tensor components is neglected (in both boreholes, measurements were conducted within a depth range smaller than 50 m); and (iv) the influence of the adit on the overcoring test results is negligible (tests considered for the inversion are located out of the range of the adit's perturbation zone).

Based on these hypotheses, a 6-parameter model is used in the inversion of the overcoring data. These parameters refer to the six components of the stress tensor at the centre of the tested rock mass volume. In borehole PD1, all the overcoring tests results are considered in the inversion. In borehole PD2, the stresses obtained at 201.5 m below the surface are questionable, considering the expected stresses at this depth due to gravity loading as well as the stress values obtained in the other tests. Furthermore, in this borehole, the stresses obtained in two tests done close to the adit are significantly higher than the stresses obtained for other tests. These three tests results were not included in the inversion. The results of the inversion are presented in Table 7.

The table shows that the maximum principal stress (σ_I) is sub-vertical and that the other two principal components (σ_{II} and σ_{III}) are sub-horizontal and of similar magnitude. Due to this, the dispersion observed for the direction of sub-horizontal principal stresses is not significant. In borehole PD1, the stresses are significantly greater than in borehole PD2, which is not explained by only the discrepancy in the depth of the two tested rock mass volumes.

Although the overcoring and hydraulic tests were conducted at locations separated by approximately 1.7 km, the results may be compared because no important faults are identified between these locations. Figure 10 shows the variation with depth of the principal stress magnitudes (σ_I , σ_{II} , σ_{III}) obtained by overcoring and hydraulic testing. In this figure, the lines represent the lower and upper bounds of a 99% confidence interval obtained from the inversion of the set of fifteen hydraulic tests, in which the far-field stress solution is presented in Table 3. The points represent the overcoring test results obtained in boreholes PD1 and PD2. The figure also shows the results of the inversion (INV) of the overcoring data at the centre of the rock mass volume tested in boreholes PD1 and PD2. In the hydraulic tests, the maximum principal stress (σ_I) is assumed to be vertical. In overcoring tests, this stress component is found to be sub-vertical.

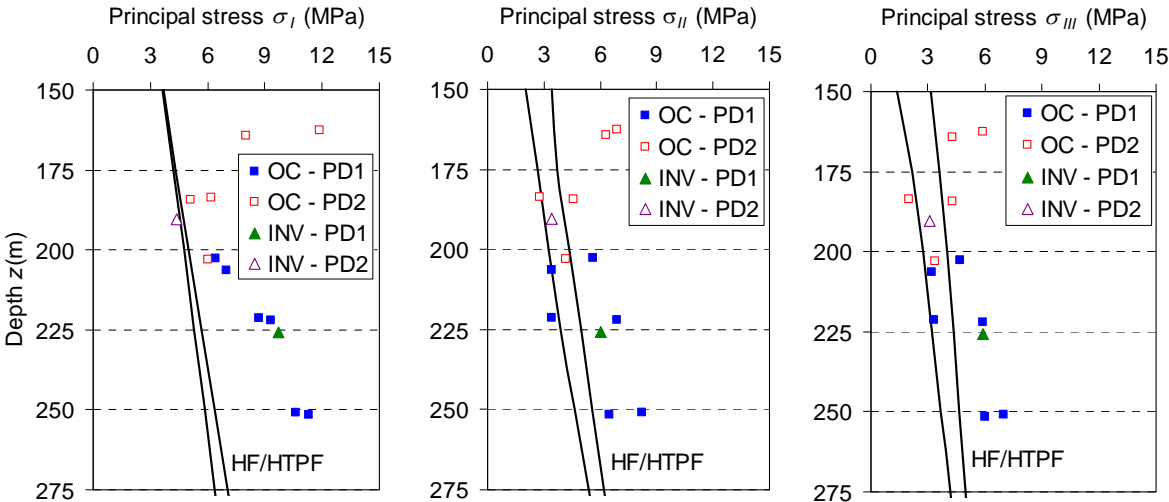


Figure 10: Comparison of the magnitudes of the principal stresses (σ_I , σ_{II} , σ_{III}) obtained by overcoring and hydraulic testing.

The figure shows that the magnitudes of the sub-vertical stress components obtained using the overcoring method in borehole PD1 are significantly higher with respect to those obtained by hydraulic testing. In fact, the overcoring technique often leads to high stresses in the direction parallel to the borehole axis. This has been justified by large deformations that occurred in this direction as a result of the glue yield caused by the heat generated during the drilling operation (Ask [4]). The magnitudes of the sub-horizontal stress components obtained by overcoring in borehole PD1 are slightly higher (about 1.5 MPa) than those obtained by hydraulic testing. This result may be attributed to the different role of topography on the distribution of *in situ* stresses at the location of hydraulic and overcoring tests.

4 SMALL FLAT JACK TESTS

The small flat jack testing method (Rocha *et al.* [19]) is based on the principle of partial stress release followed by stress compensation (Habib and Marchand [20]). In this technique, two pairs of pins are placed on the rock mass surface, and the initial distance between the pins is measured using digital transducers. Then, between the two pairs of pins, a 10 mm-thick slot with a depth of 27 cm is cut perpendicular to the rock mass surface using a diamond disk with a 60 cm diameter. Due to the partial stress relief, deformations in the direction normal to the slot occur and the distance between the pins decreases. Subsequently, a circular flat jack consisting of two thin metal plates welded together is inserted into the slot and pressurised until the distance between the pins is restored. During the test, the variation of the relative displacements in the two pairs of pins because of the applied pressure is recorded. Figure 11 shows a typical curve with the average relative displacements obtained in a typical test. Generally, non-elastic behaviour is observed because non-recoverable displacements are detected after unloading.

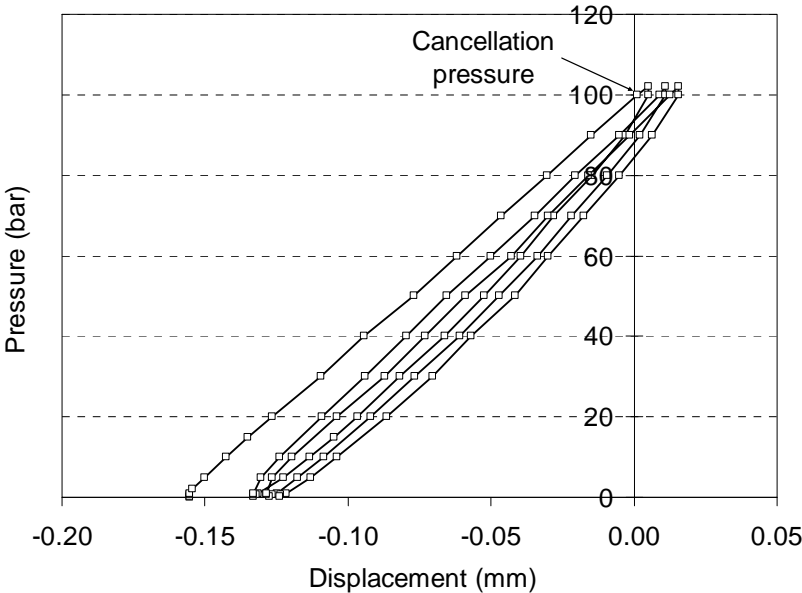


Figure 11: Typical pressure *versus* displacement curves obtained in small flat jack tests.

The pressure required to restore the initial position of the pins is called the “cancellation pressure”, and it is assumed to be equal to the stress component normal to the slot plane. In each test, the cancellation pressure is obtained from the intersection of the average displacement curve with the vertical axis. In this determination, only the loading phase in first cycle was considered.

In addition to measuring *in situ* stresses, small flat jack tests are used to determine the elastic modulus E normal to the slots from the pressure p that is applied normal to the slots, the displacement δ that is measured at the location of the pins, and a constant k that depends on the geometric characteristics of the small flat jack using the following equation (Souza Martins [21]):

$$\delta = \frac{k}{E} p. \quad [3]$$

Table 8 shows the obtained results. In this table, d is the distance between the test location and the adit's entrance, ϕ is the azimuth of the normal to the slot with respect to the North, θ is the inclination of the azimuth with respect to the vertical direction, σ_n is the normal stress, and E is the elastic modulus normal to the plane of the slot.

Table 8: Results from the small flat jack tests.

Location	Test	d (m)	ϕ (°)	θ (°)	σ_n (MPa)	E (GPa)
SFJ1	1	447	0	0	8.9	30.9
	2	448	110	45	6.4	45.1
	3	437	110	90	9.4	35.9
	4	446	290	45	3.7	30.9
SFJ2	5	332	0	0	9.9	30.8
	6	333	290	45	2.6	37.9
	7	331	290	90	2.0	26.2
	8	332.5	110	45	6.4	23.6
SFJ3	9	278	0	0	9.9	32.5
	10	275	290	45	3.2	22.9
	11	279	290	90	4.1	36.8
	12	280	110	45	3.0	31.6

In tests numbers 1, 5 and 9, similar sub-vertical stress components were measured, with values of 8.9 MPa, 9.9 MPa and 9.9 MPa, respectively.

The comparison of the horizontal stress components, obtained at the three locations, enables to conclude that the component measured in test number 3 is significantly higher than in the other tests. The rock was observed to have viscoelastic behaviour because the slot was subjected to a significant closure due to the considerable time interval that occurred between the end of the cut by the diamond

disk and the beginning of the test. This leads to a high cancellation pressure for restoring the initial position of the pins. This test result was discarded from further analyses.

By considering the set of elastic modulus values obtained in each test location, the following average and standard deviation values were obtained:

$$\text{SFJ1: } E = 35.7 \text{ GPa, } \delta E = 5.8 \text{ GPa}$$

$$\text{SFJ2: } E = 29.6 \text{ GPa, } \delta E = 5.4 \text{ GPa}$$

$$\text{SFJ3: } E = 31.0 \text{ GPa, } \delta E = 5.0 \text{ GPa}$$

The analysis of the results reveals a significant dispersion of the elastic modulus around their average values because the standard deviations are approximately 16%, 18% and 16% of the average values at locations SF1, SFJ2 and SFJ3, respectively. Comparing the elastic modulus values determined in small flat jacks with those that were obtained by the biaxial tests conducted in overcored rock cores (Table 6), it can be concluded that they are considerably smaller. This result may be explained in two ways. On the one hand, the rock mass volume tested with flat jacks is larger than that used in overcoring testing and hence includes a considerable number of existing microfissures. On the other hand, the flat jack tests were conducted on the walls of the adit, where blasting damage caused by the construction method may be significant, while overcoring tests were conducted on intact cores. This is further discussed in Part II of the paper where data are integrated in a single model.

The determination of the complete stress tensor at a given point from small flat jack tests requires a minimum of six tests conducted in six different directions. Because there are not enough small flat jack tests for such a determination, the results obtained using small flat jacks and using overcoring for tests conducted at locations close to each other are compared.

In this comparison, the following three assumptions are made: (i) the rock has a linear elastic and isotropic behaviour; (ii) the vertical gradient of the stress tensor components is negligible; and (iii) the lateral stress variation between the locations of the various tests is negligible.

The stresses provided by the small flat jack technique do not correspond to the far-field stress components because they are influenced by the existing adit. In this way, the six components of the stress tensor S^k ($i = 1, \dots, 6$) that are acting at the location of the k^{th} small flat jack test and the six components of the far-field stress tensor σ_j ($j = 1, \dots, 6$) at this location are related by the following equation:

$$S^k = A_{ij}^k \sigma_j, \quad [4]$$

where A_{ij}^k is a matrix of 36 influence coefficients that depends on the geometry of the adit at the location of the k^{th} small flat jack test.

A three-dimensional numerical model of finite differences was developed using the code FLAC3D (Itasca [22]) (Figure 12). This model is a 30 m×30 m×5 m solid and includes the rectangular cross section of the adit with dimensions 2.4 m×2.0 m. Note that the elastic modulus has no effect on the solution. A Poisson's ratio value of 0.25 obtained from uniaxial compression tests conducted on intact

cores was considered. Variations of the Poisson's ratio between 0.25 and 0.35 do not result in changes larger than 5% for the stresses in the walls of the existing adit.

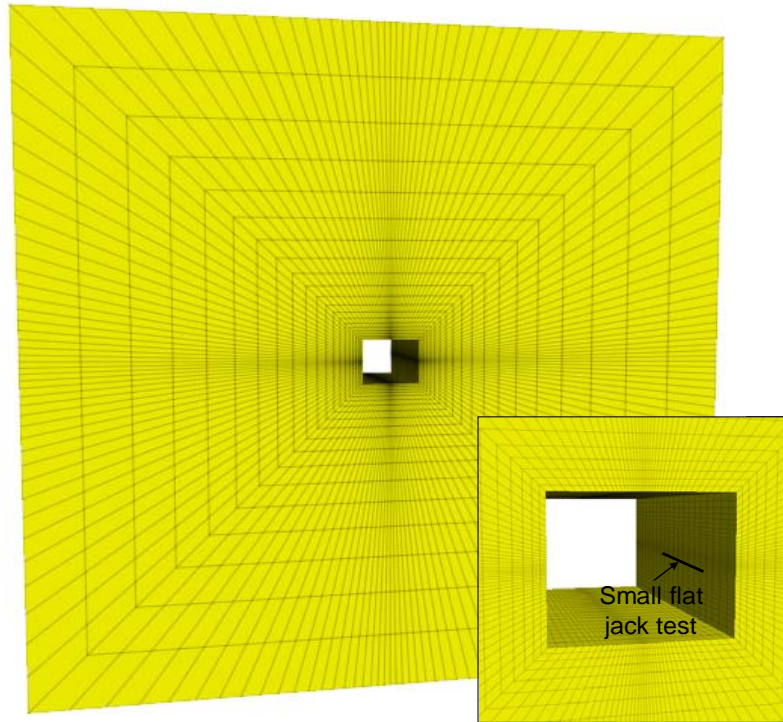


Figure 12: Three-dimensional model used for interpretation of the small flat jack tests.

The influence coefficients were determined from six calculations; in each calculation, a unit value of one of the stress tensor components σ_j ($j = 1, \dots, 6$) is used with null values for the other components. As a result of each calculation, the stress tensor components S^k ($j = 1, \dots, 6$) at the location of the k^{th} small flat jack tests are obtained. After the influence coefficients are determined, the normal stresses $\sigma_{n,calc}^k$ at the location of the k^{th} small flat jack test are calculated with the following equation:

$$\sigma_{n,calc}^k = S_i^k N_i^k \quad (i, j = 1, \dots, 6),, \quad [5]$$

where N_i^k ($i = 1, \dots, 6$) are the generalised components of the normal to the k^{th} small flat jack plane.

Equation [5] is used to calculate the normal stresses at the location of the small flat jack tests by considering the far-field stress tensor components obtained from the overcoring testing. Two different far-field stress conditions are considered. First, the stress tensor components that result from the inversion of overcoring data are considered. Second, the average stress tensor components of the overcoring tests results obtained close to the adit, in boreholes PD1 and PD2, are considered.

A comparison between the normal stresses obtained this way and the stresses actually measured with the small flat jacks is shown in Figure 13. Figure 13 shows that there is a significant discrepancy (greater than 1.0 MPa) between the stresses measured using the two testing methods in

approximately 75% of the tests. This concludes that the stresses measured in the adit walls using small flat jacks are not consistent with the stresses measured at a similar location by overcoring.

Because no local heterogeneities were identified in the borehole logs that justify these stress variations, it is concluded that the small flat jack tests and shallow overcoring tests are influenced by the adit. Detailed analysis of the causes of this disagreement remains to be conducted. It seems likely that this disagreement is associated with the mechanical behaviour of the damaged zone that was caused by blasting when the adit was constructed.

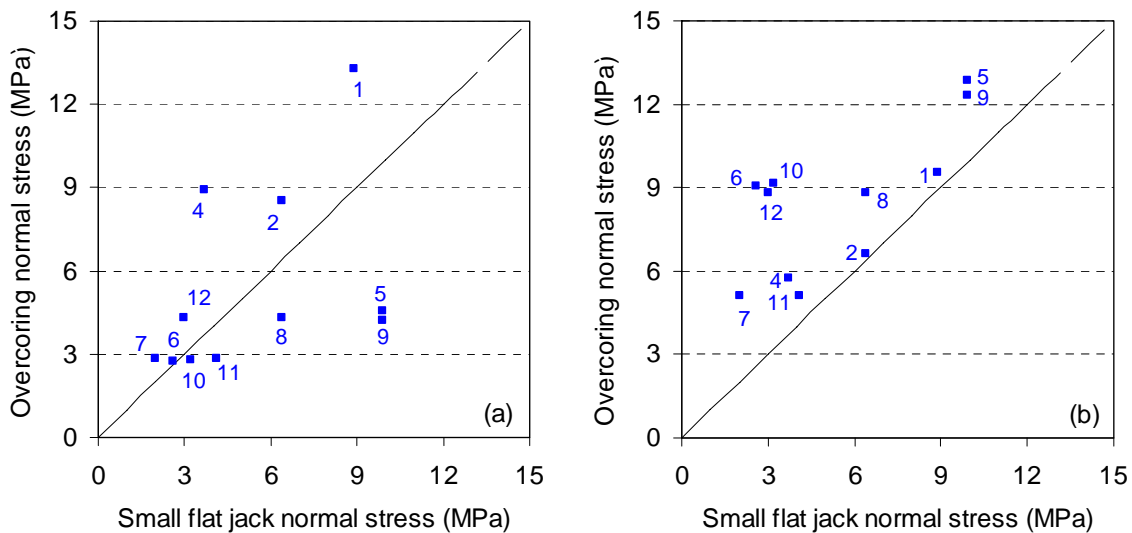


Figure 13: Comparison between small flat jack and overcoring normal stress considering the far-field stress tensor resulting from the (a) inversion of overcoring data and (b) shallow overcoring tests results.

5 DISCUSSION AND CONCLUSIONS

Several *in situ* stress measurements were conducted at the Parabela II site for the design of an underground reinforcement power scheme that includes a large powerhouse cavern and a hydraulic pressure tunnel. The measurements include hydraulic tests in two 500 m deep vertical boreholes, overcoring tests in two 60 m deep vertical boreholes drilled from an existing adit and small flat jack tests in the walls of the adit.

The data shows a significantly spatial variability of the rock mass properties and a non-elastic behaviour for the low stress levels.

The analysis of the hydraulic and overcoring data demonstrates that one principal stress component is sub-vertical within most of the volume that was tested. The other two components are sub-horizontal and of similar magnitude. Some local zones of heterogeneity were encountered, as demonstrated by the appearance of inclined fractures in the electrical imaging logs obtained for two of the hydraulic fracturing tests. Local heterogeneities explain the large uncertainty in the orientation of the maximum horizontal principal stress direction.

A comparison between the overcoring and hydraulic tests shows that, with the exception of the sub-vertical stresses obtained by overcoring in borehole PD1 and the overcoring test results obtained in borehole PD2 close to the existing adit, the stresses estimated by both techniques are of similar magnitude.

A comparison between the small flat jack and overcoring tests conducted at approximately the same location reveals significant differences in the results. It appears that, close to the adit, the stresses are most likely influenced by the rheological behaviour of the damaged zone associated with the construction of the adit.

The second part of this paper presents an approach that integrates the data obtained away from the adit in a single model to extrapolate these measurements to the volume relevant to the design of the underground hydroelectric power scheme.

ACKNOWLEDGEMENTS

This work was funded by the Portuguese Laboratory for Civil Engineering (LNEC) and the Foundation for Science and Technology (FCT) PhD grant SFRH/BD/68322/2010. The work on the stress field at the Paradelá II site was supported partially by the Portuguese Laboratory for Civil Engineering (LNEC) and Energy of Portugal (EDP).

REFERENCES

- [1] Cornet FH, Valette B. *In situ* stress determination from hydraulic injection test data. *Journal of Geophysical Research* 1984; 89: p.11527–37.
- [2] Cornet FH. A complete 3D stress determination for the design of an underground power station. *Proceedings of the 2nd North American Rock Mechanics Symposium, NARMS'96* (Eds. Aubertin, M., Hassani, F., Mitri, H.), Montréal, Canada, A.A. Balkema Publ., Rotterdam; 1996, p. 755–61.
- [3] Cornet FH, Yin JM. Analysis of induced seismicity for stress determination and pore pressure mapping, *Pageoph* 1995; 145: p. 677–700.
- [4] Ask D. *New Developments of the Integrated Stress Determination Method and Application to the Aspö Hard Rock Laboratory, Sweden*. PhD Thesis, Royal Institute of Technology; 2004.
- [5] Lamas L, Muralha J, Figueiredo B. Application of a global interpretation model for assessment of the stress field for engineering purposes. *Proceedings of the 5th International Symposium on In Situ Rock Stress*. Beijing; 2010.
- [6] Hart R. Enhancing rock stress understanding through numerical analysis. *International Journal of Rock Mechanics and Mining Sciences* 2003; 40: p. 1089–97.
- [7] Matsuki K, Nakama S, Sato T. Estimation of regional stress by FEM for a heterogeneous rock mass with a large fault. *International Journal of Rock Mechanics and Mining Sciences* 2009; 46: p. 31–50.

- [8] Muralha J, Lamas L, Esteves C. State of stress assessment for the Picote II underground powerhouse design. Proceedings of the International Symposium on Rock Mechanics - SINOROCK2009. Hong Kong; 2009.
- [9] Sousa L, Martins C, Lamas L. Development of the techniques of measurement and the interpretation of the state of stress in rock masses. Application of the Castelo do Bode tunnel. Proceeding of the 5th International Congress on IAEG. Buenos Aires; 1986.
- [10] Haimson BC, Cornet FH. ISRM Suggested Methods for rock stress estimation – Part 3: Hydraulic fracturing (HF) and/or hydraulic testing of pre-existing fractures (HTPF). International Journal of Rock Mechanics and Mining Sciences 2003; 40: p. 1011–20.
- [11] Cornet FH. The HTPF and the Integrated Stress Determination Methods. Comprehensive Rock Engineering, 3, (J. Hudson, Ed.). Pergamon Press, Oxford; 1993, p. 413–432.
- [12] Mosnier J, Cornet FH. Apparatus to provide an image of the wall of a borehole during a hydraulic fracturing experiment. In: Louwrier K, Staroste E, Garnish JD, Karkoulis V, editors. Fourth International Seminar on the Results of EC Geothermal Energy Research and Demonstration, Proceedings, Dordrecht: Commission of the European Communities, Kluwer Academic Publishers; 1989: p. 205–212.
- [13] Aamodt RL, Kuriyagawa M. Measurement of instantaneous shut-in pressure in crystalline rock. In: Zoback, M.D., Haimson, B., editors. Hydraulic fracturing stress measurements. Washington, DC: National Academy Press; 1983, p. 139–42.
- [14] Hayashi K, Haimson BC. Characteristics of shut-in curves in hydraulic fracturing stress measurements and the determination of the *in situ* minimum compressive stress. Journal of Geophysical Research 1991; 96 (B11): p. 18311–21.
- [15] Cornet FH, Doan ML, Fontbonne F. Electrical imaging and hydraulic testing for a complete stress determination. International Journal for Rock Mechanics and Mining Sciences 2003; 40: p. 1225–41.
- [16] Tarantola A, Valette B. Generalized non-linear inverse problem solved using the least square criterion. Reviews of Geophysics and Space Physics 1982; 20: p. 219–32.
- [17] Rocha M, Silvério A. A new method for the complete determination of the state of stress in rock masses. Géotechnique 1969; 19 (1): p. 116–32.
- [18] Pinto JL, Cunha AP. Rock stresses determinations with the STT and SFJ techniques. In Rock Stress and Rock Stress Measurements. Lulea: Centek; 1986
- [19] Rocha M, Lopes B, Silva N. A new technique for applying the method of flat jack in the determination of stresses inside rock masses. Proceedings of the 1st Congress of the International Society of Rock Mechanics 1966; 2: p. 57–65.
- [20] Habib P, Marchand R. Mesures des pressions de terrains par l'essai de verin plat. Annales de l'Institut Technique du Bâtiment et des Travaux Publics, Série Sols et Foundations 1952; 58: 966–71.
- [21] Souza Martins C. Contribution for the study of underground works associated with hydroelectric schemes (in Portuguese). LNEC's internal report 24/86; 1986.
- [22] Itasca. FLAC3D, Version 4.0. User's Manual. Itasca Consulting Group, Minneapolis; 2009.

PAPER 3

Determination of the stress field in a granite rock mass Part II: an integrated solution

Figueiredo, B., Cornet, F.H., Lamas, L., Muralha, J. (2013)

Submitted for publication in
International Journal of Rock Mechanics and Mining Sciences in June 2013

Determination of the stress field in a granite rock mass

Part II: an integrated solution

B. Figueiredo¹, F.H. Cornet², L. Lamas¹ & J. Muralha¹

¹ National Laboratory for Civil Engineering (LNEC), Avenida do Brasil, 101, Lisbon, Portugal

e-mail: brunof@lnec.pt

Phone number: +351218443391

² Institut de Physique du Globe de Strasbourg (IPG-S-CNRS), 5 rue René Descartes, Strasbourg, France

e-mail: Francois.Cornet@unistra.fr

Phone number: +33368850344

ABSTRACT: The regional stress field of a mountainous region in northern Portugal was investigated for the design of a large-scale underground hydroelectric power scheme. This characterisation involved a set of *in situ* stress measurements, which were presented in part I of this paper. Part II presents an integrated approach for extrapolating the results from the various *in situ* tests to the rock mass volume of interest for the hydroelectric power scheme. This approach includes the development of an equivalent continuum mechanics model, which is processed with the FLAC3D code from Itasca [1]. The model is used for identifying the parameters that minimise the misfit between the measured and calculated stresses. By performing a gravitational analysis and considering the elastic properties obtained from laboratory tests conducted on intact cores, a discrepancy is found between the sub-horizontal stresses measured *in situ* and the results obtained with the model. Then, the possible influence of tectonic stresses is investigated, and rejected, based on the data published in the World Stress Map database. In fact, the model shows that most of the hydraulic and overcoring data are consistent with a linearly elastic equivalent geomaterial, the properties of which correspond to a much softer material than suggested by laboratory tests on cores. This finding leads to conclude that the large-scale long-term stress field in this granitic massif is controlled by shear stress relaxation along the various fractures and faults that affect this massif. However, the model cannot explain the flat jack data nor two overcoring results obtained close to the adit from which the measurements were conducted. Hence, the equivalent geomaterial defined for this massif is not representative of the material close to the adit and cannot be used for evaluating the stress field in the vicinity of this adit.

KEYWORDS: regional stress field, topography, soft elastic rock mass, shear stress relaxation, natural fracture network

1 INTRODUCTION

Part I of this paper presented stress measurement data obtained at different locations in a mountainous region of northern Portugal. The objective was to characterise the regional stresses for the design of a re-powering scheme of an existing hydroelectric system that includes an underground large cavern and a hydraulic pressure tunnel. The *in situ* measurements include overcoring and hydraulic tests conducted in boreholes as well as flat jack tests performed in the walls of an existing adit.

The aim of Part II is to integrate these various data to assess the regional stress field and consequently to extrapolate the results of the various tests to the rock mass volume of interest for this hydroelectric scheme. The integration of the data faces several difficulties. First, the data were collected at different locations using different testing techniques. Second, topography effects have a significant influence on the stresses at the locations of the various measurements. Furthermore, local heterogeneities (e.g., fractured zones and faults), the spatial variability of the rock mass properties and, possibly, plasticity for zones close to the adit from which the overcoring measurements and the flat jack tests were conducted may have to be considered (see Part I).

The objective is to develop a model that is simple enough such that the constraining data are more numerous than the number of degrees of freedom of the model. Indeed, as the model becomes more complicated, the solution becomes less constrained, the apparent efficiency of the fit between the data and model becomes more illusory, and the conclusion becomes less useful.

A linearly elastic model is used for integrating results gathered away from the adit (fifteen normal stress measurements obtained by hydraulic testing and the six components of nine stress tensors determined at the location of the overcoring tests). This model considers the influence of topography effects on *in situ* stress distributions. Furthermore, this model is used to investigate the influence of the compliance of existing large-scale fractured zones and potential tectonic stresses and to determine the proper elastic constants for the equivalent geomaterial. It has provided the means to identify a simple model that satisfactorily reproduces (in a least squares sense) the different measurements obtained away from the adit.

2 INVERSE MODEL

The aim of any inversion scheme is to determine the model parameters that minimise the differences between a number of observations and predictions from a model. This determination requires a model definition, a definition of the misfit for describing the discrepancy between observed and predicted values, and a normative measure of the misfit for quantifying the residuals for all observations (Gephart and Forsyth [2]). Two types of normative methods are commonly used: the l_1 -norm considers the sum of the absolute values of the error between observations and predictions; the l_2 -norm considers the sum of the squares of the error between observations and predictions. The l_1 -norm is more robust than the l_2 -norm and yields smaller variances for the error. Furthermore, it is less influenced by atypical data (Parker and McNutt [3]).

The inverse problem concept is more general than the back analysis concept (Gioda and Sakurai [4]). With the back analysis, only one model is assumed for describing the observations, whereas for the inverse problem, several hypotheses for the model are tested.

The inverse model that is proposed here is meant to help determine the natural regional stress field that best fits the data gathered away from the existing adit (see Part I). This model considers an equivalent continuous geomaterial, and the corresponding characteristic differential equations are solved with explicit finite differences using the software FLAC3D (Itasca [1]).

Due to the influence of topography effects, models simulating rock mass volumes with different dimensions were considered when performing the gravitational analysis ($g=9.81 \text{ m.s}^{-2}$) for fitting stresses at the locations of the various tests. The results of this analysis indicated that the region 5 km long and 3 km wide shown in Figure 1 is sufficiently large for obtaining reliable estimates because for larger regions, the maximum variations in the principal stress magnitude at the locations of the various tests are less than 0.5 MPa. In this region, the elevation varies between 315 m and 1030 m above sea level (Figure 1). A 2.5 km dimension was assigned to the vertical direction so that topography effects do not influence the stresses close to the basal boundary of the model.

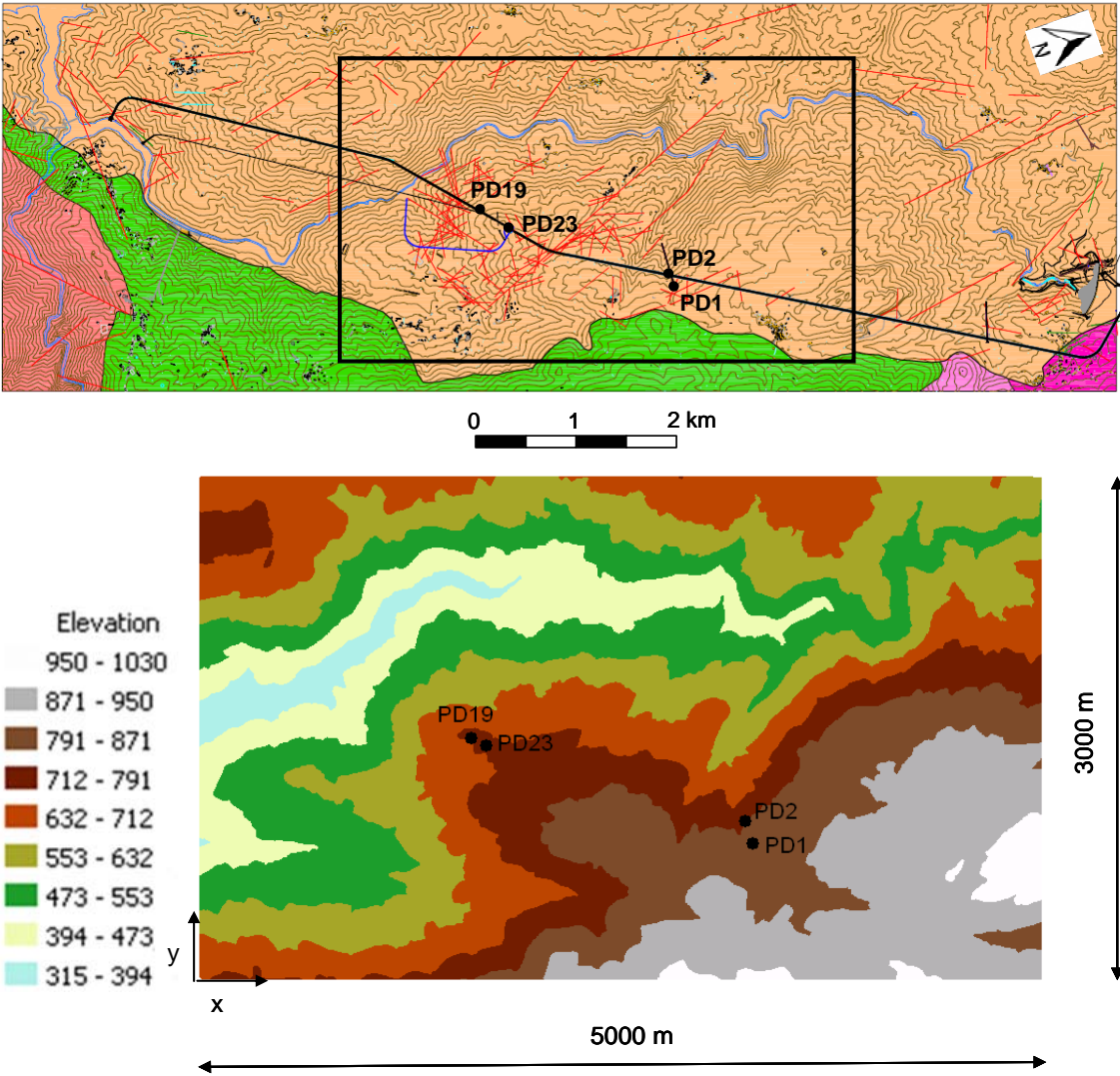


Figure 1: Limits and detailed elevation of the region considered in the FLAC3D model.

The mesh of the FLAC3D model (Figure 2) is composed of 600,000 elements. This mesh is finer above sea level, with cubic 25 m-sided elements. Below sea level, the elements are 50 m×50 m×100 m. As boundary conditions with gravity loading, displacements normal to the lateral and basal boundaries are restricted.

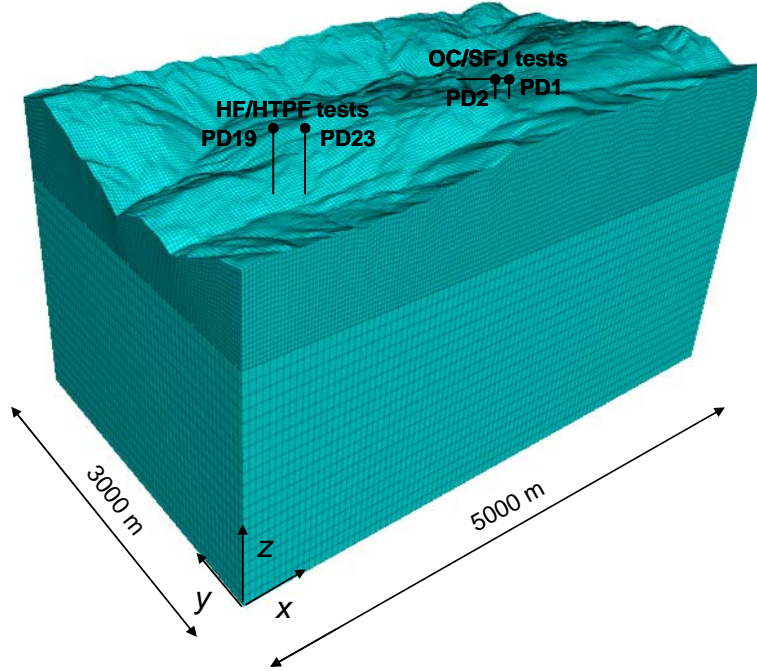


Figure 2: Mesh of the FLAC3D model.

The l_1 -norm method was used to minimise the misfit between the measured and calculated stresses, normalised by the uncertainty on the data. Consequently, the misfits are adimensional.

For hydraulic data, the misfit ψ^{HF} is expressed as follows (Yin and Cornet [5]):

$$\psi^{HF} = \sum_{m=1}^M \frac{|\sigma_{n,mes}^m - \sigma_{n,calc}^m|}{\delta_n^m + \delta_f^m}, \quad [1]$$

where M is the number of hydraulic tests; $\sigma_{n,mes}^m$ and $\sigma_{n,calc}^m$ are the measured and calculated normal stresses obtained at the location of the m^{th} hydraulic test, respectively; δ_n^m is the uncertainty on the normal stress determination for the m^{th} fracture plane; and δ_f^m is the uncertainty on the normal stress associated with uncertainties on the orientation of the m^{th} fracture plane.

The uncertainties on the normal stresses and on the fracture plane orientation that were considered correspond to a 99% confidence interval of the measurements (see Part I). The uncertainties on the normal stresses due to the uncertainty on the fracture plane orientation were estimated using the FLAC3D model. Uncertainties obtained in this way are of the same order of magnitude as the uncertainties associated with the shut-in pressure measurements.

For overcoring data, the uncertainties are associated with the strain measurement technique, the orientation of the strain gauges in the three dimensional space and the determination of elastic properties of the overcored cores. The misfit ψ^{OC} that was used is simplified and is defined as follows:

$$\psi^{OC} = \sum_{n=1}^N \frac{|\sigma_{mes}^n - \sigma_{calc}^n|}{\delta_{\sigma}^n + \delta_{bh}^n}, \quad [2]$$

where N is the number of overcoring tests; σ_{mes}^n and σ_{calc}^n are the measured and calculated stresses obtained at the location of the n^{th} overcoring test, respectively; δ_{σ}^n is the uncertainty associated with the stress determination; and δ_{bh}^n is the uncertainty on the stress associated with uncertainties on the orientation of the borehole axis.

Because the overcoring tests were conducted within a small depth range (approximately 60 m) in vertical boreholes, the uncertainty associated with the orientations of these boreholes was neglected. By considering the several pairs of the overcoring test results obtained approximately at the same depth, a maximum uncertainty of 1.5 MPa was set for the corresponding stress magnitude determinations.

The hydraulic testing and overcoring methods are of different natures. Therefore, the global misfit when combining hydraulic and overcoring data should include weighting factors. A simplified global misfit was used that considers: (1) the volume, or area, involved in a given measurement for each of the methods; (2) the individual misfit related to the misfit obtained in the combined solution. The general global misfit ψ^{HFOC} can be expressed as follows (Yin and Cornet [5]):

$$\psi^{HFOC} = \omega^{HF} \psi^{HF} + \omega^{OC} \psi^{OC}. \quad [3]$$

The weighting factors for the hydraulic and overcoring data, ω^{HF} and ω^{OC} , respectively, are given by the following expressions:

$$\omega^{HF} = \frac{A^{HF}}{A^{REV}} \cdot \frac{\psi^{HF}}{\psi_{min}^{HF}}, \quad [4]$$

$$\omega^{OC} = \frac{V^{OC}}{V^{REV}} \cdot \frac{\psi^{OC}}{\psi_{min}^{OC}}, \quad [5]$$

where A^{HF} and A^{REV} denote the measurement area and the area involved in the representative elementary volume (REV) in hydraulic testing, respectively; V^{OC} and V^{REV} are the corresponding notations associated with the overcoring technique (measurement volume and REV volume, respectively); and ψ_{min}^{HF} and ψ_{min}^{OC} are the minimums of equations [1] and [2], respectively.

The area involved during hydraulic testing depends on the injected volume, but it was set to 1 m², which corresponds to 1 litre of water injected into a fracture with a mean width of 1 m (assuming no

loss of water due to rock mass permeability). The volume involved in overcoring measurements was set to the average volume of the resulting hollow rock cylinder. The REV at the scale of the stress measurements was not determined. As an approximation, the REV was set to 1 m³ (i.e., area 1 m²). Thus, the suggested global misfit gives more weight to the hydraulic data than to the overcoring data. Once the global minimum was found (minimum of ψ^{HFOC}), the 90% confidence interval could be estimated using the following expression (Parker and McNutt [3]):

$$\psi_{90\%}^{HFOC} = \frac{1.645(\pi / 2 - 1)^{1/2}(M + N)^{1/2} + M + N}{(M + N) - W} \psi_{min}^{HFOC}, \quad [6]$$

where W is the number of unknown parameters of the model used to describe the regional stress field.

3 COMPARISON BETWEEN *IN SITU* TESTS AND RESULTS FROM THE FLAC3D MODEL WHEN CONSIDERING GRAVITY LOADING ALONE

A comparison between hydraulic and overcoring data, on the one hand, and the FLAC3D model results obtained by performing a gravitational analysis, on the other hand, was undertaken. The elastic properties used in the model were those measured during a set of uniaxial compression tests conducted on intact cores extracted from the rock mass. The average values for the elastic constants (elastic modulus E and Poisson's ratio ν) are 45 GPa and 0.25, respectively. Density measurements provided a value of 2650 kg/m³ (see Part I).

In the hydraulic tests, the comparison was first made in terms of the normal stresses (σ_n) on the tested fracture planes in boreholes PD19 and PD23 (Figure 3). In the ambiguous tests with two observed fracture planes, the stresses were associated with the fracture plane for which the difference between the measured and calculated stress values was the smallest. A 99% confidence interval, which corresponds to six standard deviations for a Gaussian law, is shown for the various normal stress measurements. In boreholes PD19 and PD23, the sum of the absolute differences between the measured and calculated normal stresses are 33.4 MPa and 10.1 MPa, respectively. The highest differences are observed for the hydraulic fracturing tests, in which sub-horizontal stresses were measured (see Part I).

Secondly, a comparison was performed in terms of the principal stress ($\sigma_I, \sigma_{II}, \sigma_{III}$) magnitudes obtained with the FLAC3D model and from the inversion of the fifteen hydraulic tests set using an 8-parameter model (see Part I). The results of this comparison are displayed in Figure 4. The FLAC3D model results obtained for borehole PD23 are not presented because they are comparatively similar to the results obtained for borehole PD19. The 99% confidence limit for the calculated stresses with an 8-parameter model is shown. In the presented depth range, the maximum principal stress (σ_I) provided by the model is sub-vertical and the other two components (σ_{II} and σ_{III}) are sub-horizontal.

As shown in Figure 4, the inversion of the hydraulic data provides values for the horizontal principal stress components that are considerably larger than the values computed using the model when considering only gravity loads.

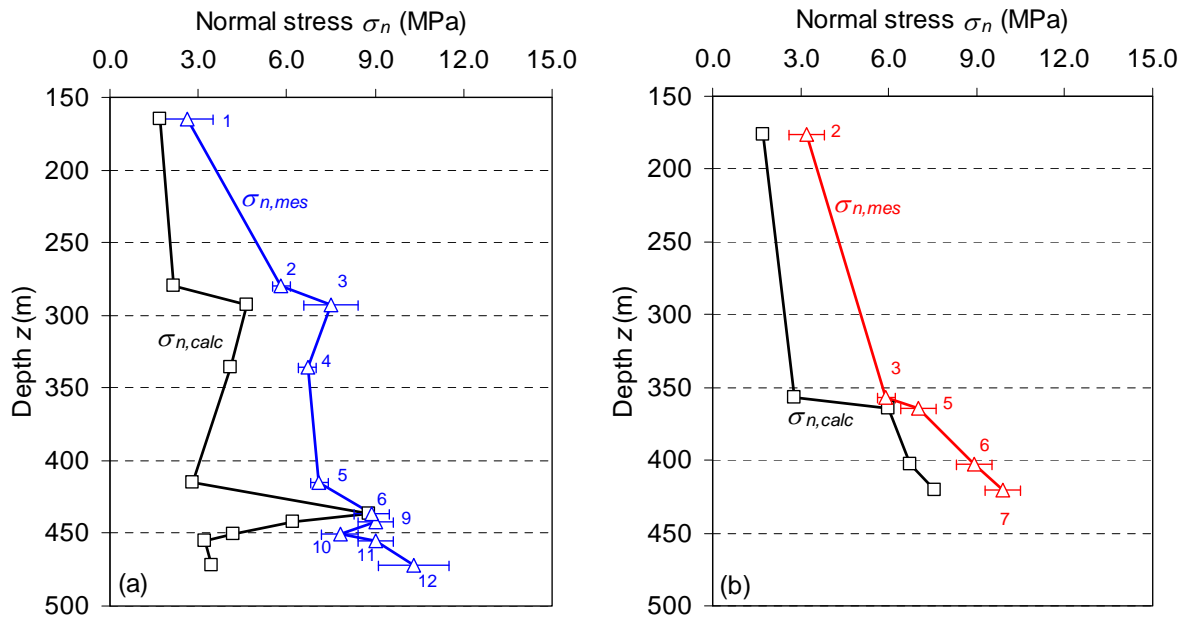


Figure 3: Variation of the magnitudes of the normal stresses obtained by hydraulic testing ($\sigma_{n,mes}$) and with the FLAC3D model ($\sigma_{n,calc}$) run with gravity loading only in boreholes (a) PD19 and (b) PD23 as a function of depth.

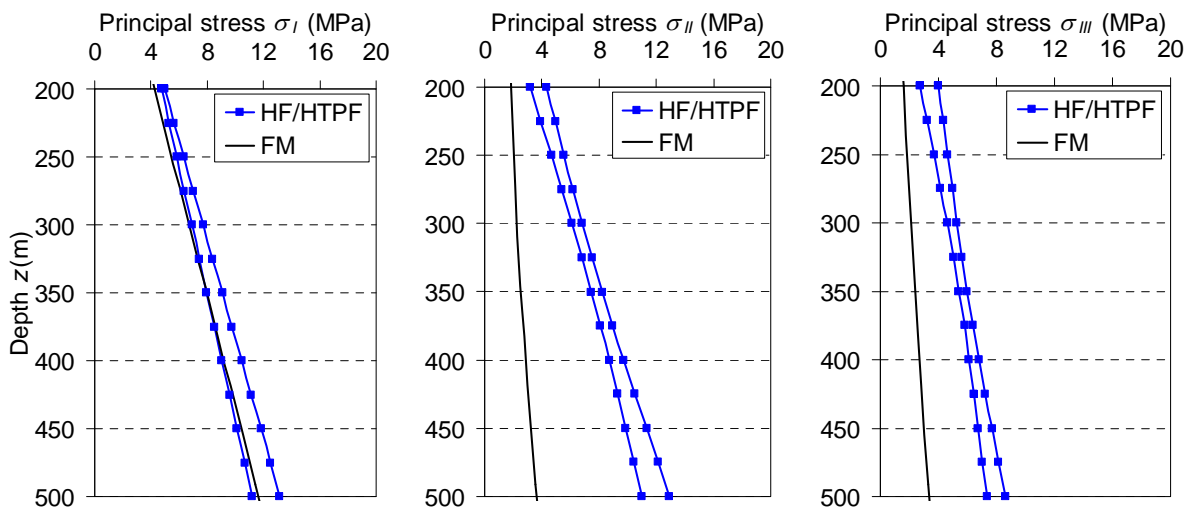


Figure 4: Variation of the magnitude of the principal stresses (σ_I , σ_{II} , σ_{III}) obtained from the inversion of the hydraulic data (HF/HTPF) and with the FLAC3D model (FM) run with gravity loading only as functions of depth.

In Figure 5, the results from the overcoring data only (as obtained in boreholes PD1 and PD2) are compared with the linearly elastic homogeneous model, as expressed in terms of the principal stress magnitudes. The lines represent the values computed with the FLAC3D model, and the dots represent the results from overcoring. The FLAC3D model results obtained for borehole PD2 are not presented because they are comparatively similar to the results obtained for borehole PD1.

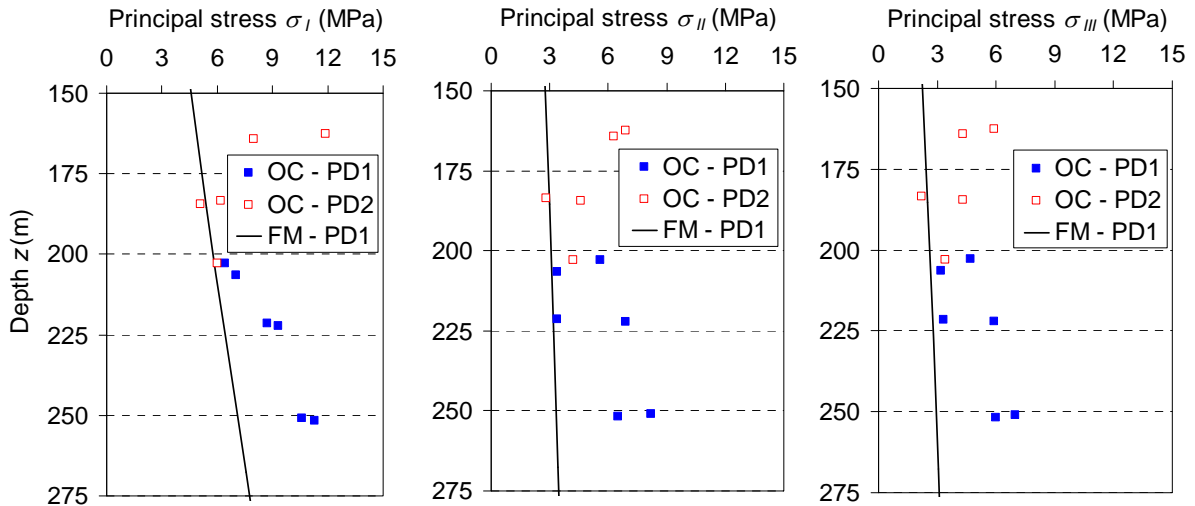


Figure 5: Variation of the principal stress magnitude (σ_I , σ_{II} , σ_{III}) as obtained by overcoring (OC) and as computed with the FLAC3D model (FM) run with gravity loading only as functions of depth.

Within the corresponding depth range, the maximum principal stresses (σ_I) obtained by overcoring and with the FLAC3D model are sub-vertical. The principal stresses σ_{II} and σ_{III} are sub-horizontal and of similar magnitudes. The figure shows that the measured sub-horizontal stresses are considerably larger than the calculated stresses. For the sub-vertical stresses, the measured and calculated stresses are only consistent in five of the eleven overcoring tests. In these tests, the differences between the measured and calculated stress values are less than 1.5 MPa.

Hence, the differences between the measured and calculated stresses obtained by overcoring and hydraulic testing are found to be larger than the uncertainties on the measurements, indicating that this model is not acceptable.

4 INFLUENCE OF FAULTS AND FRACTURED ZONES

The geological survey of the region highlights the existence of two fractured zones that include several sub-vertical fractures with a significant dispersion on their azimuths (Figure 6). The possible influence on the magnitude and orientation of the sub-horizontal stresses at location of hydraulic tests was therefore investigated. The FLAC3D model was used for a numerical analysis of this influence at the location of hydraulic tests.

The fractures constitute weakness planes and hence represent damage that can be simulated, in a very simple manner, by decreasing the elastic modulus values normal to them, thus resulting in a lower stiffness in the corresponding direction. In this numerical simulation, four assumptions are made: (i) the preferential directions of the weakness planes in fractured zones 1 and 2 are N120°E and N165°E, respectively, as shown in Figure 6; (ii) the weakness planes are vertical; (iii) the behaviour of the non-fractured zones is isotropic with the elastic properties obtained from uniaxial compression tests results; and (iv) the rock mass behaviour in the fractured zones is described by a transversely isotropic model with the planes of symmetry coincident with the weakness planes.

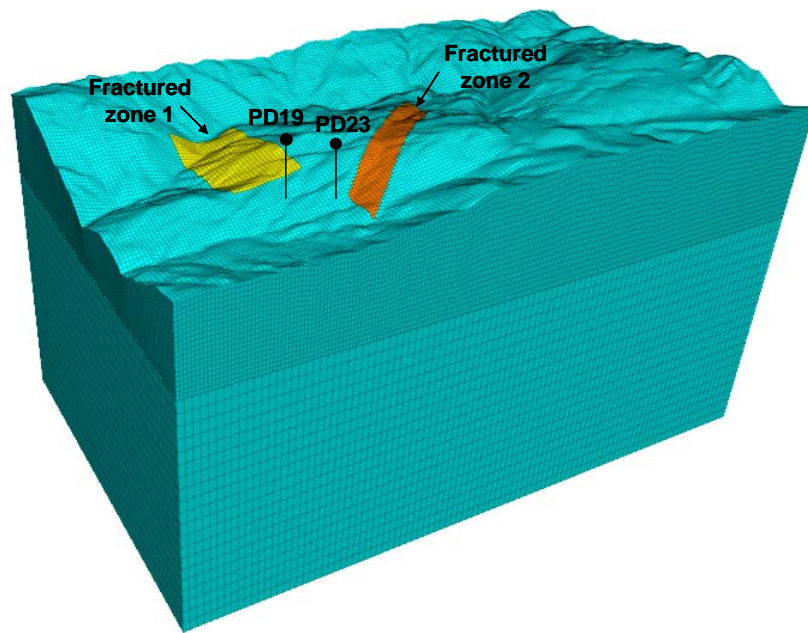
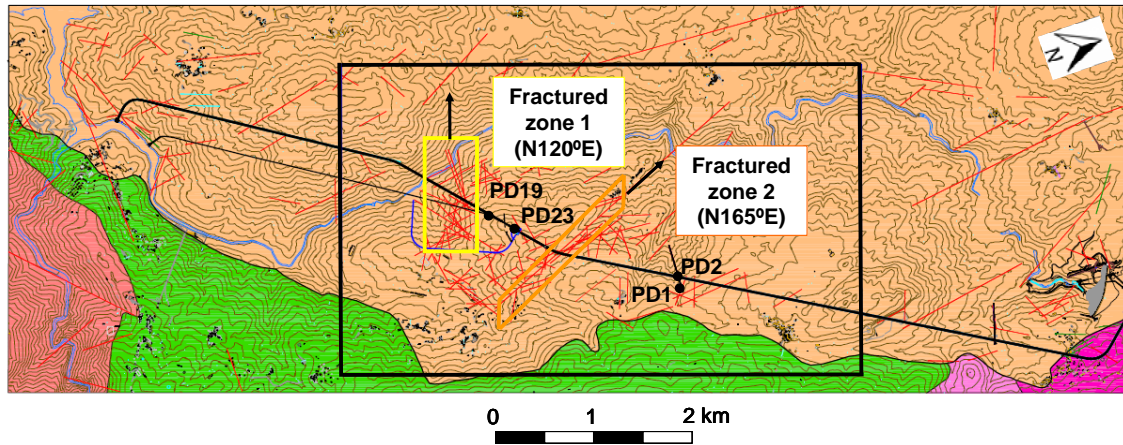


Figure 6: Location of the fractured zones in the FLAC3D model.

The transversely isotropic model is described by two angles that define the orientation of the planes of symmetry with respect to the North and five elastic constants: E_1 and E_3 are the elastic moduli in the plane of symmetry and normal to it, respectively; ν_{12} and ν_{13} are the Poisson's ratios characterising lateral contraction in the plane of symmetry when compression is applied in the plane and normal to it, respectively; and G_{13} is the shear modulus in the plane perpendicular to the plane of symmetry.

By considering the gravity loading, a parametric analysis was performed regarding the influence of the modulus E_3 normal to the planes of symmetry on the principal stress magnitude at the location of the hydraulic tests. This elastic modulus value decreased, first separately in fractured zones 1 and 2 and then in both zones. The cases that were considered are listed in Table 1.

As a simplification, the elastic constant G_{13} was calculated as a function of the other parameters using Saint Venant's principle, which is shown in the following equation:

$$G_{13} = \frac{E_1 E_3}{E_1 + E_3 + 2\nu_{13}E_1} \quad [7]$$

Table 1: Cases considered in the study of the influence of the elastic modulus E_3 on *in situ* stresses.

Case	Fractured zone	E_1 (GPa)	E_3 (GPa)	ν_{12}	ν_{13}	G_{13} (GPa)
R	1	45.0	45.0	0.25	0.25	18.0
	2	45.0	45.0	0.25	0.25	18.0
A	1	45.0	15.0	0.25	0.25	8.2
	2	45.0	45.0	0.25	0.25	18.0
B	1	45.0	45.0	0.25	0.25	18.0
	2	45.0	15.0	0.25	0.25	8.2
C	1	45.0	15.0	0.25	0.25	8.2
	2	45.0	15.0	0.25	0.25	8.2

The results were compared with those obtained in the reference case (R), in which the overall rock mass has an isotropic and elastic behaviour. Figure 7 shows the variation with depth of the sub-horizontal principal stress magnitudes obtained for borehole PD19. The results obtained in borehole PD23 were similar and are thus not presented. A comparison was performed with the respective stress profiles obtained from the inversion of the set of fifteen hydraulic tests with an 8-parameter model.

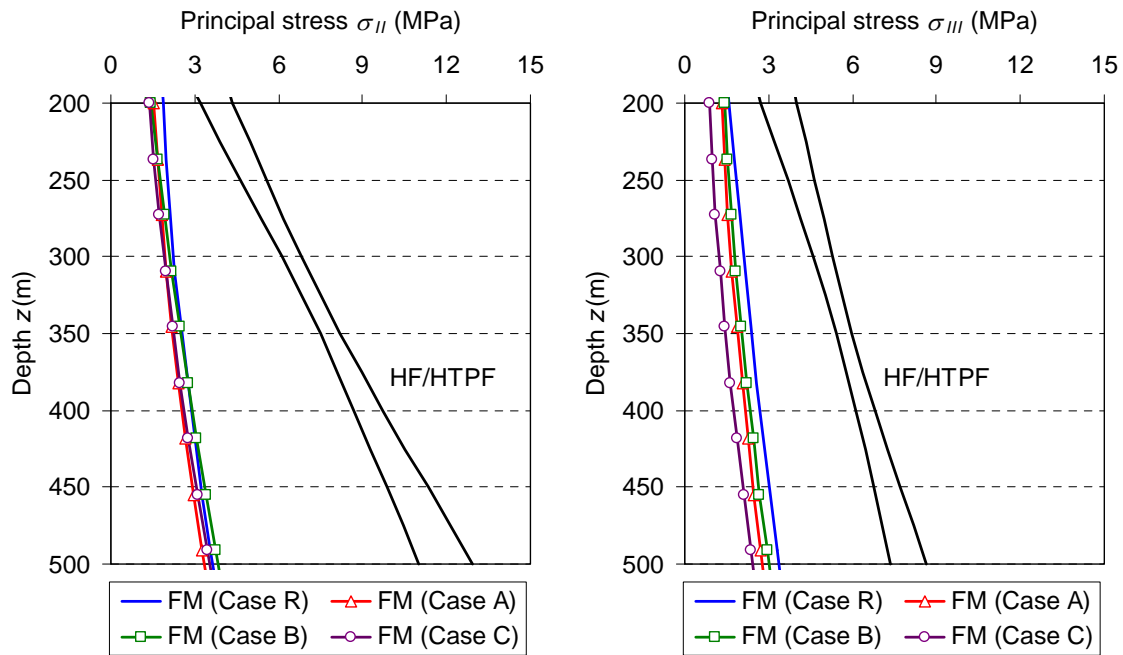


Figure 7: Variation with depth of the maximum (σ_{II}) and minimum (σ_{III}) sub-horizontal principal stresses obtained from the inversion of the hydraulic data (HF/HTPF) and with the FLAC3D model (FM) by considering the existing fractured zones.

Figure 7 shows that the inclusion of the fractured zones leads to maximum variations of 0.5 MPa and 1.0 MPa in the maximum and minimum sub-horizontal principal stresses, respectively, at a 500 m depth, and these variations are not significant. For all the cases, the discrepancies in the magnitudes of the two sub-horizontal principal stresses were less than 1.0 MPa. Because of this, the rotation of the maximum horizontal principal stress direction obtained with the FLAC3D model at a 500 m depth (between N50°E and N66°E) is not significant.

This finding shows that discrepancies between the FLAC3D model and the results from inversion cannot be explained by the presence of the fracture zones outlined by the geological survey.

5 TESTING THE EXISTENCE OF TECTONIC STRESSES

To improve the fit between the FLAC3D model and the data, the possibility of introducing a so-called tectonic component is considered, as proposed previously in the literature for different sites (Li *et al.* [6], McKinnon [7], Tonon *et al.* [8]). The horizontal stress components to be introduced in the model were calculated to reproduce the normal stress profiles obtained by hydraulic testing.

Several assumptions were made: (i) the rock mass exhibits a linear, isotropic and elastic behaviour; (ii) the total stress field may be decomposed into gravity and tectonic components; (iii) the vertical component is equal to the weight of the overlying material and is of gravitational origin; (iv) the vertical components of the far field tectonic stress tensor are zero; and (v) with exception of the zones close to the ground level, where the topography effects are important, the tectonic stresses were considered constant in depth.

Based on these assumptions, the normal stress ($\sigma_{n,mes}$) measured on each tested fracture plane can be decomposed into a normal component due to gravity ($\sigma_{n,grav}$) and a component associated with the tectonic ($\sigma_{n,tect}$) loading:

$$\sigma_{n,mes} = \sigma_{n,grav} + \sigma_{n,tect}. \quad [8]$$

Unit normal (S_{xx} , S_{yy}) and shear stress (S_{xy}) components were introduced in the model: uniform displacements at the lateral boundaries of the model to yield unit horizontal stress components for elements in contact with the basal boundary (Figueiredo *et al.* [9]). As a result, non-uniform and balanced stress distributions were generated at the lateral boundaries that consider the influence of topography effects on the stress field.

The normal stress magnitudes $\sigma_{n,Sxx}$, $\sigma_{n,Syy}$ and $\sigma_{n,Sxy}$ at the location of each tested fracture plane due to unit tectonic stress components S_{xx} , S_{yy} and S_{xy} were computed. The normal stress magnitudes due to tectonic loading ($\sigma_{n,tect}$) can be estimated as a linear combination of the unit response normal stresses according to the following equation:

$$\sigma_{n,tect} = A\sigma_{n,Sxx} + B\sigma_{n,Syy} + C\sigma_{n,Sxy}, \quad [9]$$

where the coefficients A , B and C are unknowns.

Substituting equation [9] into equation [8] yields the following:

$$\sigma_{n,mes} = \sigma_{n,grav} + A\sigma_{n,Sxx} + B\sigma_{n,Syy} + C\sigma_{n,Sxy}. \quad [10]$$

Denoting the right side of equation [10] $\sigma_{n,calc}$, the misfit in equation [1] is minimised to determine coefficients A , B and C . The following values are obtained:

$$A = 4.9, B = 5.1, C = 0.0$$

A comparison between the measured and computed normal stress (σ_n) magnitudes obtained when combining tectonic and gravity loadings is shown in Figure 8.

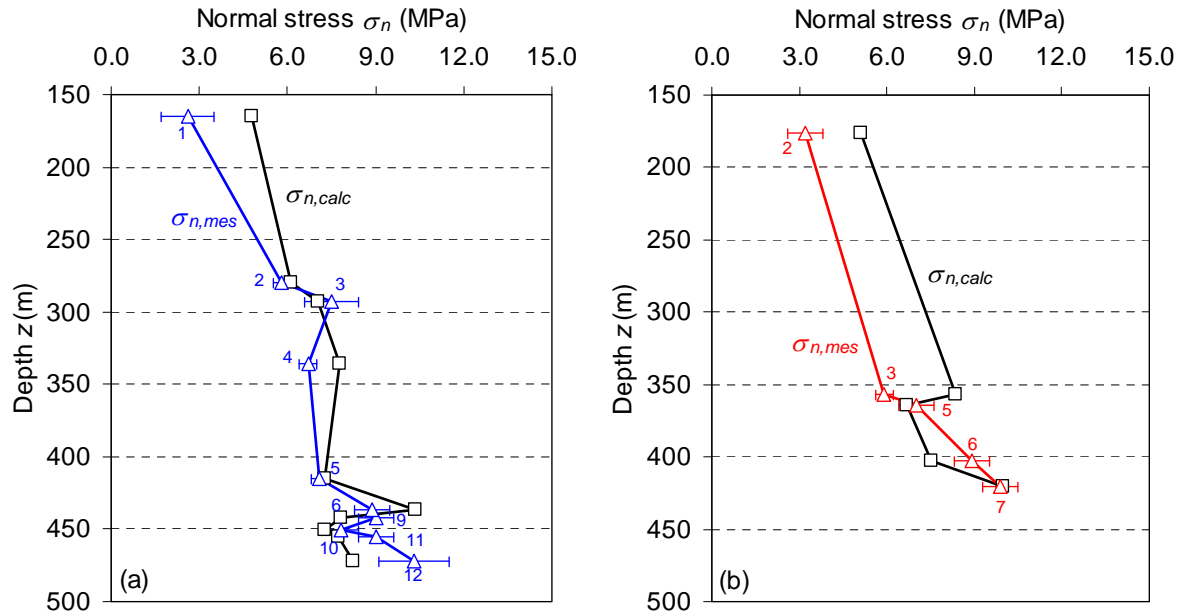


Figure 8: Variation with depth of the normal stress magnitudes as measured by hydraulic testing ($\sigma_{n,mes}$) and computed with the FLAC3D model ($\sigma_{n,calc}$) for the combined effect of gravity and tectonics in boreholes (a) PD19 and (b) PD23.

Figure 8 shows that the differences between the measured and calculated normal stress magnitudes are greater than the uncertainties on the measurements for approximately 60% of the tests. These differences may result from the various simplifying assumptions. However, note that the values for A , B and C that best fit the results are such that parameter C is null, whereas parameters A and B are similar, which means that to fit the FLAC3D model results with the data, compressive normal stresses of similar magnitudes and null shear stresses must to be introduced in the model. Furthermore, the mean orientation (N35°E) for the orientation of the maximum horizontal principal stress measured at a 475 m depth (see Part I) is nearly perpendicular to the direction given by the World Stress Map database (Figure 9), which shows that the tectonic stress in this region is

approximately orientated NO-SE. This analysis concludes that at the depth of the various stress measurements, the existence of a tectonic stress component is not likely.

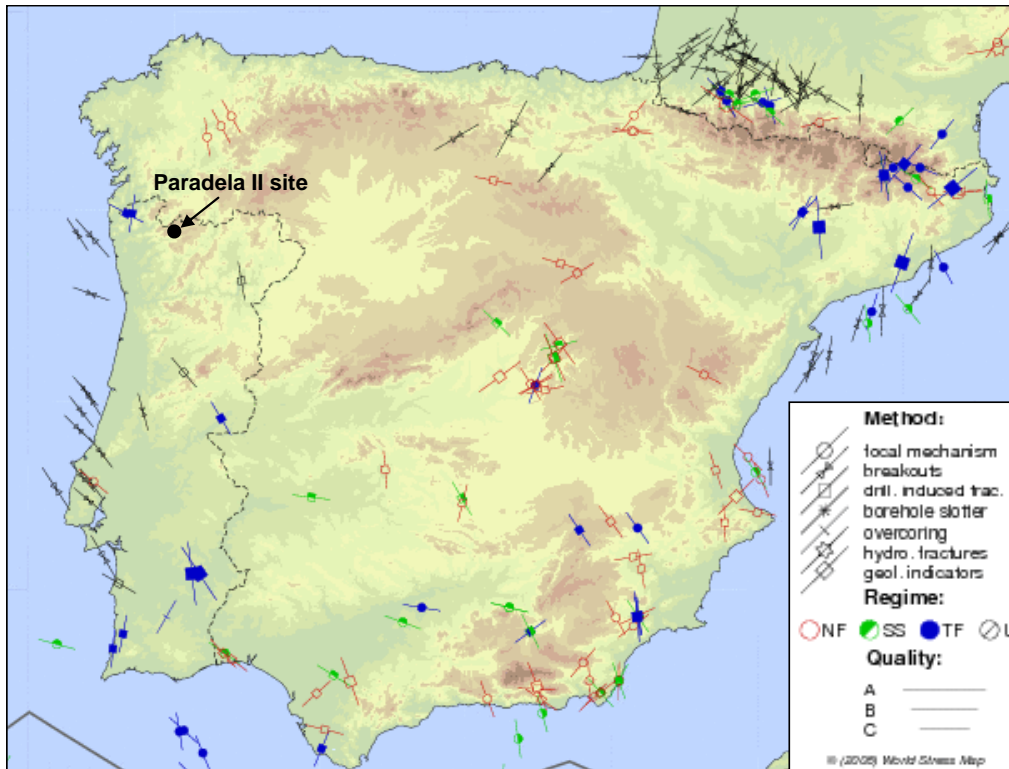


Figure 9: Orientation of the regional tectonic maximum horizontal compressive stress from the World Stress Map data base (Heidbach *et al.* [10]).

6 EXAMINING RHEOLOGICAL EFFECTS

The analysis conducted in this last section is based on the linearly elastic behaviour of the rock mass. In reality, the current stress state within a rock mass is the response of the material to a series of past geological events and depends on time. However, time effects are absent from an elastic analysis. In addition, the elastic parameters obtained from tests conducted on intact cores may be unrealistic in a simulation of rock mass behaviours at larger space and time scales because at a large space scale, the rock mass includes an important natural fracture network that may have a time-dependent behaviour. Creep, an important time-dependent effect in rock masses, is characterised by an increase in strain with time, and its influence on *in situ* stress distributions may be assessed by using a visco-elastic model (e.g., the Maxwell model). In this model, the time-dependent elastic modulus $E(t)$ and Poisson's ratio $\nu(t)$ are given by the following equations (Amadei and Stephanson [11]):

$$E(t) = E_0 e^{-(t/\xi)}, \quad [11]$$

$$\nu(t) = 0.5(1 - e^{-(t/\xi)}) + \nu_0 e^{-(t/\xi)}, \quad [12]$$

where E_0 and ν_0 are the short-term elastic modulus and Poisson's ratio, respectively; t is the time; and ξ is the relaxation time (time required for an exponential variable to decrease to $1/e$ of its initial value).

For large amounts of time, the long-term elastic modulus and Poisson's ratio approach zero and 0.5, respectively. Because simulating the transient stress field is not important for interpreting the stresses measured *in situ*, an equivalent linearly elastic material with softer elastic properties (elastic modulus E' and Poisson's ratio ν') than the properties obtained from uniaxial compression tests performed in intact cores is proposed for considering rheological effects (Figure 10).

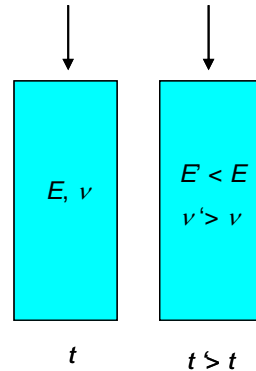


Figure 10: Soft linearly elastic material used for considering rheological effects.

Because changing the elastic modulus does not induce changes in the stress field for a homogeneous rock mass, the rheological effects were modelled by increasing the Poisson's ratio value. The FLAC3D model was used in the inversion of the Poisson's ratio value to minimise the misfits defined by equations [1] to [3]. The results presented in Table 2 show that a Poisson's ratio value of 0.47 provides a satisfactory fit between the results obtained from both hydraulic and overcoring data and those computed with the model. Equation [6] was used ($W=1$) to calculate a 90% confidence interval for the minimum of the global misfit. The interval obtained in this way corresponds to a Poisson's ratio value that ranges between 0.45 and 0.49.

The profiles of the measured and calculated normal stresses (σ_n) due to gravity loading with a 0.47 Poisson's ratio are shown in Figure 11.

Table 2: Variation of the misfit value with the Poisson's ratio.

ν	ψ^{HF}	ψ^{OC}	ψ^{HFOC}
0.25	56.7	43.9	295.0
0.35	37.1	38.5	126.3
0.45	13.2	35.3	16.4
0.46	11.8	35.1	13.2
0.47	10.9	34.9	11.5
0.48	12.2	34.3	14.2
0.49	12.6	34.6	14.9

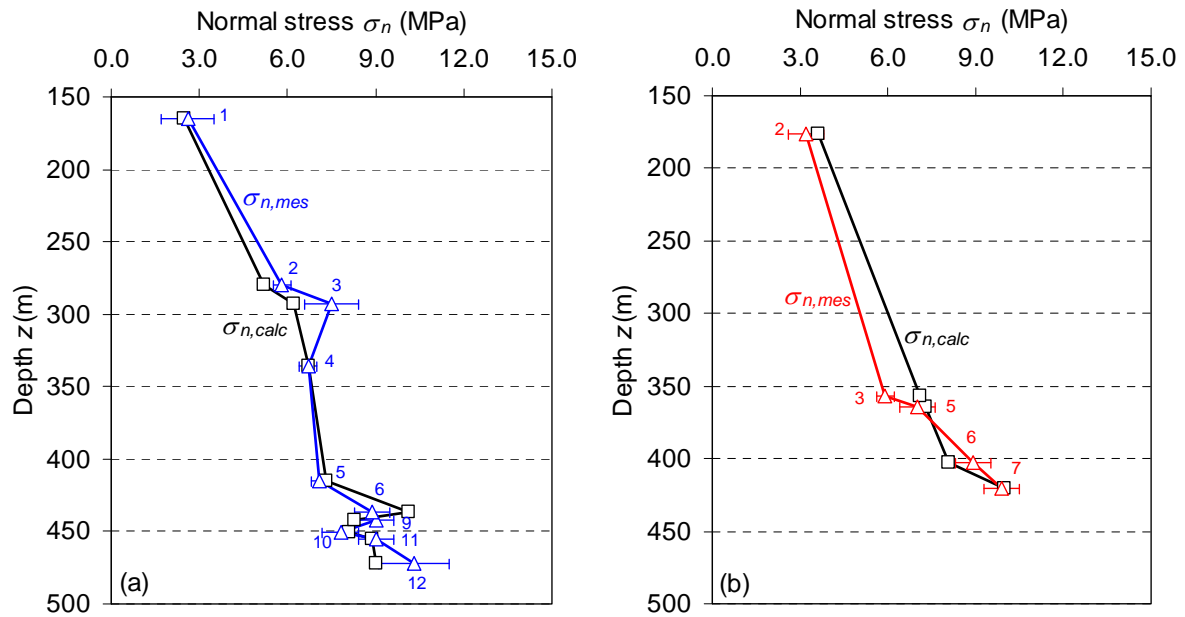


Figure 11: Variation with depth of the normal stress magnitudes as measured by hydraulic testing ($\sigma_{n,mes}$) and computed with the FLAC3D model with $\nu=0.47$, considering gravity effects only, in boreholes (a) PD19 and (b) PD23.

The difference between the measured and calculated normal stress magnitudes is less than three standard deviations of the measurements in approximately 75% of the tests. In the remaining tests, this difference varies between 1.2 MPa and 1.3 MPa and is considered acceptable given the many simplifying assumptions implied by this model.

A comparison between the principal stress profiles obtained with the linearly elastic model with a Poisson's ratio of 0.47 and those obtained from the inversion of the hydraulic data with an 8-parameter model is shown in Figure 12. This comparison shows that at a depth of 500 m, the average differences are 0.3 MPa for the sub-vertical (σ) stress and 1.0 MPa for the minimum sub-horizontal (σ_{III}) principal stress. However, this difference reaches 2.4 MPa for the maximum sub-horizontal stress (σ_I) and is larger than expected. In fact, the 8-parameter model considered in the inversion leads to a wide range of possible stress field solutions that depend on the large implicit uncertainty associated with the hypothesis of uniformity of the stress field. In practice, various heterogeneous zones exist, as demonstrated by the inclined fractures observed for some of the hydraulic fracturing tests (see Part I).

The measured and calculated stresses at the location of the small flat jack and overcoring tests were compared considering a Poisson's ratio value of 0.47 in the FLAC3D model. This comparison is shown in Figures 13 and 14 in terms of the normal stress magnitudes for small flat jack tests and principal stress magnitudes for overcoring tests, respectively.

Figure 13 shows that for approximately 55% of the small flat jack tests, the discrepancy between the measured and calculated normal stresses is greater than 1.0 MPa. Figure 14 shows that with the exception of the sub-vertical principal stresses (σ) in borehole PD1 between depths of 225 m and 250 m and the two overcoring tests conducted close to the adit and the flat jack tests, approximately 80%

of the measured and computed principal stresses are in satisfactory agreement (the difference between both values is less than 1.5 MPa).

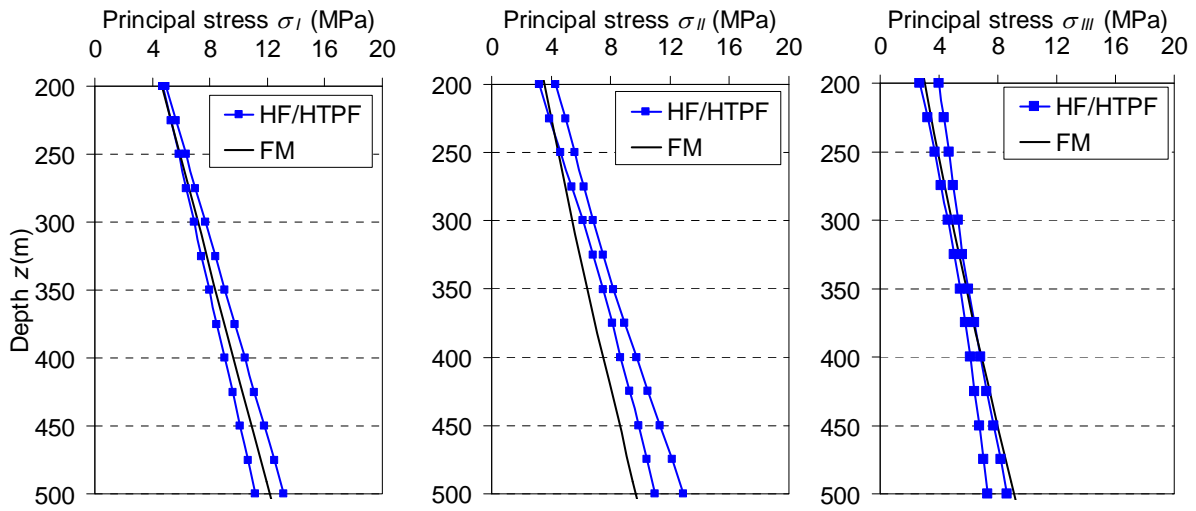


Figure 12: Variation with depth of the magnitude of the principal stresses (σ_I , σ_{II} , σ_{III}) obtained from the inversion of the hydraulic data (HF/HTPF) and with the FLAC3D model (FM) with $\nu=0.47$ considering gravity effects only.

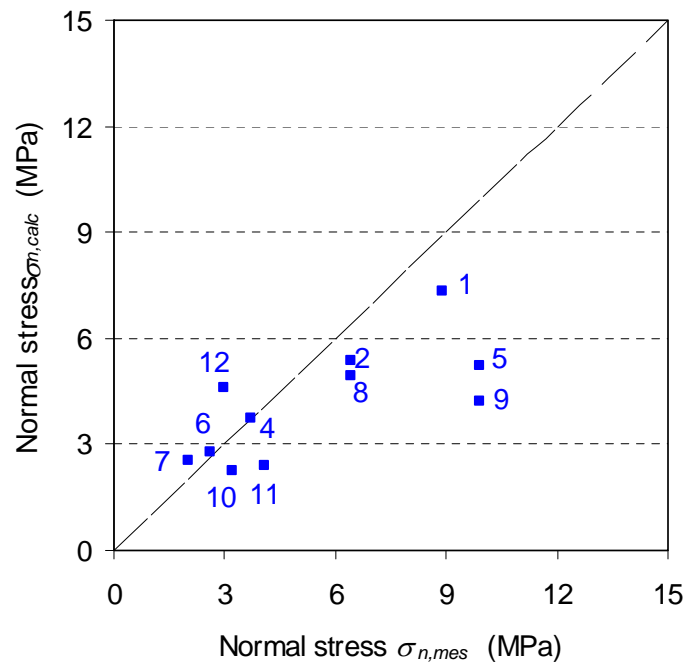


Figure 13: Comparison of the magnitudes of the normal stresses obtained by small flat jack technique ($\sigma_{n,mes}$) and with the FLAC3D model ($\sigma_{n,calc}$) with $\nu=0.47$ considering gravity effects only.

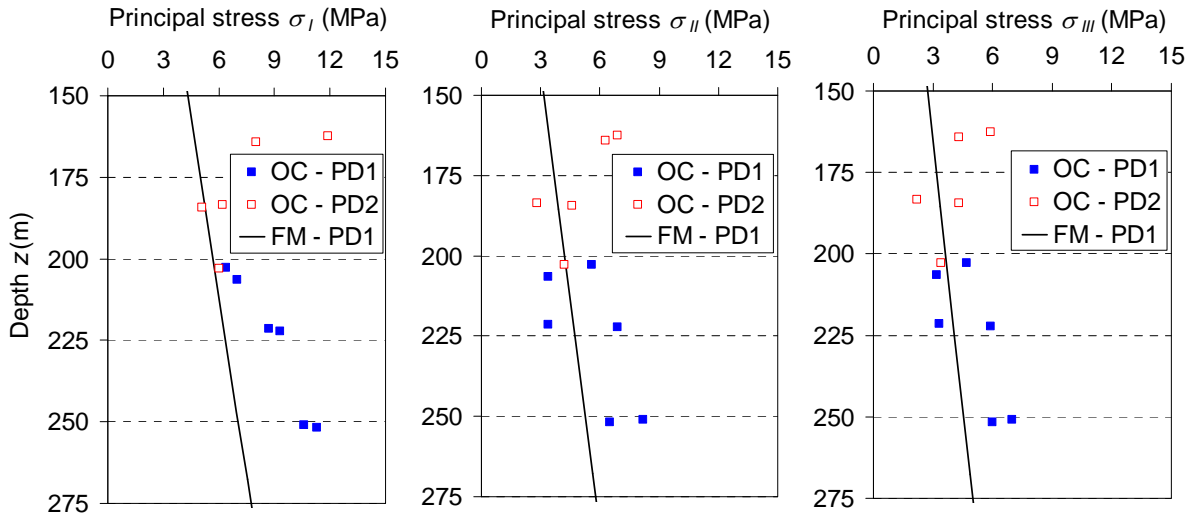


Figure 14: Variation with depth of the magnitude of the principal stresses (σ_I , σ_{II} , σ_{III}) obtained by overcoring testing (OC) and with the FLAC3D model (FM) with $\nu=0.47$ considering gravity effects only.

Hence, most of the hydraulic and overcoring data can be explained by a linearly elastic massif under a gravitational load provided that the Poisson's ratio for the equivalent material is considerably larger than that considered for the short-term response during uniaxial compression tests, which leads to conclude that the large-scale long-term stress field in this granitic massif is controlled by shear stress relaxation along the various fractures and faults that affect this massif.

However, this simple model does not explain most of the small flat jack tests nor the two overcoring tests close to the adit. It may be proposed that the equivalent material to be considered near the adit must take into account damages caused by blasting during the construction of the adit. Furthermore, for such a material, plasticity is likely to be considered when analysing the local stress components.

7 DISCUSSION AND CONCLUSIONS

Hydraulic and overcoring tests as well as small flat jack tests were conducted for the design of an underground hydroelectric power scheme located in a mountainous region of northern Portugal. These results and a preliminary interpretation were presented in Part I of this paper.

In Part II, a single linearly elastic model has been developed that helps extrapolate the *in situ* results to any point of interest for the design of the hydroelectric scheme. Several issues have been discussed, such as the influence of the compliance of local fractures and faults, the existence of tectonic stresses and the perturbations associated with the existing adit used for the small flat jack measurements.

None of these effects were found to have a significant impact on the stress determined at the various measurement locations. However, an equivalent linearly elastic model was found to fit the results reasonably well provided that a very high Poisson's ratio (0.47) is considered. The model involves a 15 km² area with a 2.5 km vertical extension and fits approximately 80% of the measurements away from the adit used for flat jack and overcoring tests. This Poisson's ratio value is

considerably larger than that measured on the cores, a feature that is attributed to the creeping of the material filling the various fractures and faults that affect the massif.

However, this model does not fit the results from the flat jack and overcoring tests conducted in the immediate vicinity of the adit. For this domain, it seems likely that blasting damages associated with the construction of the adit altered the local material properties such that the simple linearly elastic model is not relevant.

ACKNOWLEDGEMENTS

This work was funded by the Portuguese Laboratory for Civil Engineering (LNEC) and the Foundation for Science and Technology (FCT) PhD grant SFRH/BD/68322/2010. Authorisation by EDP-Energies of Portugal to publish the stress measurement results obtained at the Paradela II site are acknowledged.

REFERENCES

- [1] Itasca. FLAC3D, Version 4.0. User's Manual. Itasca Consulting Group, Minneapolis; 2009.
- [2] Gephart W, Forsyth W. An improved method for determining the regional stress tensor using earthquake focal mechanism data: application to the San Fernando Earthquake Sequence. *Journal of Geophysical Research* 1984; 89: p. 9305–20.
- [3] Parker RL, Mcnutt MK. Statistics for one-norm misfit measure. *Journal of Geophysical Research* 1980, 85: p. 4429–30.
- [4] Gioda G, Sakurai S. Back analysis procedures for the interpretation of field measurements in geomechanics. *International Journal for Numerical and Analytical Methods in Geomechanics* 1987, 16: p. 555–83.
- [5] Yin JM, Cornet FH. Integrated stress determination by joint inversion of hydraulic tests and focal mechanisms. *Geophysical Research Letters* 1994; 21: p. 219–32.
- [6] Li G, Mizuta Y, Ishida T, Li H, Nakama S, Sato T. Stress field determination from local stress measurements by numerical modelling. *International Journal of Rock Mechanics and Mining Sciences* 2009; 46: p. 138–47.
- [7] McKinnon, SD. Analysis of stress measurements using a numerical model methodology. *International Journal of Rock Mechanics and Mining Sciences* 2001; 38: p. 699–709.
- [8] Tonon F, Amadei B, Pan E, Frangopol DM. Bayesian estimation of rock mass boundary conditions with applications to the AECL underground research laboratory. *International Journal of Rock Mechanics and Mining Sciences* 2001; 38: p. 995–1027.
- [9] Figueiredo B, Cornet FH, Lamas L, Muralha J. Effect of topography on distribution of *in situ* stresses due to gravity and tectonic loadings at Paradela site. *Proceedings of the EUROCK 2012–Rock Engineering and Technology for Sustainable Underground Construction*. Stockholm; 2012.

- [10] Heidbach O, Tingay M, Barth A, Reinecker J, Kurfeß D, Müller B. The release of the World Stress Map (available online at www.world-stress-map.org); 2008.
- [11] Amadei B, Stephansson O. Rock stress and its measurements, Chapman and Hall Publ. London; 1997